NASA-Technical Memorandum 88346

USAAVSCOM Technical Report 87-A-5

Digital Control of Highly Augmented Combat Rotorcraft

Mark B. Tischler

May 1987

National Aeronautics and Space Administration

US ARMY AVIATION SYSTEMS COMMAND

AVIATION RESEARCH AND TECHNOLOGY ACTIVITY

NASA-Technical Memorandum 88346

USAAVSCOM Technical Report 87-A-5

Digital Control of Highly Augmented Combat Rotorcraft

Mark B. Tischler, Aeroflightdynamics Directorate, U.S. Army Aviation Research and Technology Activity, Ames Research Center, Moffett Field, California

May 1987

NASA

National Aeronautics and Space Administration

Ames Research Center
Moffett Field, California 94035

US ARMY
AVIATION
SYSTEMS COMMAND

AVIATION RESEARCH AND TECHNOLOGY ACTIVITY
MOFFETT FIELD, CA 94305-1099

TABLE OF CONTENTS

ACKNOWLEDGMENTS

This report is the culmination of a three-year effort that began with two excellent courses on digital control given by Professors Gene F. Franklin and Arthur E. Bryson, Jr., at Stanford University.

The control systems analysis program, LCAP2, was graciously provided by The Aerospace Corporation. The program's author, Mr. Eugene A. Lee, gave me a great deal of assistance during the long process of adapting the program to the VAX computer. Mr. Lloyd T. Lim spent two summers at NASA improving the program's capabilities and writing the graphics routines.

Special thanks go to Mr. Edwin W. Aiken, Dr. Robert T. N. Chen, Dr. J. Victor Lebacqz, and Kathryn B. Hilbert for their many helpful suggestions during this research and their conscientious proofreading and editing of the drafts.

Many thanks also go to Catharine P. Levin and Ms. Cassandra L. Parker for typing the initial drafts of this report as a personal favor to me. I am also indebted to the NASA Publications Branch, Graphics Branch, and D-K Associates for their efforts in the production of the final version.

SUMMARY

Proposed concepts for the next generation of combat (scout/attack) helicopters are to be embodied in a complex, highly maneuverable, multiroled vehicle with avionics systems which are as important to mission success as the airframe itself. Single pilot and nap-of-the-Earth operations require handling qualities which minimize the involvement of the pilot in basic stabilization tasks. To meet these requirements will demand a full authority, high-gain, multimode, multiply-redundant, digital flight-control system. The gap between these requirements and current low-authority, low-bandwidth operational rotorcraft flight-control technology is considerable. This research aims at smoothing the transition between current technology and advanced concept requirements. The report: (a) extensively reviews the state of the art of high-bandwidth digital flight-control systems; (b) exposes areas of specific concern for flight-control systems of modern combat; and (c) illustrates the important concepts in design and analysis of high-gain, digital systems with a detailed case study involving a current rotorcraft system.

Frequency-domain methods for design and analysis are stressed in this report as essential for the practical implementation of high-gain control systems for rotorcraft. Approximate and exact methods are explained and illustrated for treating the important concerns which are unique to digital systems. Proposed specifications and flight-test data concerning the handling qualities of scout/attack rotorcraft imply restrictions on the maximum effective time delay which must be carefully considered in the design process.

I. INTRODUCTION

Proposed concepts for the next generation of combat (scout/attack) rotorcraft are to be embodied in a complex, multirole vehicle with avionics systems which will be as important to mission success as is the airframe itself (ref. 1). Flight, weapons, and propulsion-control systems will be fully integrated with displays and numerous input modalities (e.g., hand, head, and voice controllers). Handling quality characteristics will be tailored for specific tasks and will vary greatly. Precision flightpath control and inherent tight attitude stability are required for nap-of-the-Earth and hover conditions, especially in degraded visual environments and single-pilot operations; while agility and high maneuverability are required for air-to-air combat capable rotorcraft.

This requirement for increased maneuverability suggests the introduction of very unstable bare airframe configurations, as has been demonstrated in recent fixed-wing combat designs. Therefore, unlike the previous generation of military rotorcraft, modern rotorcraft will have full-time, full authority, highly redundant and reliable, stability-and-control augmentation systems (SCAS). Fail/operate systems rather than current fail/off systems will be used because the high degree of bare airframe instability and coupling will preclude SCAS-off flight entirely. The requirement to survive in an electronically hostile environment leads to current design concepts which emphasize optically transmitted flight-control commands. Clearly, these requirements dictate avionics systems which are much more sophisticated than those employed in the present state of the art in fleet rotorcraft.

In order to meet all of the above requirements, the modern combat rotorcraft will feature a high-gain, multiply-redundant, digital flight-control system. Such systems will allow the flexibility needed to realize multiroled, task-oriented handling qualities, and full systems integration. Digital implementation also permits the use of complex nonlinear flight-control laws, mode changing, and gain scheduling. As important an aspect of modern digital systems is the detection of failures in sensors, actuators, and computers. Automatic reconfiguration in flight enables the modern rotorcraft to survive in the hostile environment even after multiple system failures.

The motivations for developing high gain, digital systems for fixed-wing combat aircraft were similar to those cited. Ten years of difficult lessons have shown, however, that the advantages of such high-bandwidth systems cannot be realized without careful attention to design and implementation details. Among the best documented examples of fixed-wing, digital flight-control system development are the AFTI/F-16, F-18, DFBW F-8, F-104-G, and the Space Shuttle. The literature[1] (refs. 2-5) indicates a number of problems common to many of the first generation of

[1]Lock, W. P.: Presentation on F-8 DFBW Control System Design and Testing for Panel Discussion; Design and Flight Test of Critical Systems. AIAA Aerospace Conference and Show, Los Angeles, CA, 1985.

digital high-gain systems. These include insufficient attention to, or appreciation of:

1. The importance of high-frequency dynamics (filters) and actuator limiting in the design and gain selection process.
2. The importance of the total effective time delay (τ_e) to piloted handling qualities.
3. The details of implementing the digital flight control laws and software architecture.
4. The difficulty during simulator testing of effectively exposing latent tendencies for pilot-induced-oscillation (PIO) in high workload tasks.

As a result of these problems, many of the first generation fixed-wing digitally controlled aircraft underwent considerable modification to correct unsatisfactory (and in some cases unsafe) handling quality deficiencies (refs. 2,3,5). These modification efforts were often made after the initial software release and flight tests and, therefore, involved a substantial increase of time and cost associated with the needed additional flight testing.

Modern combat rotorcraft, with their requirements for precision nap-of-the-Earth (NOE) and hover flight characteristics in degraded environments, will have onboard sensor systems of substantially greater complexity than did their first generation fixed-wing counterparts. The AH-64 (Apache) US Army rotorcraft is the first of this new class of systems (ref. 6). The sensor package for this aircraft includes devices to measure attitude, attitude rate, velocity, and inertial position. This package contains about twice the number of sensors employed in modern fixed-wing combat aircraft. However, the relatively conventional (bare-airframe) flying qualities of the Apache allow the use of a limited authority automatic flight-control system (15% of the available control power), thereby reducing the level of needed stability-and-control augmentation, and digital system reliability.

The first attempt to develop a full flight envelope, full authority digital fiber-optic flight-control system is the Advanced Digital Optical/Control System program (ADOCS), a demonstrator system being tested on the UH-60 Black Hawk aircraft (refs. 7 and 8). A high-bandwidth, model-following control-system design is employed to provide task-tailored handling qualities for a variety of missions. The objective of this program is to show the potential for improved performance and survivability using the digital/optical system and to demonstrate the technology required for the next generation of combat rotorcraft--the US Army's light helicopter program (LHX).

The Army's Advanced Rotorcraft Technology Integration (ARTI) program is also directed at demonstrating LHX technology. Under this program, the major United States helicopter manufacturers are developing advanced test-bed vehicles to demonstrate key LHX flight control and display technologies. Since these efforts are ongoing and much of the design and performance details are proprietary, the available documentation is limited. An informative discussion of the design and flight testing of the Bell Helicopter ARTI demonstrator--a highly modified B-249--is given in reference 9.

The needed improvements to the current state of the art in helicopter control systems are considerable if the preceding capabilities are to be achieved. The high inherent complexity of modern rotorcraft make such strides even more difficult than were those tackled by the fixed-wing community. Thus, it is essential to capitalize on relevant and extensive experience with high-gain digital systems outside of the rotorcraft community.

The specific objectives of this study are to:

1. Extensively review the state of the art of high-bandwidth digital flight-control systems.
2. Expose areas of specific concern for flight-control systems of modern combat rotorcraft.
3. Illustrate the important concepts in design and analysis of high-gain digital systems with a detailed case study of a current rotorcraft system.

The history of rotorcraft development in the last ten years has shown that the amount of time required from design conception to final certification has been much higher in the rotorcraft community than in the fixed-wing community.[2] With the addition of these new and highly complex avionics systems, the potential for greatly increasing this development period must be confronted. Therefore, the overall goal of this study is to provide practical methods for the analysis and design of high-gain digital control systems for rotorcraft. Hopefully, using these methods will reduce the heavy reliance on flight tests and post-design modification so commonplace in the development of first generation digital systems in the fixed-wing community.

The remainder of this report is organized into three major sections: Section II presents an overview of high-bandwidth analog and digital systems for rotorcraft and relates documented fixed-wing experience where it is appropriate. This section concentrates on introducing system analysis and design concepts. Section III presents a detailed case study based on the ADOCS Black Hawk pitch-attitude system. The objective here is to illustrate the important analysis and design techniques for digital flight-control systems and expose areas of concern. Important conclusions and recommendations are summarized in Section IV.

[2]Panel discussion at International Conference on Rotorcraft Basic Research. Sponsored by the American Helicopter Society and the U.S. Army Research Office, Research Triangle Park, North Carolina, Feb. 1985.

II. OVERVIEW OF ROTORCRAFT FLIGHT-CONTROL SYSTEMS, ANALYSIS, AND DESIGN METHODS

This section introduces the basic concepts of high-bandwidth analog and digital flight-control systems, and draws on published experience where appropriate. The methods discussed in this report all come under the broad characterization of "classical control techniques." While "modern control methods" could clearly be used to design rotorcraft systems, the author believes that the salient physical concepts can best be illustrated with the classical frequency-domain descriptions.

In Section II.A, a generic, high-bandwidth, analog flight-control system for a combat helicopter is introduced. The selection of an analog system allows a discussion of the implications of high-bandwidth flight-control systems separate from the specific concerns of the digital implementation of such high-bandwidth systems. The digital counterpart of the generic flight control system is presented in Section II.B, where the basic concepts of sampling and data reconstruction are introduced. Section II.C discusses methods of analysis and design of high-bandwidth digital flight-control systems; this discussion is separated into three parts. First, the implications of high-bandwidth rotorcraft control systems are considered. Second, approximate design methods for high-bandwidth digital systems using a high sample rate are discussed. Since the closed-loop dynamics of the high sample rate digital system are nearly the same as its analog counterpart, approximate design and analysis methods are often suitable. The final discussion focuses on the analysis of digital systems, for which the detailed sampler and data reconstruction dynamics have a significant impact. Here, direct digital analysis methods are used.

II.A Generic High-Bandwidth Analog Flight-Control System for Combat Rotorcraft

A generic, high-bandwidth, analog model-following flight-control system for a combat rotorcraft is shown in figure 1. Pilot command inputs (δ_s) are through a multiaxis sidestick (a less space and weight consuming controller than is the standard mechanical centerstick and its related linkages). The sidestick controller may be rigid or allow limited deflection, and can be either force or displacement sensing. Electrical or optical signals from the controller are transmitted to the flight-control system. Pilot commands are first processed through dead-bands and filtering functions, and are then used to drive the command model (M(s)). The command model contains desired vehicle characteristics as appropriate for the task-tailored mode. For example, an attitude-command system may be desirable for low speed and hover, while a rate-command system may be preferable for high-speed maneuvering. In this case, the command model for the attitude-command system might contain a second-order transfer function for attitude response to stick input; the parameters of the transfer function are based on appropriate values of stick sensitivity, dominant mode damping, and natural frequency. The output from the command model is the desired closed-loop system response, denoted by (θ_m) in figure 1.

Following the command model is a feedforward element (F(s)). This "quickening" offsets the feedback damping and natural (open-loop) damping which would otherwise retard the command response. The output from the feedforward element is the command signal denoted by δ_{com} in figure 1.

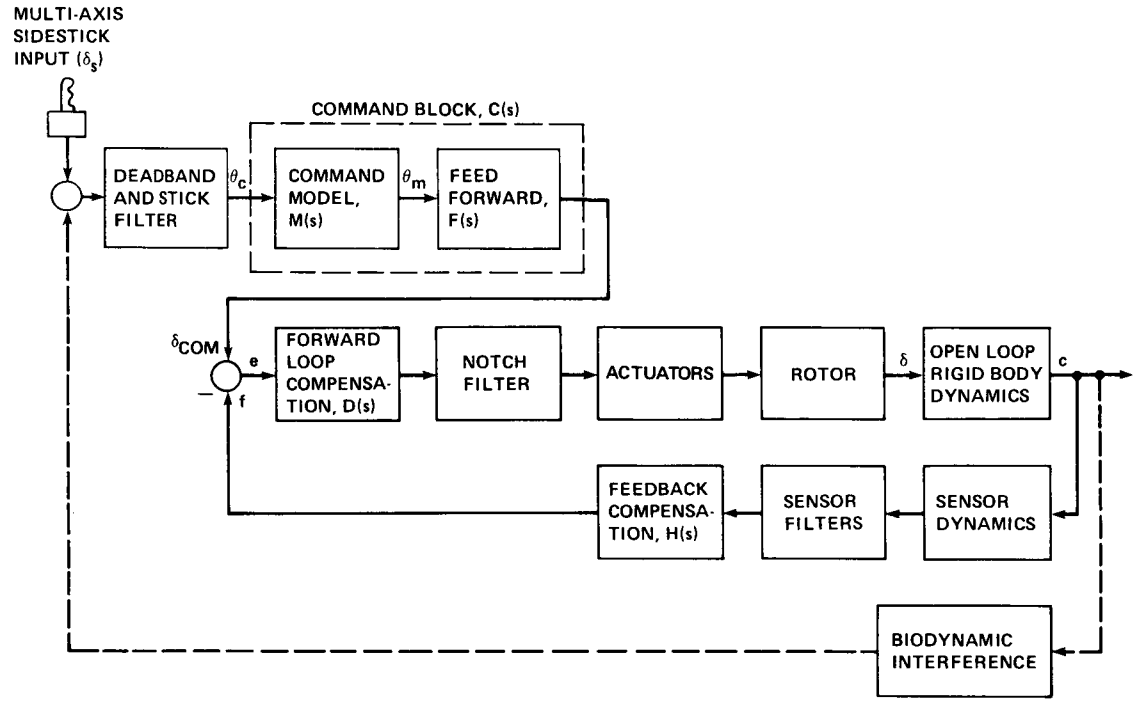

Figure 1.- Generic high-bandwidth analog flight-control system.

The feedback signal (f) is derived from the sensors. For the ADOCS system, sensors provide measurements of attitude, inertial velocity, and inertial position. The filters shown in figure 1 are used to remove undesirable noise components or, in some cases, to estimate mathematically unmeasured vehicle states based on available system parameters. For example, the F-18 digital system (ref. 3) uses a sophisticated Kalman filtering scheme to derive a sideslip rate ($\dot{\beta}$) signal, and the ADOCS system (ref. 8) estimates pitch rate from pitch-attitude measurements and uses complementary filtering to derive a suitable airspeed signal. Feedback compensation (H(s)) may also be highly sophisticated or very simple, as in the pure feedback gain approach used in the AH-64 (ref. 6) and ADOCS systems.

The command and feedback signals are compared to produce the error signal (e). Forward loop compensation (D(s)) is applied to the signal to obtain the desired open-loop response characteristics (f/e) and crossover frequency (ω_c). In the X-29 (forward-swept wing) and Space Shuttle systems, the forward-loop compensation includes both proportional and integral paths (ref. 5).[3] In the ADOCS design,

[3]Chin, J.: Presentation on X-29 Control System and Design and Testing given at Panel Discussion; Design and Flight Test of Critical Digital Systems. AIAA Aerospace Engineering Conference and Show, Los Angeles, CA, 1985.

forward-loop integrators were ruled out because of concerns over failure and redundancy management. The ADOCS system runs fully asynchronously without cross-channel communication (which is not necessarily desirable), so forward-loop integrators would quickly create discrepancies between the channels and trip the failure detectors. The Bell-ARTI demonstrator uses proportional and integral paths in the forward loop to reduce sensitivity to low-frequency variations in the airframe dynamics (ref. 9). System trips caused by the discrepancies between the asynchronous (duplex) channels are avoided by employing cross-channel communication.

As shown in figure 1, notch filter compensation may also be required in the forward (and feedback) path to eliminate undesirable interactions with the high-frequency rotor and structural dynamic modes. In fixed-wing aircraft with conventional controllers, the notch filter is typically inserted in the feedback path to avoid exciting the first wing-bending mode with the sensor signals. In rotorcraft with conventional sticks, notch filters are often included to eliminate n/rev and structural vibration pickup in the sensors. If a small deflection stick is used, the notch filters must be moved to the forward stabilization loop to also remove significant and undesirable biodynamic inferference ($c \rightarrow \delta_s$) (ref. 10), as shown in the dashed path in figure 1 (see Section III.F.2 for further discussion).

Besides the loop-gain reductions needed to attenuate biodynamic interactions, the high-gain feedbacks may aggravate the rotor lead-lag dynamics. Such a problem has already led to the 40% reduction of feedback gains (and an equivalent crossover frequency reduction) in the ADOCS flight-control system as compared to the simulation values. Properly placed notch filters may be useful in attenuating these and other rotor-mode interactions, without requiring drastic crossover frequency reductions.

High-gain flight-control systems require high-bandwidth/high-authority actuators. The details of the rate and deflection limit characteristics are very important for realizing a successful highly augmented system.

The dominant system component in rotorcraft flight-control design is the rotor system itself. In the hover flight condition, the effective rotor system bandwidth is roughly on the order of the rotor rpm; this frequency may be only three or four times greater than the closed-loop system bandwidth. Thus, like the structural-mode stability problem in fixed-wing aircraft, the large phase lags introduced by the rotor flapping response impose dominant limitations on the obtainable system bandwidth. Since vehicle control is achieved through the (rate and displacement limited) rotor tip-path-plane system, it is not possible to compensate for these lags in the feedforward element. This limitation leads many current design concepts to feature higher bandwidth rotor systems--such as the hingeless rotor.

For high-bandwidth systems, the classical low-frequency flight dynamics are largely masked by the flight-control system parameters (ref. 11). The maximum achievable bandwidth is determined by the high-frequency dynamic characteristics, especially those which are due to rotor dynamics and to the various filters. These high-frequency dynamics, which have often in the past been only crudely estimated (or totally ignored), now dominate the analysis-and-design process. A good example

of the recent appreciation of these high-frequency dynamics is in the ADOCS design. Feedback gains were calculated based on an extremely simple (but adequate) rigid-body dynamics model ($c/\delta = K/s^2$) and detailed model of the high-frequency rotor and actuator dynamics (ref. 7). Many of the recent design, analysis, and identification approaches are based on frequency-domain (Bode) techniques which clearly expose the high-frequency details. Attempts to implement high-bandwidth systems whose designs are based on time domain methods (e.g., Linear Quadratic Gaussian (LQG)) have often proved unsuccessful because the dynamic compensators were too highly tuned to the assumed high-frequency dynamics (e.g., AFTI/F-16, ref. 2). Thus, when the compensators are used with the actual vehicle with additional unmodeled dynamics, unacceptable system sensitivity and instability result. A parameter optimization method developed by Ly et al. (ref. 12) allows the LQG compensator to be "de-tuned," so it will be more robust to unmodeled dynamics. Research efforts aimed at combining the LQG methodology with frequency-domain based design specifications (ref. 13) may also help solve some of these problems in the future.

Even when the high-frequency dynamics are properly included and sufficient stability margins are insured, large effective time delays ($\tau_e > 100$ msec) have serious ramifications for pilot handling-qualities for high workload tasks. Time-domain criteria (e.g., time-history envelopes) are not sufficiently sensitive to such effects, and time-domain flight-test techniques (e.g., step responses) cannot be completed with sufficient precision to demonstrate criteria compliance adequately. Extensive fixed-wing experience led to the adoption of frequency-domain based specifications (ref. 14) which clearly expose such problems. Similar criteria, which are appropriate for combat rotorcraft tasks, are needed to avoid repeating the fixed-wing handling-qualities problems associated with large time delays. The currently proposed handling-qualities specifications for the LHX contain frequency-domain criteria (ref. 15).

II.B Generic Digital Flight-Control Implementation

The digital version of the generic analog system is depicted in figure 2. The key change from the "analog world" to the "digital world" is the shift from a system in which all of the data are a continuous function of time, to one in which the system is based on both sampled data and continuous data (loosely referred to as a "digital system" for the remainder of this report).

The decision concerning which elements should be absorbed within the digital flight controller and which should remain as analog components is an important design tradeoff. For example, some systems implement the sensor filters with a high-rate digital system (digital F-104-G, ref. 4), while other systems implement the filters in an analog fashion (ADOCS). The samplers monitor feedback and stick signals at a fixed sampling interval (T). The sampling rate (ω_s) is a key descriptor of the digital system and is determined from the sampling interval as $\omega_s = 1/T$ (Hz). (While some systems, such as the ADOCS, use different sample rates in the various control loops, the present discussion is limited to single-rate systems.) Preceding each sampler is an analog anti-aliasing filter which keeps

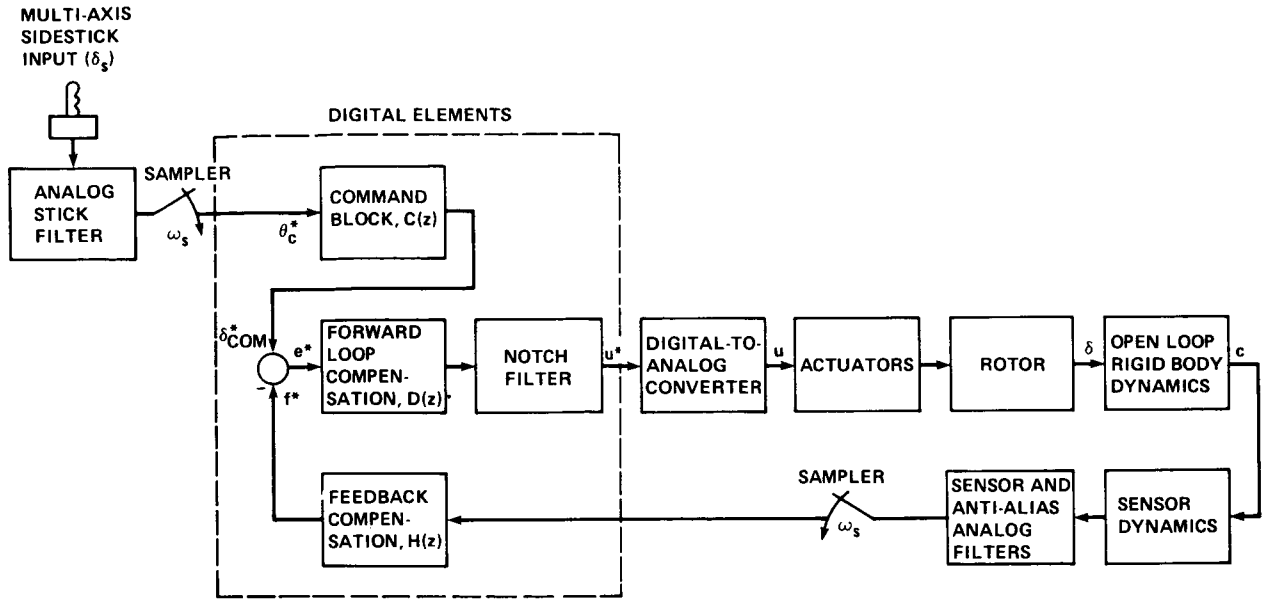

Figure 2.- Generic digital control implementation.

broad-band sensor noise and high-frequency modes from affecting the low-frequency dynamics as a result of the sampling process ("foldback"). The digital signals are then passed to the microprocessor by electronic or optical data link. Within the computer, command, feedback, and feedforward compensation laws are implemented with difference equations. These equations may be characterized by z-plane transfer functions (denoted by D(z), etc., in fig. 2), which are the counterparts of the continuous time s-plane transfer functions. The transport delay (τ_c) between updated sensor (or command) signals and actuator commands is an important factor in the digital system dynamics and also contributes to the total effective time delay (τ_e). In addition to the flight-control laws, the computer(s) must also monitor sensor and actuator health and redundancy/failure management systems. The digital actuator command signal is coupled to the actuator system with a digital-to-analog converter. This typically consists of a zero-order-hold (i.e., stair-step function) element.

The entire system is multiply redundant to allow for failures of one or more components without degrading the system performance. The level of redundancy, typically triplex or quad, depends on the decision whether to have a back-up system and on the assumed hostile environment. The redundant systems may be synchronized to a degree which varies from fully synchronous to fully asynchronous operation. The selected level of synchronization involves consideration of single point failures and undesired ("nuisance") system trips. Asynchronous and moderately synchronized systems are both currently used in fixed-wing aircraft.

The various digital system elements introduce important dynamic characteristics which are not encountered in analog systems. Unlike the linear time-invariant character of the continuous data system, the discrete data system is (in general)

time varying and aperiodic in its basic nature. By virtue of the sampling process, continuous sine waves of one frequency (ω) generate discrete (sampled) responses at this fundamental frequency (ω) and an infinite number of aliases and sub-aliases (e.g., $\omega + \omega_s$, $\omega - \omega_s$, $\omega + 2\omega_s$, etc.). Thus, discrete sinusoidal frequency responses are not completely analogous to continuous frequency responses. Further, the digital-to-analog conversion using a zero-order-hold introduces dynamic distortions in the response, as does the difference equation representation of the continuous control equations. The software architecture and calculation timing (order) has a significant impact on the effective transport delay between sensor signal updates and the associated control command outputs. The delay distorts the frequency response as well.

The degree to which the dynamics of the digital system are similar to the dynamics of the continuous system may be largely parameterized by the sample rate, ω_s. When the sample rate is very high (compared to the closed-loop system bandwidth), the digital system approaches the continuous system (neglecting finite word-length effects). The limit on maximum sample rate is bounded by computer capability, speed, space for future growth, and word length. Since, in a typical central processor architecture, roughly 70% of the available frame time is used for noncontrol functions (such as failure management), there is a limited amount of space in which control law expansion can be accommodated. (Distributed process architectures might alleviate this problem.) The inevitable growth of a system through its development and testing often causes reductions in the design sample rate. For example, in the development of the ADOCS system, the original sample rate of 40 Hz was reduced to 30 Hz to keep within the available computational capacity. One alternative to progressively reducing the sample rate is to use a larger computer, but this approach results in increased computer costs, and added complexity in redundancy and failure management systems. Moreover, once a computer system is selected and the basic design is complete, it is very costly to switch computer systems and to redesign all of the previously debugged software. Thus inevitably, the original computer system is retained, and the frame time is increased. Methods which allow the analyst to accurately evaluate the effects of sample-rate reduction on an originally high frame rate design and to determine lower sample-rate bounds are, therefore, of much practical interest.

An alternate design option is to initially select a lower sample rate, thereby retaining spare capacity for future growth without requiring redesign of (earlier) high sample rate configurations. Direct digital methods allow the successful design and implementation of low rate systems. Such low rate systems were developed and implemented for the F-104-G aircraft (16 Hz) (ref. 4) and Navion aircraft (10 Hz), (ref. 16) without redesign during testing.

The most important concern in the development of high-bandwidth digital flight-control systems for rotorcraft is piloted handling qualities. As previously mentioned, total effective time delay (τ_e) is an important quantity in determining piloted handling quality ratings for high workload tasks. Fixed-wing experience (refs. 3 and 5) indicates that the largest contributions to the total effective time delay between pilot input and closed-loop system response are lags resulting from

filters and actuators, rather than computational delay (τ_c) or sample period (T). Therefore, (small) increases in time delay resulting from moderate reductions in sample rate are not an important handling qualities concern. However, for very low sample rates (ω_s < 10 Hz) the zero-order hold introduces roughness to the control response, which has been shown to be objectionable to pilots (ref. 16). Also, excessive sample rate reductions can cause actuator limiting and intersample ripple problems (ref. 17).

The preceding issues associated with high-bandwidth digital flight-control systems are discussed in detail in the remainder of this section.

II.C Design and Analysis of High-Bandwidth Digital Flight-Control Systems

In discussing the application of high-bandwidth digital flight-control systems to combat rotorcraft, it is necessary to separate those considerations associated with high-bandwidth control (either analog or digital) from those considerations associated purely with the digital implementation. In the first part of this section, design analysis and handling qualities implications of high-bandwidth model-following control systems for combat rotorcraft are explored. The second part of this section focuses on the implementation of the high-bandwidth system using a digital flight controller. Two approaches are considered--a high sample-rate (approximate) method, and an exact digital method. The approximate method is based on standard continuous-time (analog) techniques, using simple models for the digital system elements. This design technique is commonly used for high sample-rate systems. Lower sample-rate systems and the high-bandwidth elements of higher sample-rate systems (e.g., actuators) require more exact methods of treating the digital effects to guarantee satisfactory system performance. The last part of this section presents an overview of classical discrete analysis methods for these applications.

II.C.1 High-Bandwidth Control Systems for Combat Rotorcraft- Regardless of the sample rate which is selected for the final digital system, the key driver of the control system design is to achieve a high-bandwidth of the closed-loop system response. One commonly used definition for bandwidth in the handling qualities community (ω_{BW}) is the frequency at which the overall augmented-vehicle response to the pilot's stick input (c/δ_s) exhibits 45 deg of phase margin or 6 dB of gain margin, whichever is less (ref. 14). (These "stability margins" refer to the augmented-vehicle as an open-loop element in the pilot/vehicle closed-loop system.) The bandwidth is easily evaluated from a Bode (frequency response) plot of the closed-loop attitude response to longitudinal controller input (θ/δ_s), as shown in figure 3. The currently proposed specification for the family of light helicopters (LHX) with attitude-command/attitude-hold (ACAH) pitch response characteristics requires an attitude bandwidth (based only on the 45 deg phase margin frequency) of ω_{BW_θ} = 2-4 rad/sec (ref. 15). From a classical design standpoint, this criterion reflects a required open-loop (f/e in fig. 1) crossover frequency in roughly the same range (ω_{c_θ} = 2-4 rad/sec), with associated satisfactory phase and gain margins. The open-loop rigid-body dynamics of a conventional rotorcraft in

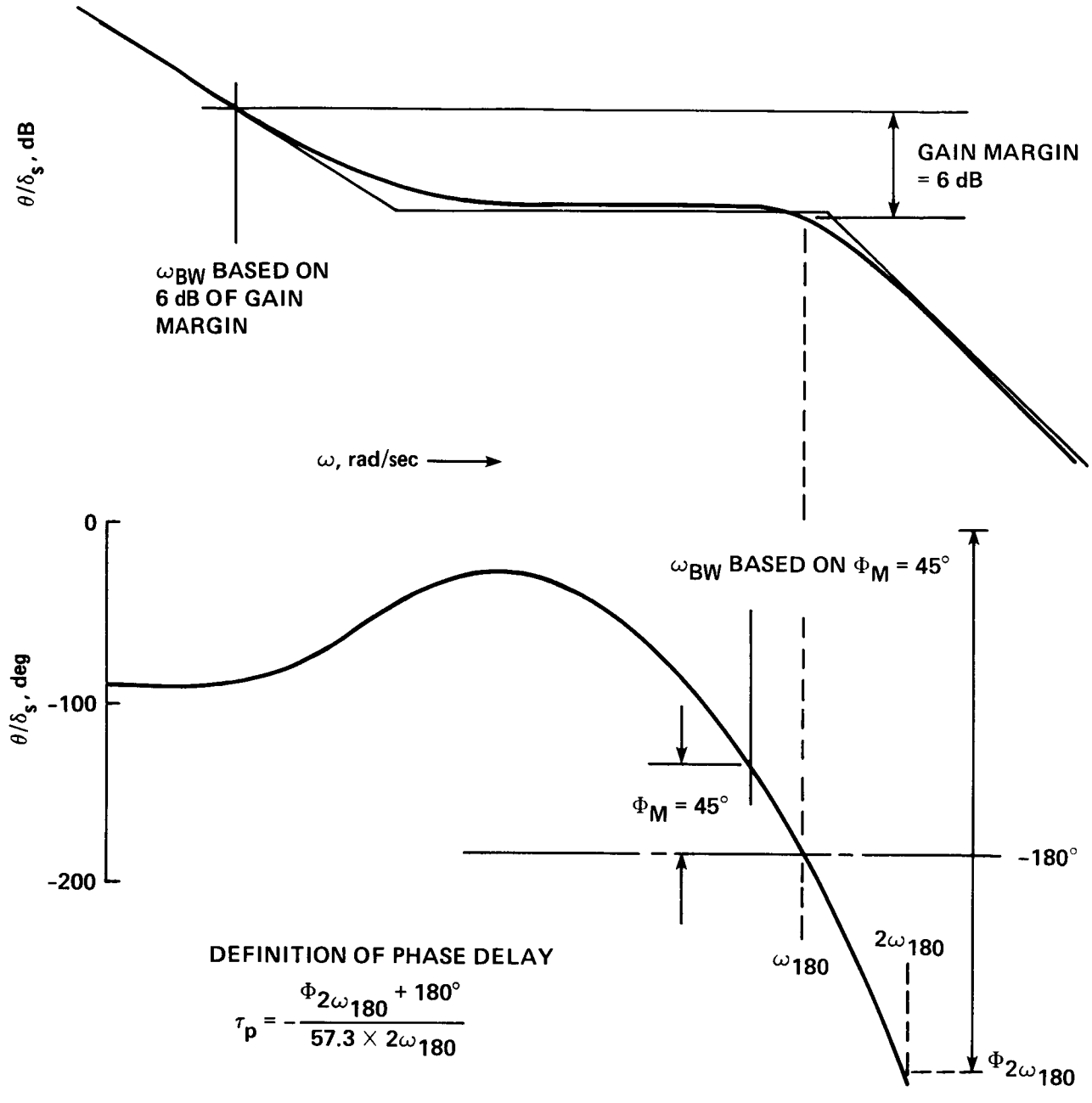

Figure 3.- Definition of pitch attitude bandwidth (ω_{BW}) and phase delay (τ_p); for this case the bandwidth is governed by the gain margin requirement.

hover or low-speed flight are characterized by relatively low-frequency modes compared to a fixed-wing aircraft. Therefore, when a high crossover frequency is imposed, the low-frequency dynamics are largely cancelled by the zeroes of open-loop transfer function and lead compensation (lead compensation is provided by simultaneously feeding back pitch rate and pitch attitude).

A typical root locus plot based on the longitudinal dynamics of the ADOCS Black Hawk is presented in figure 4. This plot shows the locus of roots with varying pitch attitude feedback gain K_θ and a fixed ratio of pitch attitude to pitch rate feedback gains of $K_\theta/K_q = 2.125$. Notice that when the forward loop gain is set at the value required for an open-loop crossover frequency of $\omega_{c_\theta} = 6$ rad/sec ($K_\theta = 34$ in./rad), which was used in the ADOCS simulation (ref. 7), all of the low-frequency dynamics are heavily damped or cancelled by associated numerator dynamics. The maximum feedback gains are limited by a number of factors:

1. Sensor noise amplification
2. In-plane (lead-lag) rotor coupling
3. Phase margin requirements and high-frequency modeling uncertainty (flexible structure modes)
4. Actuator limiting (position and rate)

The sensor noise and rotor coupling problems can be alleviated with the proper selection of feedback and forward loop filters, as discussed earlier.

The design values of open-loop crossover frequency (ω_c) and phase margin (Φ_m) limit the total allowable phase lag contributions from the various high-frequency elements in the stabilization loop (f/e in fig. 1), including the filters, actuators, and rotor system. A good measure of this combined phase lag is the effective time delay (τ_{SL}) obtained from an equivalent system fit in the crossover-frequency range of $\phi = e^{-\tau s}$ to the high-frequency elements of f/e. The phase lag contribution from the high-frequency elements is then determined from τ_{SL} by the simple linear relationship:

$$\Phi(\omega) = -57.3\ \tau_{SL}\omega\ ,\ \text{deg} \tag{1}$$

To obtain the relationship between ω_c, Φ_m, and τ_{SL}, we assume that:

1. The closed-loop bandwidth is high enough to suppress the lower-frequency open-loop dynamics (as in fig. 4), and allow the use of the simple rigid-body transfer function model (fig. 1):

$$\frac{\theta}{\delta}(s) = M_\delta/s^2 \tag{2}$$

2. The feedback compensation uses pure gains on the pitch-attitude and pitch-rate signals (as in fig. 4):

$$H(s) = K_q s + K_\theta$$

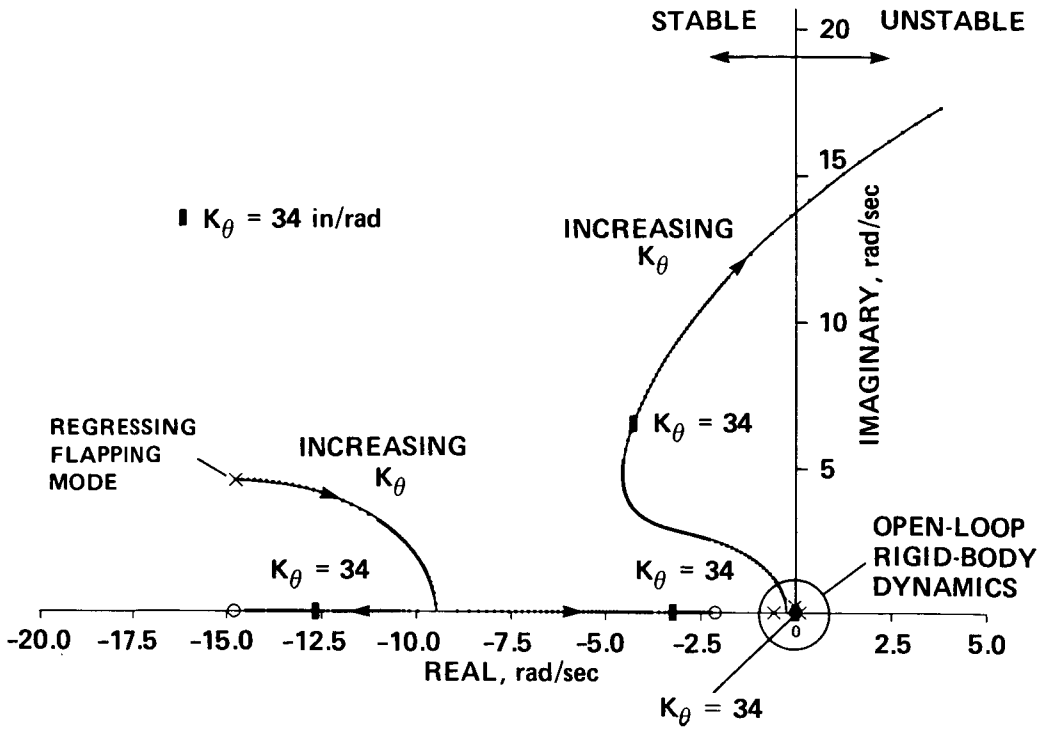

Figure 4.- Sample root locus for ADOCS Black Hawk; design gain, K_θ = 34 in./rad.

or

$$H(s) = \left(\frac{K_q}{K_\theta} s + 1\right)K_\theta$$

defining $T_q \equiv K_q/K_\theta$,

$$H(s) = (T_q s + 1)K_\theta \tag{3}$$

3. The feedback parameters of equation (3) are selected to yield:
   a. Φ_m = 45 deg
   b. Gain margin ≥ 6 dB
   c. The crossover frequency ω_c occurs at the point of maximum phase (a good design rule of thumb),

$$\left.\frac{\partial \Phi}{\partial \omega}\right|_{\omega_c} = 0$$

Equations (1), (2) and (3) yield the phase response:

$$\Phi(\omega) = -180 - 57.3\ \tau_{SL}\omega + \tan^{-1} T_q\omega \tag{4}$$

Taking the partial derivative with respect to ω:

$$\frac{\partial}{\partial\omega}\,\Phi(\omega) = -57.3\,\tau_{SL} + \frac{57.3\,T_q}{1 + T_q^2\omega^2} \tag{5}$$

Applying condition 3a to equation (4) gives:

$$\Phi(\omega_c) = -180 - 57.3\,\tau_{SL}\omega_c + \tan^{-1} T_q\omega_c = -135$$

or

$$-57.3\,\tau_{SL}\omega_c + \tan^{-1} T_q\omega_c = 45 = \Phi_m \tag{6}$$

Applying condition 3c to equation (5) gives:

$$\left.\frac{\partial\Phi}{\partial\omega}\right|_{\omega_c} = -57.3\,\tau_{SL} + \frac{57.3\,T_q}{1 + T_q^2\omega_c^2} \tag{7}$$

The relationships among ω_c, τ_{SL}, and T_q are obtained by numerically solving equations (6) and (7). Then, K_θ and the Gain Margin are solved using the open-loop transfer-function amplitude. The results are the following simple design rules:

$$\begin{aligned} \omega_c &= \frac{0.370}{\tau_{SL}} \\ \frac{1}{T_q} &= 0.442\,\omega_c \\ K_\theta &= \frac{\omega_c^2}{2.48\,M_\delta} \end{aligned} \tag{8}$$

$$\text{Gain Margin} = 12\ \text{dB}$$

Equations (8) indicate, for example, that a stabilization-loop equivalent time-delay of $\tau_{SL} = 100$ msec limits the attainable stabilization loop crossover frequency to $\omega_c = 3.7$ rad/sec. Higher crossover frequencies can be achieved if additional lead compensation is used but at the expense of reduced gain margin and increased control authority demands (Section III.E.3).

This simple analysis shows that two key quantities which determine the design and performance of the system are the open-loop transfer function gain (M_δ) and the effective time delay (τ_{SL}); as illustrated in the case study (Section III), the actuator authority limits also restrict the attainable performance. Much of the previous work in rotorcraft control system design was based on crude estimates of the actuator and rotor dynamics and elaborate models for the bare airframe dynamics. But, as illustrated here, high-bandwidth control systems require the opposite

emphasis--most of the emphasis should be placed on developing accurate models of the high-frequency elements.

The importance of accurately modeling the high-frequency dynamics has also been cited by Chen (ref. 18) in his work on digital control-system design for the variable stability CH-47 rotorcraft. As previously noted, the importance of the high-frequency dynamics was already recognized in the development of the ADOCS Black Hawk system. The selection of feedback gains was based on a crude attitude model (K/s^2) with a detailed model of the high-frequency servo and rotor dynamics (ref. 7). However, additional important high-frequency elements such as analog pre-filters, rotor in-plane dynamics, and vibration notch filters were omitted from the initial design. The key conclusion of this discussion is obvious but often ignored--high-frequency dynamics must be very accurately defined before good high-bandwidth designs (continuous or discrete) can be developed.

The advanced fighter technology integration program for the F-16 (AFTI/F-16) is a good example of the problems associated with high-bandwidth flight-control systems (ref. 2). The control system for this advanced version was designed using digital linear quadratic synthesis (LQS) design methods. The design used very high gains and did not consider the associated excessive surface actuator limiting. Studies of the high-bandwidth model-following AFTI system showed that some of the flight control gains were many times greater than those of the original analog F-16 design and resulted in an impractical design. An extensive report (ref. 2) concerning the experience with the AFTI/F-16 design indicates that the "modern control" approach masked the effect of high gains.

A second problem with the AFTI/F-16 system was the interaction between the failure-sensing algorithms and the asynchronous computer functions. The decision to operate the computers in an asynchronous mode was based on the desire to avoid single point failures which were due to external sources such as electromagnetic impulse (EMI) and lightning strikes. Since the computers were operating in an asynchronous mode, time skews of up to 8 msec (T/2) could be encountered. With the large transients in the control system resulting from the very high flight control system gains, the error-sensing algorithms detected large differences between the redundant channels, thus repeatedly triggering failures in flight.

The final operational AFTI/F-16 design used reduced, more reasonable, gain levels (ref. 2). This example shows the importance of accurately modeling the high-frequency dynamics for high-bandwidth control systems and carefully considering the effect of large flight control system gains on noise amplification, actuator saturation, and failure management systems. While the lower gain digital controller eventually yielded a satisfactory AFTI/F-16 system, significant flight test and simulator support was expended to reconfigure the original AFTI design.

II.C.2 Approximate Methods for High Sample-Rate Digital Control Systems- A digital system is considered to be operating at a high sample rate when the ratio of sampling frequency to the closed-loop system bandwidth is large, typically on the order of $\omega_S/\omega_{BW} = 30$ or higher. In this section, analysis and design concepts for high sample-rate digital control systems are presented.

When the sample rate is high compared to the closed-loop system bandwidth, the sampler and zero-order-hold elements generate only mild distortions in the continuous system output response. Figure 5 shows the effect of a high-rate sample and hold circuit on a continuous signal. A good approximation to the "stair-step" output of the zero-order hold operating at a sample rate, $\omega_s = 2\pi/T$ rad/sec, is a continuous signal which is identical to the original input, but is delayed by T/2 sec. Based on this approximation, the s-plane transfer function for the sample and hold circuit is

$$G_{ZOH}(s) = e^{-\tau s} \; ; \quad \tau = T/2 \tag{9}$$

This transfer function gives a magnitude ratio of unity and a phase lag of

$$\begin{aligned} |G_{ZOH}(j\omega)| &= 1 \\ \Phi[G_{ZOH}(j\omega)] &= -\omega T/2, \text{ rad} \end{aligned} \tag{10}$$

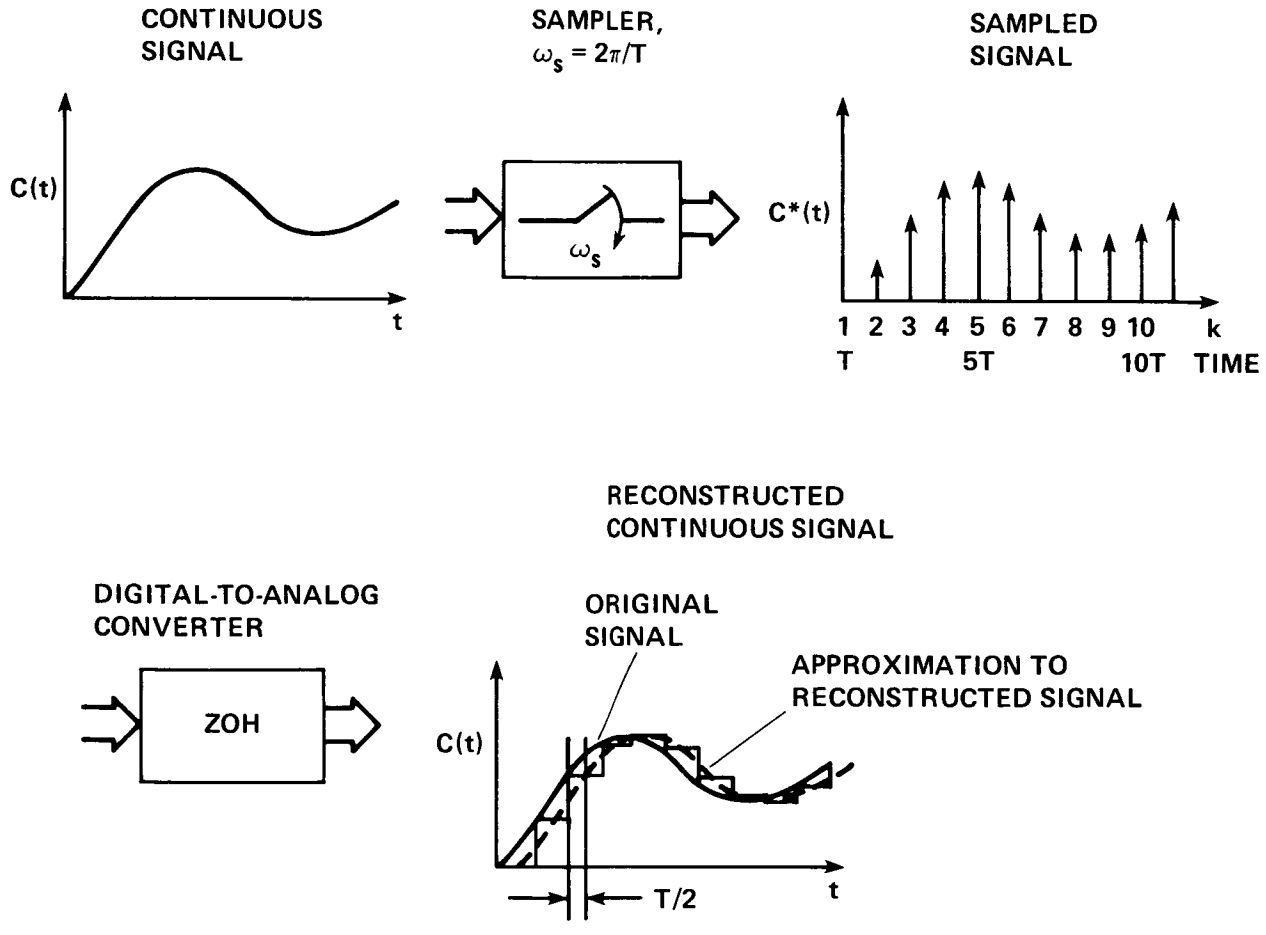

Figure 5.- Origin of T/2 delay approximation for sample and hold circuit.

For a typical high sample rate of $\omega_s = 30\ \omega_{BW}$, the phase lag is -6 deg at $\omega = \omega_{BW}$, and should be included in the design process. An additional time delay increment τ_c is often introduced to account for computational delays in the digital computer; thus the total sample and hold delay in equation (9) is

$$\tau = T/2 + \tau_c \tag{11}$$

The pure transport delay approximation for the sample and hold element is commonly adopted for analyzing high sample-rate digital systems, and as shown in Section II.C.3 is quite satisfactory for sample rates above $\omega_s \geq 10\ \omega_{BW}$. Another time delay element must be included for the stick sampler (fig. 2) to account for the timing skew (ref. 19). Since on the average, half of the pilot's continuous inputs will be missed by the flight-control computer until the next sample is taken, an effective transport delay of T/2 sec will be observed by the pilot and must be included in the analysis (Section II.C.4.D.c).

So, for a high sample-rate system, the (analog) s-plane block diagram is used, and time-delay elements are inserted to represent the sample-and-hold device and stick sampler skewing. The analysis and design then continue in conventional analog fashion with the selection of appropriate feedback and command-loop s-plane transfer functions. Once the analog compensation is selected to provide the desired crossover frequency and phase margins, the needed (discrete) difference equations are generated from the continuous transfer functions, using a numerical integration transform. The trapezoidal rule approximation (Tustin's transform), which is commonly used for this purpose, involves the following substitution for the Laplace variable "s":

$$s = \frac{2}{T}\frac{z - 1}{z + 1} \tag{12}$$

The z-plane transform functions are expanded in terms of negative powers of "z," where z^{-1} represents a shift of 1 sample period (T, sec). These z-plane transfer functions are then easily converted to difference equations. (Note that constant gain feedbacks are unchanged by the Tustin conversion process.) When the sample rate is relatively high compared to the highest filter frequency, ($\omega_s \geq 30\ \omega_n$), the trapezoidal rule integration formula produces very satisfactory results. Even when the sample rate is reduced somewhat ($5\ \omega_n \leq \omega_s \leq 30\ \omega_n$), and mild frequency response distortions begin to appear, significant improvements can be achieved by using the pre-warping technique (ref. 20).

The preceding approach of using a discrete approximation of the continuous system design is called "emulation," since the s-plane characteristics are emulated using z-plane transfer functions. This is a common method of digital design and has been used heavily in both the fixed and rotary wing communities. The advantages and disadvantages of the emulation approach are discussed in many references:

II.C.2.a Advantages of emulation design (ref. 21):

- This approach yields a flyable, continuous controller. The continuous controller provides a strong base for exposing the effects of the sample time parameter on performance, since it corresponds to the limiting case (i.e., T approaching zero).

- Structural and stability properties of the controller dynamics are invariant with respect to the sample time parameter. There is a one-to-one correspondence between the continuous controller dynamics (i.e., lead-lag networks) and the software dynamics (i.e., corresponding difference equations), providing a good starting point in practical digital controller design for a given sample rate. The coefficients of the difference equations can be computed efficiently as a function of sample time based on the transform approximation.

- Sample rate estimates based on this approach are on the safe side, and the resulting digital control software is generally flyable.

II.C.2.b Disadvantages of emulation design (refs. 17, 22-24):

- There is no way of detecting when the time delay and analog-to-discrete (e.g., Tustin) transformations are beginning to introduce significant errors in the analysis and design.

- There is no information on actuator responses to the zero-order-hold command signal. While the time delay approximation gives a good estimate of the average control time history, for output response analysis, the actual stair-step commands can cause serious limiting problems which will be completely masked in the design. These actuator considerations generally set the lower limit on allowable reductions of the sample rate.

- There is no information on intersample output response since emulation is based on matching responses at the even sample times, so undesirable ripple and oscillations can occur between the even sample periods. (This is not usually a problem for high sample-rate systems.)

- No information is available on the effects of aliasing. Aliasing may be an especially troublesome problem with n/rev vibration components which are usually well beyond the Nyquist frequency ($\omega_{Nyq} = \omega_s/2$). These vibration components will be folded down into the lower frequency range.

- Design by emulation yields a conservative choice of sample rate in order to validate the continuous-to-discrete approximations.

- There is no information on the sensitivity of the z-plane performance characteristics to changes in timing and word length.

- System designs with the emulation method often need retuning using exact digital methods to correct dynamic distortions even when sample rates are relatively high.

Despite the above concerns with the emulation approach, this method has proven to be very successful for high sample-rate systems. Except for the n/rev aliasing problem, the emulation design will lead to a generally flyable rotorcraft control system, if the original continuous system design is satisfactory. Thus, for the high sample-rate system, the key ingredient for success is the accurate modeling of the high-frequency dynamics in the s-plane, so that the selected gains can be realized. The final digital system will closely approximate the analog system with only slight degradation resulting from zero-order hold delays and Tustin transform distortions. That is, the resulting digital system will be nearly as good as the original s-plane design.

II.C.3 Fixed-Wing Experience with Digital-Control Systems Based on Emulation Design- The vast majority of existing digital flight-control systems for fixed-wing aircraft have been designed using the emulation technique. One reason for this approach is that most of the digital systems had previous analog counterparts, so the emulation approach was a logical way to build on a previously acceptable design. The only operational digital combat rotorcraft is the AH-64 (Apache) aircraft which was also designed with the emulation technique (ref. 6). However, this system is very limited in its authority (15%) to avoid potential problems associated with "hard over" failures. Also there is little documentation of the developmental history and flight-test experience with the AH-64. Other military rotorcraft, such as the CH53E, Heavy-Lift Helicopter (HLH), and the Tactical Aircraft Guidance System (TAGS), had digital flight-control systems, but were not developed for the scout/attack mission. The performance and handling quality requirements, therefore, were not as severe as the ones proposed for LHX missions.

Unquestionably, the biggest problem for fixed-wing aircraft with digital flight control systems has been the handling qualities deficiencies which are associated with unacceptable levels of total effective time delay τ_e in the overall command response (c/δ_s in fig. 1) and are only secondarily attributable to the emulation design method. Numerous studies have correlated levels of time delay with degraded handling qualities ratings for various configurations and tasks (refs. 25-27). The data show that in low-gain pilot tasks (such as up-and-away flying and normal landings), the pilot ratings are not very sensitive to the level of time delay. However, when the task requires tighter tracking precision (such as offset spot landing, air-refueling, and air-to-air tracking) small increases in the level of time delay can cause rapid tendencies toward pilot-induced oscillations (PIO). Video tapes of longitudinal PIOs in final flare and landing for the F-8 DFBW time-delay experiment and Space Shuttle are startling illustrations of the effect that time delays can have on the piloting performance. Data from the F-8 experiment (ref. 25, fig. 6) show the effect of task on the sensitivity of handling-qualities ratings to incremental time delay. The NT-33 data of reference 26 (fig. 7) show degradations in handling-qualities ratings for total effective time delays exceeding 120 msec.

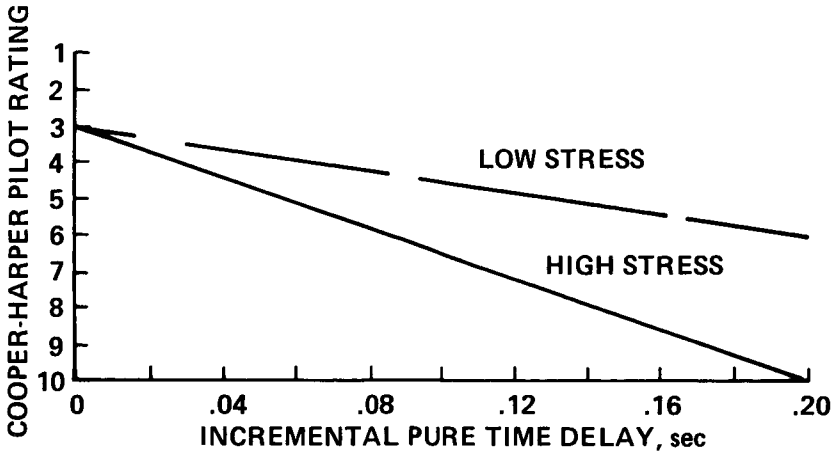

Figure 6.- Data from the F-8 experiment (ref. 25) showing the effect of task on the sensitivity of handling-qualities ratings to incremental time delay.

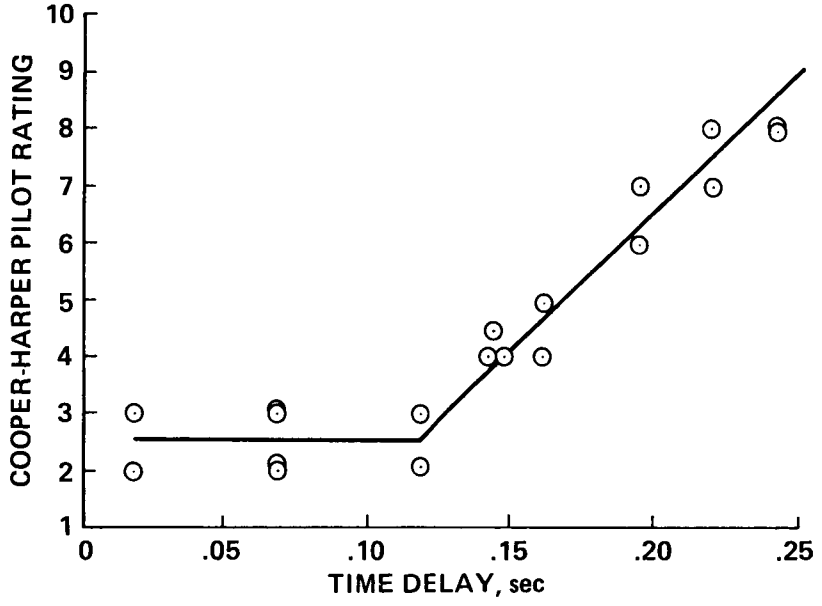

Figure 7.- Data from the NT-33 experiment (ref. 26) showing the degradation in handling-qualities ratings with total effective time delay.

Currently proposed specifications for fixed-wing military aircraft (ref. 15) and the proposed LHX handling-qualities specifications place a limit on phase delay τ_p (an estimate of the total effective time delay τ_e; the phase delay is obtainable from the closed-loop Bode plot as in fig. 3) which reflects these results.

While the time-delay phenomenon has been repeatedly observed in flight, quantitatively consistent results have not appeared in simulators. Numerous studies have concluded that the reduced level of urgency in the simulator environment, distortions which are due to visual and motion system dynamics, and the lack of visual scene texture alter the piloting strategy and pilot/vehicle closed-loop performance, and thus can seriously compromise the quantitative applicability of simulation results (refs. 15 and 28). Since latent time-delay problems often do not show up until flight testing, their possible existence must be carefully considered during design.

The most important contributions to the total effective time delay for a digital system are (in roughly descending order):

1. Actuator dynamics (including rotor response)
2. Filters--stick, sensor, antialias
3. Sample and hold delay (T/2)
4. Stick sampler skewing (T/2)
5. Computational delay (τ_c)
6. Discrete (e.g., Tustin) transform approximations

The reported fixed-wing experience bears out the conclusion that time delay is perhaps the single biggest problem for modern aircraft with high-bandwidth digital flight-control systems. The two most notable operational examples are the F-18 and the Space Shuttle aircraft, both of which were designed using emulation methods. These vehicles experienced unsatisfactory handling qualities when high workload/precision control was attempted in flight. Both aircraft underwent subsequent flight-control system modifications to rectify this problem.

The F-18 is an excellent case study since it is the first fleet aircraft to employ a digital flight-control system, and also its development is extremely well documented (refs. 3 and 29). The initial configuration had good in-flight stability characteristics but was considered by the pilots to have poor controllability characteristics resulting from the unacceptably large effective time delay, predominantly in the lateral axis. For the original F-18 system, the longitudinal time delay was τ_e = 170 msec, and the lateral time delay was τ_e = 240 msec; as can be seen, both levels are considerably above the τ_e = 100 msec tolerance level. As detailed in reference 3, the key contributors to these large effective time delays were:

1. Stick dynamics (dead zone and threshold)
2. Structural filters
3. Computational delays
4. Tustin conversion effects
5. Forward loop integrators

This original configuration was found to be especially sensitive to PIOs during the air-refueling task, in which pilot workload is at a maximum. To correct the initial handling-qualities problems associated with the original design, a number of significant changes were made to the F-18 system (refs. 3 and 29):

1. The sampling rate was increased from 40 Hz to 80 Hz.

2. The software architecture was modified to reduce the throughput (computational) delay, τ_c. All calculations which do not depend on the current sample value are precalculated at the end of the previous frame. Thus when a new sample is taken, the final calculations are completed, and the updated control signal is quickly released. The remainder of the sample period is then used for precalculations for the next cycle.

3. In the lateral axis, the forward loop integrators were removed; these integrators were felt to contribute unacceptable levels of computational delay, and to result in long transients in reaching the steady-state condition.

4. The force-sensing limited displacement controller was replaced by a displacement sensing controller. Since the displacement controller is not as sensitive to biodynamic feedback, it was then possible to move the notch filters from the forward loop to the feedback loop (sensor feedback of the structural mode still needs to be treated). This reduced the effective time delay.

5. The high-gain model-following system design was dropped entirely in favor of a scheduled (lower) gain approach. This corrected some of the problems associated with interaction between the structural and actuator dynamics.

As a result of the above changes, the effective time delay was significantly reduced in both axes. The longitudinal time delay was reduced to 70 msec, and the lateral time delay was reduced to 120 msec, roughly a factor of two in each axis. The piloted handling-qualities ratings for the air-refueling task improved from Level III ("deficiencies require improvement") for the original system to Level I ("satisfactory without improvement") for the final configuration.

The Space Shuttle exhibited handling-qualities deficiencies in the flare and landing during the ALT (approach and landing) configuration flight testing (ref. 5).[4] A tendency to develop longitudinal PIOs, which did not occur in the simulation evaluations (ref. 5), was found to result from unacceptably large effective time delays between pilot inputs and flightpath (n_z) responses (greater than 250 msec). Major sources of these time delays were stick filters, surface limiting, and pilot location effects, and a low outer loop sampling rate (6-2/3 Hz). Because of the lengthy process involved in altering and recertifying the Space Shuttle's basic flight control system, an "add-on" PIO suppression filter was developed. This filter automatically reduces the stick gain (sensitivity) for high-frequency inputs, thus restricting the attainable pilot crossover frequency. No changes were made to the basic flight-control system.

[4]Scobee, F. R.: Presentation on Space Shuttle Control System and Testing for Panel Discussion. Design and Flight Test of Critical Digital Systems. AIAA Aerospace Engineering Conference and Show, Los Angeles, CA, Feb. 1985.

The implications of the fixed-wing experience for modern combat rotorcraft are significant. Clearly, a key concern must be to control the level of total effective time delay. Up until now, there has not been a requirement for very high-precision attitude and path control for rotorcraft. However, the introduction of nap-of-the-Earth and air-to-air flying requirements, along with single pilot operation of vehicle trajectory and weapons control systems in degraded visual and hostile environments, will place extreme demands on the pilot and his rotorcraft system. The levels of aggressiveness and required tracking precision are much greater than those demanded of the previous generation of rotorcraft. These new stringent demands can be expected to expose time delay related PIO tendencies which appeared in the fixed-wing aircraft when high precision tracking tasks were first attempted in flight. Based on the fixed-wing experience, such problems will not be exposed in the simulator and must, therefore, be anticipated during the analytical design.

Current generation rotorcraft with their relatively sluggish servos and often articulated rotor systems have large inherent time delays. For example, the Bell ARTI demonstrator exhibits 200-250 msec delays in all three attitude responses (ref. 9). In the ADOCS Black Hawk aircraft, the actuators and rotor system alone accounts for a delay of τ_p = 97 msec, not even considering the digital system or additional filters (Section III.C). The case study (Section III) indicates a minimum total effective time delay of about τ_p = 217 msec for an operational articulated digital rotorcraft. Based on the fixed-wing experience, PIO tendencies should be expected for high-workload tasks such as nap-of-the-Earth and air-to-air maneuvering, and slope landings especially in degraded visual environments. The attainment of satisfactory handling qualities for these high workload tasks suggests a requirement for much faster actuator and rotor systems, and a much closer monitoring of delay contributions from filters and software architecture.

The history of fixed-wing development and flight-test programs shows that digital systems tend to "grow" and spare computational capacity is inevitably depleted. Eventually, increases in frame time are made to balance the computational capacity with the design sample rate demands. The relatively high level of complexity of the combat rotorcraft's digital control system as compared to the current generation of fixed-wing aircraft will aggravate this problem. For example, the ADOCS system employs roughly twice as many sensors as the digital F-18; thus, including the associated software, sensors and microprocessors, the overall control system is probably more complex than that of state-of-the-art operational fixed-wing aircraft by an order of magnitude. In the rotorcraft community such concerns have already surfaced in the development of the ADOCS system. The original design was based on a 40-Hz sample rate; however, because the control law software grew by 100% during development, the sampling rate had to be reduced to 30 Hz. Once flight testing and the inevitable modifications begin, the sample rate may need to be reduced further to accommodate the growth in the system. Such reductions in the sample rate aggravate the time delay and actuator limiting problems and generally degrade the performance of the emulation-based design. With continued reductions in sample rate, assumptions associated with the original emulation approach begin to weaken. Design methods which allow the direct analysis of digital dynamics are needed to set lower bounds on sample rate selection, and to accurately analyze and

design systems with reduced sample rates (e.g., low-rate backup systems). This is the subject of the next section.

II.C.4 Digital Flight-Control System Analysis and Design by Direct Digital Methods- When the sampling rate is reduced, the approximations employed in the emulation approach begin to break down. Even for high sample-rate systems, the dynamics of the digital elements may interact with with high-frequency actuator dynamics and cause distortions of the s-plane emulation response. Digital distortions arise from a number of sources:

- Zero-order hold dynamics
- Aliasing
- Trapezoidal rule (Tustin) transformation
- Intersample response
- Hidden oscillations
- Computational delays
- Sensitivity to parameter variations
- Computer quantization and roundoff

Although the actual sampled-data system is in general time-varying, resulting from the finite amount of time needed to extract a sample, a good approximation for the digital signal is a train of impulses. This approximation allows the use of the convolution (impulse response) concept and associated Laplace transform techniques, and is the basis for classical linear sampled-data theory. This theory was originally developed in the mid- and late 1950s by such authors as Jury (ref. 30), Raggazini and Franklin (ref. 31), Truxal (ref. 32), and Kuo (ref. 33). Considerable experience with these direct digital methods was gained during the development of booster and spacecraft systems in the mid-1960s. Since the digital computers of this period were relatively slow as compared to those presently used, there was a great deal of concern for accurately analyzing the dynamics of low sample-rate systems. Also, the booster and spacecraft systems had (and still have) many flexible modes which were often above the Nyquist frequency; as a result, there were strong interactions with the sampling dynamics that needed to be accurately considered in the analysis. A great wealth of knowledge in applied problems and design techniques was accumulated and documented during the space program of the 60s and 70s (refs. 34-36). Analytical methods covered the full range from classical frequency-domain methods to modern state-space approaches. Also, excellent computational facilities such as LCAP2 (current documentation in ref. 37) and DIGIKON (current documentation in ref. 38) were developed to support these analysis efforts.

Design and analysis studies in the spacecraft community are still based on the direct digital methods, as opposed to emulation techniques. This ensures that the many lightly damped fuel-sloshing and flexible structure modes are accurately included in the analysis. The coupling of narrowly separated structural and rigid body dynamics make simplified rigid body analysis and digital redesign (emulation) techniques very risky. As the bandwidth of the rotorcraft control systems is increased, a similar coupling between the rigid body dynamics and the rotor and actuator modes becomes more important, suggesting the need to apply these more exact digital techniques. The following discussion is an overview of some of the most

useful methods for the direct analysis of digital systems. This discussion introduces the reader to the analysis techniques which are used in the case study of Section III. Many excellent textbooks are available if a more detailed presentation is desired (refs. 20,33,39-43).

A. Sampled Signals

Suppose a continuous sensor signal has a power spectrum $F(\omega)$ which is band-limited by the frequency ω_o, as illustrated in figure 8(a). If this signal is then sampled at a frequency ω_s, such that the Nyquist frequency ($\equiv \omega_s/2$) is greater than ω_o, the frequency content of the sampled sensor signal $F^*(\omega)$ will be that shown in figure 8(b). This sampled-data signal has the (scaled) spectral content of the original primary continuous signal with band limiting at frequency ω_o, in addition to sidebands (aliases) at higher frequencies corresponding to combinations of the input band frequency and the sample frequency such as $\omega_o + \omega_s$, $\omega_o - \omega_s$, $\omega_o + 2\omega_s$, etc. The negative frequencies imply a 180 deg phase shift between the original signal and the aliased signal. This aliasing behavior is easily seen in the time domain. Suppose that a single continuous sinusoid of frequency

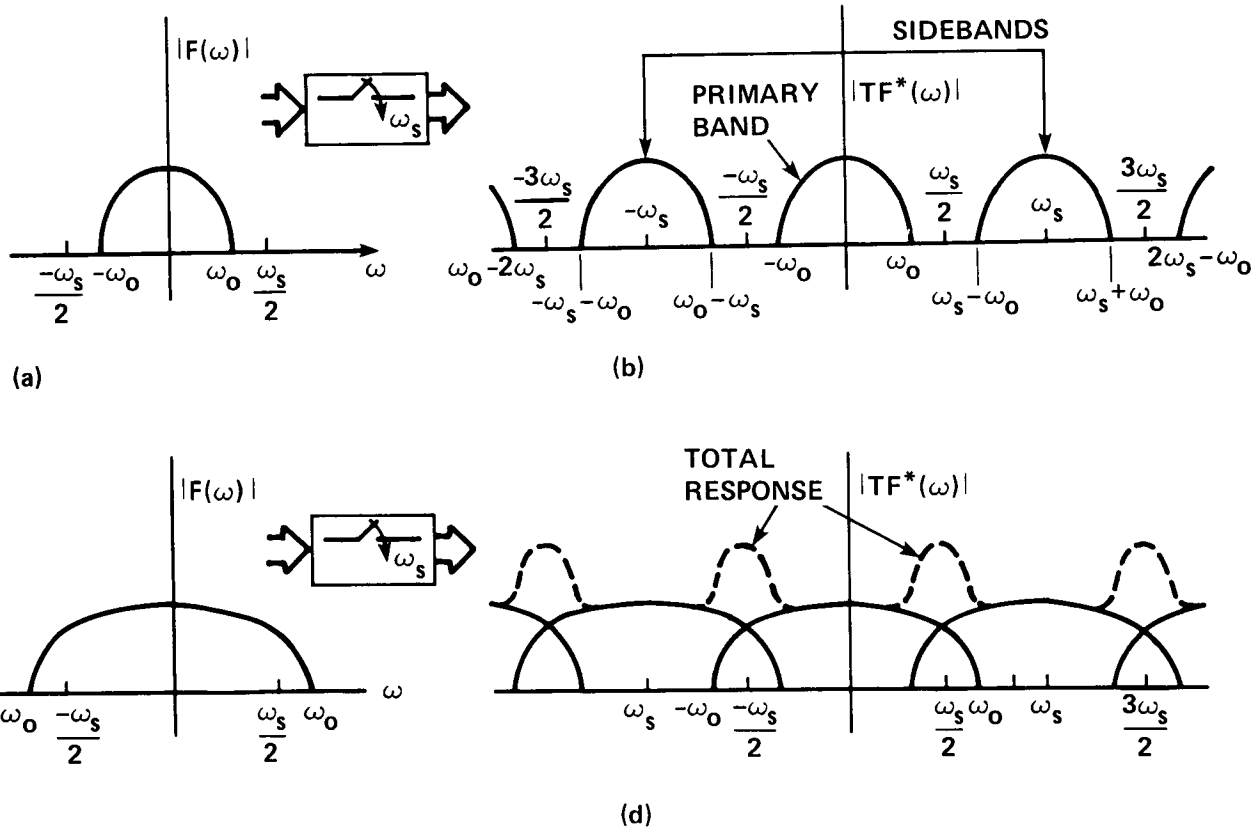

Figure 8.- Frequency domain illustration of aliasing. (a) Continuous input spectrum, $\omega_o < \omega_s/2$; (b) sampled output spectrum, no distortion of primary spectral band; (c) continuous input spectrum, $\omega_o > \omega_s/2$; (d) sampled output spectrum, distortion of primary spectral band is evident.

n samples. This is a rational sequence which can be represented in a closed-form transfer function in the variable z.

These z-plane transfer functions are the discrete equivalents of the s-plane transfer functions; while the Laplace operator s^{-1} represents integration, the discrete operator z^{-1} represents a one sample period delay. All of the continuous system elements, including the zero-order hold, can be digitized using the impulse function approach to obtain equivalent z-plane transfer functions. The change of variables which results from the mapping of equation (15) alters the familiar continuous-time stability criterion. The continuous criterion for all s-plane eigenvalues to have negative real parts is replaced by the discrete-time criterion for all z-plane roots to have magnitudes less than one. Thus, the imaginary axis stability boundary is replaced by a unit circle stability boundary. With this change in mind, root locus techniques are applied in exactly the same manner as in the s-plane case. Feedback compensation laws are synthesized based on desirable z-plane root locations. These can easily be obtained from s-plane specifications by employing the exponential transformation. Lines of constant damping ratio, natural frequency, and 1% settling times (s-plane real parts) in the continuous domain can be mapped into contours on the z-plane for design purposes as shown in figure 11.

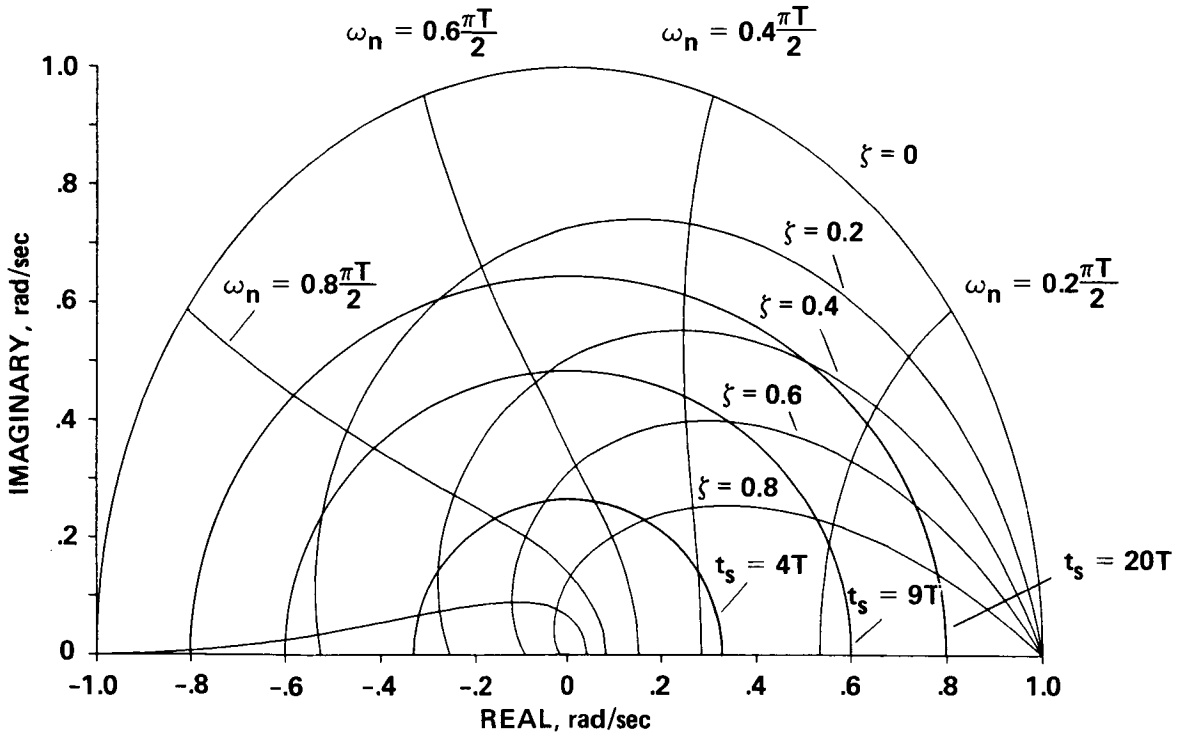

Figure 11.- Mappings of s-plane contours on the z-plane.

A problem occurs with z-plane analysis techniques as the sample rate is increased. Referring to exponential expression $z = e^{Ts}$, when the relative sample period is very small ($sT \ll 1$), the magnitude of the z-plane roots will approach unity--regardless of the value of the s-plane roots. Numerical problems with the z-plane analysis techniques quickly arise when the system is of fairly large order, and when the dynamic modes are at very low frequency compared to the sample rate. In such cases, increased precision must be used to represent the z-plane roots and to complete z-plane transfer function calculations. This applies to the on-board flight-control law calculations as well. For frequency domain analyses, transformation to the w-plane (Section C) improves the numerical precision considerably.

In addition to the root locus design techniques, it is desirable to obtain frequency responses of the digital system. For the continuous system, the sinusoidal frequency response is obtained by substituting the expression $s = j\omega$ into the s-plane transfer function and evaluating the complex transfer function for the magnitude and phase versus frequency, ω. Substituting $s = j\omega$ into the exponential transformation for z gives the corresponding expression for the discrete frequency response $z = e^{j\omega T}$. Substituting for z in the transfer function expressions gives the frequency response for various discrete input sinusoids. The time domain interpretation of the discrete frequency response is that a system is driven with a constant discrete input frequency ω which is less than the Nyquist frequency $\omega < \omega_{Nyq}$. The continuous output signal is fitted with a sinusoid of the same frequency as the input (ω), but with the appropriate magnitude attenuation and phase shift. This fitting procedure is based on the value of the continuous output at the sample instants only and provides no information on the dynamics of the system in between the sample values. Therefore, intersample ripple and hidden oscillations are not detected by the discrete frequency response. Since rotorcraft dynamics are generally low-pass, the assumption of a ripple-free output response is usually sufficient for handling qualities and overall response evaluations. The discrete frequency response allows direct evaluation of the bandwidth and time-delay handling quality parameters for the digital system, and is an excellent basis for exposing differences with s-plane (continuous) designs. However, there may be intersample transients in the control signal which are important for actuator performance and failure management. Therefore, it is important to monitor the response of the continuous system elements in between the even sample instants. A number of methods for analyzing the intersample response are discussed in the literature. The most commonly referenced techniques are:

1. Advanced z-transform (refs. 31,33,41)
2. Multirate switch decomposition (refs. 17,33,35)
3. Hybrid frequency response (ref. 17)

The advanced (or modified) z-transform allows the calculation of the intersample time response by (time) shifting the input and output samples. Frequency-domain sideband information is not available since the (shifted) output sample still operates at the basic system rate. Multirate switch decomposition uses an output sampler operating at a rate which is an integer multiple of the basic system rate. The result is a closed-form multirate transfer function, from which inter-sample

time responses and side-band spectral content are calculated. However, the order of these higher-rate transfer functions increases as a multiple of the number of additional inter-sample points. For example, if the response at one inter-sample point (and the associated spectral content up to $\omega = 2\omega_{Nyq}$, the first sideband) is to be determined, the order of the required multirate transfer function is double that of the original transfer function. Thus, analyses of systems of moderate order (of perhaps 10-15) are numerically troublesome.

The hybrid frequency response is a generalization of the multirate decomposition technique. By letting the output sample rate approach infinity, the continuous output spectral content is determined for all sidebands of the discrete input frequency. This useful approach is the so-called "continuous-frequency response of the digital system."

In the analysis of Section III, the advanced z-transform and hybrid frequency response techniques are used to study inter-sample characteristics.

Analysis and design using frequency-response methods based on z-plane transfer functions are cumbersome because the z-plane zeros and poles do not correspond to break-points in the asymptotic frequency response. Also for higher-order systems, the numerical problems mentioned above become severe, and large errors often occur for the low-frequency calculations. A solution for these deficiencies is to transform the discrete transfer function from the z-plane to the w-plane.

C. Analysis in the w-plane

The transformation from the z-plane to the w-plane (referred to by some authors, e.g., ref. 22, as the w'-plane) is completed with the mapping:

$$z = \frac{1 + (T/2)w}{1 - (T/2)w} \tag{16}$$

This maps the interior of the unit circle in the z-plane to the left half of the w-plane. Thus, the stability criteria for the w-plane are the same as for the original s-plane. In fact, using the w transformation as defined above, the poles and zeros of the w-plane transfer function will be numerically similar to those of the s-plane transfer function. In the limit, as the sample rate becomes infinite ($T \to 0$), the s- and w-plane transfer functions become identical. For finite sampling rates, there are additional zeros in the w-plane transfer function at frequencies corresponding to 2/T, which are due to the influence of the zero-order hold. Thus the w-plane transfer function embodies all of the digital characteristics associated with the sampler and zero-order hold, while maintaining the familiar root-locus and frequency response stability criteria and similar pole-zero locations of the s-plane design.

The w-plane Bode plots and compensation designs can be easily generated using standard s-plane techniques, since the break points on the asymptotic $j\nu$ (fictitious frequency) Bode plot correspond to the pole and zero locations in the w-plane transfer function. Frequency responses versus actual frequency, $\omega = (2/T)\tan^{-1}(\nu T/2)$, are easily computed and allow direct comparisons of s-plane

and w-plane behavior. Also, the mapping of the interior of the unit circle to the entire left half plane eliminates the numerical problems associated with z-plane analysis, and so it is advantageous to conduct digital analyses of higher order systems completely in the w-plane. Ultimately, conversion back to the z-plane is completed to obtain the needed difference equations:

$$w = \frac{2}{T}\frac{z - 1}{z + 1} \tag{17}$$

The direct w-plane design approach is widely used in the spacecraft community, rather than risking unknown problems with the approximate emulation methods. These problems are of special concern for flexible space systems in which folding and aliasing effects can rapidly destabilize the many lightly damped high-frequency modes.

D. Other Important Issues in Digital System Design

The previous sections have introduced methods for analyzing and designing digital control laws. There are a number of additional issues associated with the design implementation which are important to the performance of the digital flight-control system.

(a) Software Architecture

The software implementation of the digital (difference) equations has a significant effect on the effective time delay of the overall system. For example, a common practice in the design of first generation fixed- and rotary-wing digital systems was to synchronize the zero-order hold with the sampler; then, the updated control command is issued at the end of the frame which is at the same instant that the new sensor signal is obtained (fig. 12(a)). This introduces a full sample period delay in the calculation and yields an additional phase lag $\phi = -\omega T$ which must be included in the analysis. Since the difference equations depend on the current and previous sensor signal values, it is possible to precalculate much of the control law in the interim time before sensor information is updated (fig. 12(b)). Then when the new sample is taken, the calculations can be finished rapidly and the updated control value can be released with a minimum delay. In the remaining time before the following sample is taken, all of the precalculations and management system functions needed for the next cycle can be performed. Thus, synchronized input/output timing yields unnecessarily large computational delays, as experienced in the F-18 system before the software architecture was properly redesigned (ref. 3).

(b) Finite Word Length and Quantization

Since the computer has a finite number of bits with which to represent a given signal level, roundoff will occur in calculations. When the sample rate is very high, the z-plane poles of the system will all be nearly unity, and the finite word length in the computer will lead to errors in the actual system frequency response when compared to the calculated values. This puts an upper limit on the maximum

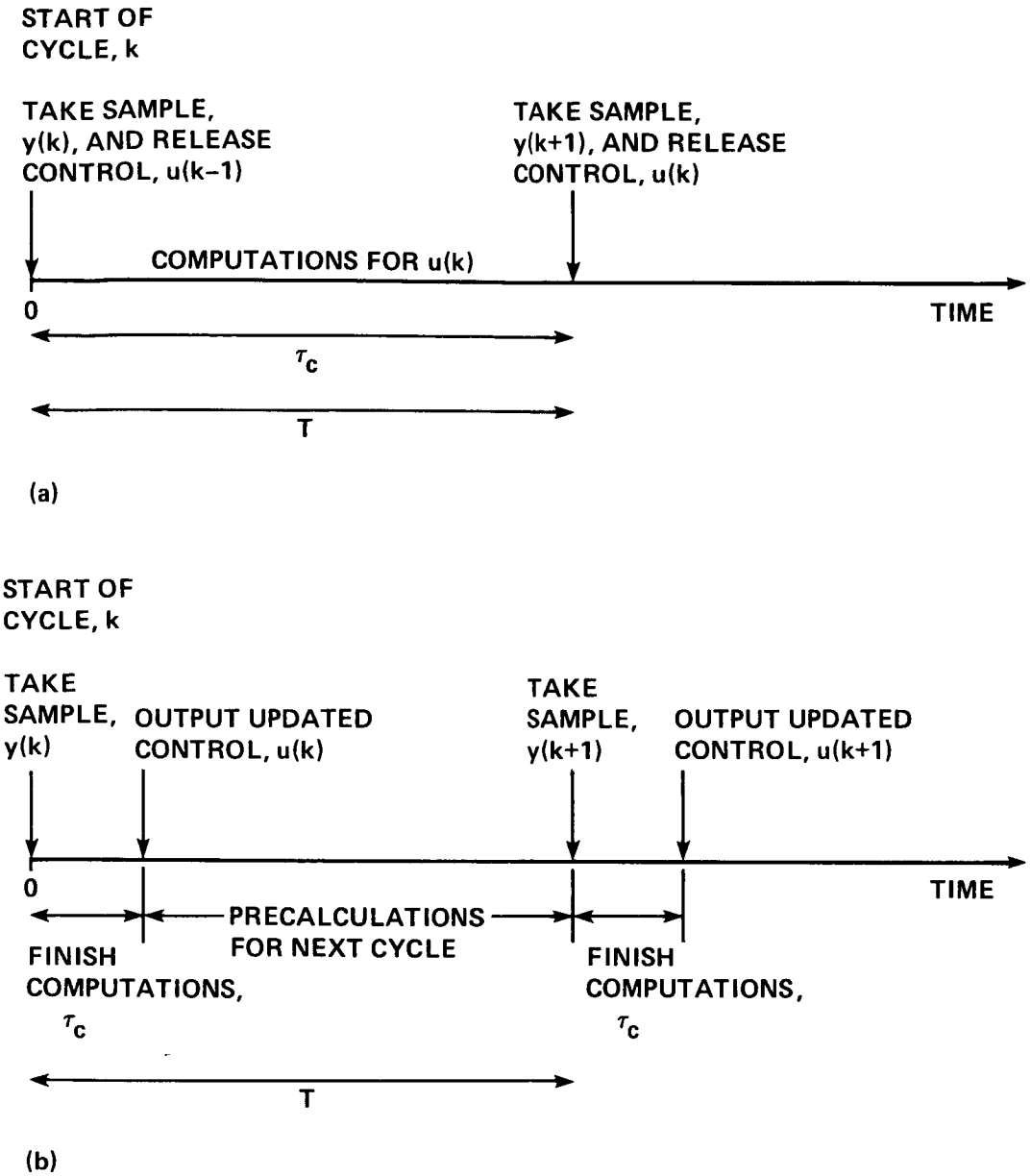

Figure 12.- The effect of timing sequence on computational time delay, τ_c. (a) Synchronized input/output software architecture creates a large computational time delay, $\tau_c = T$; (b) reduction of computational time delay by precalculating $\tau_c < T$.

usable sampling rate as a function of word length. Quantization is due to the discrete nature of the analog-to-digital converter (sampler). This element will sense changes in signal level only when they are above a certain threshold value. This creates a dead-band in the system dynamics and can cause limit cycle behavior. Quantization and word length effects can be evaluated with analytical and simulations models. Methods for treating these problems are discussed extensively in the literature (refs. 19,20,40) and will not be covered here; however, these are

important issues for practical digital flight-control design and should not be overlooked.

(c) Stick-Sampling Skew

In the previous sections, the analysis methods have assumed that the (analog) control inputs were synchronized with the stick-sampler. This implies that there is no time delay between the initiation of a transient control input by the pilot and the detection of a stick signal change by the digital system. However, in reality the pilot will initiate control changes during the period between the samples; thus a delay time τ_{sk} will transpire during which no control change is detected at δ_s^* in figure 2. This stick-sampling skew τ_{sk} must be included in the stick sampler of figure 2. Reference 19 suggests that a full cycle delay ($\tau_{sk} = T$, sec) should be used here to allow for the worst case behavior. However, on the average the pilot will perceive an effective time delay of $\tau_{sk} = T/2$.

This stick-sampling skew is an inter-sample effect which is not a duplication of the zero-order hold delay of figure 5. To further clarify this point, figure 13 illustrates the various independent contributions to the total digital delay for a simple system. This figure compares the control surface response $u(t)$ to a step stick input $\delta_s(t)$ for an analog implementation and a simple digital implementation of a low-pass stick filter. Since the analog system responds instantly to the step input at $t = 0$, there is no stick-sampling skew or other delays for this implementation. The digital system, however, does not sense a change of δ_s^* until the sampler "fires" at $t = \tau_{sk}$. The digital computations require τ_c seconds before the zero-order hold can be updated. Finally, the zero-order hold itself introduces $T/2$ seconds of effective delay, as before in figure 5. Thus the total delay introduced by the digital system is the sum of these contributions:

1. Stick-sampling skew, $\tau_{sk} \doteq T/2$
2. Computational delay, τ_c
3. Zero-order hold delay, $T/2$

Total delay: $T + \tau_c$

For a moderate sample rate of about 30 Hz, and synchronized input/output software architecture (fig. 12), these digital delays add up to 66 msec or roughly 33% of the maximum time delay of $\tau_e \doteq 100$ msec which is suggested from data of figure 7.

In the simple Euler rule implementation used for illustration in figure 13 (but not used in practice or in the case study), the current control value $u^*(k)$ depends only on the previous control and stick samples $[u^*(k - 1), \delta_s^*(k - 1)]$; this explains why the control update $u^*(k)$ does not jump when the sampled step-input $\delta_s^*(k)$ first jumps. This is a rough approximation to the function of the complete digital system (fig. 2). In actual digital control system implementations, the pilot inputs are first smoothed by an analog stick filter before sampling occurs (fig. 2). Also, as in the ADOCS, digital derivative-rate limiters may be included after the sampler to further attenuate jumps in θ_c^* (fig. 2) that occur with the Tustin implementation (the recommended method) when the sampler first senses a change in the stick filter output. These additional elements complicate the analyses of stick sampling skew

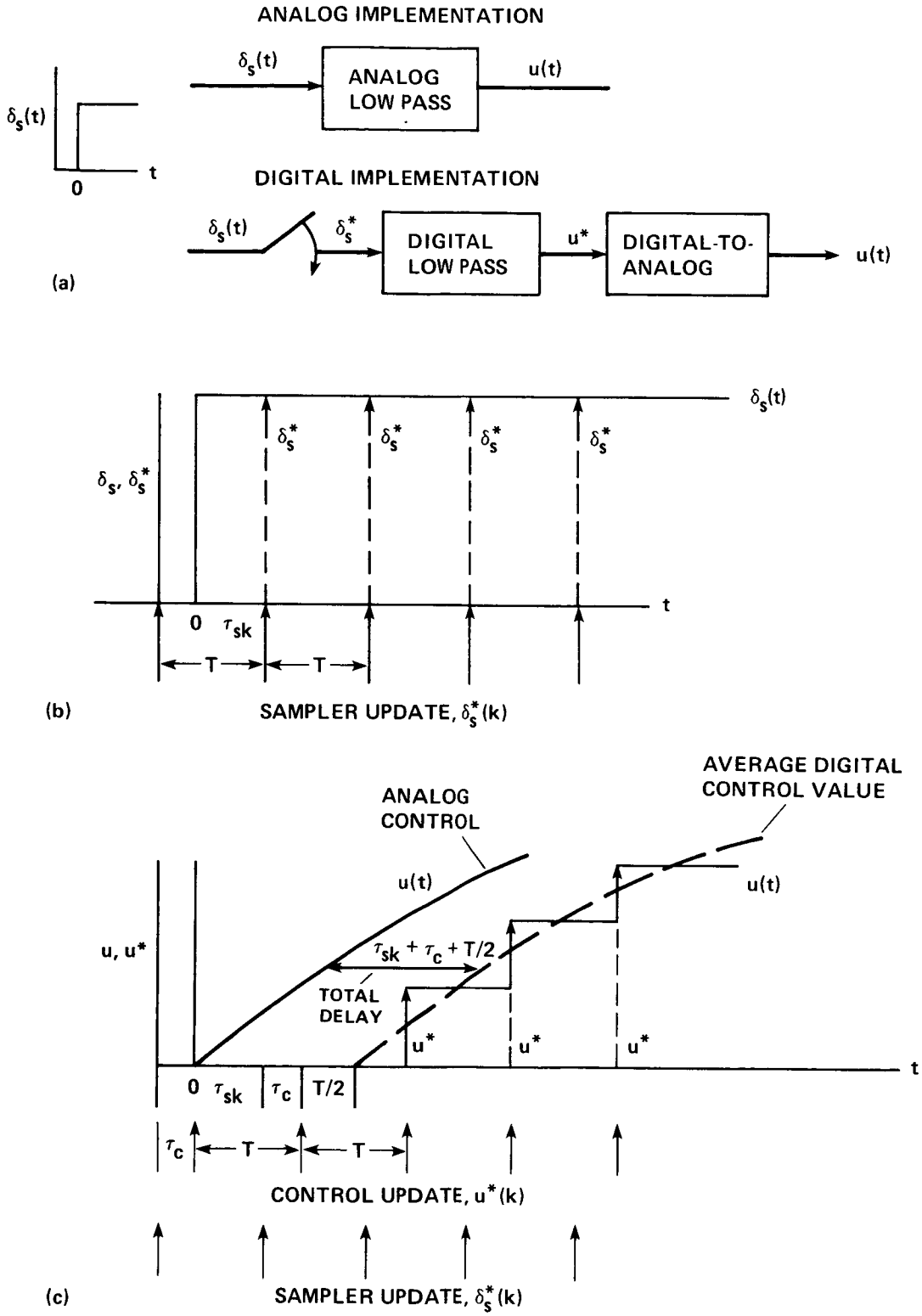

Figure 13.- Contributions to the total digital system delay. (a) Analog and digital system implementations; (b) stick command input; (c) control surface response.

considerably. In the context of a fully linear analysis, modeling the average skewing effect as a one-half cycle throughput-delay is a satisfactory approximation.

II.C.5 Experience with Low Sample-Rate Digital Flight-Control Systems Designed by Direct Digital Methods- In a low sample-rate system, the distortions which are due to the digital elements such as samples and zero-order holds are not adequately approximated using the emulation technique. Some of the best examples of careful direct digital design for low sample-rate systems are documented in the spacecraft booster community. Booster vehicles are highly flexible systems with many lightly damped modes, and quite often have unstable dynamic characteristics at low frequency. Active high-frequency control is needed to stabilize modes which would otherwise be destabilized by the basic rigid body attitude feedbacks. Since many of these flexible modes are well beyond the sampling frequency, aliasing effects must be carefully considered in the design; so exact direct digital methods are exclusively employed. Detailed calculations of gain and phase margins for each of the flexible modes is a key aspect of the design procedure for these vehicles.

Multirate systems are quite often used since guidance loops have very low bandwidths and thus require only lower sampling rates, while higher bandwidth stabilization loops require higher sampling rates. Complex interactions between the fast and slow rate loops can occur, and have been extensively studied in the spacecraft community. Among the best references in this field are the reports by Lee (ref. 34) and Holzman et al. (ref. 35), which carefully describe analysis methods and present actual case studies. As a matter of standard practice, the spacecraft community conducts dynamic analyses in the z- and w-planes, in large part because the exact w-plane analysis techniques are so similar to the s-plane methods that there is no advantage to using the approximate emulation technique.

Within the fixed-wing community, the best examples of careful direct digital design using a low sample rate are the digital F-104-G aircraft (refs. 4 and 42) and the Princeton University digital Navion research aircraft (ref. 16). The digital flight-control system for the F-104-G aircraft was developed by MBB Aircraft of the Federal Republic of Germany. This system uses a 16-2/3 Hz sample rate for the basic control laws, and a 50 Hz sample rate for the digital notch filters needed to eliminate structural mode interaction. Using the 50 Hz sample rate avoids dynamic distortion which would occur if the (high-frequency) notch filters were implemented at the basic low sample rate. The digital F-104-G aircraft has a model-following control system, developed with modern control methods, which provides normal acceleration (n_z) command response and attitude stabilization. Also, there is nonlinear stick shaping to optimize the control sensitivity characteristics. The basic system is quad-redundant and operates asynchronously. A digital backup system, which uses simple rate feedback stabilization, is always active and can be switched in by the pilot or by the redundancy management system at any time.

The digital F-104-G flight-control system design and analysis was completed using direct digital methods, to account accurately for the digital distortions which result from the relatively low sample rate. The system employs a full complement of sensors including attitude, attitude-rate, acceleration, and inertial position; in terms of system complexity, the F-104-G represents the state-of-the-art in

digital flight control. Flight experiments were conducted to examine the feasibility of the low-rate digital system for various levels of static instability. Good handling and performance characteristics with negative static margins of up to 22% of the mean-aerodynamic-chord were successfully demonstrated (ref. 4). The success of this aircraft shows that good handling qualities and performance are feasible using a low-rate system if digital design methods are used.

A second important data point for illustrating the utility of direct digital methods for low-sample rate systems is the Princeton University digital Navion research aircraft. Flight-control systems were designed using direct digital methods with sample rates ranging from $\omega_s = 4$ to 10 Hz. Studies were conducted to evaluate the effect of sample rate and effective time delay on piloted handling qualities. The evaluation tasks included rapid maneuvering, ground object tracking, and landing approach using an aircraft carrier approach mirror, and angle-of-attack meter/indexer. The results showed that the 10 Hz system was completely adequate, with only a slight sensation of abruptness for the 8 Hz system. A 6 Hz sample rate was considered to be the minimum acceptable value from a handling qualities standpoint. At a sample rate of 5 Hz pilots reported unacceptable levels of "jerkiness" and "erratic behavior." Even though pilot acceptance becomes a critical issue for sampling rates below about 5 Hz, the Navion study shows that system performance can be maintained to even lower sample rates using the direct digital approach.

The flight experience with the F-104-G and Navion aircraft shows that practical lower sample-rate systems can be developed based on the direct digital design approach. The adoption of a conservative sample rate of about 15 Hz for at least the lower bandwidth outer control loops would reduce commonly used sample rates in the fixed-wing and rotary-wing communities by a factor of 2 or 3. This would allow for more flexibility and system growth before re-design or increased computer capability would be required. Even when higher sample rates are used, analysis on the w-plane methods allow an accurate representation of the important actuator response dynamics while still maintaining a close analogy with the s-plane methods.

Autonomous backup control systems are necessary in the event of failure of the primary system. While analog computers (X-29, see footnote 3, page 6) and mechanical links (F-18, ref. 29) are commonly used for this purpose, an autonomous low sample rate digital backup system (as used for example on the F-104-G, ref. 4), is an attractive alternative. The low sample-rate digital backup system eliminates heavy mechanical links and requires a minimum computational capacity, while providing adequate multimode handling qualities and systems integration that an analog backup system cannot provide. Direct digital design methods and existing successful flight experience with low-sample rate systems make digital backup flight-control systems worth considering for future combat rotorcraft.

A number of excellent computational tools are available for conducting direct digital design and analysis. Among the best documented commercial packages are MATRIXX (ref. 43) and CNTL-C (ref. 44). These programs draw on modern and classical techniques in both the digital and continuous domains. An excellent facility for classical analysis of continuous and multirate digital systems is the program LCAP2 developed by E. A. Lee of the Aerospace Corporation (ref. 37) and adapted for

operation on the VAX computer by the author. Classical analyses in the time and frequency domain are easily conducted in the s-, z-, and w-planes. Modern graphics capabilites are very useful for quickly generating Bode and root locus plots, which are basic tools in the analysis of complex digital systems. The LCAP2 program was used extensively in the case study analysis presented in Section III.

The next section presents a detailed case study of digital high-bandwidth control system, based on the ADOCS Black Hawk aircraft. The intent is to illustrate the analysis procedures introduced in the previous sections and to expose problems of particular concern to developers of new rotorcraft using digital flight-control systems.

III. CASE STUDY OF A DIGITAL CONTROL SYSTEM DESIGN FOR A MODERN COMBAT ROTORCRAFT

III.A Introduction

This section presents a detailed case study of a high-bandwidth, model-following digital flight-control system for a modern combat rotorcraft. The objective of this study is to illustrate the analysis and design methods for high-bandwidth digital rotorcraft systems which were introduced in the previous sections. The Advanced Digital/Optical Control System (ADOCS) Black Hawk was selected as the basis for the present case study because this system represents the state of the art in modern combat rotorcraft. Ongoing flight test evaluations of the aircraft will be useful for analysis validation and will be a key data point for future Army designs (JVX and LHX). Extensive documentation on design, philosophy, implementation, and simulator studies of the ADOCS system are presented in references 7 and 45.

For the most part, the basic philosophy and control system architecture of the ADOCS design has been retained in this case study. Some aspects of the detailed implementation which are not pertinent to the handling qualities or control problems are omitted. Also, the analyses and discussion are limited to the longitudinal (pitch) attitude characteristics.

The UH-60 Black Hawk (fig. 14) is a four-bladed, articulated single main rotor helicopter developed by Sikorsky Aircraft. Commands to the ADOCS control system (developed by Boeing-Vertol) are through a multi-axis, small deflection, sidestick controller. The ADOCS is a high-bandwidth, model-following system. The original ADOCS design (ref. 7) used a 40 Hz sample rate and had a pitch attitude crossover frequency of $\omega_{c_\theta} = 6$ rad/sec for the stabilization loops. Control system architecture is largely based on previous HLH and TAGS system designs (also developed by Boeing-Vertol, refs. 46 and 47). The ADOCS flight control system was designed using the emulation method (Section II.C.2). Tustin transforms are completed within the on-board flight control processor as a function of selected sample rate. This approach allows the sample rate to be easily changed but does not expose the associated digital artifacts. A digital analysis of the discrete data system is not presented in the available referenced documentation.

During the development of the flight hardware and software, the computational requirements were found to exceed the microprocessor capability at the 40 Hz sample rate. There was insufficient time to complete all the needed computations and system checks, even with the full sample period computational delay built-in to the software architecture (fig. 12(b)). Therefore, the sample rate of the feedback loops was reduced to 30 Hz to alleviate this throughput delay problem. Also, analyses and simulation studies conducted by Boeing-Vertol subsequent to the original design suggested unacceptable levels of in-plane (lead-lag) rotor mode excitation. As a result, the feedback gains were reduced by 40%, thereby lowering the crossover

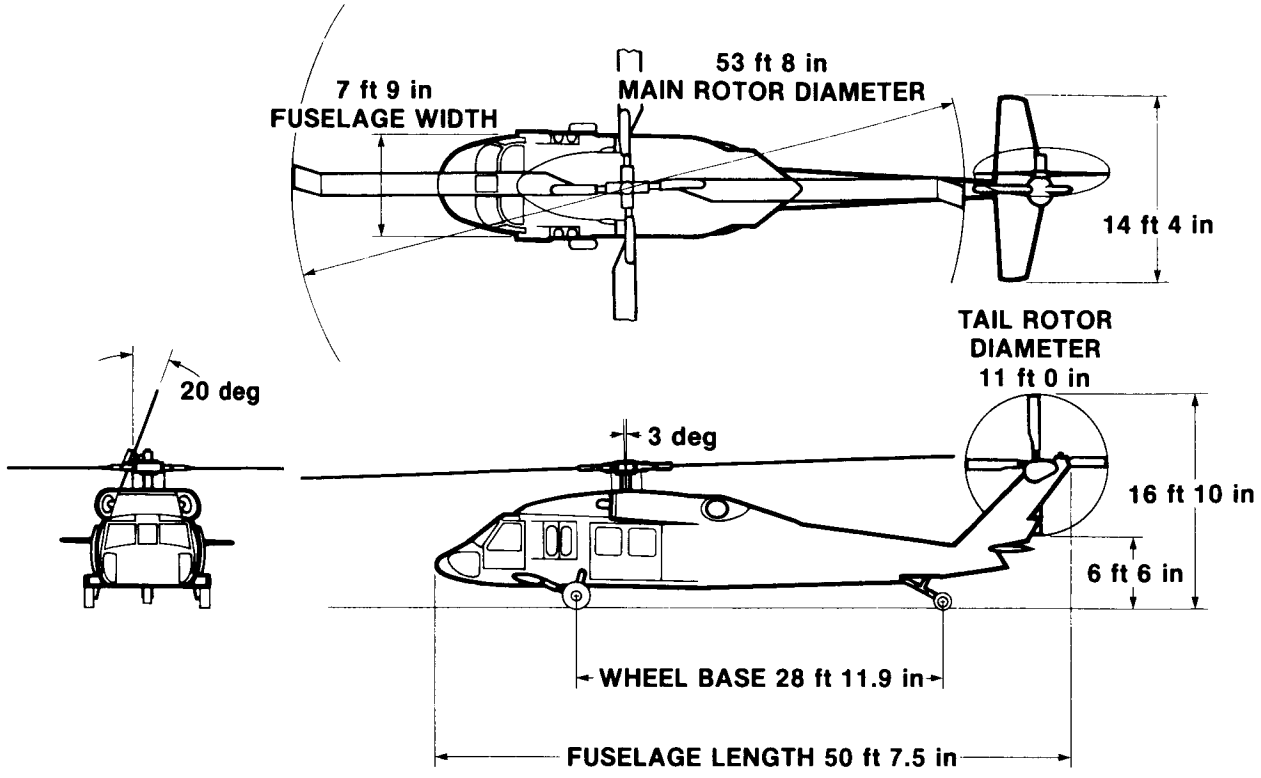

Figure 14.- UH-60A Black Hawk general arrangement.

frequency of the stabilization loop to ω_{c_θ} = 4 rad/sec. Current ADOCS flight gains are even further reduced.

The following case study is broadly based on the ADOCS system as described in the simulation document, but does not reflect the actual detailed final flight system design. This analysis is meant to illustrate important generic considerations for high-bandwidth digital rotorcraft, rather than to evaluate the expected performance of the ADOCS design specifically.

The case study discussion is organized into ten major sections:

Section III.B - Criteria for Assessing System Performance

Section III.C - Overview of ADOCS Pitch Attitude Flight Control System

Section III.D - Open-Loop Dynamics of Rigid Body/Rotor/Actuator System

Section III.E = s-Plane Analysis of the Nominal (ω_s = 40 Hz, ω_{c_θ} = 6 rad/sec) Design

Section III.F - Practical Implementation Considerations for the Nominal (ω_{c_θ} = 6 rad/sec) Design

Section III.G - s-Plane Performance of a ω_{c_θ} = 4 rad/sec, ω_s = 30.3 Hz Emulation Design

Section III.H - Digital Control Laws for the ω_{c_θ} = 4 rad/sec, ω_s = 30.3 Hz Emulation Design

Section III.I - Digital Analysis of the ω_{c_θ} = 4 rad/sec, ω_s = 30.3 Hz Design

Section III.J - A 15 Hz Digital Design

Section III.K - Case Study Assessments and Conclusions

The evaluation of the original (nominal) design (ω_{c_θ} = 6 rad/sec, ω_s= 40 Hz) is based on the simulation model documentation of reference 7, and forms a standard for later comparison with the lower bandwidth systems. An evaluation of command response and performance, stability and control margins, and handling qualities implications is presented. Based on the available documentation, there are a number of important aspects associated with the practical digital implementation of the original (40 Hz) design which were omitted in the reference 7 analysis; also, the inability of the flight hardware to run at the high 40 Hz sample rate makes a full digital evaluation of this system rather academic. Instead, an analysis of a 30.3 Hz (ω_{c_θ} = 6 rad/sec) system, including the omitted system components (such as antialiasing filters, and notch filters), is presented. These changes significantly degrade the performance of the original 40 Hz design (as shown in the discussion) and require a reduction in the crossover frequency to ω_{c_θ} = 4 rad/sec. This lower bandwidth system is then analyzed using both emulation and direct digital methods.

The last part of this case study considers the feasibility of implementing a low sample-rate (15 Hz) digital system for the ADOCS Black Hawk aircraft. Such a system would allow for the probable future software growth without further reductions in the design sample rate. Also a low-sample rate design could be used for a digital backup control system rather than the current analog backup system on the ADOCS. The 15 Hz design is based on the direct digital methods to account for the digital distortions, which are important for this lower rate system. Finally, assessments and overall conclusions based on this detailed case study are discussed.

III.B Criteria for Assessing System Performance

Since the ADOCS Black Hawk is intended to demonstrate advanced rotorcraft system performance and handling, it is logical to use the proposed LHX handling qualities specifications (ref. 15) as a guide to assess the response characteristics in this case study. This proposed LHX specification is a major revision of the much older MIL-H-8501A helicopter handling-qualities specification (ref. 48). The format of the various LHX criteria reflect the proper conserns for highly augmented combat rotorcraft, such as the need for frequency-domain based response characterization. However, the available flight-test data base from which the criterion values were obtained is extremely limited, as discussed in Section II. As new data on advanced rotorcraft have become available, these criterion values have been adjusted

considerably. For example, the initial criterion values for bandwidth (ω_{BW_θ}) and time delay τ_p (fig. 3) were based primarily on rotorcraft simulation data (e.g., refs. 7 and 49) and fixed-wing flight data (such as contained in figs. 6 and 7). The initial boundaries for Level I handling quantities (satisfactory without improvement) and Level II handling qualities (deficiencies warrant improvement) are shown in figure 15, obtained from reference 50. Notice that the time delay limit of τ_p = 100 msec is consistent with the fixed wing data (fig. 7). The current boundaries (ref. 15), also shown in figure 15, are heavily based on flight data from tests of the (Canadian) National Research Council variable stability rotorcraft, a Bell-205 (teetering rotor) helicopter equipped with a sidestick controller and a digital flight control system (ref. 51). Based on these latest data, the newer boundaries allow a lower bandwidth and a much higher time-delay (ref. 15). Other interim versions of this document indicated even less stringent requirements. Also, the current criterion defines ω_{BW} based only on 45 deg of phase margin for attitude-response type systems; the initial specification defines the bandwidth as the lesser of the 6 dB gain margin or 45 deg phase margin frequencies (fig. 3). For the purposes of this report, the initial (more conservative) criterion values of figure 15 and reference 50 and the bandwidth definition in figure 3 are used.

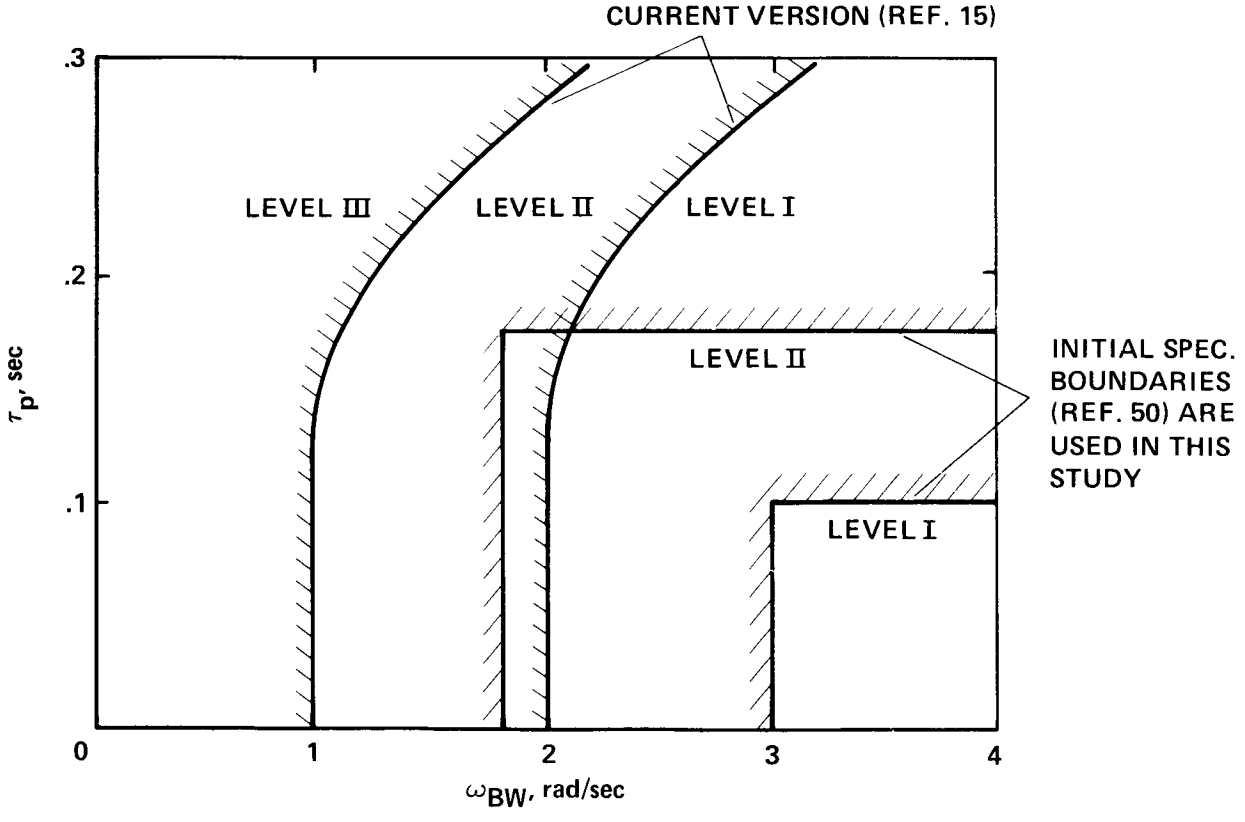

Figure 15.- Bandwidth and phase delay requirements for pitch (roll) attitude response types--hover and low speed, from references 15 and 50.

III.C Overview of the ADOCS Longitudinal Flight-Control System

The ADOCS control system is very versatile, allowing a wide variety of selectable command and stabilization modes ranging from acceleration-command to velocity-command/position-hold. In the simulation study (refs. 7 and 45) which supported the development of the ADOCS system, a variety of controllers were also examined; these ranged from a conventional center stick to a four-axis force-sensing sidestick controller. For the purposes of this case study, it was necessary to select a representative control law and controller configuration. The attitude-command/attitude-stabilization system was chosen since, in the simulation study, it was considered to be a requirement for satisfactory handling qualities in hover and low speed NOE flight in the day/visual environment. The assumed controller is a limited displacement side-stick.

The ADOCS control system is based on the model-following concept which is generically illustrated in figure 16. The sketch is divided into three sections: command model $M(s)$, feedforward $F(s)$, and stabilization which follows the structure of figure 1. The vehicle dynamics are represented by the appropriate transfer functions $P(s)$, and the feedback compensation is denoted by $H(s)$. The stabilization section provides disturbance rejection and improves the model-following performance in the presence of uncancelled dynamics (e.g., rotor and actuator dynamics). The stabilization loop bandwidth is generally set as high as possible to produce a stable and insensitive platform, while maintaining adequate phase and gain margins. The ADOCS feedback gains are scheduled as a function of airspeed to provide a roughly constant crossover frequency of $\omega_{c_\theta} = 6$ rad/sec in the original (nominal) design. The feedback gains are not scheduled as a function of the command mode (i.e., attitude command or rate command). The closed-loop response of the stabilization section is determined from the transfer function from δ_{com} to the output (c):

$$\frac{c}{\delta_{com}}(s) = \frac{P(s)}{1 + P(s)H(s)} \tag{18}$$

For high values of loop gain ($P(s)H(s) \gg 1$), the closed-loop transfer function approaches the limiting condition

$$\frac{c}{\delta_{com}}(s) \doteq \frac{1}{H(s)}$$

which is independent of parameter variations in the airframe $P(s)$.

The second portion is the feedforward element $F(s)$, which contains an inverse model of the plant $P^{-1}(s)$ and a model of the feedback compensation $H(s)$. (Note that in the control system architecture of figure 16 the plant model $P(s)$ cannot contain right-half plane zeroes, since $P^{-1}(s)$ would then contain unstable dynamics.) The transfer function of the feedworward section is:

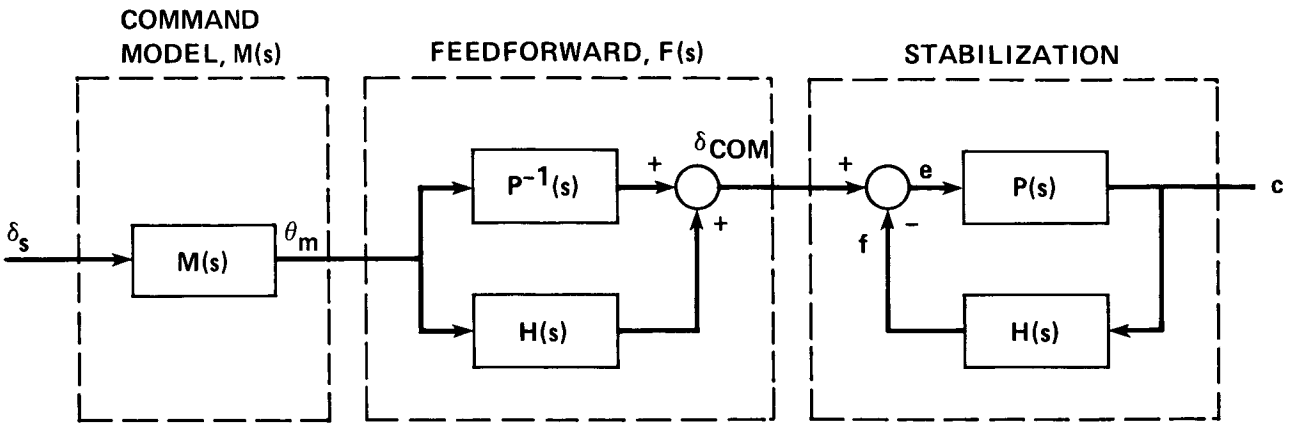

Figure 16.- ADOCS generic model-following concept.

$$\frac{\delta_{com}}{\theta_m}(s) \equiv F(s) = P^{-1}(s) + H(s) \tag{19}$$

The combined transfer function for the feedforward and stabilization sections is:

$$\frac{c}{\theta_m}(s) = [P^{-1}(s) + H(s)] \frac{P(s)}{1 + P(s)H(s)} = \frac{1 + P(s)H(s)}{1 + P(s)H(s)} = 1 \tag{20}$$

This shows that the feedforward and stabilization portions have a combined (ideal) transfer function of unity. Thus the vehicle response c exactly follows the model response θ_m.

The first section is the command model, M(s). This section generally contains simple transfer functions which represent the desired handling quality characteristics, as determined from simulation or flight experiments. (The stick filter and deadband of fig. 1 can be thought of as contributing to the command model dynamics, M(s).) For example, if a rate-command system is desired, the command model might have the form:

$$\frac{\theta_m}{\delta_s}(s) = \frac{M_\delta}{s(s + a)} \tag{21}$$

Thus, the model's pitch attitude response to a step-stick input will ramp asymptotically, with a first-order pitch rate response having a desired time constant of 1/a. For an attitude-command system, the model will typically have a standard second order form:

$$\frac{\theta_m}{\delta_s}(s) = \frac{M_\delta \omega^2}{s^2 + 2\zeta\omega s + \omega^2} \tag{22}$$

where M_δ is the pitch stick sensitivity, and ζ and ω are the desired attitude response characteristics. Since the combined feedforward and stabilization sections ideally have a transfer function of unity, the total system output c will follow the command-model response exactly. Typically, the bandwidth of the command model will be 2 to 3 times lower than that of the stabilization section. For good disturbance rejection, the open-loop crossover frequencies for the stabilization loop are typically in the range of ω_{c_θ} = 3-6 rad/sec. Desirable attitude and rate-command bandwidth characteristics are typically ω_{BW_θ} = 2-4 rad/sec. This capability to set stabilization and command-response characteristics independently is a key advantage of the model-following concept. In terms of the schematic diagram of figure 1 and the notation of reference 7, the feedforward and command-model sections are combined and are referred to together as the "command block" ($C(s) = \delta_{com}/\delta_s$).

The preceding discussion of the model-following concept is based on the ideal assumption that an exact inverse model of the plant $P^{-1}(s)$ is available in closed form. As a practical matter, such a representation is neither available nor necessary. For a rotorcraft, the inverse model may be a highly simplified approximation of a nominal linear transfer function, and is not varied with speed. This simplified inverse model excludes the rotor and actuator dynamics, since attempts to "cancel" these high-frequency elements would lead to unreasonable surface deflections and rates. The inverse model is typically a first- or second-order decoupled transfer function.

The use of this highly simplified inverse plant model means that the ideal result of

$$\frac{c}{\theta_m}(s) = 1$$

(eq. 20) is realized only for a frequency range below the first rotor or actuator mode, which is the limitation on the model-following capability of the system. The low-frequency dynamics that are not completely cancelled, a result of using a highly simplified inverse plant model, are suppressed by the high feedback gains. To ensure that the aircraft response follows the model for frequencies up to the model bandwidth, the stabilization loop bandwidth is generally selected to be 2 or 3 times greater than the command-model bandwidth.

The model-following concept as presented above reflects the design philosophy used in the ADOCS system and its forerunners--the TAGS and the HLH programs (refs. 46 and 47). An in-depth analysis of the SH-3 model-following control system, also based on this concept, is presented by Ringland (ref. 52). The following discussion is largely based on Ringland's analysis approach.

An s-plane schematic diagram of the ADOCS attitude-command/attitude-stabilization control system is presented in figure 17. Some aspects of the full control system schematic of reference 7 are omitted in figure 17, for illustrative clarity; these include deflection and rate limits, port limiting, and nonlinear command shaping. Also, the computational time delay τ_c (which adds to the time delay of the zero-order hold) is omitted for the present. There are a number of

important additional aspects which were omitted in the documented ADOCS control-system diagram and the related analyses, including: anti-aliasing and notch filters, and gyro and sensor dynamics. The importance of these omitted elements will be examined in detail in later sections.

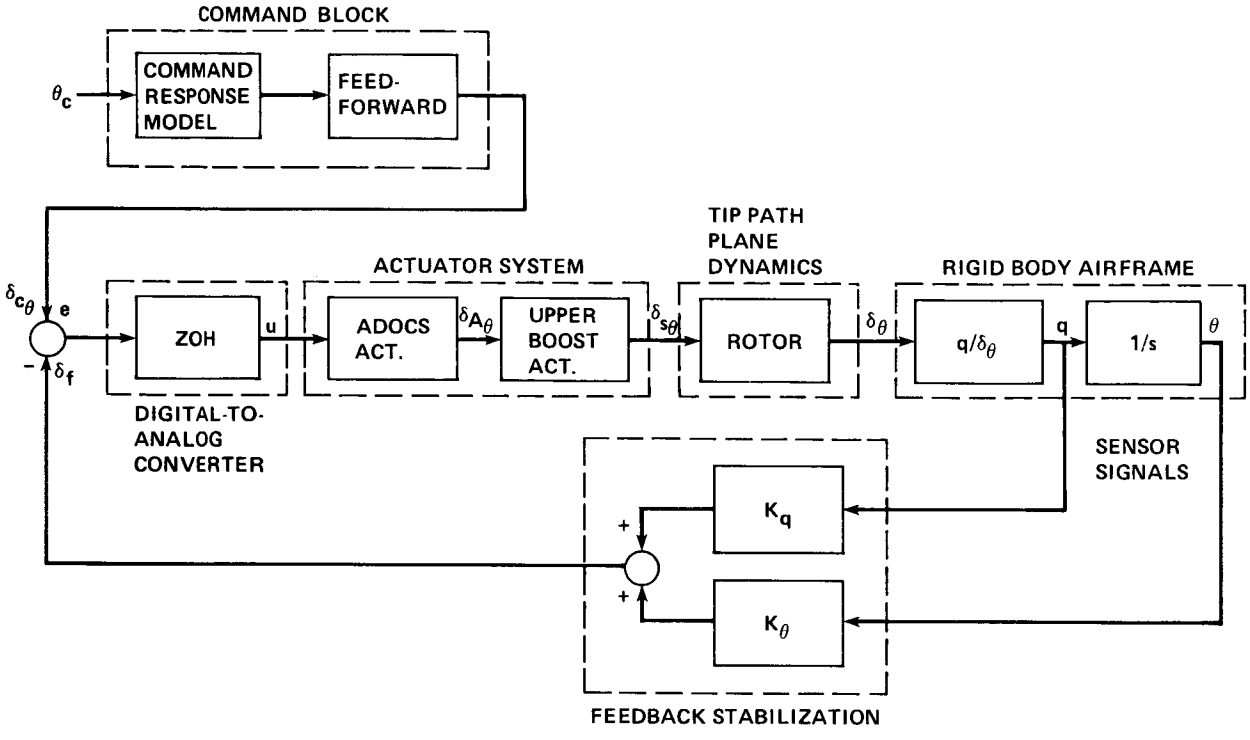

Figure 17.- Pitch attitude channel for simplified ADOCS control system.

The pertinent rigid body transfer function for the longitudinal analysis is the pitch-attitude response to rotor tip-path-plane deflection (θ/δ_θ). The decoupled pitch response transfer function is second-order over fourth-order. For hover, one denominator root (natural mode) represents the decoupled heave mode, and the remaining three roots form the classic hovering cubic. The response of the tip-path-plane to swashplate inputs is represented by the "rotor block," which contains a fourth-order transfer-function representation of the first two flapping modes (regressing and advancing). The in-plane (lead-lag) rotor dynamics were not included in reference 7 analysis. However, the regressing lead-lag dynamics are located near the 1/rev frequency, which is relatively close to the stabilization loop crossover frequency. Therefore, in order to avoid excessively exciting this mode, care must be taken to reduce the loop gain in the 1/rev frequency range. This problem is discussed in Section III.F.

The ADOCS Black Hawk actuator system is composed of the basic upper boost actuators in series with the additional ADOCS actuators. The upper boost actuator is modeled by a first-order transfer function, and the ADOCS actuator is modeled by

a second-order transfer function. The zero-order hold is represented by a pure time delay (T/2) approximation (emulation analysis), and ignores additional computational delays (for the present). The attitude stabilization system uses pitch attitude and pitch rate feedbacks (K_θ and K_q, respectively), which are scheduled as a function of speed. For the present analysis, these gains are considered to be constant at their reference hover values.

The command block contains the command response model and the feedforward compensation. For good hovering and low-speed (NOE) flying qualities, a second-order attitude command response is desirable (ref. 49). The selectable transfer function parameters determine the stick sensitivity, response damping, and natural frequency. These are based on handling qualities data (ref. 49). The feedforward element contains the feedback compensation and a very simple inverse model of the rigid body airframe dynamics.

In the detailed block diagrams of the actual ADOCS implementation, a distinction is made between the "primary" flight control system (PFCS) and the "automatic" flight control system (AFCS). This division yields a high-reliability backup system, which is based on forward loop shaping alone (adequate handling-qualities are maintained in the event of sensor failure). Since the total (effective) transfer function between the stick input and vehicle response works out the same as outlined above, this division unnecessarily complicates the present analysis, and is omitted in figure 17. The following section discusses the open-loop dynamics of the vehicle/rotor/actuator system.

III.D Open Loop Dynamics of the Rigid-Body/Rotor/Actuator System

The present analysis is based on a six degree-of-freedom fully coupled linearized representation of the Black Hawk helicopter in hovering flight. The linearized stability derivatives used in this analysis are given in table 1 and were obtained from reference 7, Vol. 2. Pitch motions are primarily controlled by longitudinal cyclic inputs, but secondary (cross-coupled) responses result from lateral cyclic, and pedal inputs. Since inherent dynamic coupling through the lateral degrees-of-freedom can be significant, pole/zero cancellation of the lateral modes may not be complete or obvious from inspection of the longitudinal transfer function. There are three alternate methods to treat interaxis coupling in the full-system matrix without including the coupled degrees-of-freedom explicitly:

1. Drop the coupling terms in the system matrix--in this standard method of analysis, the cross-coupling terms such as M_p and L_q are omitted, so the longitudinal and lateral transfer functions decouple. This method of analysis is satisfactory for very mildly coupled systems (e.g., fixed-wing aircraft in cruise), but can introduce significant errors when lateral and longitudinal motions are highly coupled, such as in a single rotor helicopter in a hovering flight condition. Even more extreme coupling will occur if the rotor system is not articulated (hingeless or bearingless), rather than that used in the present UH-60 articulated system.

2. Lower-order equivalent transfer function fitting--this procedure uses a least-squares method to adjust the transfer function parameters of a lower-order (approximate) model to a best fit of the frequency response of the complete higher-order open-loop system. This method does not account for the changes in the primary transfer function (say, θ/δ_θ) which will occur when the secondary, coupled loops are closed (as for example, $\phi \rightarrow \delta_\phi$).

3. Constrained variable method (refs. 52 and 53)--this method includes the off-axis dynamics, but assumes that infinitely tight feedback loops are used to constrain the coupled degrees-of-freedom. The assumption is reasonable since the coupled motion is stabilized by (high-gain) feedbacks as well. The result is that the order of the longitudinal transfer function is the same as if decoupled dynamics were assumed (as in method 1); however the parameters in the pitch response transfer functions contain the one-way coupling effects of the lateral/directional feedbacks into the longitudinal motions. This method is more accurate than methods 1 and 2 for coupled, augmented systems, and leads to satisfactory results as shown in reference 52.

TABLE 1.- UH-60A STABILITY DERIVATIVES--HOVER CASE

G.W. = 16824.91 lb	Vel. = 0.50 knots	Alt. = 25.00 ft
C.G. = -9.20 in.	R/C = 0.00 fpm	Temp = 59.00 deg

	L/IXX	M/IYY	N/IZZ	X/M	Y/M	Z/M
δ_θ	-0.0627	-0.3286	-0.0021	1.7041	-0.0845	0.1134
δ_ϕ	1.3118	-0.0051	0.0266	0.0478	0.9664	0.0036
δ_ψ	-0.9313	0.0411	0.7153	1.1265	-1.7151	0.6799
δ_c	-0.0620	-0.0183	0.0665	1.0893	0.2289	-8.5827
p	-3.3484	0.2938	-0.1856	-1.6106	-1.5152	-0.1703
q	-1.6917	-0.5193	-0.4165	1.3499	-1.4242	0.1135
r	0.2119	-0.0687	-0.2879	-0.3497	0.4485	2.0788
u	0.0386	0.0005	0.0018	-0.0150	0.0168	-0.0050
v	-0.0260	0.0085	0.0081	-0.0092	-0.0465	-0.0097
w	0.0024	0.0021	-0.0010	0.0212	0.0038	-0.2748
IHT	0.0000	0.0009	0.0000	-0.0009	0.0000	0.0024

Units: $\delta_\theta, \delta_\phi$ inches of stick
δ_ψ inches of pedal
δ_c inches of collective
p,q,r rad/sec
u,v,w ft/sec
IHT deg

The method 3 approach is adopted here since the Black Hawk is fairly coupled and highly augmented in all angular degrees-of-freedom, and since future combat rotorcraft will probably utilize a hingeless rotor or some other high-bandwidth, highly coupled system.

The transfer function for pitch attitude response to longitudinal tip-path-plane inputs (θ/δ_θ), with roll and heading attitudes constrained, is calculated from:

$$\frac{\theta}{\delta_\theta} = \frac{N\delta^{\theta}_{\theta}\delta^{\phi}_{\phi}\delta^{\psi}_{\psi}}{N\delta^{\phi}_{\phi}\delta^{\psi}_{\psi}} \tag{23}$$

The "coupling" numerator polynomial is obtained by simultaneously substituting the forcing function columns for longitudinal, lateral, and yaw control inputs into the columns of the system matrix (sI - A) associated with pitch, roll, and yaw responses, respectively, and then evaluating the determinant. This technique is a generalization of Cramer's Rule for determining numerators of a transfer function (refs. 53-55). The denominator of equation (23) is obtained by simultaneously substituting only for roll and yaw inputs.

Since the lateral velocity v is not constrained (low-bandwidth feedback loop compared to pitch loop bandwidth), the denominator of equation (23) is fifth order rather than fourth order (for fully constrained off-axis dynamics). This yields a third-over-fifth-order pitch attitude response, rather than the normal (decoupled) second-over-fourth order. The second-over-fourth order form could be obtained by approximate cancellation as in reference 53. The present analysis and that of reference 52 retains the complete fifth order form.

Substituting the six degree-of-freedom system matrix of table 1 into equation (23) yields the following pitch response transfer function:

$$\frac{\theta}{\delta_\theta} = \frac{M_{\delta_\theta}[\zeta_\theta,\omega_\theta](1/T_\theta)}{(1/T_p)(1/T_{sp_1})(1/T_{sp_2})[\zeta_p,\omega_p]} \; * \tag{24}$$

$$M_{\delta_\theta} = -0.329 \text{ rad/sec}^2/\text{in.}$$

$$[\zeta_\theta,\omega_\theta] = [0.766,\ 0.0209]$$

$$1/T_\theta = 0.272 \text{ rad/sec}$$

$$1/T_p = -0.091 \text{ rad/sec}$$

*Shorthand notation; $(1/T) \rightarrow (s + 1/T)$; $[\zeta,\omega] \rightarrow [s^2 + 2\zeta\omega s + \omega^2]$.

$$1/T_{sp_1} = 0.262 \text{ rad/sec}$$

$$1/T_{sp_2} = 0.58 \text{ rad/sec}$$

$$[\zeta_p, \omega_p] = [0.146, 0.214]$$

The constrained transfer function parameters of equation (24) are significantly different from those which are obtained from the fully coupled (unconstrained) six degree-of-freedom system matrix. The coupling in the Black Hawk helicopter is largely due to its canted tail rotor configuration.

Each denominator factor (eigenvalue) of equation (24) represents a natural mode of the (constrained) open-loop rigid-body helicopter. The model designations are standard for hovering vehicles. Associated with each of these natural modes is a mode shape (eigenvector) which describes the motion of the vehicle within the respective mode.

The lowest frequency mode ($1/T_p$) is comprised of a coupled longitudinal and lateral translational motion. The negative sign (of the inverse time constant) indicates that the mode is divergent, but the small magnitude means a long time-to-double-amplitude of 7.6 sec. The significance of this mode is that lateral and longitudinal velocity disturbances will grow (slowly) without bound. Physically this instability results from the small level of inherent (drag) damping in the hovering vehicle and the destabilizing effect that the canted tail-rotor has on the longitudinal motion when the yaw degree-of-freedom is constrained. For the control system configurations without linear velocity stabilization, precision hovering flight will require constant pilot attention to growing translational drifts in the lateral and longitudinal axes. Simulator studies show that linear velocity feedbacks are especially useful in reducing the workload level for precision hover tasks (refs. 7 and 49). For this reason, the ADOCS control laws contain a selectable inertial linear-velocity stabilization mode.

The second aperiodic mode ($1/T_{sp_1}$) is associated with heave (vertical) motions. The time constant of this stable mode is determined by the inherent vertical damping of the rotor system. The Black Hawk value of $T_{sp_1} = 3.8$ sec is typical for single rotor helicopters.

The remaining two modes are associated with the dominant pitch motion of the vehicle. These (three eigenvalues) are often referred to as the "hovering cubic." The dominant motion involves oscillations in forward velocity and pitch rate. The first-order factor ($1/T_{sp_2}$) has a stable time constant of 1.7 sec. The second-order factor, sometimes referred to as the "longitudinal phugoid mode," is lightly damped ($\zeta_p = 0.146$), and is at a lower frequency ($\omega_p = 0.214$ rad/sec) than the real root ($1/T_{sp_2}$).

The numerator factor ($1/T_\theta$) is associated with the heave motions and is nearly equal to the heave mode frequency ($1/T_{sp_1} \doteq 1/T_\theta$). Hereafter this numerator-denominator pair is dropped from the analysis since the cancellation is nearly exact. This cancellation essentially decouples the heave degree-of-freedom from the pitch response. The second-order numerator factor is at very low frequency and can be approximated by s^2. If the low frequency lateral/longitudinal mode ($1/T_p$) is also approximated by a free integration, the pitch response transfer function can be simplified to the familiar first-order/third-order form. The third-order denominator is the hovering cubic.

The high-frequency gain of the transfer function (M_{δ_θ}) is essentially equal to the static pitch sensitivity, with some correction resulting from the coupling effect of the canted tail-rotor.

When the crossover frequency for the attitude loop (ω_{c_θ}) is set at 6 rad/sec (a reasonable value for a $\omega_{BW_\theta} = 3$ rad/sec model-following system) the highest frequency open-loop mode is a full decade lower. Since the low-frequency unmodeled dynamics are suppressed by the feedback action, the design model needs to be very accurate only for the frequencies in the crossover range and higher. Thus, one suitable lower-order approximation is:

$$\frac{\theta}{\delta_\theta} = \frac{M_\delta}{s(s + 1/T_E)} \tag{25}$$

where $1/T_E$ represents the gross pitch damping of the system. The value of this parameter can be determined from an equivalent system fit (method 2, above), or roughly obtained from the pitch rate damping ($1/T_E \doteq -M_q$). For the present case ($M_q = -0.519$), the value of $1/T_E$ is nearly the same as that of the pitch mode ($1/T_{sp_2}$).

Since the cross-over frequency for high-bandwidth systems ($\omega_{c_\theta} \doteq 6$ rad/sec) is a decade above this equivalent mode, the phase contribution is almost $\Phi = -90$ deg. Thus, an even lower-order approximation (than eq. (25)) of the entire rigid body response is the simple transfer function:

$$\theta/\delta_\theta \doteq M_{\delta_\theta}/s^2 \tag{26}$$

which is just a pure inertia system (same as eq. (2)). This model was used in reference 7 for the selection of the ADOCS feedback gains. The present discussion uses the more exact model of equation (25), but the results obtained are nearly identical.

This analysis shows that the low-frequency, rigid-body dynamics are not important for designing the attitude loops for high-bandwidth rotorcraft control systems. As has been mentioned earlier (and will be emphasized in subsequent analyses), careful modeling of the high-frequency dynamics and actuator limiting characteristics is much more important to the design. This design approach is at variance with the long-standing emphasis on accurately modeling the helicopter's

low-frequency rigid body flight dynamics, with only very crude models for the high-frequency dynamics.

The rotor system is represented by the following first-order over fourth-order transfer function model (ref. 7):

$$\frac{\delta_\theta}{\delta_{s_\theta}} = \frac{-42957.8\ (14.8)}{[0.28,51.7][0.96,15.4]} \quad \text{in./in.} \tag{27}$$

which is a one-way coupled (actuator) approximation of the two-way coupled rotor/body dynamics. This approximation is satisfactory for the UH-60 articulated rotor; but for hingeless rotor vehicles, a fully coupled rotor/body model is needed (ref. 56). The two second-order modes represent the tip-path plane response to cyclic pitch input, and are appropriate for hovering and low-speed flight. The location of the dominant (first) regressing rotor mode (ω_{r_1} = 15.4 rad/sec) is a key limitation on the attainable bandwidth of the system. Since it is not possible to "cancel out" the flapping dynamics of the rotor system, the rotor modes can become unstable for large feedback gains, thereby restricting the attainable crossover frequency. This limitation suggests the need to examine higher bandwidth rotor systems (e.g., hingeless rotor) and rotor state control for such high-bandwidth control systems.

A related concern is the excitation of the in-plane (lead-lag) rotor dynamics which <u>are not included</u> in the rotor model of equation (27). The location of the regressing in-plane mode varies from about 0.4/rev (nonrotating frame) for a hingeless rotor (e.g., the BO-105) to 0.8/rev for an articulated rotor (e.g., the UH-60) (refs. 56 and 57). Thus, the relatively close proximity of the in-plane rotor dynamics and the crossover frequency [$\omega_c \doteq 6.0$ rad/sec = 1/4 (1/rev)] may cause coupling which restricts the allowable loop gain; so, rotor models which include in-plane dynamics should be used for the design of high-gain flight control systems (ref. 56). Coupling with rotor pylon and other structural modes may restrict the loop gain as well, and so may also have to be included in the design model.

The other major source of high-frequency dynamics is the actuator system (fig. 17). The transfer functions for the ADOCS and upper boost (swashplate) actuators are given in reference 7:

$$\frac{\delta_{s_\theta}}{u} = \underset{\text{ADOCS}}{\frac{89^2}{[0.8,\ 89]}} \cdot \underset{\text{UPPER BOOST}}{\frac{76.9}{(76.9)}} \quad \text{in./in.} \tag{28}$$

The Bode plot of figure 18 shows the various phase contributions from the actuator and roptor systems. The combined phase lag at the crossover frequency ω_{c_θ} = 6 rad/sec is Φ = -33.6 deg. This is very substantial when compared with the analogous actuator phase lag for a typical fixed-wing aircraft (typical value

Φ = -17 deg for 50 msec time constant actuator), and reflects the dominant contribution of the rotor system dynamics. The combined high-frequency phase lag at ω_{c_θ} = 6 rad/sec can be converted to an equivalent time delay by the linear relation $\Phi_c = -\omega_c \tau_e$, which gives:

$$\tau_e = \frac{-\Phi_c}{\omega_c} = 0.0977 \text{ sec} \doteq 100 \text{ msec} \tag{29}$$

Since the feedbacks do not substantially alter the high-frequency forward stabilization loop time delay, the unaugmented and augmented system values of τ_e will be about the same. Thus, without considering additional significant sources of high-frequency dynamics (including sampling effects, forward loop filters, and computational delays), the suggested handling qualities limit of $\tau_p \doteq \tau_e$ = 100 msec based on the augmented characteristics has already been reached. The phase lag from the remaining sources of high-frequency dynamics can easily double or triple this 100 msec value. Since the large effective time delay primarily reflects the contribution of the articulated rotor system, it would appear that compliance with the proposed LHX specification may require different rotor system characteristics (e.g., a hingeless rotor).

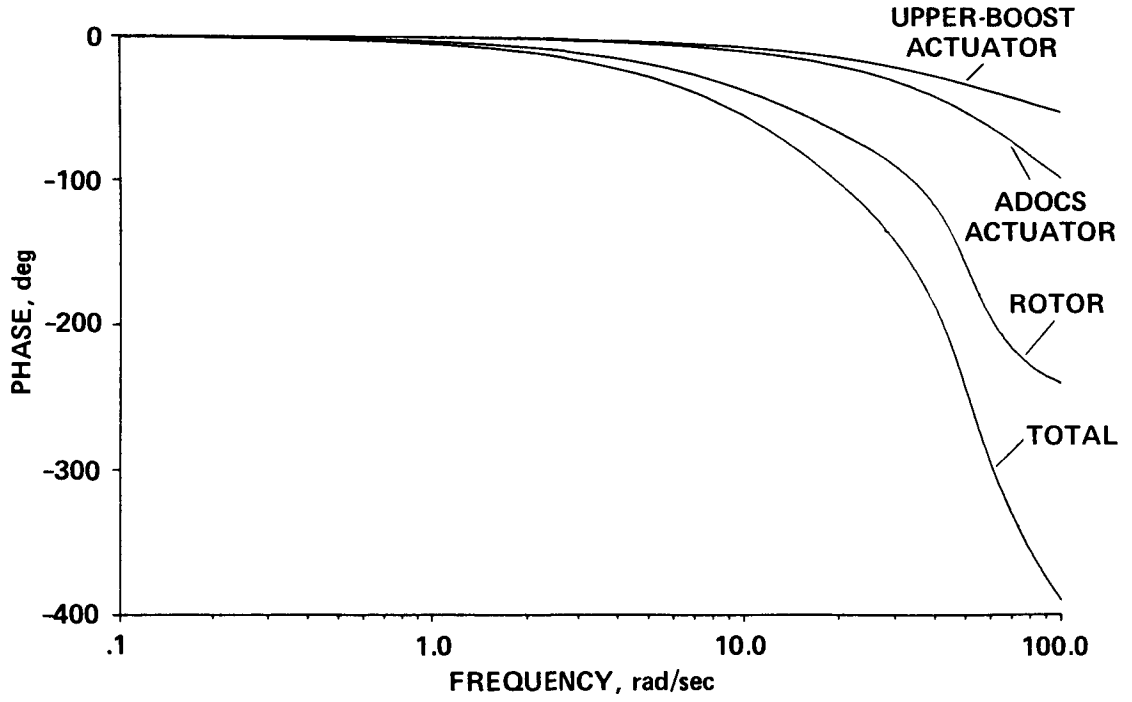

Figure 18.- Phase responses of the actuator and rotor systems.

The large combined effective time delay also presents a problem in the design of the feedback stabilization system, as is clear from reference to equation (8). This equation indicates a maximum attainable crossover frequency of

ω_c = 3.7 rad/sec for the present time delay of $\tau_{SL} = \tau_e$ = 100 msec, if a 45 deg phase margin is to be achieved. Figure 18 shows that to achieve this phase margin, the feedback compensation must provide about 66 deg of phase lead at ω_c = 3.7 rad/sec. (Total phase lag is (-180 - 21) = -201 deg, Φ_{lead} = 201 - 135 = 66 deg.) Since the maximum amount of phase lead which can be generated with attitude and rate feedback is about 75 deg (the theoretical maximum value of 90 deg requires infinite rate feedback gain), this leaves only 9 deg of lead to offset the remaining lags which are due to the zero-order hold, filters, and computational delay. The available amount of lead is clearly insufficient to provide the needed compensation, so additional lead filters will be required. However, with the attitude and rate feedbacks, the magnitude response in the crossover region will already have a slope of -20 dB per decade; so, additional lead compensation will reduce the slope of the magnitude curve to nearly zero in the crossover range. Thus, the desired phase margin can only be achieved at the expense of reducing the gain margin.

The tradeoff of phase and gain margins is a classic problem for compensating systems with large effective time delays. Methods for compensating such systems are extremely limited and almost always result in the requirement for reducing the crossover range to alleviate some of the lead compensation requirement. In turn, this reduces the overall performance of the system. Alternative methods for compensating such systems could be used, such as nonlinear filtering schemes which, in principle, allow the generation of phase lead without substantial magnitude response distortions (ref. 58).

This completes the discussions of the open-loop dynamics of the Black Hawk aircraft. A detailed discussion of the analysis and design of the ADOCS model-following control system is presented in the following sections. First, an analysis of the nominal (40 Hz, ω_{c_θ} = 6 rad/sec) design is presented. This analysis verifies the performance of the ADOCS system as modeled in reference 7, but does not include the needed additional filters and other high-frequency elements.

III.E s-Plane Analysis of the Nominal (ω_s = 40 Hz, ω_{c_θ} = 6 rad/sec) System

This section presents an s-plane analysis of the ADOCS attitude-command/attitude-stabilization system using the nominal flight control system gains given in reference 7. This analysis verifies the system performance based on the simulator model design and provides a basis for comparison with configurations discussed later.

The feedback gains for the pitch rate and pitch attitude signals are given in reference 7 as:

$$K_q = 16.0 \text{ in./rad/sec}$$
$$K_\theta = 34.0 \text{ in./rad} \qquad (30)$$

This yields a feedback transfer function of:

$$H(s) = 16.0s + 34.0 \tag{31}$$

which adds a zero at:

$$1/T_q = K_\theta/K_q = 2.13 \text{ rad/sec} \tag{32}$$

The uncompensated and compensated open-loop frequency responses $\delta_f(s)/e(s)$ and $\theta(s)/e(s)$, respectively, of figure 17 are presented in figure 19(a) and (b). The dashed lines in figure 19(a) are the asymptotic magnitude plots which are useful in exposing the various break points. Specifically, the rate feedback compensation adds the zero ($1/T_q$ = 2.13 rad/sec) which provides the needed phase lead (fig. 19(b)). Figure 19(a) shows the 0 dB line for the selected attitude gain (K_θ = 34); this results in a (compensated) open-loop crossover frequency of about:

$$\omega_{c_\theta} = 6 \text{ rad/sec} \tag{33}$$

with associated phase and gain margins of:

$$\begin{aligned} \Phi_m &= 38 \text{ deg} \\ GM &= 10 \text{ dB} \end{aligned} \tag{34}$$

The somewhat low phase margin value is also reflected in the K_θ/K_q ratio and crossover frequency being higher than the values obtained from equation (8) for $\tau_{SL} \doteq 0.100$ sec.

A standard root-locus plot showing the migration of the open-loop poles with the variations of pitch attitude gain (K_θ) was shown in figure 4. The closed-loop root locations for the nominal design are indicated on the figure. It is clear from this figure that the low-frequency open-loop dynamics are driven into the nearby zeros and suppressed. The closed-loop transfer-function (θ/δ_{c_θ}) emphasizes this point:

$$\left.\begin{aligned} \frac{\theta}{\delta_{c_\theta}} &= \frac{9.044\times10^9[0.766,0.0209](14.81)[-0.866,277.13]}{(1/T'_{p_1})(1/T'_{p_2})(1/T'_{sp_2})[\zeta'_p,\omega'_p](1/T'_{r_1})(80.5)[0.791,90.5][0.866,277.13]} \text{ rad/in.} \\ 1/T'_{p_1} &= 0.0095 \text{ rad/sec} \\ 1/T'_{p_2} &= 0.0243 \text{ rad/sec} \\ 1/T'_{sp_2} &= 3.24 \text{ rad/sec} \\ [\zeta'_p,\omega'_p] &= [0.549,7.763] \\ 1/T'_{r_1} &= 12.67 \text{ rad/sec} \end{aligned}\right\} \tag{35}$$

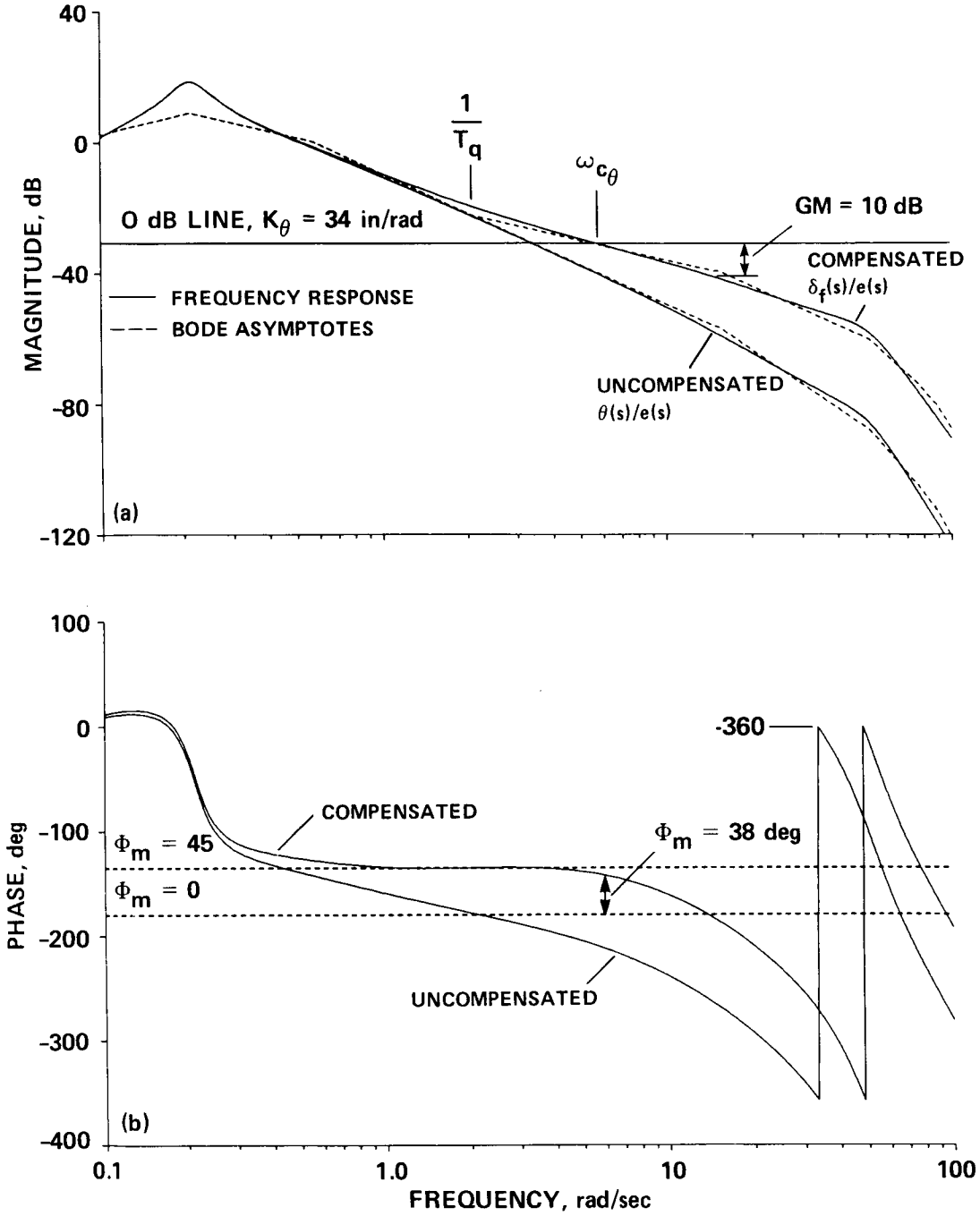

Figure 19.- Open-loop frequency responses for the uncompensated and compensated nominal design. (a) Magnitude; (b) phase.

where the primes (') denote that the modes are for the closed-loop system, and the naming convention is the same as in equation (24) to show the relation between the open- and closed-loop modes.

The closed-loop hovering cubic is comprised of a first-order pitch mode ($1/T'_{sp_2}$), which is located close to the compensation zero ($1/T_q$), and a coupled second-order pitch/rotor mode (ω'_p). This second-order mode has a damping ratio $\zeta'_p = 0.55$ which is slightly less than the desirable value ($\zeta \doteq 0.7$), and reflects the somewhat low open-loop phase margin ($\Phi_m = 38$ deg). Thus, the dominant closed-loop pitch responses are those associated with the higher-frequency coupled closed-loop pitch attitude and rotor modes ($1/T'_{sp_2}$, ω'_p, $1/T'_{r_1}$).

A useful alternate format which combines the results of figures 4 and 19 is "Bode root-locus plot" of figure 20 (ref. 54). This figure is simply a replot of the root-locus information (fig. 4) in Bode format overlaid on the open-loop Bode plot (fig. 19(a)). For the root-loci, the vertical axis locates the attitude gain (K_θ, dB), and the horizontal axis locates the corresponding closed-loop modal frequencies. Left half plane (stable) real roots are designated by closed dots, and right half plane (unstable) real roots are designated by open dots (none in the plotted range of fig. 20). Complex modes are represented by their natural closed-loop frequency ω'_n. Stable complex modes are denoted by a cross symbol, and unstable complex modes are denoted by a diamond. The pitch attitude gain (K_θ) is referenced to the ($K_\theta = 1$) 0 dB line. For example, the closed-loop root locations for the nominal gain ($K_\theta = 34$) are located at the intersection of the root-loci and the -30.6 dB line as shown in figure 20; these roots match the values given in equation (35). When the pitch attitude gain is halved ($K_\theta = 17$), the open-loop crossover frequency is reduced to $\omega_{c_\theta} = 3.2$ rad/sec, and the phase margin increased to $\Phi_m = 45$ deg (fig. 19(b)) (this is roughly the design condition given by eq. (8)); now the closed-loop root locations are those associated with the -24.6 dB line (shown in fig. 20).

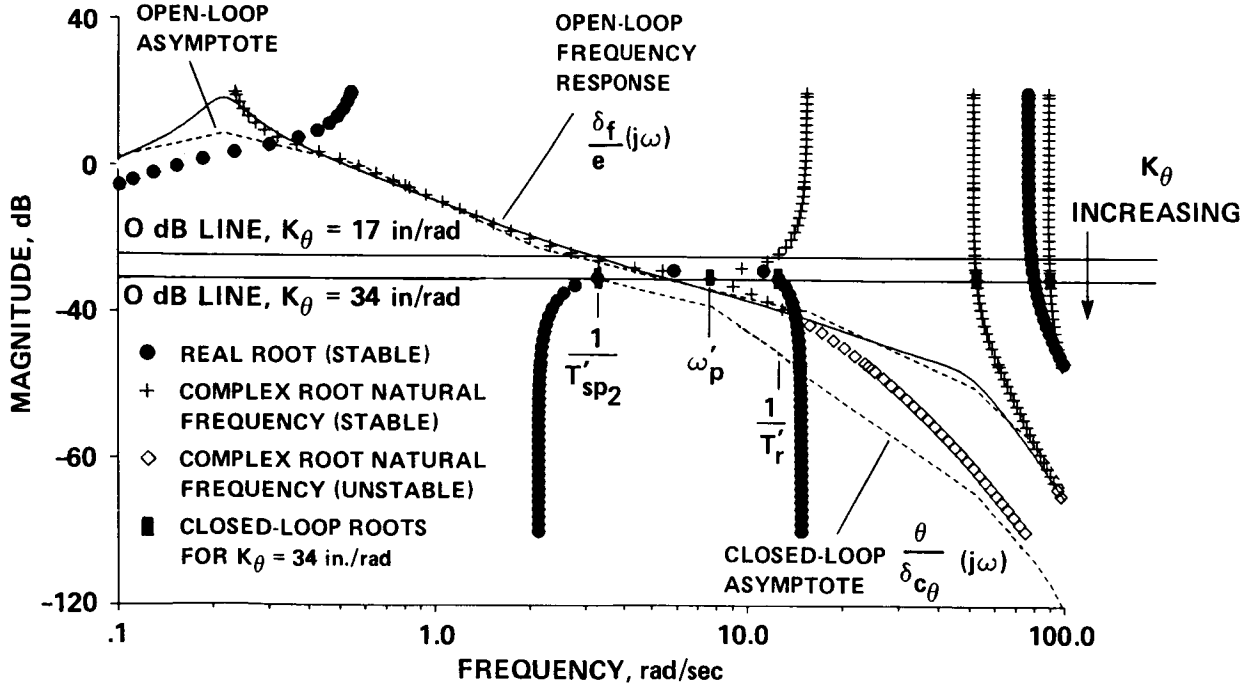

Figure 20.- Bode root-locus plot.

The advantage of the Bode root-locus format is that both open- and closed-loop Bode plots can be on the same figure, along with an explicit presentation of the sensitivity of the closed-loop roots to changes in the root-locus gain. Based on the closed-loop root locations for the nominal gain (K_θ = 34), the θ/δ_{c_θ} closed-loop (asymptotic) Bode plot is easily added by hand, as shown in figure 20. Referring to the root-loci and the closed-loop Bode plot, it is clear that for pitch attitude gains approaching the nominal value, the low-frequency dynamics are almost entirely cancelled in the closed-loop attitude response. Also, the dominant open-loop rotor mode ω_{r_1} = 15 rad/sec is seen to couple with the rigid body pitch mode (ω_p), while the higher frequency actuator and rotor modes (ω > 40 rad/sec) are largely unaffected (at this crossover frequency).

The nature of the coupling between the closed-loop rotor and attitude dynamics is exposed in the eigenvector and time-vector diagrams (ref. 54) of figures 21 and 22. Figure 21(a) is a phasor diagram of the major components of the (normalized) eigenvector for the closed-loop real mode ($1/T'_{sp_2}$). The motion is composed of variations in pitch attitude and rate, and longitudinal translation. The closed-loop rotor response is 0.15 in. per deg/sec of pitch rate. The relative contribution of each motion variable in the pitching moment equation is determined from:

$$sq = M_u \hat{u} + M_q \hat{q} + M_{\delta_\theta} \hat{\delta}_\theta \tag{36}$$

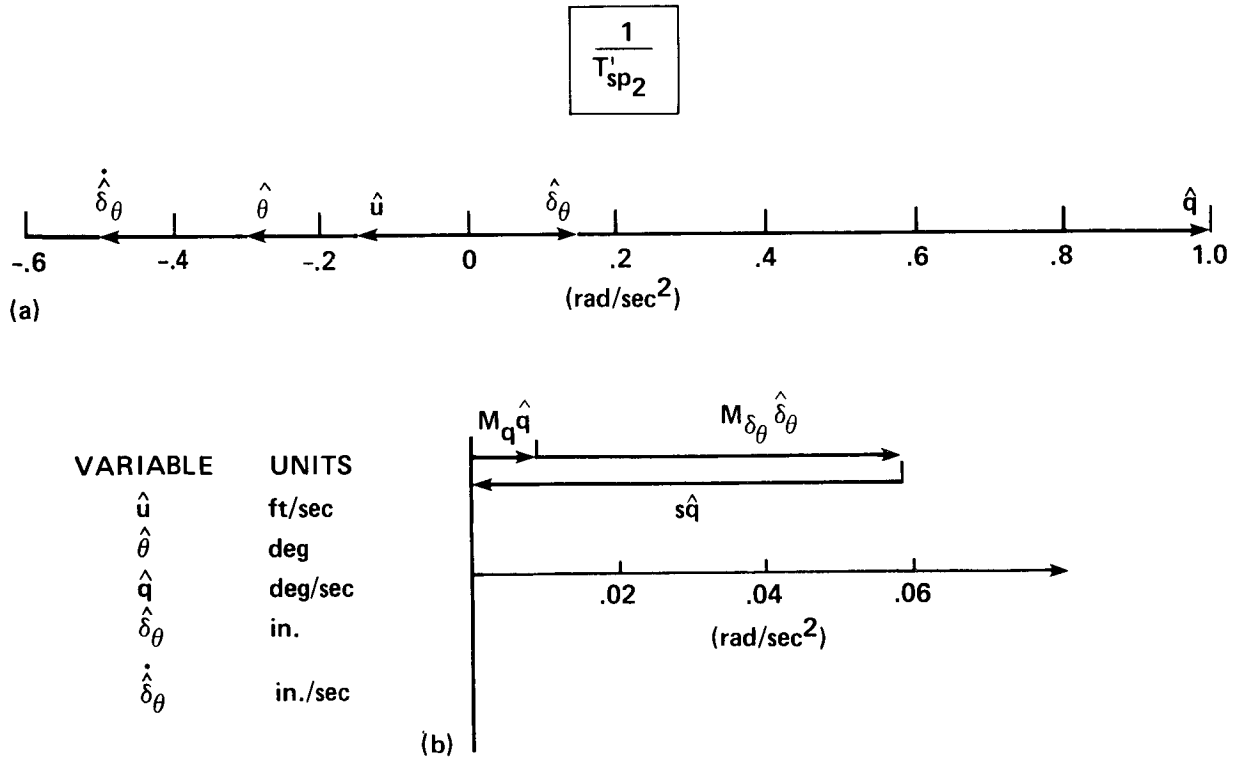

Figure 21.- Dynamics of the closed-loop real mode ($1/T'_{sp_2}$). (a) Eigenvector diagram; (b) time-vector diagram.

where $\hat{q}$, $\hat{u}$, $\hat{\delta}_\theta$ are the phasors of figure 21(a), and M_u, M_q, M_{δ_θ} are given as before in table 1. This equation is plotted in the "time-vector" diagram of figure 21(b), and shows that the contribution of the speed component is negligible. The pitching moment equation is dominated by the inertial moment (left hand side of eq. (36)) and the feedback control (last term in eq. (36)), with a relatively small contribution from the inherent airframe pitching aerodynamics. This dominance of the feedback dynamics is even stronger in the second-order closed-loop mode (ω_p').

The phasor and time-vector diagrams for the second-order mode (ω_p') are presented in figure 22(a) and (b). Once again, the motion consists of pitch rate and attitude, longitudinal translation, and rotor tip-path-plane (control) variations. Note that the rotor plane variations are twice as large relative to the pitching variations, when compared with the previous mode ($1/T_{sp_2}$). The time-vector diagram for the pitching moment equation (fig. 22(b)) shows that the aerodynamic damping moment contribution $M_q\hat{q}$) is very small (also, $M_u\hat{u} \doteq 0$), compared to the feedback ($M_{\delta_\theta}\hat{\delta}_\theta$) and inertial ($s\hat{q}$) moments. When the feedback term is further resolved into pitch attitude and pitch rate components ($M_{\delta_\theta}K_\theta\hat{\theta}$ and $M_{\delta_\theta}K_q\hat{q}$, respectively), the aerodynamic moment contribution is less than 8% of the total damping moment term. The time-vector diagram is nearly the isosceles triangle which would result if the aerodynamics were ignored entirely--the M_{δ_θ}/s^2 Then the damping ratio would be (ref. 54):

$$\zeta' = \sin\theta = \sin(32.0) = 0.53$$

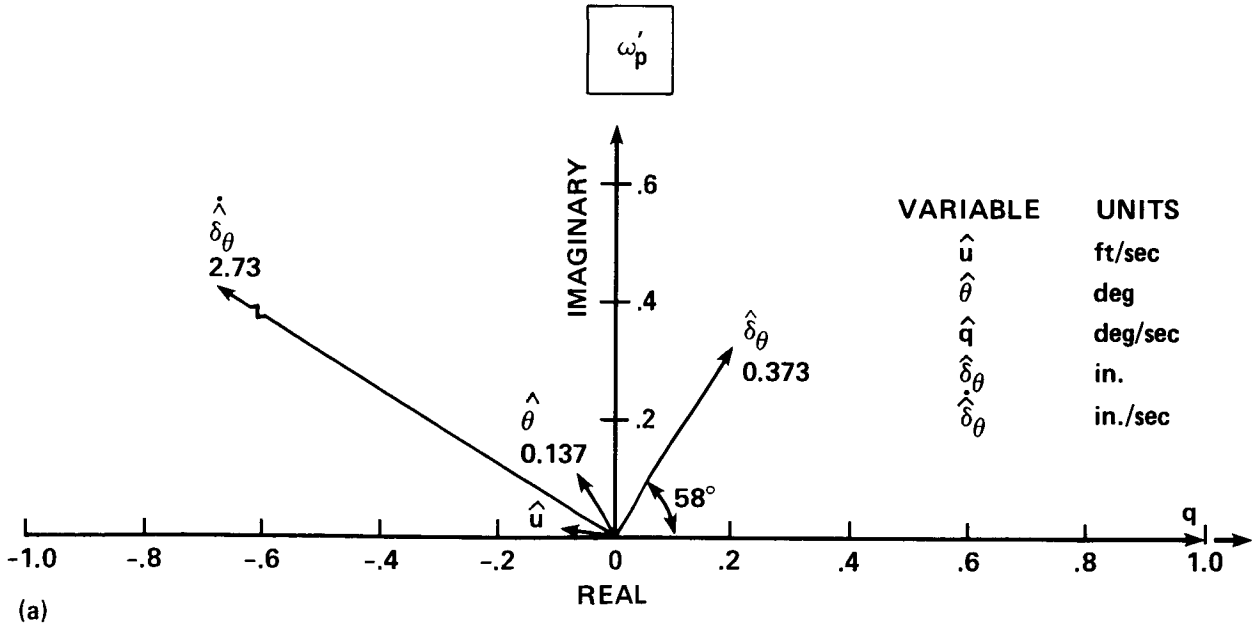

Figure 22.- Dynamics of the closed-loop complex mode (ω_p'). (a) Eigenvector diagram; (b) time-vector diagram.

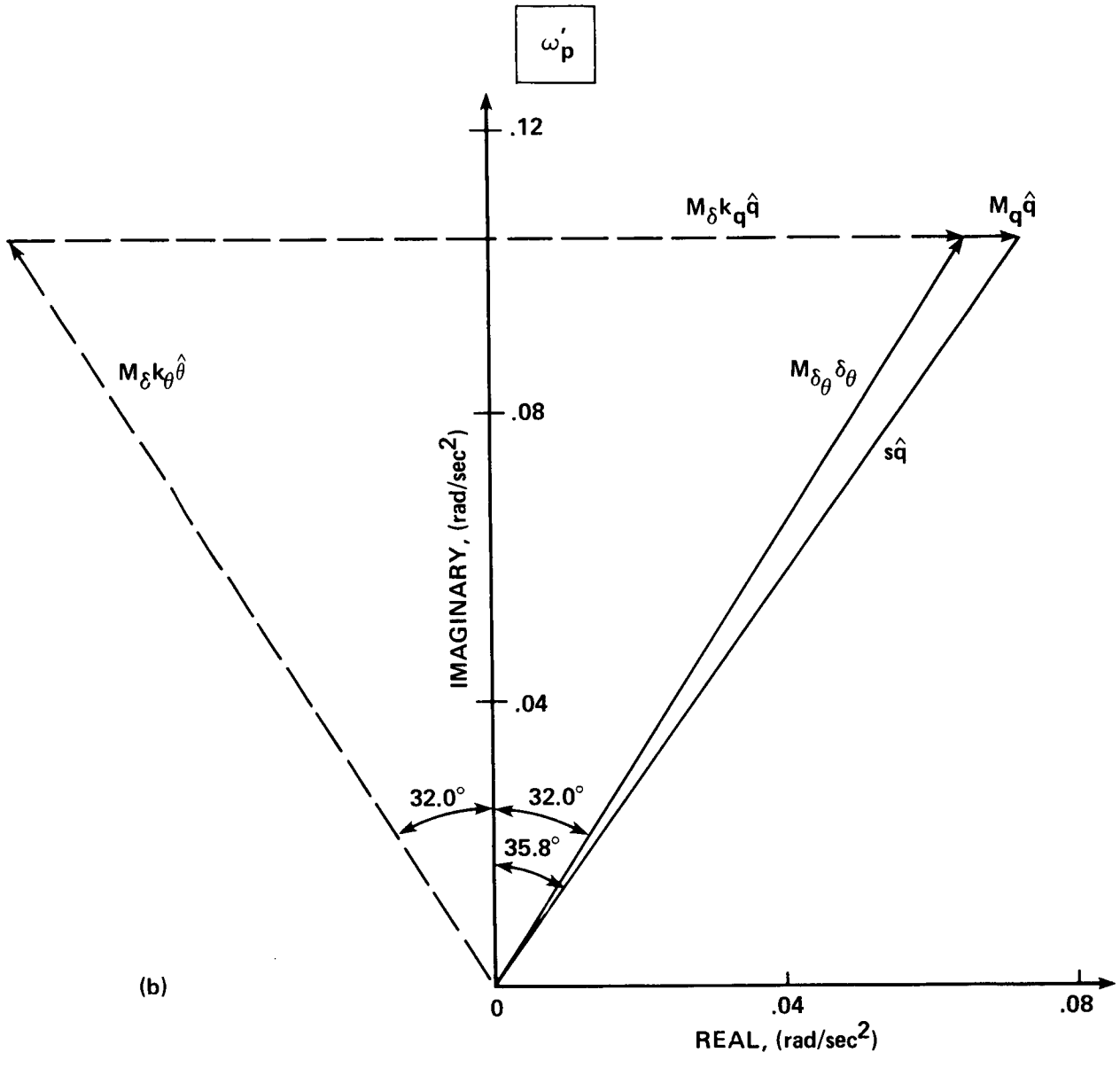

Figure 22.- Concluded.

which is only slightly less than the actual value (ζ' = 0.55, eq. (35)). Clearly, the closed-loop response is dominated by the feedbacks, which heavily couple the rotor and pitch attitude dynamics. Excessive rotor mode coupling can produce undesirable fatigue and vibration loads.

A key objective of the feedback system is to attenuate undesired responses to disturbances. Disturbances result from both atmospheric turbulence inputs, which contribute to the pitch response of the aircraft, and spurious electrical inputs which contribute directly to the actuator command. In reference 7, a 1-in. pulse input (δ_{c_θ}) of a 0.5 sec duration is used to evaluate the disturbance rejection performance of the closed-loop system. This approach is also found in the proposed

LHX handling qualities specification (ref. 15). Time histories of the disturbance and pitch response for the closed-loop system are shown in figure 23(a)-(c). These results match the analysis results of reference 7 closely. The associated rotor flapping angle (δ_θ) for this disturbance encounter is shown in figure 23(d). The ratio of maximum rotor tip-path-plane deflection to maximum pitch rate is 0.358 in./deg/sec, which is consistent with the closed-loop eigenvector results of figure 22(a), as is the phasing.

Overall, the nominal feedback gains are seen to yield relatively well damped closed-loop dynamics and good disturbance rejection. Thus, the performance goals of the feedback stabilization system are achieved.

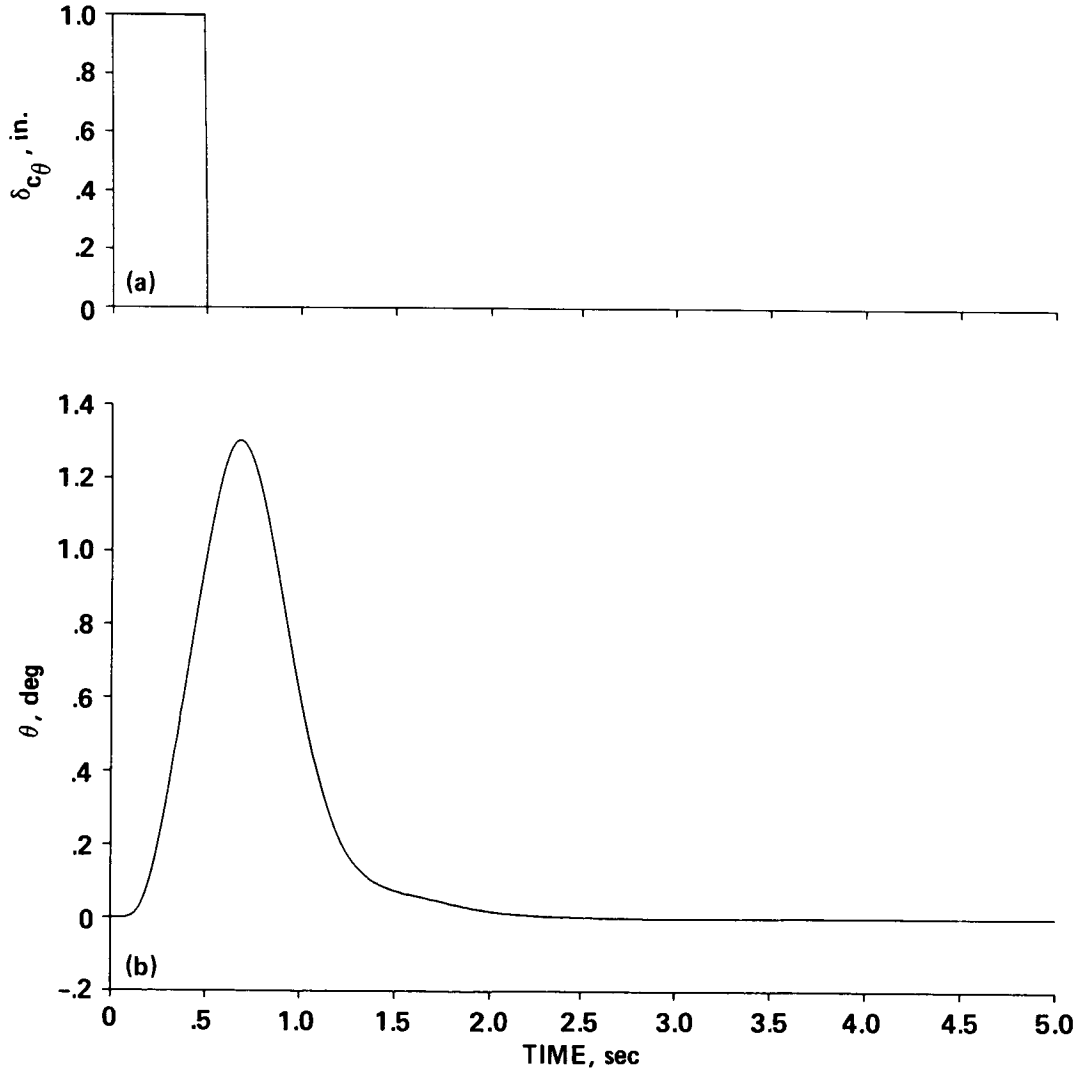

Figure 23.- Response to a pulse disturbance. (a) Input, δ_{c_θ}; (b) pitch attitude, θ; (c) pitch rate, q; (d) rotor flapping angle, δ_θ.

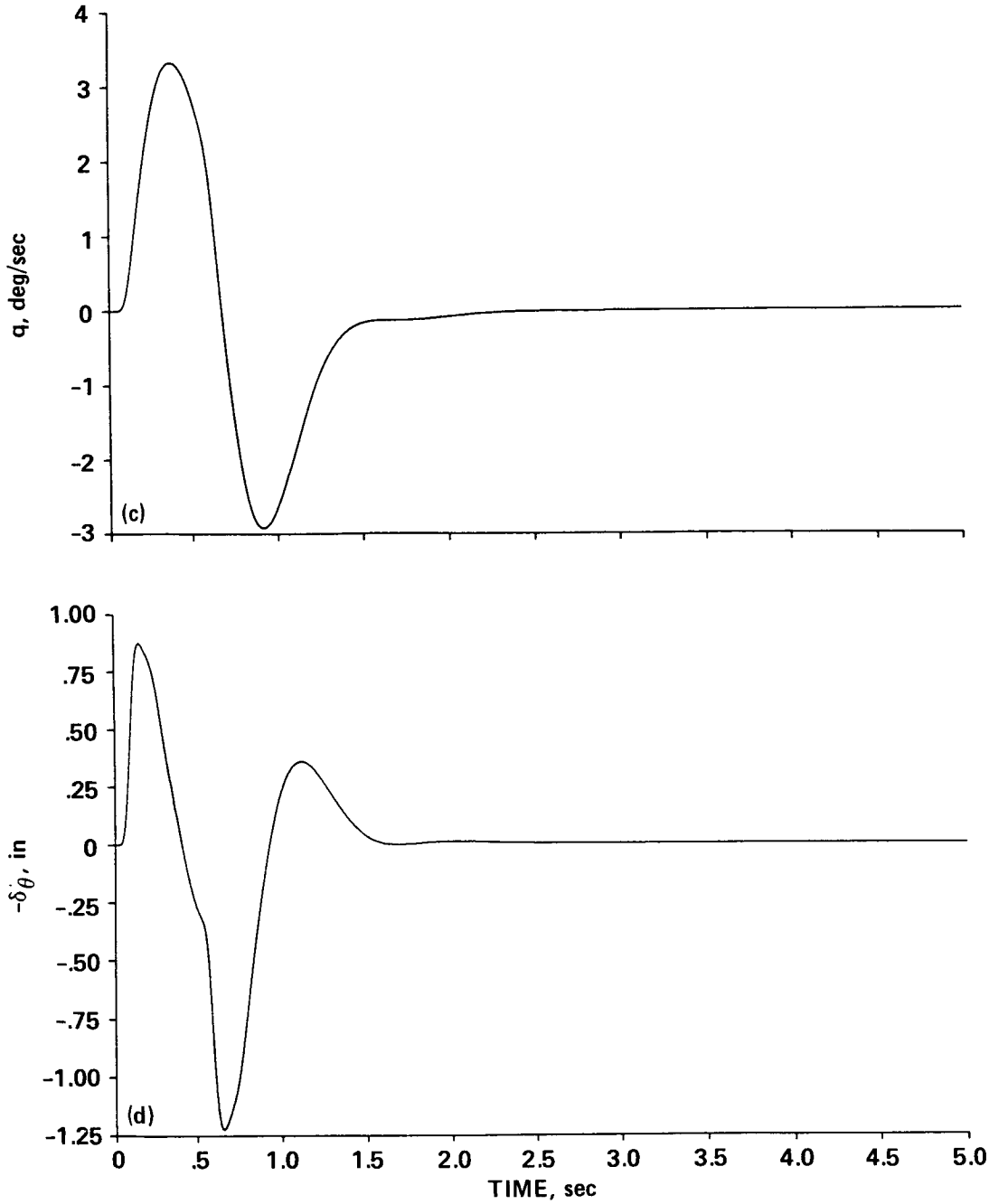

Figure 23.- Concluded.

The design of the command block (figs. 16 and 17) in the following paragraph is broadly based on the ADOCS methodology as presented in reference 7 and given as an overview in Section III.C. However, the present analysis uses a different (more responsive) command model, which is based on the data of reference 49. Also as previously mentioned, the more complex structure and associated numerical parameters of the ADOCS forward-loops are not adopted here. So, the present design is for a

generic high-bandwidth, model-following system and does not reflect the expected response characteristics of the ADOCS.

As discussed earlier, the command block is comprised of a feedforward (cancellation) section and a response-model section. The feedforward transfer function, as given in equation (19), requires an approximate inverse model of rigid body dynamics (excluding the rotor and actuator dynamics), and a model of the stabilization loop (eq. (31)). A suitable inverse model also adopted in reference 52, is based on the transfer function of equation (25). The dominant time constant, $1/T_E$, is roughly equal to the open-loop pitch mode, $1/T_{sp_2} = 0.58$ rad/sec. Combining equations (19), (25), and (31), the feedforward transfer function is:

$$\frac{\delta_{c_\theta}}{\theta_m} = (16s + 34) + \frac{s(s + 0.58)}{0.329} \text{ , in./rad}$$

or

$$\frac{\delta_{c_\theta}}{\theta_m} = 3.04[0.87,3.35] \text{ , in./rad} \tag{37}$$

The closed-loop transfer function between the model response (θ_m) and the pitch attitude response (θ) as shown in figure 17 is:

$$\frac{\theta}{\theta_m}(s) = \tag{38}$$

THE NUMERATOR ROOTS ARE:

NO.	REAL	IMAG.	OMEGA	ZETA
1	240.00000	-138.56407	277.12813	-0.86602539
2	240.00000	138.56407	277.12813	-0.86602539
3	-0.15991542E-01	0.13430029E-01	0.20882890E-01	0.76577246
4	-0.15991542E-01	-0.13430029E-01	0.20882890E-01	0.76577246
5	-2.9215462	-1.6275069	3.3442803	0.87359490
6	-2.9215462	1.6275069	3.3442803	0.87359490
7	-14.814814	0.00000000E+00		

THE DENOMINATOR ROOTS ARE:

NO.	REAL	IMAG.	OMEGA	ZETA
1	-240.00000	-138.56407	277.12813	0.86602539
2	-240.00000	138.56407	277.12813	0.86602539
3	-4.2609167	-6.4886332	7.7625879	0.54890415
4	-4.2609167	6.4886332	7.7625879	0.54890415
5	-15.249969	50.673706	52.918674	0.28817745
6	-15.249969	-50.673706	52.918674	0.28817745
7	-71.529579	55.397793	90.473179	0.79061640
8	-71.529579	-55.397793	90.473179	0.79061640
9	-0.94451196E-02	0.00000000E+00		
10	-0.24251182E-01	0.00000000E+00		
11	-3.2352383	0.00000000E+00		
12	-12.668704	0.00000000E+00		
13	-80.453796	0.00000000E+00		

LOW-FREQUENCY GAIN = 1.9040680

The frequency response of this transfer function is shown in figure 24. Ideally, the response should be unity for all frequencies. However, the inverse

model excludes the rotor and actuator modes; so the cancellation breaks down for frequencies beyond which the first excluded open-loop mode begins to affect the closed-loop dynamics. As seen in figure 24(a), the magnitude response first falls below the 0 dB (unity) line for $\omega > 14.5$ rad/sec, which is due to the lowest frequency (open-loop) rotor mode (ω_{r_1}). Amplitude overshoot is apparent for $\omega = 7$ rad/sec, which is the location of the closed-loop coupled pitch/rotor mode, ω'_p (fig. 20). Phase response following is maintained up to a frequency of $\omega = 5$ rad/sec, beyond which the excluded rotor mode contributes significant phase lag distortion. These frequency responses show that good model-following performance is maintained to a frequency of about 5 rad/sec; clearly the command response model must have a bandwidth of less than this value for model-following fidelity to be maintained. The proposed Level I LHX requirement for a minimum closed-loop

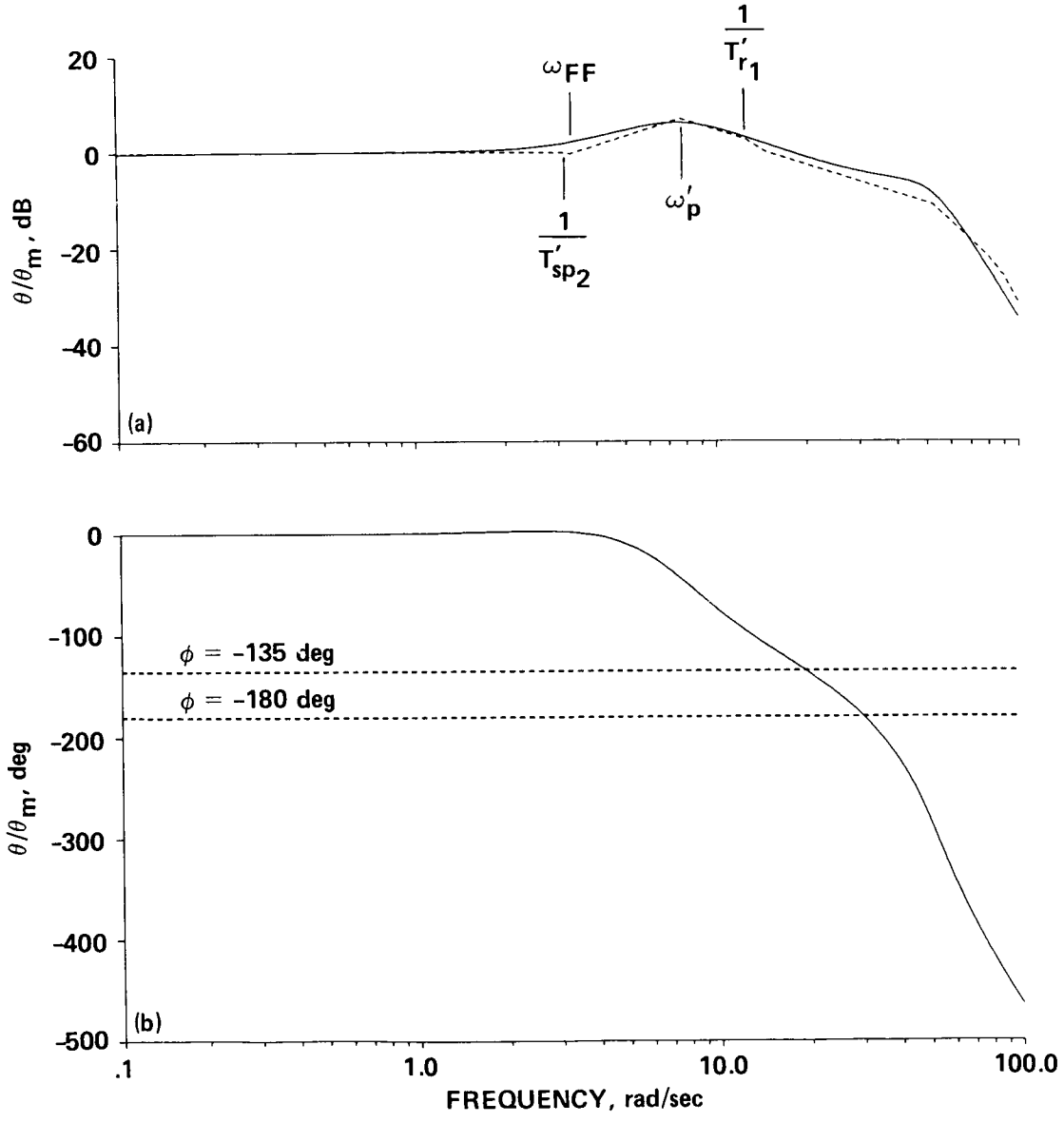

Figure 24.- Frequency response of θ/θ_m. (a) Magnitude; (b) phase.

response bandwidth of ω_{BW_θ} = 3 rad/sec (fig. 15, ref. 50) can therefore be achieved (if the remaining omitted dynamics are ignored; e.g., filters, delays, etc.).

The following second-order attitude-command response-model (eq. (22)) meets the LHX bandwidth requirement and is based on the handling qualities data of reference 49:

$$\frac{\theta_m}{\theta_c} = \frac{A_m}{[0.75,2.0]} \tag{39}$$

When this transfer function is combined with the closed-loop response to θ_m (eq. (38)), the overall attitude response of the system to normalized stick inputs (θ/θ_c) is obtained:

$\frac{\theta}{\theta_c}(s)$ = (40)

THE NUMERATOR ROOTS ARE:

NO.	REAL	IMAG.	OMEGA	ZETA
1	240.00000	-138.56407	277.12813	-0.86602539
2	240.00000	138.56407	277.12813	-0.86602539
3	-0.15991542E-01	0.13430029E-01	0.20882890E-01	0.76577246
4	-0.15991542E-01	-0.13430029E-01	0.20882890E-01	0.76577246
5	-2.9215462	-1.6275069	3.3442803	0.87359490
6	-2.9215462	1.6275069	3.3442803	0.87359490
7	-14.814814	0.00000000E+00		

THE DENOMINATOR ROOTS ARE:

NO.	REAL	IMAG.	OMEGA	ZETA
1	-240.00000	-138.56407	277.12813	0.86602539
2	-240.00000	138.56407	277.12813	0.86602539
3	-4.2609167	-6.4886332	7.7625879	0.54890415
4	-4.2609167	6.4886332	7.7625879	0.54890415
5	-15.249969	50.673706	52.918674	0.28817745
6	-15.249969	-50.673706	52.918674	0.28817745
7	-71.529579	55.397793	90.473179	0.79061640
8	-71.529579	-55.397793	90.473179	0.79061640
9	-1.5000000	-1.3228756	2.0000000	0.75000001
10	-1.5000000	1.3228756	2.0000000	0.75000001
11	-0.94451196E-02	0.00000000E+00		
12	-0.24251182E-01	0.00000000E+00		
13	-3.2352383	0.00000000E+00		
14	-12.668704	0.00000000E+00		
15	-80.453796	0.00000000E+00		

LOW-FREQUENCY GAIN = 1.9040680

The frequency response of this overall transfer function is co-plotted with the response of the command model alone (eq. (39)) in figure 25. The match between these responses is a good measure of the fidelity of the model-tracking performance of the system. Figure 25 shows that good model-following is achieved for frequencies $\omega \leq 4$ rad/sec; beyond this frequency, discrepancies in the magnitude and phase responses become very noticeable. Since the magnitude response of the model at $\omega = 4$ rad/sec is already attenuated to -12 dB (75% reduction), the magnitude deviations are probably not very important and could be corrected by adjusting the stick sensitivity (A_m in eq. (39)). Much more important is the rapid roll off in the

phase characteristics of the total system in comparison with the second order model. As previously noted, the stabilization and feedforward loops do not improve the system time delay (high-frequency phase response), which remains roughly at its open-loop value. The effective time delay measure (τ_p, "phase-delay" of fig. 3) is determined to be τ_p = 117 msec as shown in figure 25(b). The difference between this value and the previous τ_p = 100 msec value (eq. (29)) is mostly due to the zero-order hold delay of 13 msec (= T/2). The attitude response bandwidth (fig. 3) is also determined from figure 25. Since the frequency for a 45 deg phase margin (ω = 3.9 rad/sec) is greater than that for a 6 dB gain margin (ω = 3.6 rad/sec), the system is "gain margin limited," and the bandwidth is ω_{BW_θ} = 3.6 rad/sec. Thus, the frequency-domain handling qualities parameters for the nominal system are:

$$\omega_{BW_\theta} = 3.6 \text{ rad/sec}$$
$$\tau_p = 0.117 \text{ sec} \qquad (41)$$

Comparing these results with the proposed LHX handling qualities specifications (fig. 15) shows that the design (as modeled at this stage) exceeds the Level I time delay boundaries. Any additional time delays, such as stick sampling skew (Section II.E), and anti-aliasing and biodynamic filters will push the time delay value well into the Level II range (adequate performance is achievable, but with high pilot workload).

Figure 25 also shows that the bandwidth of the overall response (θ/θ_c; ω_{BW_θ} = 3.6 rad/sec) is slightly less than that of the command model (θ_m/θ_c; ω_{BW_θ} = 3.8 rad/sec). Thus, the current ω_{c_θ} = 6 rad/sec open-loop crossover frequency could not be much further reduced without significantly compromising the desired system performance (i.e., the model bandwidth). This suggests the following rule-of-thumb:

$$\frac{\omega_{c_\theta}}{\omega_m} \geq 2 \text{ to } 3$$

which places a lower limit on the feedback loop crossover frequency (ω_{c_θ}) as a function of the corner frequency (ω_m) of the desired attitude response model (θ_m/θ_c).

The pitch attitude response of the overall system to a normalized step input of stick deflection (θ_c) is shown in figure 26(a). One unit of normalized stick deflection yields 1 radian (57.3 deg) of steady-state pitch attitude change. Also shown in this figure is the response of the command model (eq. (39)). Note that the fairly large differences which were apparent in the frequency domain (especially in the high-frequency phase characteristics) are somewhat obscured in the time-domain. Otherwise, the step response of the overall system follows the model well.

In addition to the proposed frequency-domain requirements, reference 50 (and ref. 15) gives analogous time-domain requirements based on the parameterized step

response of figures 27 and 28. The proposed numerical values for Level I and Level II handling qualities (ref. 50) are given in figure 29. For the step response of figure 26(a), these parameters are:

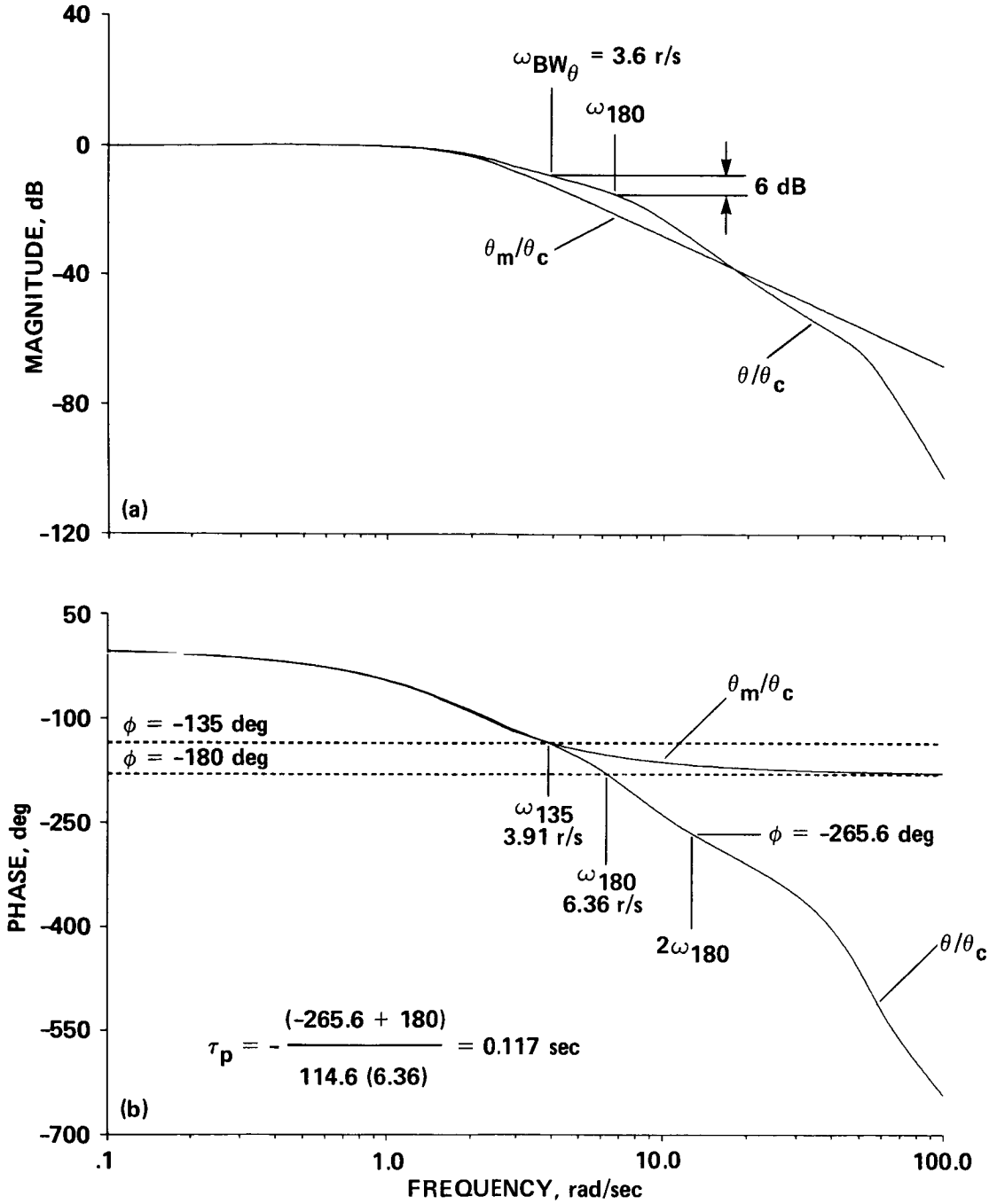

Figure 25.- Frequency response of the overall system (θ/θ_c) compared with the command model (θ_m/θ_c). (a) Magnitude; (b) phase.

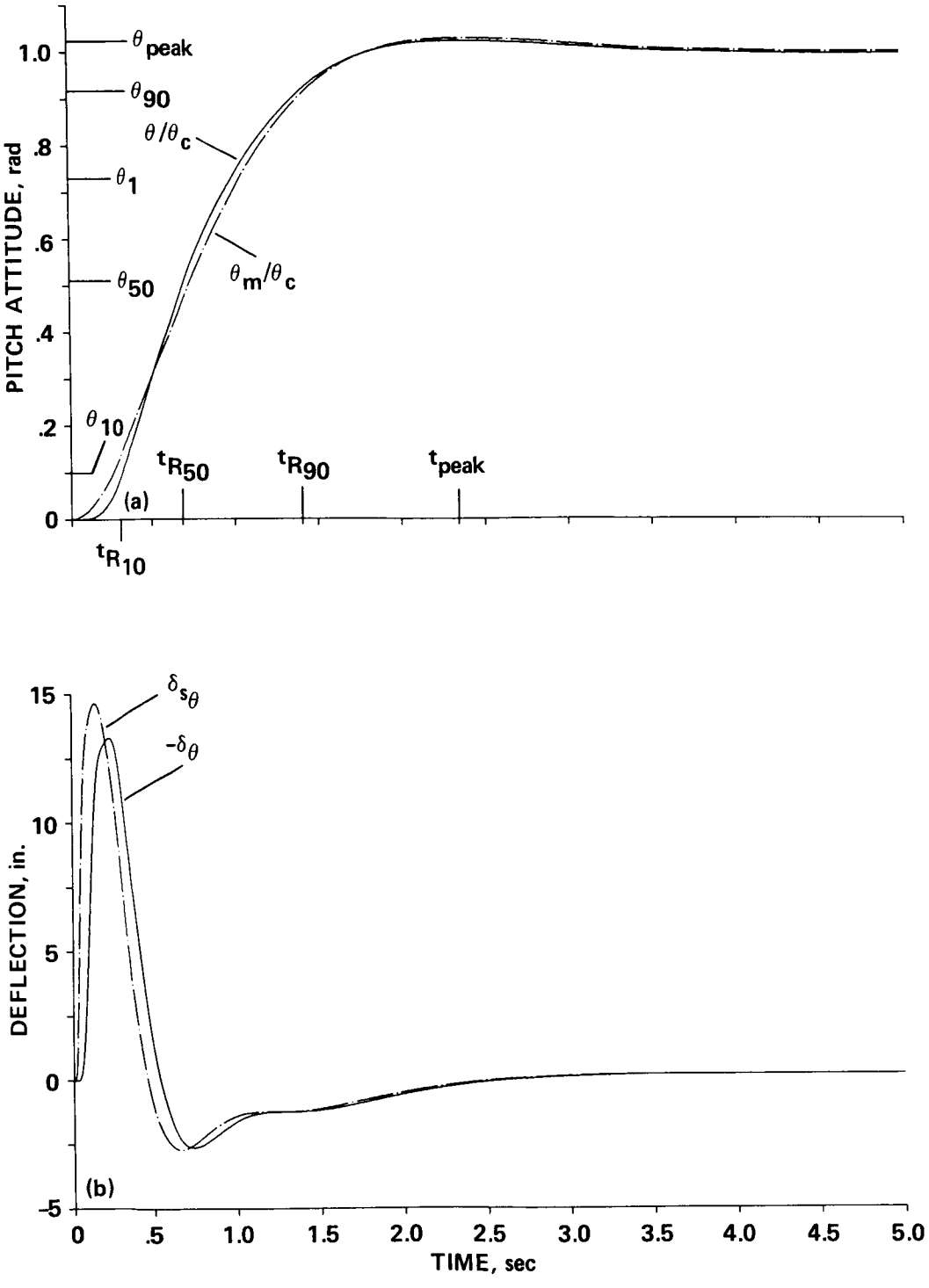

Figure 26.- Time response of the overall system (θ/θ_c) to a normalized step input ($\theta_c = 1$) compared with the command model response. (a) Pitch attitude response (θ); (b) swashplate (δ_{s_θ}) and flapping angle (δ_θ) responses; (c) swashplate rate ($\dot{\delta}_{s_\theta}$) response; (d) swashplate rate ($\dot{\delta}_{s_\theta}$) response shown on an expanded time scale.

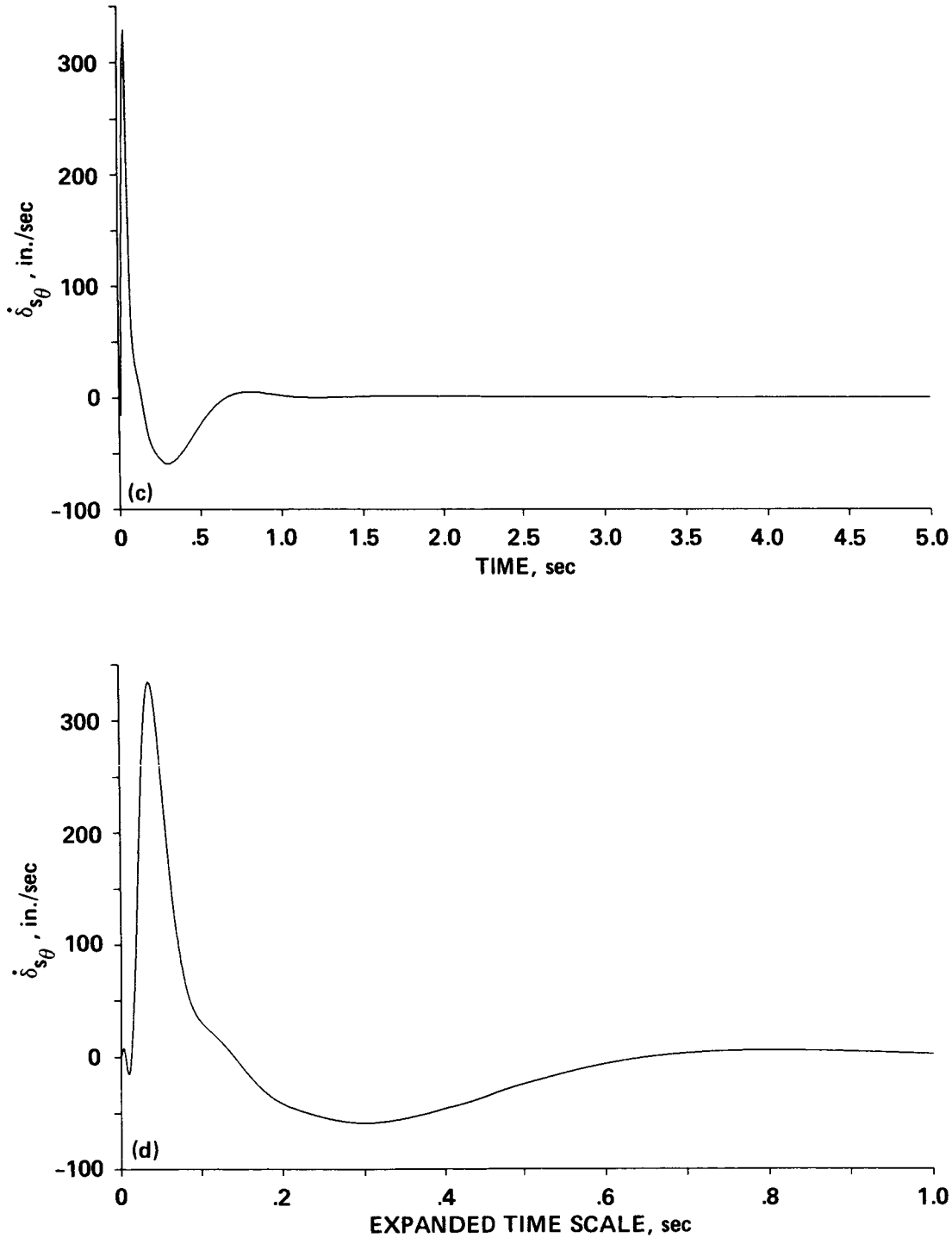

Figure 26.- Concluded.

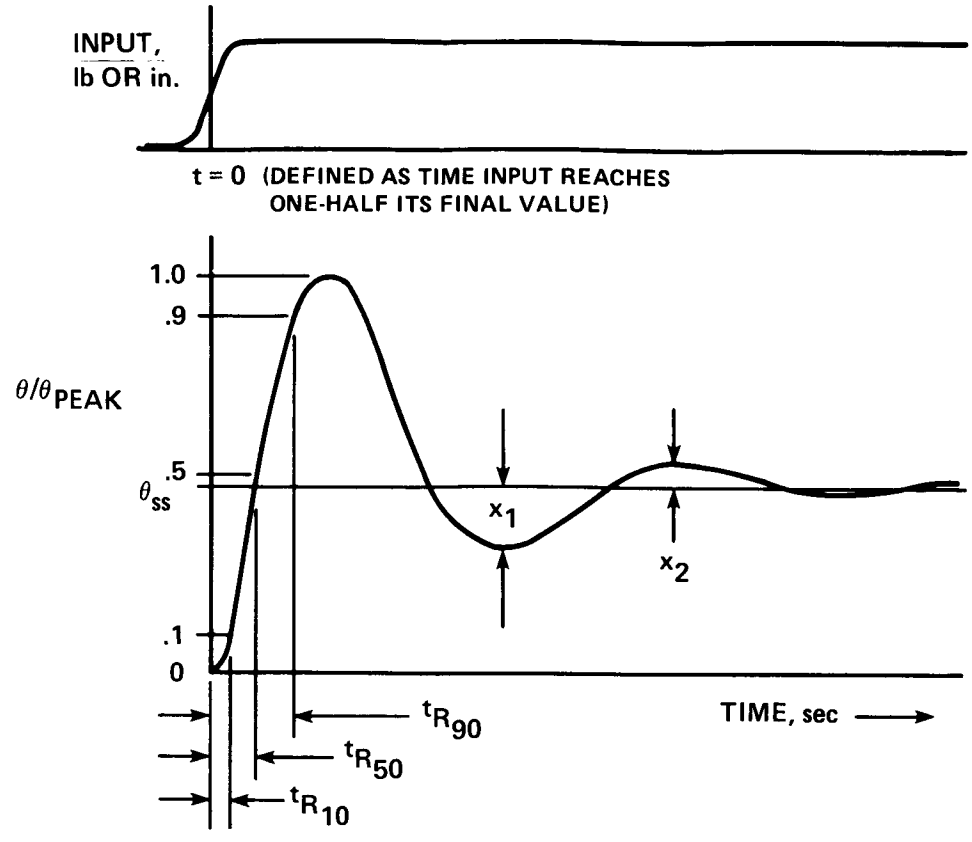

Figure 27.- Definitions of time response parameters for rate and attitude response types--hover and low speed (reproduced from ref. 50).

$$t_{R_{10}} = 0.32 \text{ sec}$$

$$t_{R_{50}} = 0.71 \text{ sec}$$

$$t_{R_{90}} = 1.43 \text{ sec} \qquad (42)$$

$$\zeta_e = 0.75 \text{ (same as command model)}^{\dagger}$$

which are well within the Level I time response criteria.

The fact that the $t_{R_{10}}$ criteria (fig. 29) are satisfied, while the τ_p criteria (fig. 15) are not, shows an inconsistency between the time and frequency-domain requirements. Besides, the feasibility of generating step-response data in

† The equivalent damping ratio is obtained herein by a second-order equivalent system fit of the frequency response, a more exact method than that of figure 28.

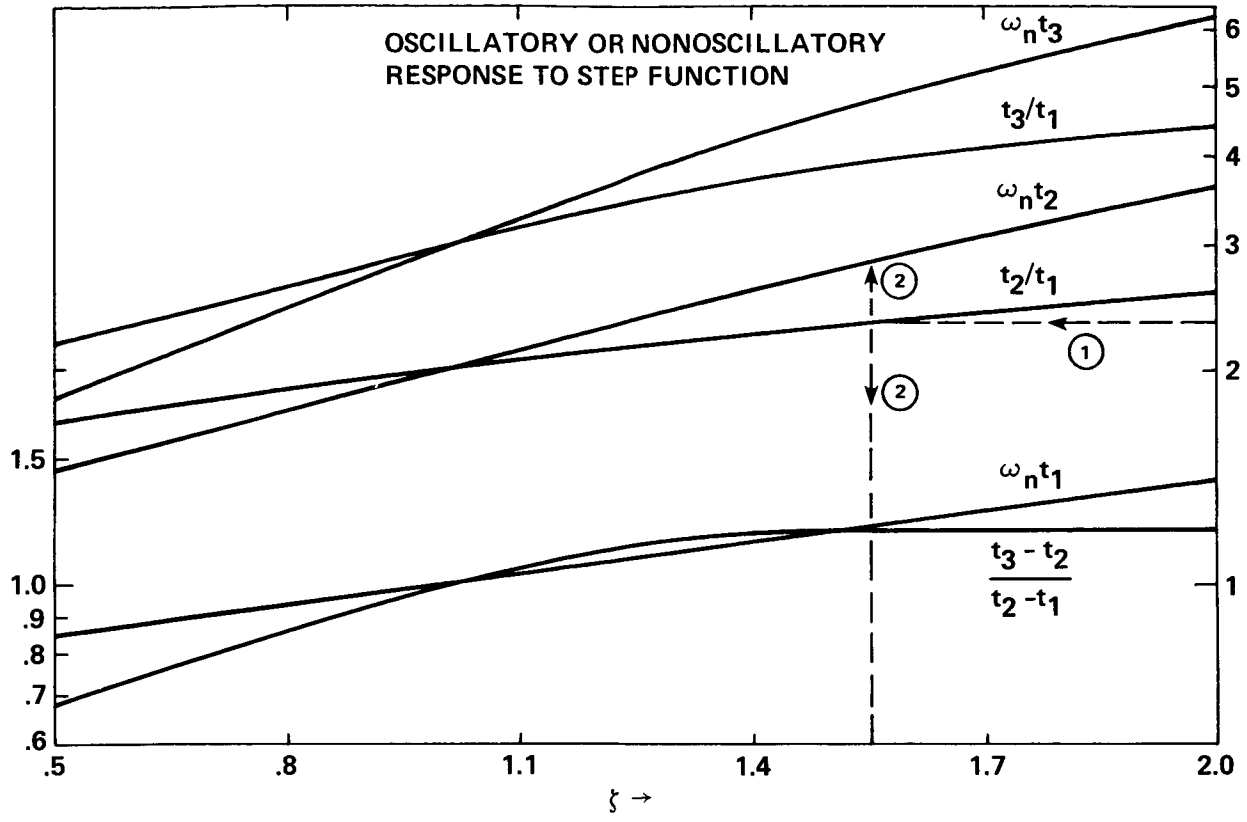

$t_1 \Rightarrow$ TIME $\theta/\theta_{PEAK} = 0.264$

$t_2 \Rightarrow$ TIME $\theta/\theta_{PEAK} = 0.594$

$t_3 \Rightarrow$ TIME $\theta/\theta_{PEAK} = 0.801$

Figure 28.- Determination of equivalent damping ratio (ζ_e) for highly damped systems (from ref. 50).

flight which would be precise enough to expose time delay deficiencies using the $t_{R_{10}}$ parameter is questionable, because the time-domain description compresses the high-frequency information into a very short time frame at the start of the step response, where unsteady initial conditions can create gross errors. Yet, the needed high-frequency data are easily extracted from Bode plots (fig. 25) which are rapidly and accurately generated in flight (ref. 59). Moreover, the frequency-domain format separates the response characteristics according to modes, allowing a clear understanding of the underlying vehicle characteristics. In contrast, the step-response format results from a convolution integral of all of the modes combined together. Therefore, for highly augmented vehicles with many closed-loop modes, the mapping of criteria from the frequency-domain to the time-domain based on lower-order system analyses breaks down, as it does in the present case. Allowing for nonsharp step inputs, which are needed to facilitate flight testing (as in fig. 27), further obscures this mapping. In the later (current) LHX spec version

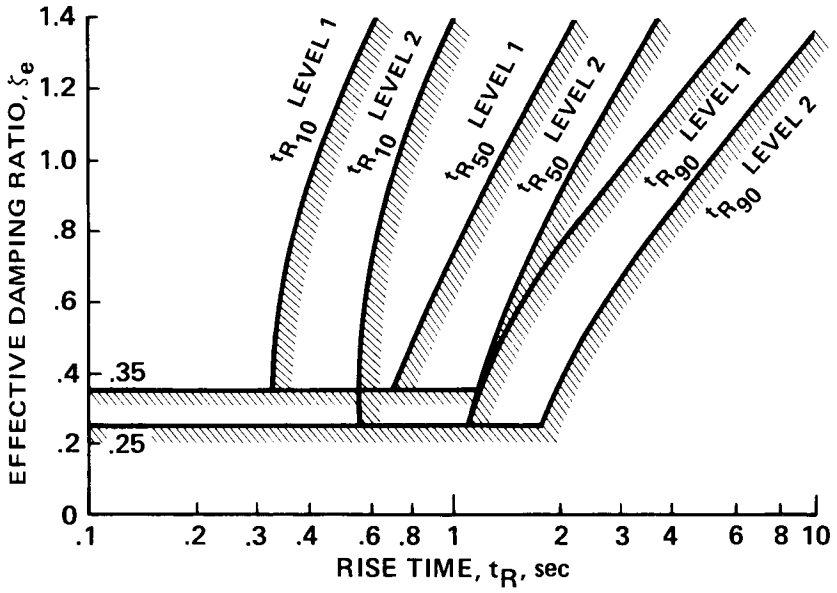

Figure 29.- Proposed LHX specification for rise time limits for attitude response types--hover and low speed (reproduced from ref. 50).

(ref. 15), these problems with time-domain criteria are recognized; the frequency-domain criteria (fig. 15) are retained as the requirement, while the time-domain criteria (an updated version of fig. 29) are recommended for use in preliminary design assessment only.

Large amplitude response requirements for attitude command systems are given (refs. 15 and 50) in terms of attitude change in a fixed time period. In reference 50, the Level I requirement for aggressive maneuvering is to achieve 5 deg of attitude change within 1 sec ($\equiv \theta_1 = 5$ deg). For a given bandwidth ω_{BW_θ}, the ability to achieve this response depends on the authority limits of the rotor and actuators, and on the rate of stick deflection. The following analysis determines the maximum allowable stick deflection, and the resulting large amplitude response under the (linear) assumption that the actuator and rotor deflection and rate limits are just reached. Faster responses can be achieved with larger inputs that cause the actuators to limit and render the feedbacks ineffective; then the analysis of the overall behavior requires nonlinear simulation. Further, if the rotorcraft is open-loop unstable (as in the present case) this actuator saturation in the initiation of the maneuver may result in aircraft response rates which exceed the recovery capability of the (reverse) saturated actuators. For this reason, the following linear analysis is restricted to the conservative case of the actuators just reaching their limits.

The rotor flapping-angle response corresponding to the step input of figure 26(a) is shown in figure 26(b). The flapping angle (δ_θ) is given in terms of effective stick inches, with ±5 in. being the nominal maximum values. The associated upper boost (swashplate) actuator (fig. 17) deflection (δ_{S_θ}) is also shown in

figure 26(b). The control power ratio of maximum flapping angle to pitch attitude response after 1 sec is obtained from figure 26(a),(b):

$$\left(\frac{\delta_\theta}{\theta_1}\right)_{\underline{max}} = \frac{13.0}{(0.73)(57.3)} = 0.31 \text{ in./deg in 1 sec} \tag{43}$$

which for $|\delta_\theta| \leq 5$ in., yields a maximum attainable attitude change in 1 sec of $(\theta_1)_{max} = 16.1$ deg. If the swashplate travel is also limited to $|\delta_{s_\theta}| \leq 5$ in., a slightly lower maximum attitude change is obtained:

$$\left(\frac{\delta_{s_\theta}}{\theta_1}\right)_{\underline{max}} = \frac{14.0}{(0.73)(57.3)} = 0.34 \text{ in./deg in 1 sec} \tag{44}$$

$$\Rightarrow (\theta_1)_{max} = 14.9 \text{ deg}$$

This level of available attitude control power is much larger than the (ref. 50) requirement of $\theta_1 = 5$ deg.

The time-history response of the swashplate rate ($\dot{\delta}_{s_\theta}$) is shown in figure 26(c) and in an expanded time scale in figure 26(d). This yields a swashplate rate-to-attitude response ratio of:

$$\left(\frac{\dot{\delta}_{s_\theta}}{\theta_1}\right)_{max} = \frac{335.8}{(0.73)(57.3)} = 8.03 \text{ in./sec/deg in 1 sec} \tag{45}$$

Since the upper-boost actuator rate limit for the Black Hawk is:

$$|\dot{\delta}_{s_\theta}| \leq 10 \text{ in./sec (equivalent stick in./sec)}$$

the attitude response capability becomes:

$$(\theta_1)_{max} = \frac{10 \text{ in./sec}}{8.03 \text{ in./sec/deg in 1 sec}} = 1.25 \text{ deg} \tag{46}$$

which is unsatisfactory. As is often the case for high-bandwidth systems, the actuator rate capability imposes key design and performance constraints. In the ADOCS system, this problem is alleviated with the incorporation of a "derivative rate limiter," which restricts sharp stick inputs from being transmitted to the command model. (Other designs use low-pass stick filters and/or actuator command filters for this purpose.) Therefore, the actuator-rate response to an <u>ideal</u> step input is not an appropriate metric for evaluating the available control power. A more reasonable input for this evaluation is the "ramp-step" shown in figure 30(a). Clearly, the level of control activity will be a strong function of the rise time of the input (Δt). The pitch attitude (θ), flapping angle (δ_θ), and

actuator rate ($\dot{\delta}_{s_\theta}$) responses for $\Delta t = 0.5$ sec and $\Delta t = 1$ sec are co-plotted with the sharp step response ($\Delta t = 0$) in figure 30(b), (c), (d), and (e).

One way to set a criterion value for the step rise time (Δt) is to compare the pitch-attitude responses (fig. 30(b)) with the time-response requirements of figure 29, while employing the definitions of the starting time as in figure 27. Unfortunately, as the rise-time is increased, the criterion time $t_{R_{10}}$ decreases rapidly while the remaining criterion times ($t_{R_{50}}$, $t_{R_{90}}$) increase slightly, as shown in figure 30(b). Decreasing $t_{R_{10}}$ parameter with increasing rise-time suggests that slower inputs result in better handling quality ratings. Again, the implications for flight-test certification based on time-response criteria compliance are troublesome. In any event, the ADOCS derivative-rate limiter does transmit "ramp-like" inputs ($\Delta t \neq 0$) rather than pure steps; so, a criterion value of $\Delta t = 0.5$ is

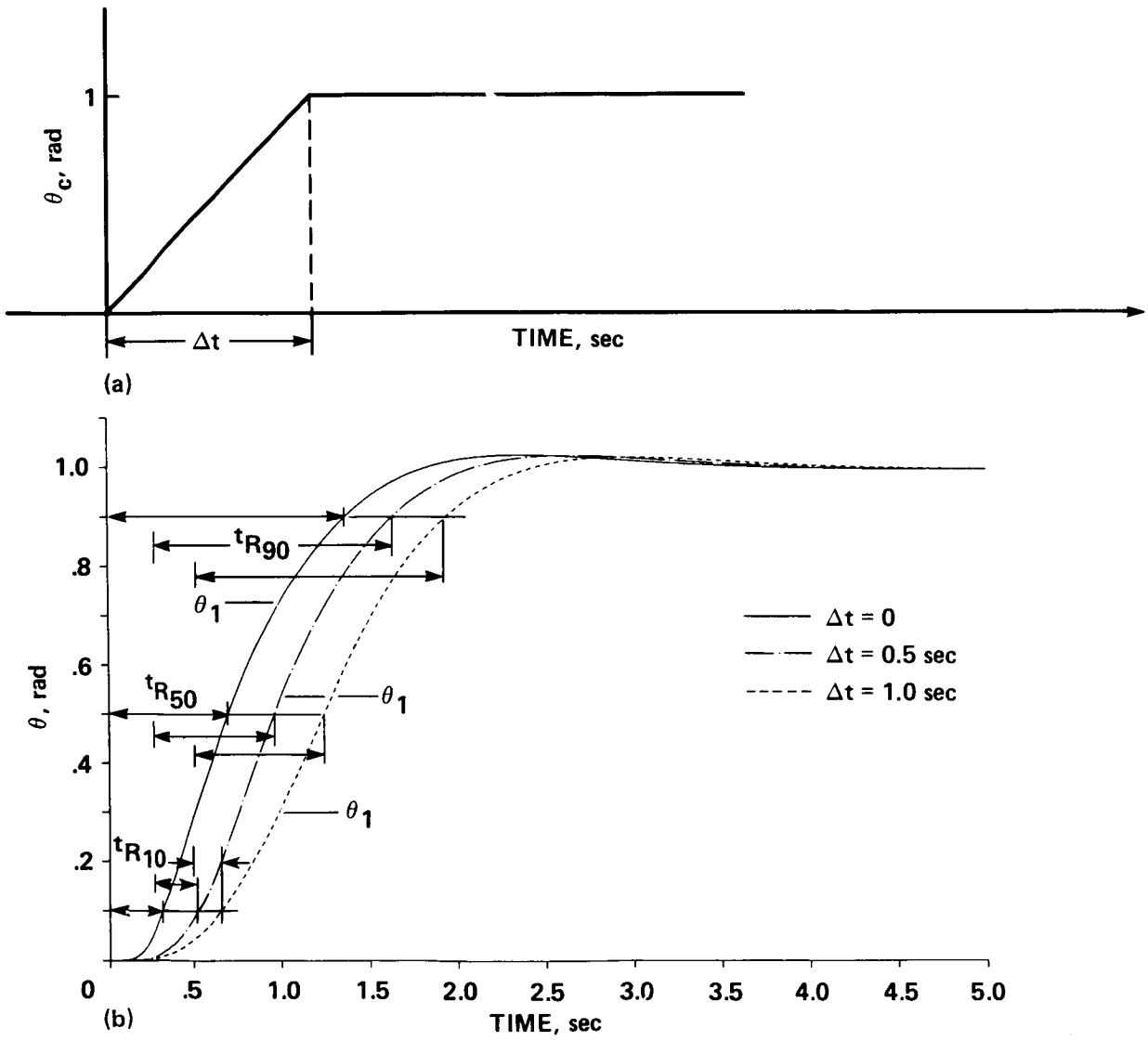

Figure 30.- Ramp-step response. (a) stick input (δ_s); (b) pitch attitude response (θ); (c) flapping angle (δ_θ); (d) swashplate actuator rate ($\dot{\delta}_{s_\theta}$); (e) swashplate actuator rate ($\dot{\delta}_{s_\theta}$) shown on an expanded time scale.

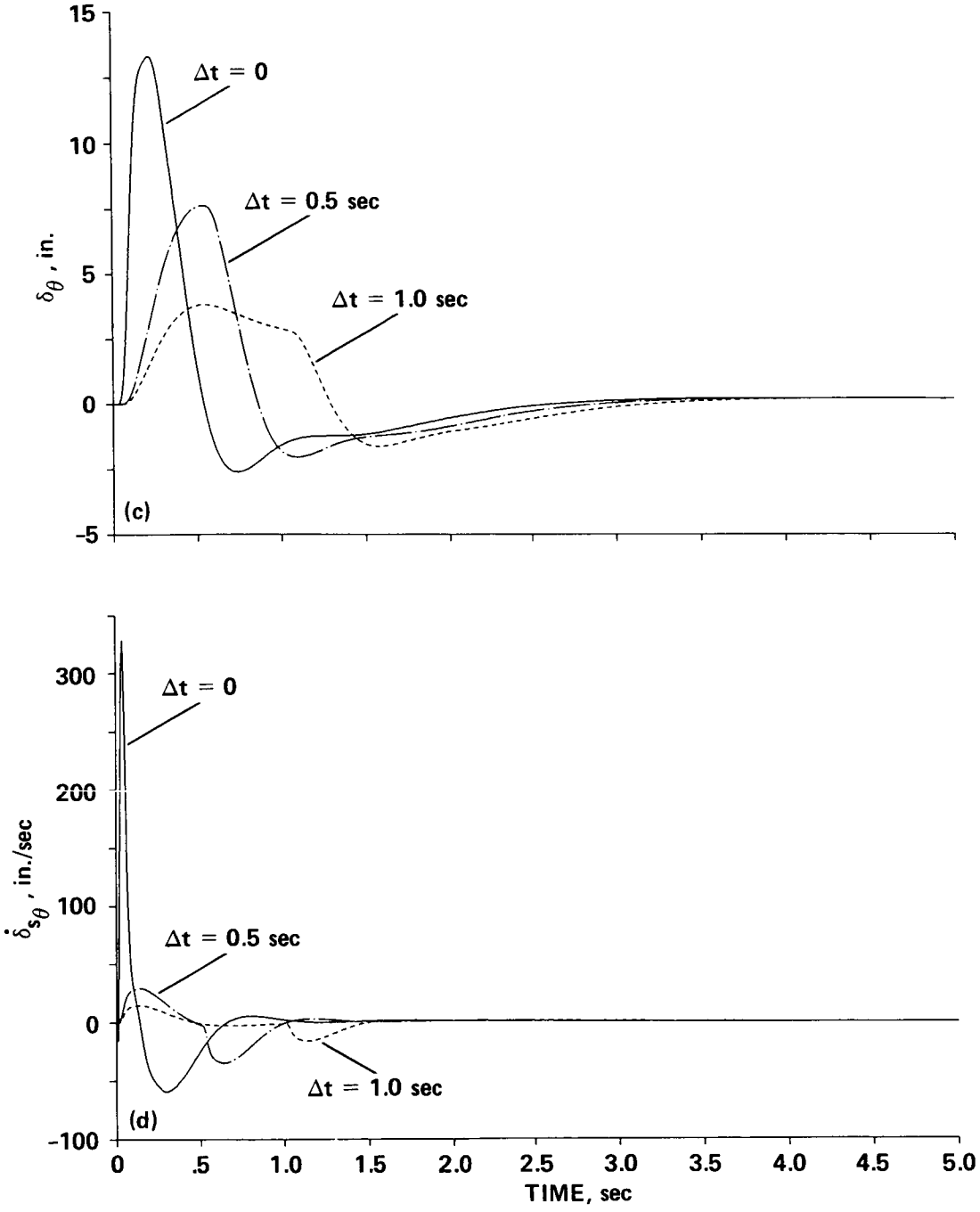

Figure 30.- Continued.

selected for the present actuator authority analysis. The pure step inputs ($\Delta t = 0$) are retained in the evaluation of the overall attitude response (as in fig. 26(a)) to ensure maximum consistency between the time and frequency domain criteria metrics.

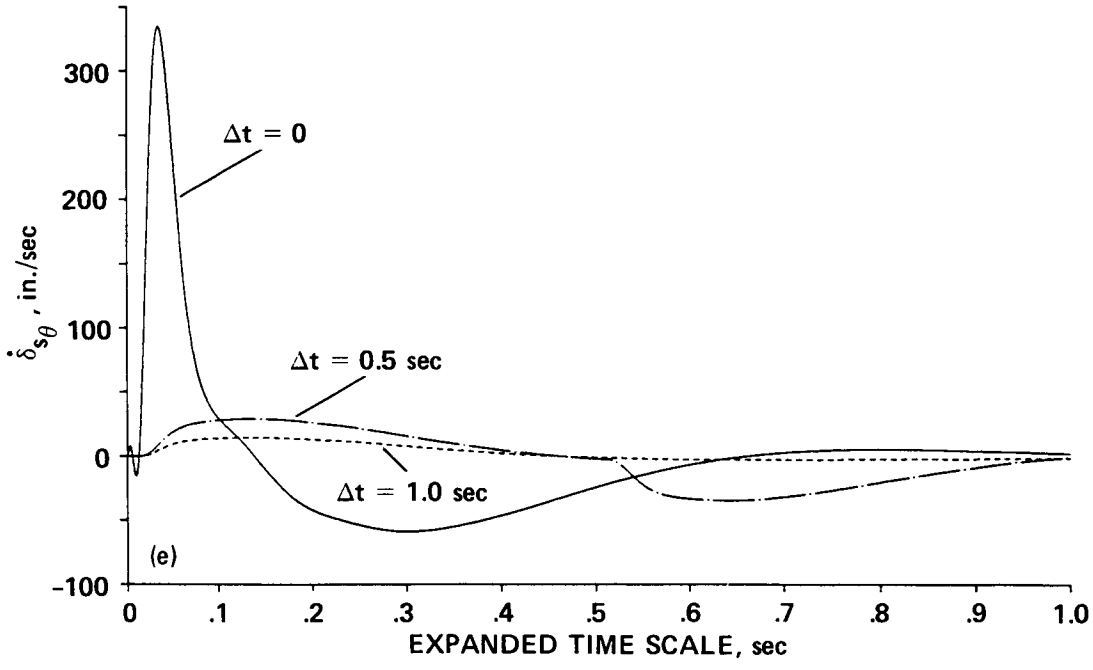

Figure 30.- Concluded.

The maximum flapping angle and swashplate actuator rate decrease with increasing values of step rise time (Δt) much faster than the associated reductions in θ_1, as seen in figures 30(b), (c), (d), and (e). (The $t = 0$ reference point for calculating θ_1 is taken at the initiation of the control input (refs. 15 and 50), and does not change with ramp duration.) The relative flapping angle reduction for $\Delta t = 0.5$, yields a maximum attitude change after 1 sec of $(\theta_1)_{max} = 20.4$ deg, while the dramatic relative reduction in actuator rate (90%) results in an associated maximum attitude change of $(\theta_1)_{max} = 9.0$ deg. Thus, the attitude response limit is still determined by the actuator rate limiting, but the present value of $(\theta_1)_{max} = 9.0$ deg is well within the requirement.

This completes the s-plane analysis of the nominal (simulation) control system model ($\omega_{c_\theta} = 6$ rad/sec, $\omega_s = 40$ Hz) as documented in reference 7. The previous results have shown that, for this design model, the handling qualities and performance specifications have largely been met. If the emulation design approach of reference 7 is followed, then the additional high-frequency dynamics (such as filters, computational delays, and stick sampling skews) are ignored, and no further control system analyses are needed before this final design is implemented. At this point, the feedback and command block transfer functions are converted, using Tustin transform (Section II.C.2), to difference equations which are programmed into the onboard computer system. If no additional high-frequency dynamics were considered, one would be led to the conclusion that, except for the undesirable coupling between the rotor and rigid body dynamics, an acceptable and practical control-system design had been achieved. Such conclusions, based on inadequate high-frequency modeling,

led to an over-estimation of attainable bandwidth of many of the first generation of high-gain fixed-wing systems.

III.F Practical Implementation Considerations for the Nominal (ω_{c_θ} = 6 rad/sec) Design

In the following sections, the (ω_{c_θ} = 6 rad/sec) system is appended with the additional elements which are needed for the practical digital implementation of the preceding s-plane design. The discussion will focus on the most important of the implementation concerns:

- Anti-alias filtering
- Biodynamic interference filtering
- Lead-lag rotor mode notch filtering
- Sample rate reduction
- Stick sampling skew

The origin of each of these elements was discussed in detail in Sections I and II. Briefly reviewing, anti-alias filtering restricts "fold down" of spurious high-frequency signals. Biodynamic interference filters eliminate involuntary stick inputs caused by 1/rev and 4/rev vibrations and structural mode excitations. Notch filtering of the actuator signal is needed to attenuate excitations of the in-plane (lead-lag) rotor mode. (This will be especially important for high-bandwidth (hingeless) rotor systems.) The reduction in sample rate from 40 Hz to 30 Hz on the ADOCS Black Hawk was needed to allow sufficient computational time to process all of the required AFCS functions. In this case study, the lower sample rate is taken to be ω_s = 30.3 Hz which yields an even sample period of T = 0.033 sec. Finally, stick-sampling skew occurs because the pilot's transient inputs are not synchronized with the even sample instants. The attitude channel schematic of figure 17 is updated in figure 31 to reflect these additional elements.

The combined effect of these additional system elements is the generation of significant amounts of phase lag in the crossover frequency range which degrades the phase and gain margins of the stabilization loop. These additional elements also reduce the overall system bandwidth and increase the total effective time delay. The reduction in sample rate to ω_s = 30.3 Hz also introduces some additional phase lag. However, the reduced sample rate is still well above the actuator and rotor modes, so folding effects other than the 4/rev vibration will still not be a significant problem. Thus, design-by-emulation is still a plausible approach.

Computational delay (τ_c) (which was not listed above) is also important since it can add a sizable increment to the total time delay of the system. As detailed earlier, significant reductions in the computational delay were made possible on the F-18 system by altering the software architecture to minimize the delay between sensor and control updates (as in fig. 12). Such methods were used to substantially reduce the full cycle time delay (τ_c = T) which was embodied in the preflight test ADOCS system. This relatively common full frame delay implementation unnecessarily leads to a requirement of higher sample rates, since the computational delay and the

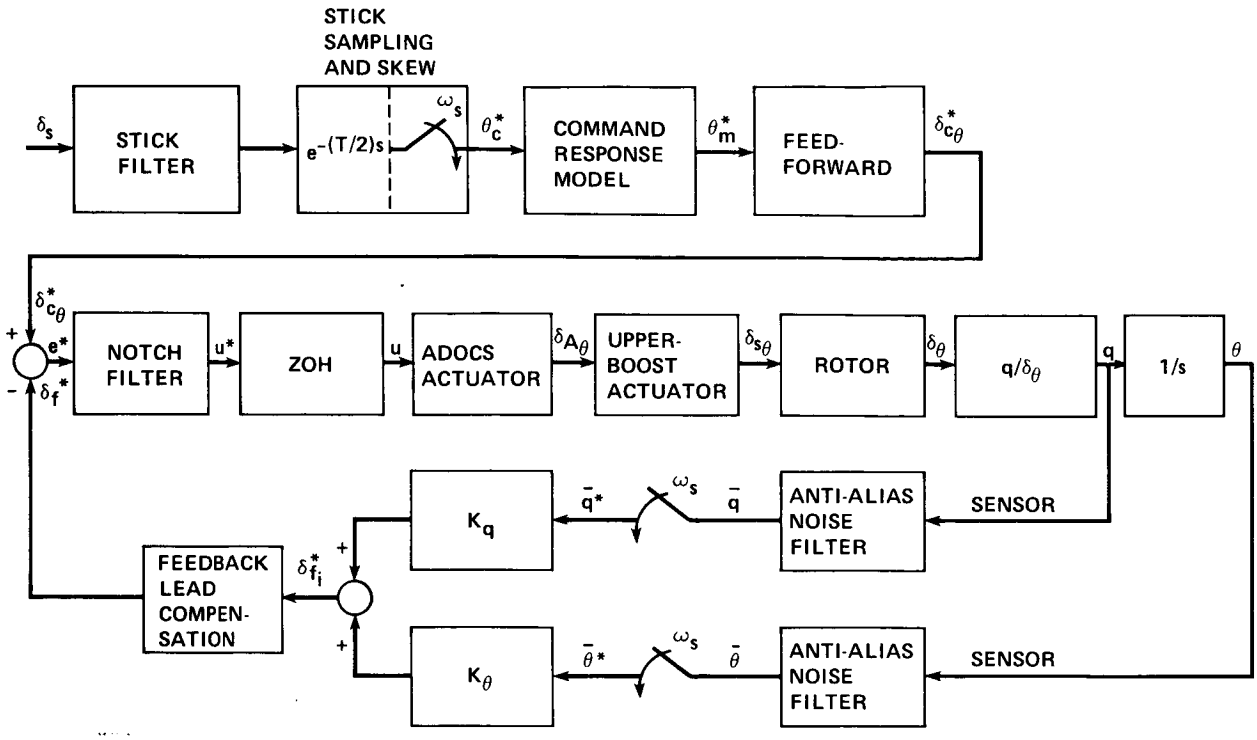

Figure 31.- Attitude channel with appended dynamics.

sample rates are tied together. Thus, the total transport delay caused by the combined zero-order hold and computational delays is $\tau = 3T/2$, which is 200% higher than that strictly associated with the zero-order hold (T/2).

In terms of the present emulation analysis, the computational delay will add to that of the zero-order hold, contributing to the phase lag and further reducing the design phase margin. While important, this represents a straightforward adjustment to the s-plane phase curve and does not cause a fundamental change in the emulation design. However, as the sample rate is reduced, there is a complex interaction in the discrete system response between the sample rate and (pure) time delay, which destroys the simple linear relation between transport delay and overall system phase lag. This is because large amounts of computational delay relative to the sample rate ($\tau_c/T \doteq 1$) can cause significant folding distortion. Thus, as the sample rate is reduced, it is important to check the effects of the computational delay and to reduce this delay as much as possible. An illustration of this effect is presented in Section III.I.3.

Sensor dynamics, also omitted from the preceding list, will contribute to the phase lag and associated reduction in the phase margin; if these dynamics are important, they should be considered in the design process. However, in terms of the present illustration, sensor dynamics are considered to change the effective plant dynamics, and do not constitute a fundamental change in the control system response or analysis techniques.

The first system adjustment considered in this section is the effect of reducing the sample rate from ω_s = 40 Hz to ω_s = 30.3 Hz. The increase in the zero-order hold delay from T/2 = 12.5 msec to T/2 = 16.5 msec adds only a small increment of phase lag (1.4 deg) at the crossover frequency ω_{c_θ} = 6 rad/sec. Thus, in terms of pure phase lag or transport delay, the effects of reduced sample rate do not appear to be significant. However, one very important change occurs with this reduction in sample rate. With the original design rate ω_s = 40 Hz, the associated Nyquist frequency is 1/2 of this value, or ω_{Nyq} = 125.66 rad/sec. This Nyquist frequency is well above the actuator and airframe dynamics and is also well above the dominant vibration component at the 4/rev frequency of ω_4 = 108 rad/sec. This 4/rev vibration appears in the feedback sensor signals which are passed into the control system. With the reduction in sample rate to ω_s = 30.3 Hz, the Nyquist frequency is reduced to ω_{Nyq} = 95.2 rad/sec which is now below the 4/rev frequency. Thus the 4/rev vibrations sampled at ω_s = 30.3 Hz will be folded down to the lower frequency of ω = 82.4 rad/sec. Reference to equation (28) shows that this reflected 4/rev frequency is essentially identical to the dominant frequency of the ADOCS actuator. Thus, 4/rev vibrations will be folded directly on top of the actuator's natural resonant frequency and can, therefore, be expected to cause a great deal of actuator jitter and unnecessary wear.

The feedback signals must be filtered to remove this 4/rev vibration component before the signals are sampled. One approach is to use an analog notch filter, centered at the 4/rev frequency. A second approach is to design a low-pass filter which serves both the 4/rev and anti-aliasing filter requirements, thus minimizing the additional phase lag. This is the approach taken for the present case study design (fig. 31). The anti-aliasing/vibration-suppression analog filter eliminates actuator response to, and fold down of, the 4/rev signal through the sensor path; yet this strong vibration component will also interact with the biodynamic environment leading to 4/rev feedthroughs from the pilot's stick inputs. Thus, an identical analog filter is also applied ahead of the stick sampler (fig. 31).

A digital notch filter is placed in the forward stabilization loop (fig. 31) to attenuate the lower frequency biodynamic feedthrough assumed for the present case to be only due to 1/rev vibration, and to reduce the loop gain at the lead-lag rotor mode (assumed for the present study to also be located at ω = 1/rev). In principle, the insertion of a lead-lag mode notch filter allows higher crossover frequencies than would be achievable by a comparable fixed gain reduction (in K_θ and K_q). In fact, however, the additional filter lag requires a crossover frequency reduction as well. Perhaps a nonlinear filter which provides the needed attenuation without introducing as much phase lag would improve this situation. In the present case, the forward loop linear notch filter contributes significant additional effective time delay.

III.F.1 Sampled Signal Filter. As discussed in Section II.C.4, the periodic nature of the spectrum of sampled signals causes high-frequency continuous signals to be aliased to their lower frequency reflections. Thus, sampled high-frequency sensor and vibratory noise components will appear in the system as spurious low-frequency signals. Lower frequency noise components, which are not aliased but are

well above the control bandwidth, cause unnecessary wear on the actuators. Sampled signal filters are used to avert these problems.

Since the power spectrum of sensor noise is generally broad-band in nature, low-pass filtering must be used to remove the undesirable components. Significant levels of attenuation must be achieved for the segment of the analog signal spectrum above the Nyquist frequency ($\omega > \omega_{Nyq}$) to avoid aliasing effects. Thus, an "anti-aliasing filter" is placed ahead of each control system sampler, including the stick sampler (stick filter in fig. 31), and is usually an analog device. Some designs, especially in booster applications, have employed high sample-rate digital processors which were dedicated to the sensor filtering task. Once the digital filtering is completed, these high rate signals are then resampled at the basic control system rate (ref. 35).

The selection of anti-alias filter parameters, as described in the literature, is largely based on rules-of-thumb. The filters are generally simple first- or second-order low-pass elements, which provide an attenuation of between -10 dB and -20 dB at the Nyquist frequency (refs. 20,39,60,61). In many cases, the sensor instruments have embedded analog filters, which may be suitable for both noise filtering and anti-alias filtering functions (depending on the filter characteristics). Since it is common for the sensor system dynamics to be ignored in the design process, the embedded analog prefilters may also be inadvertently duplicated.

In the present case, it is desirable to synthesize a single analog filter which serves the sensor, anti-alias, and 4/rev filtering functions. The following second-order filter was selected based on a compromise between desired attenuation and undesired phase lag:

$$G_F = \frac{1600}{[0.6,\ 40]} \tag{47}$$

This filter provides -15 dB (82%) attenuation at the Nyquist frequency, -17 dB (86%) attenuation at the 4/rev frequency, and contributes 12 deg of phase lag at the ω_{c_θ} = 6 rad/sec crossover frequency. Most of the literature concerning the design of anti-alias filters suggests the use of simple first-order elements. However, to obtain the desired attenuation at the Nyquist frequency, the first-order filter would contribute more phase lag at the crossover frequency (14 deg compared to 12 deg) and would have slightly less attenuation at the 4/rev frequency than the second-order filter. Since the single second-order filter is serving three separate roles, the additional complexity of implementing this filter compared to the first-order analog element is felt to be justified.

III.F.2 Biodynamic Interference Filter for 1/rev Excitations. Biodynamic interference occurs when vehicle vibrations are involuntarily passed through the pilot's body into the control manipulators (fig. 1). While large displacement, conventional centersticks usually act to suppress the phenomenon, small displacement centersticks and sidesticks aggravate it considerably. The fixed-wing F-18 and Space Shuttle aircraft experienced problems which were due to coupling between structural modes and the pilot/sidestick biodynamic system. It was necessary to attenuate the involuntary biodynamic feedthrough signals with digital notch

filters. In both cases, these filters contributed significant phase lag to the system resulting in a degradation in system performance and handling quality ratings. In the case of the F-18, the small displacement force stick was replaced by a (standard) displacement stick; this change allowed the notch filter to be moved to the feedback path in sensor signal filtering only (ref. 29). In the Space Shuttle, the use of a limited displacement sidestick necessitated forward-loop notch filtering, which contributed to the large overall effective time delay of the system (ref. 5). Biodynamic interference was also encountered with the sidestick controller on the AFTI-F-16. Changes to the control laws were made to correct the problem (ref. 62).

Although the 4/rev component is the major source of vibration for the four-bladed rotor system, lower frequency and amplitude 1/rev vibrations are often encountered since rotor balance is not optimum for all flight conditions. Also, vibration which is due to structural dynamic modes of the tail boom and rotor pylon will be present. In conventional centerstick systems, only the larger n/rev vibration component is attenuated to eliminate excessive high-frequency "noise" feedback into the actuator systems. However, recent rotorcraft flight experience with limited displacement, force sensing sidestick controllers raises concerns over the biodynamic effects of the lower amplitude, lower frequency vibrations as well. Excessive one-per-rev (5 Hz) biodynamic feedthrough to the sidestick of the Bell ARTI demonstrator was eliminated by incorporating a low-pass digital stick filter in the command path (ref. 9). Command path notch filtering was also required in the ADOCS system to eliminate 6 Hz biodynamic feedthrough in the pitch, roll, and heave axes which was encountered in forward flight conditions (ref. 8). The yaw axis notch filter was placed in the forward stabilization loop to eliminate biodynamic/tail-boom mode/AFCS coupling.

Simulator experiments in Israel (ref. 10) have shown that such biodynamic interactions become more severe as the level of pilot workload increases and the pilot's grip on the stick becomes tighter. Thus, periods of maximum piloting urgency will also represent critical conditions for biodynamic interference. Serious biodynamic coupling can be triggered by excitation levels which might otherwise be considered unimportant when the excitation frequency and the biodynamic frequency (typically about 6 Hz) are close together (as in the ADOCS case) or when the stick sensitivity is too high (ref. 10). Although a low-pass filter as is used in the Bell ARTI demonstrator is effective in eliminating 1/rev and structural mode biodynamic feedthrough, it also introduces considerable phase lag since the required break frequency is relatively close to the crossover frequency. Alternatively, adaptive notch filters self-adjust to cancel involuntary stick inputs at varying biodynamic frequencies (ref. 10). These adaptive filters become "dormant" when biodynamic feedthrough is not present, so command-response distortion is minimized. A fixed-parameter linear notch filter may be suitable when specific and constant forcing frequencies are identifiable, such as the biodynamic/tail-boom mode coupling in the ADOCS. Because the rotor speed is held at a constant level by the governor system, a fixed-parameter notch filter may also be suitable to attenuate 1/rev biodynamic interference.

For the present case study, biodynamic interference is considered due only to 1/rev and 4/rev rotor vibration. The 4/rev interference is eliminated by the stick filter (eq. (47)).

For 1/rev interference, the following second-order notch filter provides an attenuation of -12 dB (75%) at the 1/rev frequency of $\omega = 27$ rad/sec:

$$G_N(s) = \frac{[0.1,\ 27]}{[0.6,\ 27]} \tag{48}$$

Since the lead-lag rotor mode is also assumed to be located at the 1/rev frequency, the notch filter $G_N(s)$ is placed in the forward stabilization path (fig. 31) to attenuate both 1/rev biodynamic feedthrough and 1/rev loop gain.

III.F.3 Combined Effect of the Additional Elements on the Nominal Design- When the nominal stabilization system (fig. 17, with the gains of eq. (30)) is appended with the feedback filter, notch filter, and reduced sample rate, the open-loop s-plane Bode plot of figure 32 is obtained. Also shown in this figure is the previous frequency response for the nominal 40 Hz system (fig. 19). The added system elements are seen to contribute 25 deg of phase lag at the crossover frequency of $\omega_{c_\theta} = 6$ rad/sec, reducing the phase margin from an already low value of 38 deg to an unacceptable value of 13 deg. Since the lead compensation introduced by a reasonable pitch rate feedback gain provides a maximum phase of about 75 deg, and its nominal contribution for the 40 Hz system is 70.5 deg, it is not possible to offset all of the additional phase lag with the simple state feedback architecture. This problem is addressed with the following design changes:

1. Open-loop crossover frequency is reduced from $\omega_{c_\theta} = 6$ rad/sec to $\omega_{c_\theta} = 4$ rad/sec. The $\omega_{c_\theta} = 4$ rad/sec crossover frequency is within the recommended value

$$\frac{\omega_{c_\theta}}{\omega_m} \geq 2 \text{ to } 3$$

so reasonable command following is maintained.

2. The ratio of pitch rate gain to pitch attitude gain is increased to $T_q = 0.63$, thereby reducing the location of the compensation zero to $1/T_q = 1.58$ rad/sec from $1/T_q = 2.13$ rad/sec.

3. A lead compensation element of

$$G_{1c} = \frac{1.52(s + 3.24)}{(s + 4.93)}$$

is inserted in the feedback path (fig. 31).

The open-loop frequency response δ_f/e of figure 31, including all of the appended dynamics and design changes, is shown in figure 33. A careful study of this figure clarifies the reasons for the design changes. The lowering of the lead

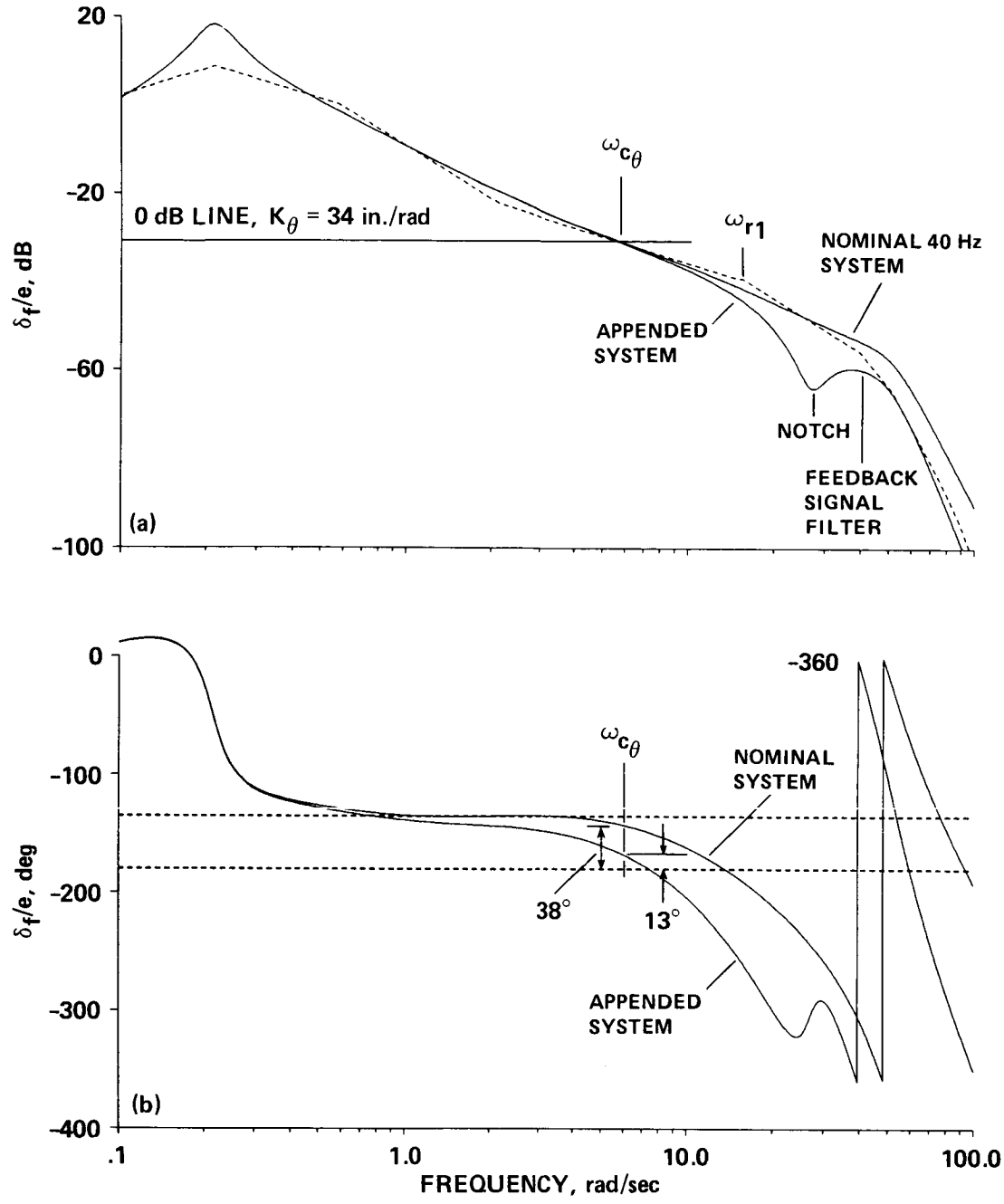

Figure 32.- Effect of appended system dynamics on the nominal design. (a) Magnitude; (b) phase.

equalization zero to $1/T_q$ = 1.58 rad/sec and the inclusion of a lead compensation element, G_{1c}, both add phase lead to the open-loop response. If the crossover frequency was maintained at ω_{c_θ} = 6 rad/sec, the phase margin would be Φ_m = 28 deg (fig. 33), which is still too low; so, additional lead compensation would be required (e.g., further lowering of $1/T_q$ or wider pole-zero separation in G_{1c}). However, the gain margin for ω_{c_θ} = 6 rad/sec is GM = 3.7 dB, which is already too

low; the extra lead which is needed to restore the phase margin at ω_{c_θ} = 6 rad/sec would degrade the gain margin even further. Therefore, the only option is to reduce the crossover frequency.

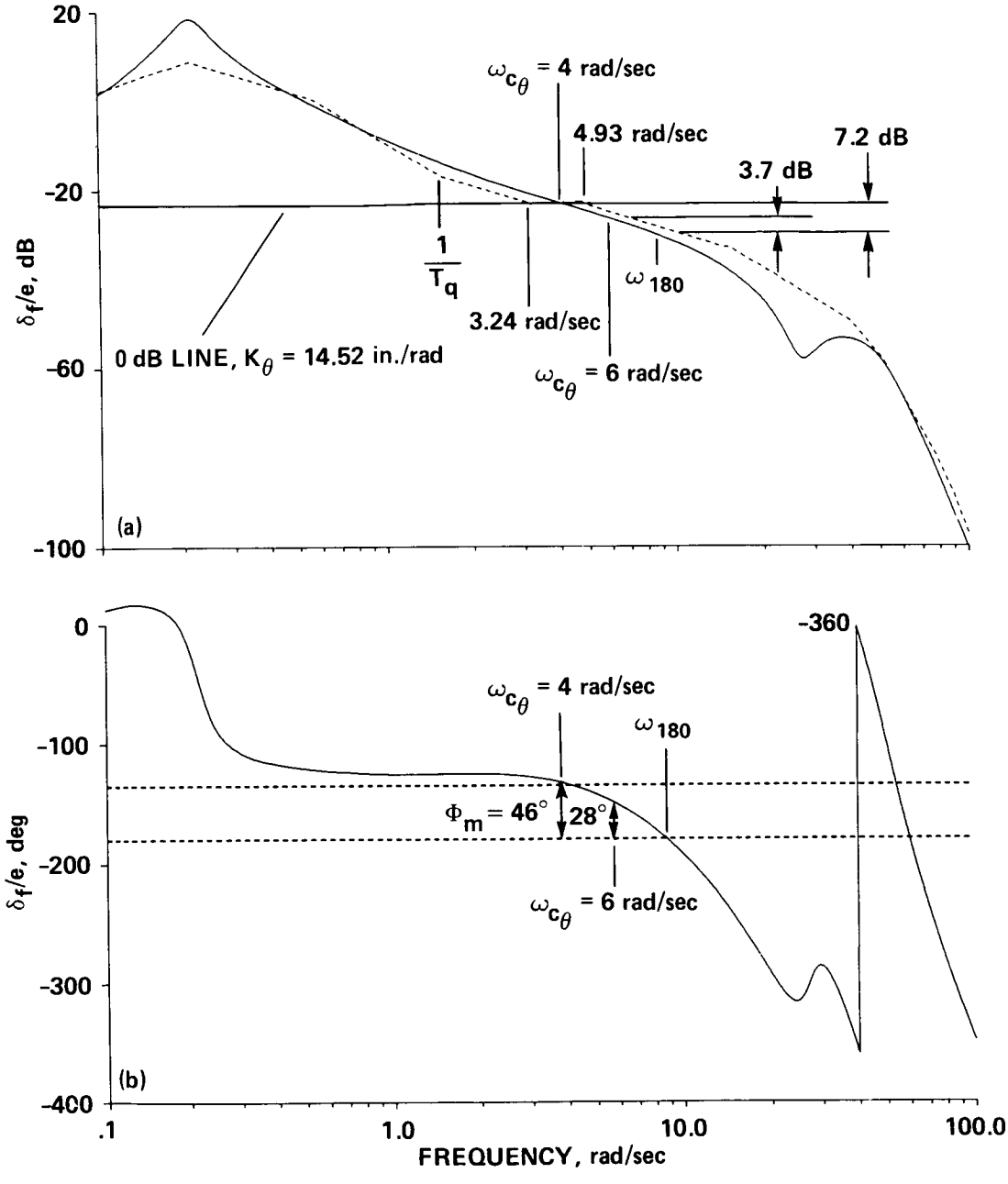

Figure 33.- Compensated open-loop frequency response including all of the appended dynamics and design changes. (a) Magnitude; (b) phase.

If the crossover frequency is reduced to ω_{c_θ} = 4 rad/sec, the phase and gain margins become:

$$\Phi_m = 46 \text{ deg}$$
$$GM = 7.2 \text{ dB} \tag{49}$$

The phase margin here is greater than for the nominal design, but the gain margin has been reduced. These margins still allow sufficient leeway for unmodelled sensor dynamics and computational delays. This design study shows that the choice of pitch rate gain and lead compensation is severely limited by the tradeoff between phase margin improvement and gain margin degradation. This is typical of systems which exhibit large amounts of effective time delay (high-frequency dynamics) as in the present case.

The required pitch rate and attitude feedback gains are determined from figure 33 and the value of $1/T_q$, respectively:

$$K_q = 9.19 \text{ in./rad/sec}$$
$$K_\theta = 14.52 \text{ in./rad} \tag{50}$$

III.G s-Plane Performance of the $\omega_{c_\theta} = 4$ rad/sec Emulation Design

The design changes of Section III.F.3 yield the closed-loop transfer function θ/δ_{c_θ}:

$$\frac{\theta}{\delta_{c_\theta}}(s) = \qquad (51)$$

THE NUMERATOR ROOTS ARE:

NO.	REAL	IMAG.	OMEGA	ZETA
1	179.64716	-103.71191	207.43495	-0.86604091
2	179.64716	103.71191	207.43495	-0.86604091
3	-0.15991542E-01	0.13430029E-01	0.20882890E-01	0.76577246
4	-0.15991542E-01	-0.13430029E-01	0.20882890E-01	0.76577246
5	-2.7000000	-26.864660	26.999999	0.10000000
6	-2.7000000	26.864660	26.999999	0.10000000
7	-24.000000	-32.000000	40.000000	0.60000000
8	-24.000000	32.000000	40.000000	0.60000000
9	-14.814814	0.00000000E+00		
10	-4.9299998	0.00000000E+00		

THE DENOMINATOR ROOTS ARE:

NO.	REAL	IMAG.	OMEGA	ZETA
1	-1.9309250	-1.0068296	2.1776541	0.88669961
2	-1.9309250	1.0068296	2.1776541	0.88669961
3	-2.9371331	-6.3884296	7.0312719	0.41772429
4	-2.9371331	6.3884296	7.0312719	0.41772429
5	-12.374792	-26.119011	28.902218	0.42816064
6	-12.374792	26.119011	28.902218	0.42816064
7	-32.460335	36.001732	48.474715	0.66963436
8	-32.460335	-36.001732	48.474715	0.66963436
9	-13.685993	-49.806011	51.652155	0.26496461
10	-13.685993	49.806011	51.652155	0.26496461
11	-71.624611	-54.134315	89.780894	0.79777119
12	-71.624611	54.134315	89.780894	0.79777119
13	-179.64716	-103.71191	207.43495	0.86604091
14	-179.64716	103.71191	207.43495	0.86604091
15	0.13033364E-02	0.00000000E+00		
16	-0.37460167E-01	0.00000000E+00		
17	-14.190777	0.00000000E+00		
18	-79.548866	0.00000000E+00		

LOW-FREQUENCY GAIN = -0.61595535

Mode	Symbol
Pitch (low freq.)	$[\zeta'_{sp}, \omega'_{sp}]$
Pitch/rotor	$[\zeta'_{p}, \omega'_{p}]$
Notch filter	$[\zeta'_{N}, \omega'_{N}]$
Anti-alias filter	$[\zeta'_{F}, \omega'_{F}]$

A comparison of these results with the closed-loop roots for the nominal system (eq. (35)) shows that the previous first-order pitch mode ($1/T'_{sp_2}$ = 3.24 rad/sec) is now replaced by a highly damped second-order mode, ω'_{sp} = 2.18 rad/sec. Also the frequency and damping of the coupled pitch/rotor mode have been reduced from ζ'_p = 0.55, ω'_p = 7.76 to ζ'_p = 0.42 and ω'_p = 7.03 rad/sec. The remaining roots are essentially unaltered from their previous values, except for the additional poles associated with the notch and anti-alias filters. The eigenvector diagrams for the pitch modes (ω'_{sp}, ω'_p) are shown in figures 34 and 35. A comparison with the similar results for the nominal case (figs. 21 and 22) shows that the new system has a slightly lower level of pitch-attitude/rotor flapping coupling, resulting largely from the reduced feedback gains, K_θ and K_q used. Sizable reductions in the coupling which would have otherwise been achieved by the crossover frequency reduction are offset by the added lead compensation.

A comparison of the compensation transfer function $[H(s)G_N(s)]$ calculated for the two designs (fig. 36) shows the difference in loop gain and associated noise amplification. Relative to the nominal design, the ω_{c_θ} = 4 rad/sec system has a low-frequency gain that is reduced by 7.4 dB (57% reduction), with a 2.7 dB (27%) reduction at ω'_p = 7.03 rad/sec. The gain reduction at the 1/rev frequency,

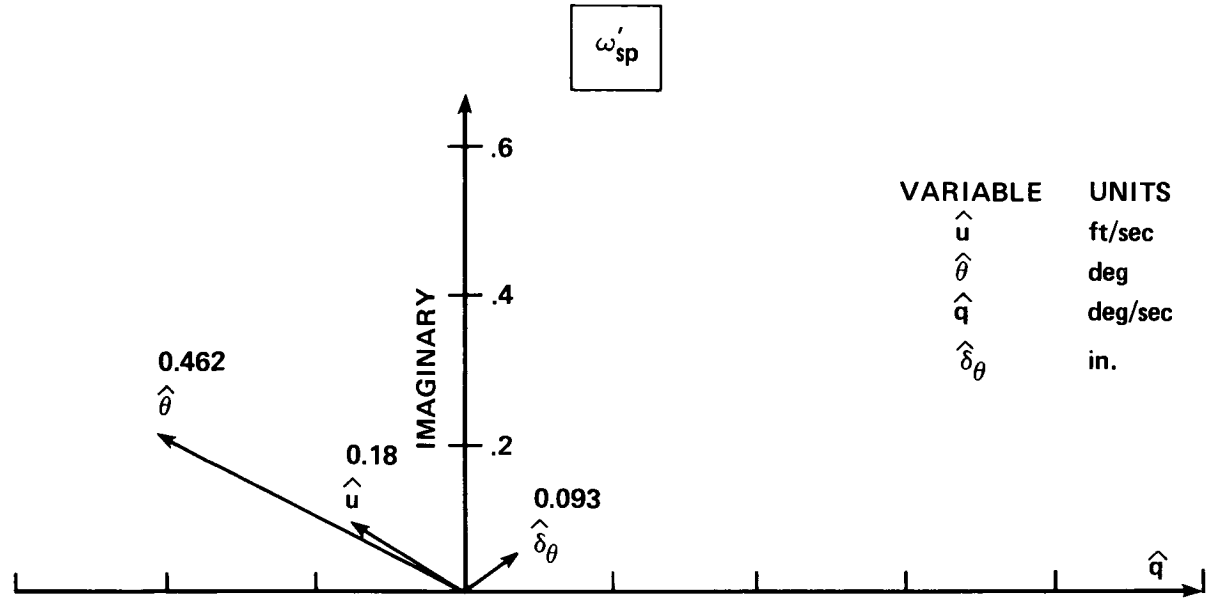

Figure 34.- Eigenvector diagram for the closed-loop pitch mode (ω'_{sp}) of the 4 rad/sec design.

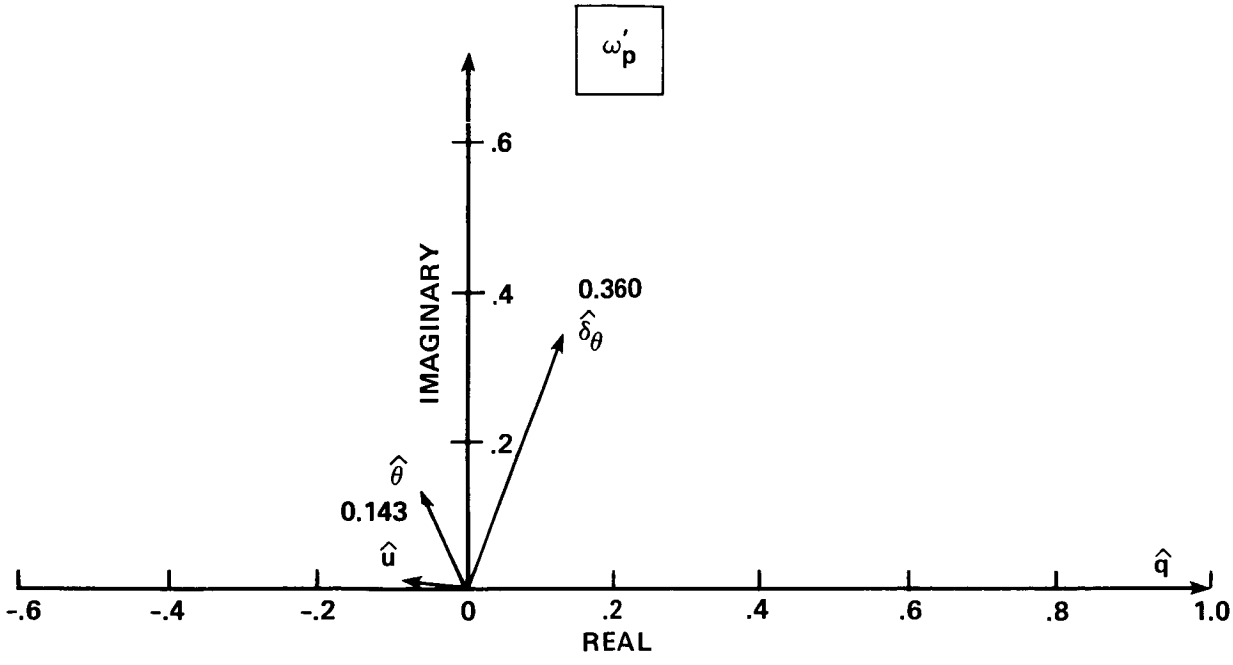

Figure 35.- Eigenvector diagram for the closed-loop pitch/rotor mode (ω'_p) of the 4 rad/sec design.

ω = 27 rad/sec, is the 16.7 dB (85%) relative to the nominal design. Thus, the effectiveness of the notch filter has been maintained even with the additional lead compensation.

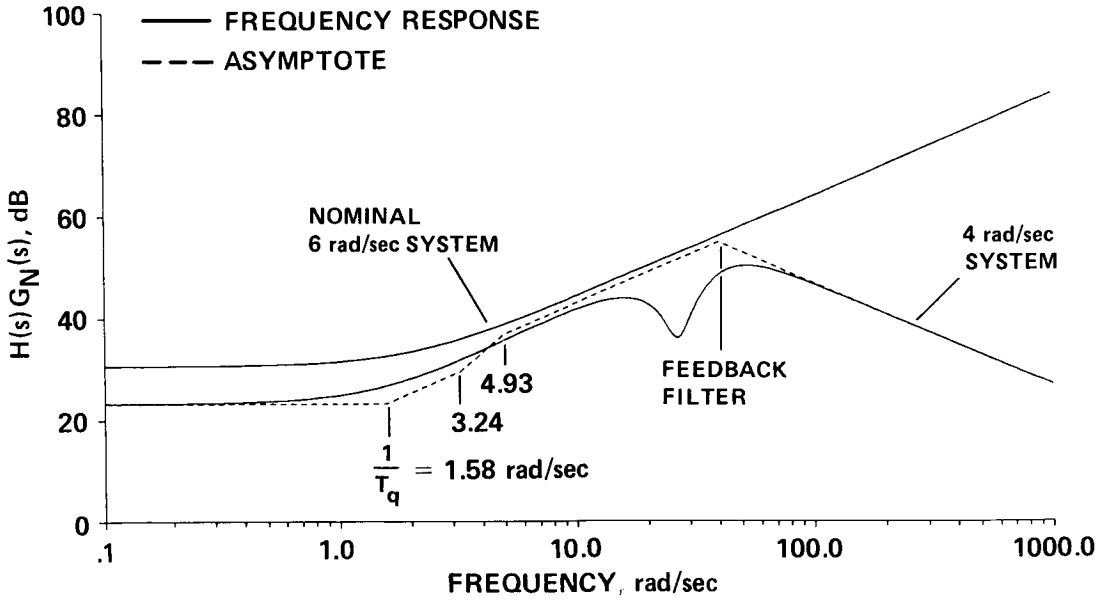

Figure 36.- Comparison of compensation transfer functions for the ω_{c_θ} = 4 rad/sec and ω_{c_θ} = 6 rad/sec designs.

The closed-loop pitch attitude response of the ω_{c_θ} = 4 rad/sec stabilization system to a 1 in. pulse upset is shown in figure 37(a). Also shown in this figure is the pitch attitude response of the nominal 6 rad/sec, 40 Hz system (same as fig. 23(b)). As expected, the lower bandwidth system has a larger maximum response (70% greater) and takes more time for the transient to die out. As shown in figure 37(b), the maximum flapping angle (δ_θ) is about the same for the ω_{c_θ} = 4 rad/sec system, which is consistent with the eigenvector results discussed earlier.

The design of the command block for the new system follows the same methodology as discussed in Section III.E. For the present case, the feedback block H contains the lead compensation elements G_{1c}, in addition to the pitch attitude and pitch rate feedback gains. The inverse plant model P^{-1} is unaltered from the previous case; specifically note that the notch and antialias filters are not included in the inverse plant model, since attempts to cancel these elements would restore the attenuation that the filters are intended to generate. The feedforward element transfer function, $H + P^{-1}$ is thus:

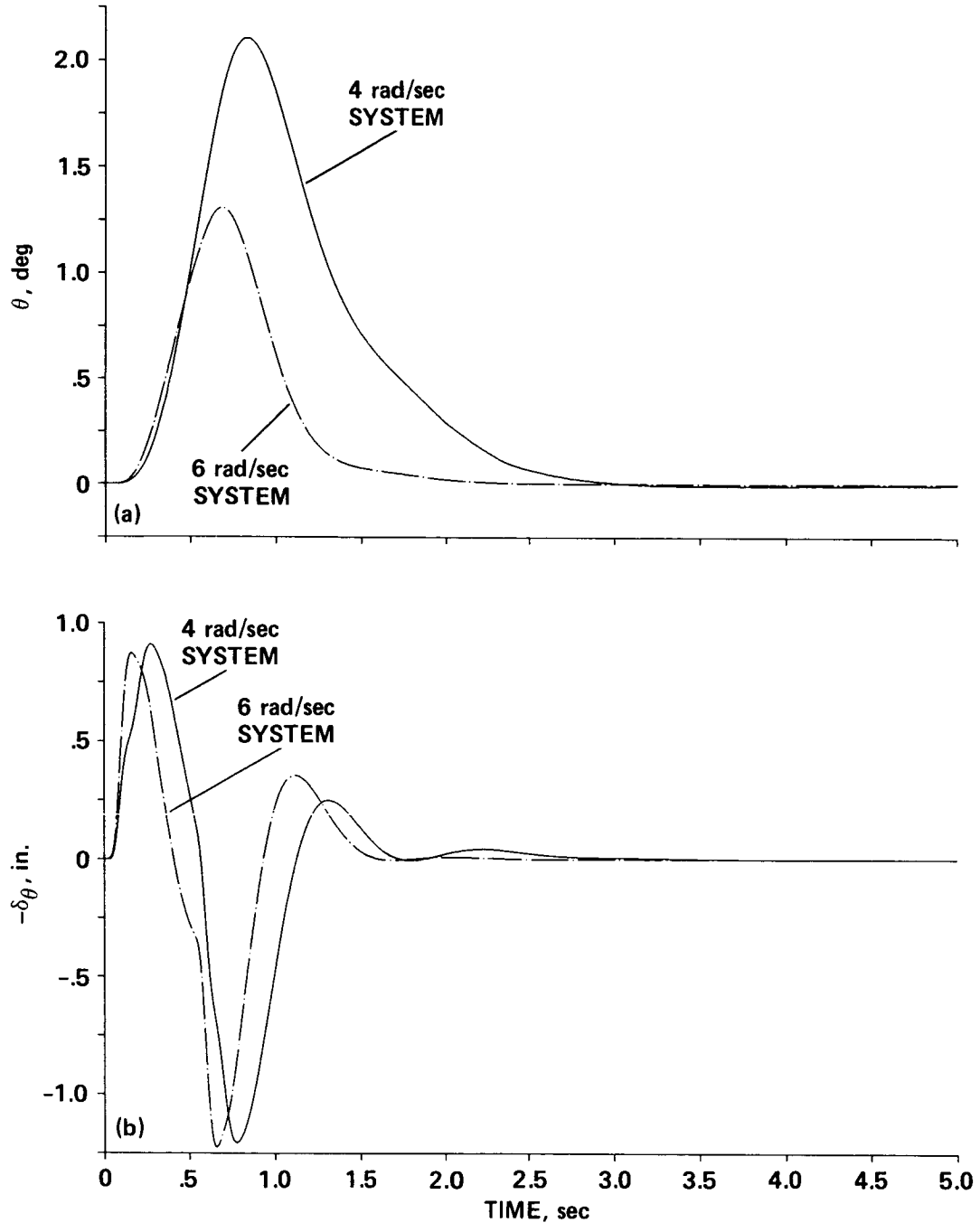

Figure 37.- Response to a pulse disturbance, δ_{c_θ} = 1 in. (a) Pitch attitude response (θ); (b) flapping angle response (δ_θ).

$$\frac{\delta_{c_\theta}}{\theta_m}(s) =$$ (52)

THE NUMERATOR ROOTS ARE:

NO.	REAL	IMAG.	OMEGA	ZETA
1	-1.5423145	-0.99271899	1.8341824	0.84087304
2	-1.5423145	0.99271899	1.8341824	0.84087304
3	-6.9993057	0.00000000E+00		

THE DENOMINATOR ROOTS ARE:

NO.	REAL	IMAG.	OMEGA	ZETA
1	-4.9299998	0.00000000E+00		

LOW-FREQUENCY GAIN = 14.520001

The θ/θ_m transfer function is calculated as before:

$$\frac{\theta}{\theta_m}(s) = \frac{\theta}{\delta_{c_\theta}} \cdot \frac{\delta_{c_\theta}}{\theta_m} =$$ (53)

THE NUMERATOR ROOTS ARE:

NO.	REAL	IMAG.	OMEGA	ZETA
1	-1.5423145	-0.99271899	1.8341824	0.84087304
2	-1.5423145	0.99271899	1.8341824	0.84087304
3	179.64716	-103.71191	207.43495	-0.86604091
4	179.64716	103.71191	207.43495	-0.86604091
5	-0.15991542E-01	0.13430029E-01	0.20882890E-01	0.76577246
6	-0.15991542E-01	-0.13430029E-01	0.20882890E-01	0.76577246
7	-2.7000000	-26.864660	26.999999	0.10000000
8	-2.7000000	26.864660	26.999999	0.10000000
9	-24.000000	-32.000000	40.000000	0.60000000
10	-24.000000	32.000000	40.000000	0.60000000
11	-6.9993057	0.00000000E+00		
12	-14.814814	0.00000000E+00		

THE DENOMINATOR ROOTS ARE:

NO.	REAL	IMAG.	OMEGA	ZETA
1	-1.9309250	-1.0068296	2.1776541	0.88669961
2	-1.9309250	1.0068296	2.1776541	0.88669961
3	-2.9371331	-6.3884296	7.0312719	0.41772429
4	-2.9371331	6.3884296	7.0312719	0.41772429
5	-12.374792	-26.119011	28.902218	0.42816064
6	-12.374792	26.119011	28.902218	0.42816064
7	-32.460335	36.001732	48.474715	0.66963436
8	-32.460335	-36.001732	48.474715	0.66963436
9	-13.685993	-49.806011	51.652155	0.26496461
10	-13.685993	49.806011	51.652155	0.26496461
11	-71.624611	-54.134315	89.780894	0.79777119
12	-71.624611	54.134315	89.780894	0.79777119
13	-179.64716	-103.71191	207.43495	0.86604091
14	-179.64716	103.71191	207.43495	0.86604091
15	0.13033364E-02	0.00000000E+00		
16	-0.37460167E-01	0.00000000E+00		
17	-14.190777	0.00000000E+00		
18	-79.548866	0.00000000E+00		

LOW-FREQUENCY GAIN = -8.9436724

The θ/θ_m frequency response is shown in figure 38.

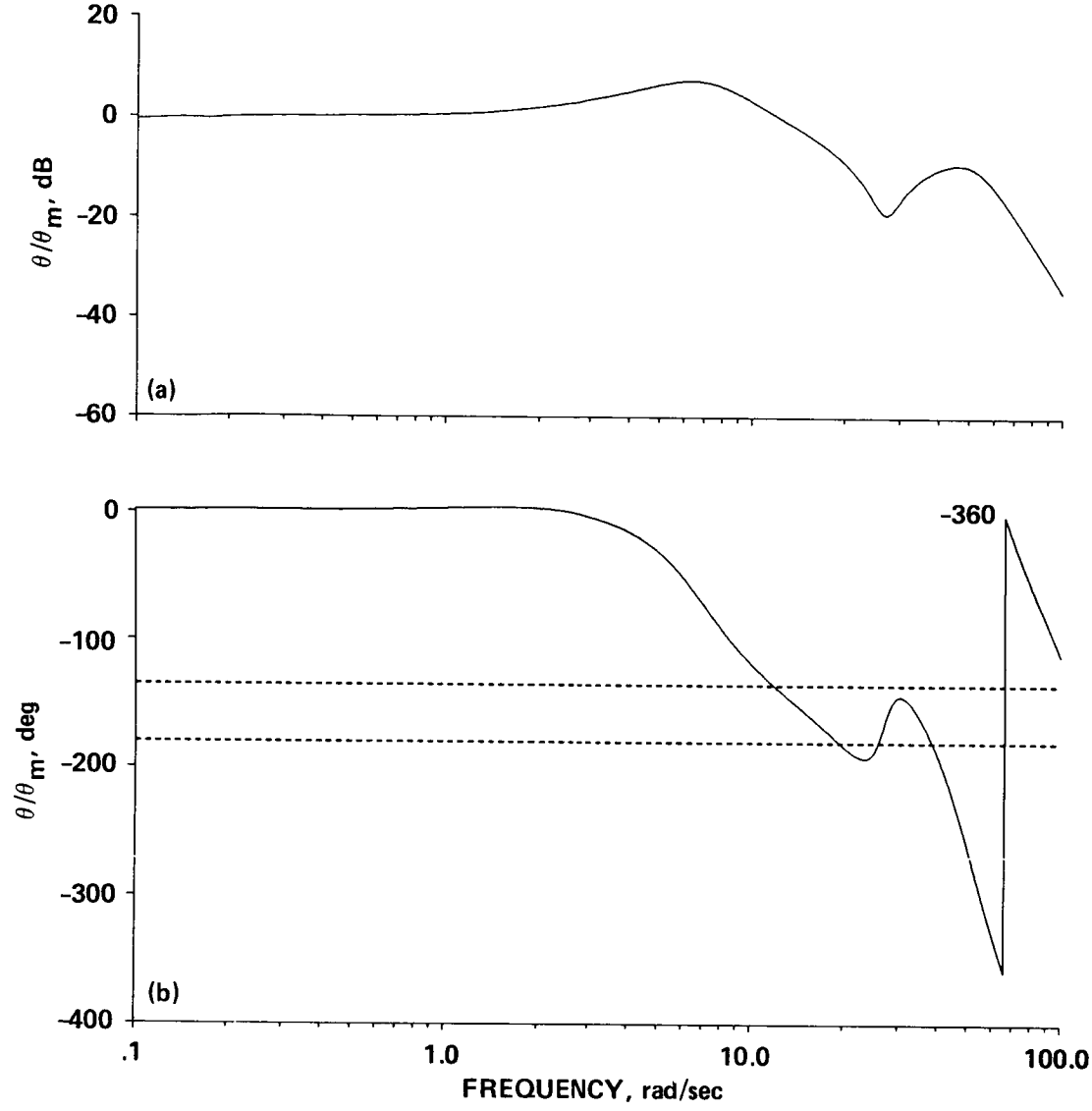

Figure 38.- Frequency response of θ/θ_m for the 4 rad/sec system. (a) Magnitude; (b) phase.

The flat phase characteristic (fig. 38(b)) is maintained out to nearly ω = 3 rad/sec, but a significant amount of magnitude distortion is now apparent (fig. 38(a)). When the command model (eq. (39)), stick filter (eq. (47)), and stick sampling skew ($e^{-sT/2}$) are appended to the system, the total frequency response (θ/δ_s) of figure 39 is obtained. Also plotted in this figure are the frequency responses for the model alone (θ_m/θ_c), and for the nominal (40 Hz, 6 rad/sec) system (fig. 25). The response of the ω_{c_θ} = 4 rad/sec system departs strongly from the desired second-order model in both magnitude and phase.

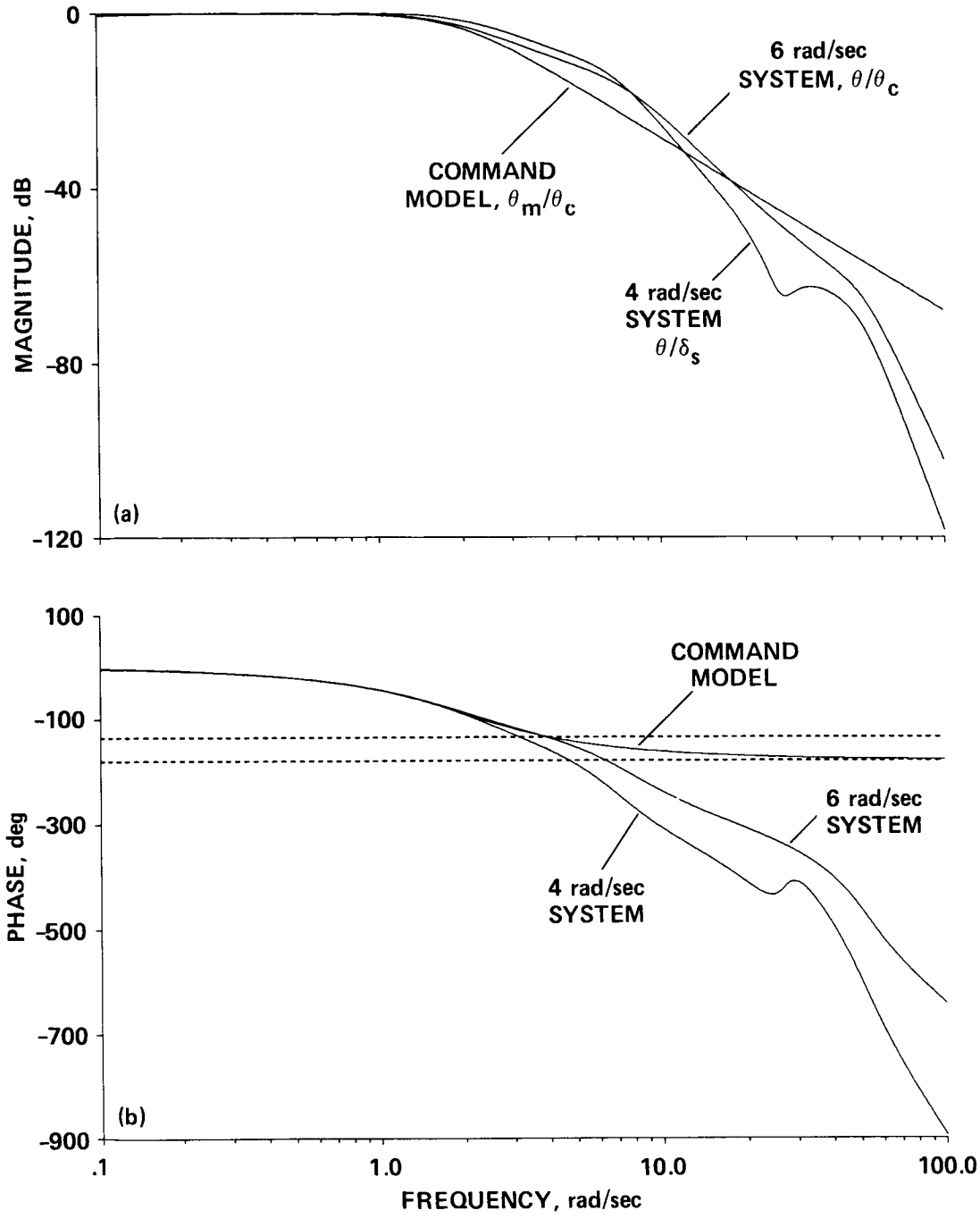

Figure 39.- Overall pitch attitude response (θ/δ_s) for the 4 rad/sec system compared with the response of the 6 rad/sec system and the command model.

The relatively shallow magnitude rolloff of the appended system yields a much poorer gain margin than before; the resulting pitch attitude bandwidth is gain margin limited:

$$\omega_{BW_\theta} = 2.5 \text{ rad/sec}$$
$$\tau_p = 0.217 \text{ sec} \qquad (54)$$

Compared with the nominal system (eq. (41)), the bandwidth has been reduced by 30% and the phase delay has been doubled. Referring to the proposed LHX handling qualities specifications of figure 15, the bandwidth meets the Level II criterion of $\omega_{BW_\theta} = 1.8$ rad/sec, while the phase delay is much greater than the Level II limit $\tau_p = 0.17$ sec. The breakdown of contributions by the various forward loop elements to the total phase delay is summarized in table 2. (The slight discrepancy in total phase delay is due to the effect of the feedback loops.) Clearly, the rotor and filter dynamics are dominating the high level of delay. The stick-skewing and zero-order hold delays are a small fraction of the total value. Notice that the sensor filter (eq. (47)) is not included in table 2, since elements in the feedback path do not substantially contribute to the high-frequency time delay (less than 4 msec by comparing table 2 total with τ_p of eq. (54)).

TABLE 2.- SUMMARY OF PHASE DELAY CONTRIBUTIONS

Element	τ_p, msec
Stick sampling skew	17
Stick prefilter	32
Command block	0
Notch filter	40
Zero-order hold	17
ADOCS actuator	18
Upper boost actuator	13
Rotor	64
Rigid body dynamics	12
	213 msec

The normalized step response for the $\omega_{c_\theta} = 4$ rad/sec system is shown in figure 40 and is compared with the nominal system and the second-order command model. Note the degradation in the command following performance of the 4 rad/sec system. The criteria times for comparison with the proposed LHX specification are obtained from figure 40:

$$t_{R_{10}} = 0.41 \text{ sec}$$

$$t_{R_{50}} = 0.75 \text{ sec} \qquad (55)$$

$$t_{R_{90}} = 1.33 \text{ sec}$$

$$\zeta_e = 0.77 \ (\doteq \text{command model damping ratio})$$

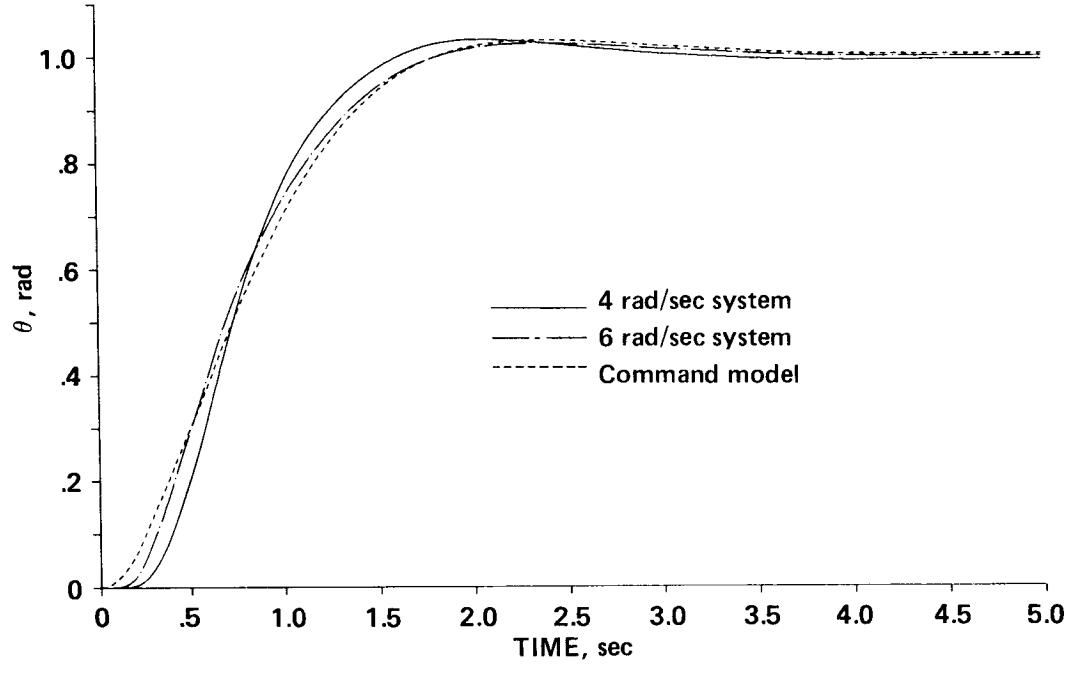

Figure 40.- Normalized step response (θ/δ_s) for the 4 rad/sec (30.3 Hz) system compared with the responses of the 6 rad/sec system and the command model.

A comparison of these results with the proposed Level I and Level II boundaries (fig. 29) shows that, except for the criteria on delay time $t_{R_{10}}$, the time responses are within the Level I requirements. The delay time is just beyond a Level I boundary, and well within the allowable Level II flying qualities. This inconsistency between the time-domain and frequency-domain criteria worsens as the order of the augmented system increases, since the appropriate choice of time-domain parameters for correlating handling qualities becomes extremely configuration sensitive. On the other hand, the frequency-response plot has a broad region over which the phase characteristics are quite linear and well defined as seen in figure 39. Once again, the deficiency of time domain specifications for highly augmented systems is apparent.

The swashplate deflection (δ_{s_θ}) and rate ($\dot{\delta}_{s_\theta}$) responses to a ramp-step input ($\Delta t = 0.5$ sec) for the $\omega_{c_\theta} = 4$ rad/sec system are shown in figure 41(a) and (b)

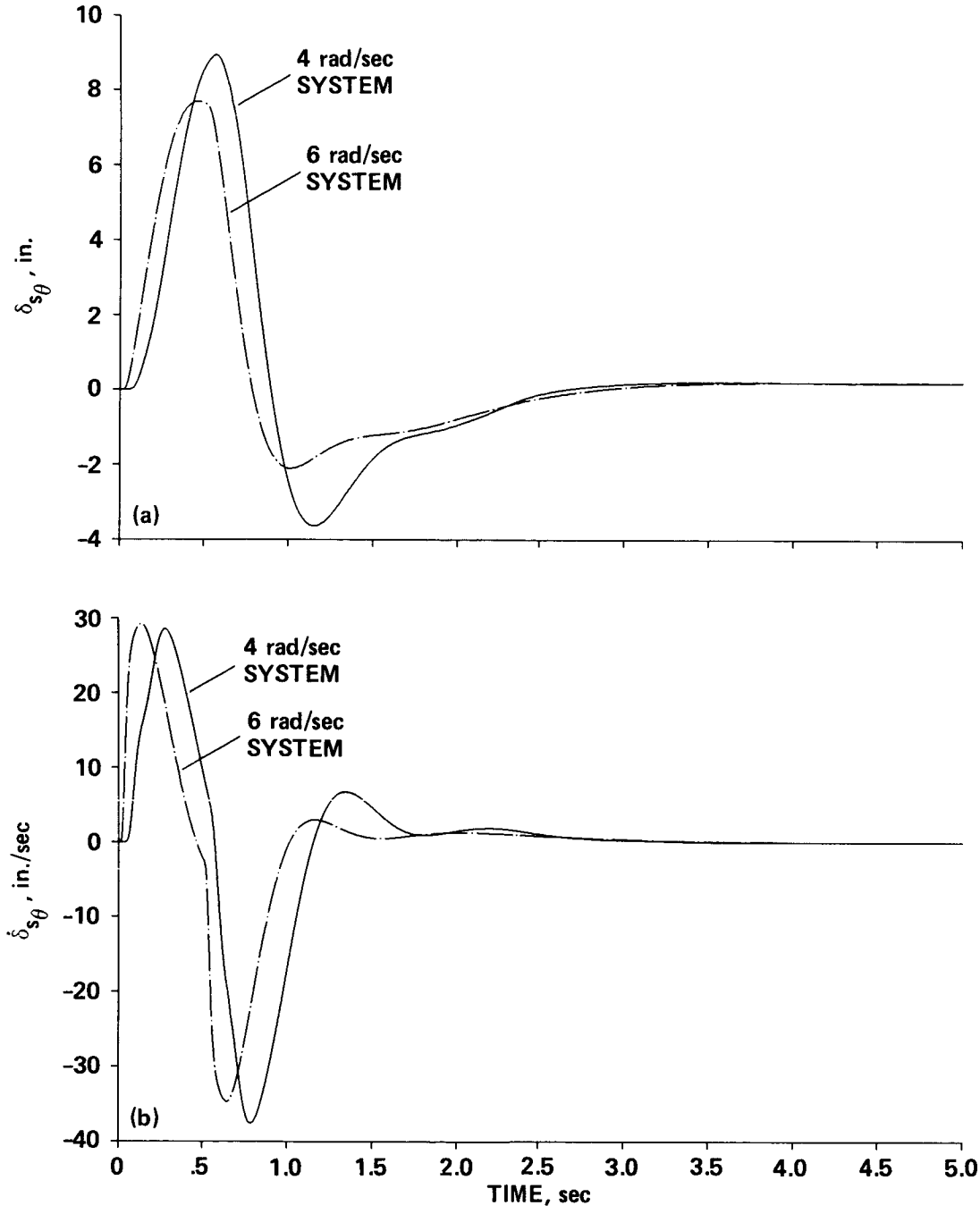

Figure 41.- Comparison of the swashplate response to a ramp-step stick input δ_s, (Δt = 0.5) for the ω_{c_θ} = 4 rad/sec and ω_{c_θ} = 6 rad/sec systems. (a) Swashplate angle (δ_{s_θ}); (b) swashplate rate ($\dot{\delta}_{s_\theta}$); (c) pitch attitude (θ).

along with the analogous results for the nominal (ω_{c_θ} = 6 rad/sec) design. There is a 16% increase in the maximum deflection required (8.9 in. compared with 7.7 in.) and an 11% increase in the maximum surface rate (-37.6 in./sec compared with -34.0 in./sec). The associated pitch attitude (θ) responses for the Δt = 0.5 sec

C-2

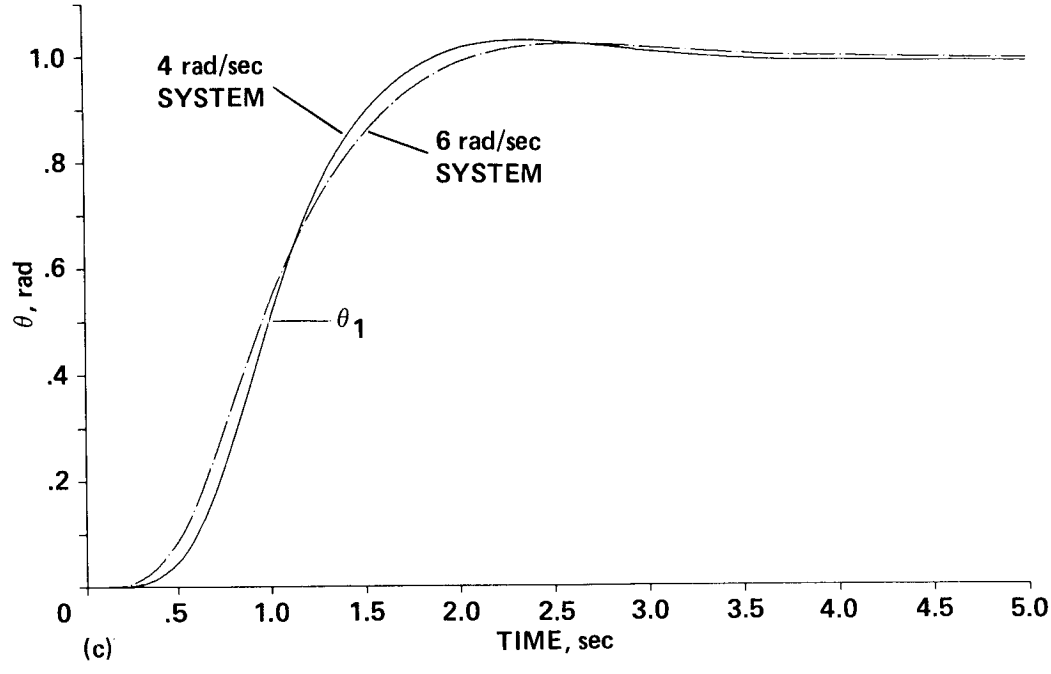

Figure 41.- Concluded.

input are shown in figure 41(c) and indicate a 7% reduction in θ_1 for the 4 rad/sec system (0.5 rad compared with 0.54 rad). The maximum achievable attitude response at 1 sec is calculated as before from θ_1, $(\delta_{s_{\theta\ max}})$, $(\dot{\delta}_{s_{\theta\ max}})$ and the actuator authority limits. As in the 6 rad/sec case, the critical factor is the swashplate maximum rate response compared to its authority. The results of figure 41(b) and (c) give $(\theta_1)_{max}$ = 7.6 deg, which is a 15% reduction in achievable response compared to the 6 rad/sec system, but is still above the θ_1 = 5 deg requirement.

The results of this section show that a number of high-frequency elements which are typically omitted in design, development, and simulation can have significant effects on the attainable performance of the system. Additional increments in phase lag demanded a reduction in the crossover frequency, which led to degradation of the model-following performance of the system. The total phase delay of the appended system is roughly twice as high as that for the nominal system, and is well beyond the suggested Level II boundary of reference 50. Such degradations in "real system" performance compared with the "ideal system" have been widely cited in the literature. Alternate methods are needed for compensating high bandwidth rotorcraft systems with large effective time (phase) delays as in the present case. Finally, reliance on time-domain criteria for specifying the short-term response of high-order, highly augmented systems is not a good approach when viewed in the context of similar fixed-wing experiences. Frequency-domain descriptions are a much more natural format to describe the short-term characteristics of such high-order systems. Time-domain descriptions are still desirable for long term responses.

At this point in the emulation design method, the s-plane design and analysis are complete, including all of the important system elements (except for computational time delay). The final step is to convert the s-plane control laws into z-plane difference equations, using the Tustin transform method.

III.H Digital Control Laws for the $\omega_{c_\theta} = 4$ rad/sec, $\omega_s = 30.3$ Hz Emulation Design

A practical s-plane design for a $\omega_{c_\theta} = 4$ rad/sec system was completed and analyzed in Sections III.F,G. The final step in the emulation design process is to approximate the analog control laws with digital (difference) equations. In this section, the Tustin transform is used to derive z-plane transfer functions for the command block, lead compensation, and notch filter elements. Then the required difference equations are written by inspection. The anti-alias filter must, of course, be implemented in analog hardware.

The conversion from s-plane to z-plane transfer functions using the Tustin transform involves the substitution given in equation (12). For the 30.3 Hz sample rate, the sample period is $T = 0.033$ sec, which yields:

$$s \leftarrow 60.61 \frac{(z - 1)}{(z + 1)} \tag{56}$$

Substituting for s in the command model (eq. (39)) results in the z-plane transfer function:

$$\frac{\theta_m}{\theta_c}(z) = \tag{57}$$

THE NUMERATOR ROOTS ARE:

NO.	REAL	IMAG.	OMEGA	ZETA
1	-1.0000000	0.00000000E+00		
2	-1.0000000	0.00000000E+00		

THE DENOMINATOR ROOTS ARE:

NO.	REAL	IMAG.	OMEGA	ZETA
1	0.95082098	-0.41559331E-01	0.95172881	-0.99904613
2	0.95082098	0.41559331E-01	0.95172881	-0.99904613

Z-PLANE DC GAIN (Z=1) = 1.0000000

This z-plane transfer function can be manipulated to yield a time-domain difference equation using a number of methods. In the ADOCS system, the control equations are implemented in canonical form. In the following direct development, the z-plane transfer functions are inverted directly. The direct method is used to illustrate the relationship between the z-plane and the time domain; but as is pointed out in reference 20, it is not the most desirable inversion method from a numerical accuracy standpoint.

Dividing the numerator and the denominator of equation (57) by the highest power of z (z^2, in this case) yields the following z-plane transfer function expressed in terms of negative powers of z:

$$\frac{\theta_m}{\theta_c}(z) = \frac{(1.0364385E\text{-}03)z^{-2} + (2.0728770E\text{-}03)z^{-1} + (1.0364385E\text{-}03)z^{o}}{(0.9057877)z^{-2} + (-1.901642)z^{-1} + (1.000000)z^{o}} \tag{58}$$

Cross multiply and transpose all the terms except for the zeroth-order term of the model response:

$$\theta_m = (-0.9057877)z^{-2}\theta_m + (1.901642)z^{-1}\theta_m + (1.0364385E\text{-}03)z^{-2}\theta_c + (2.0728770E\text{-}03)z^{-1}\theta_c + (1.0364385E\text{-}03)\theta_c \tag{59}$$

Recognizing that z^{-1} represents a time shift of 1-sample period, and z^{-n} represents a time shift of n-sample periods, the required difference equation can be written by inspection:

$$\theta_m[k] = (-0.9057877)\theta_m[k-2] + (1.901642)\theta_m[k-1] + (1.0364385E\text{-}03)\theta_c[k-2] + (2.0728770E\text{-}03)\theta_c[k-1] + (1.0364385E\text{-}03)\theta_c[k] \tag{60}$$

This equation gives the current response of a model $[\theta_m[k]]$ in terms of previous values of the model $[\theta_m(k-1), \theta_m(k-2)]$, and current and previous values of the model command $[\theta_c(k), \theta_c(k-1), \theta_c(k-2)]$. Since the model output $\theta_m(k)$ depends on the command input at the same time instant $\theta_c(k)$, computation lag (τ_c) will introduce some errors in the expected response. For high sample-rate systems, as in the present case, these effects can easily be analyzed in the s-plane.

Repeating this discretization technique, the difference equations for the feedforward and feedback lead compensation elements (fig. 31) can be similarly obtained:

$$\delta_{c_\theta}[k] = (0.8495575)\delta_{c_\theta}[k-3] + (0.6991150)\delta_{c_\theta}[k-2] + (-1.150442)\delta_{c_\theta}[k-1] + (-8678.438)\theta_m[k-3] + (29197.72)\theta_m[k-2] + (-32627.65)\theta_m[k-1] + (12117.10)\theta_m[k] \tag{61}$$

$$\delta_f[k] = (0.8495575)\delta_f[k-1] + (-1.330522)\delta_{f_i}[k-1] + (1.480806)\delta_{f_i}[k] \tag{62}$$

The last element of the digital control system that needs to be converted is the 1/rev notch filter. Since the filter frequency is much higher than that of the elements considered up until now, the distortion introduced by the Tustin transform is also greater. If the Tustin substitution of equation (56) is used without correction, the center frequency of the resulting digital filter will not be properly located. To avoid this distortion problem, a prewarping technique (refs. 20 and 21)

is used. With this method the notch-filter center-frequency, ω_1 = 27 rad/sec, is shifted to the prewarped center-frequency ω_a:

$$\omega_a = (2/T)\tan(\omega_1 T/2) \tag{63}$$

This results in the adjusted s-plane notch-filter frequency:

$$\omega_a = 28.94 \text{ rad/sec} \tag{64}$$

The Tustin transformation is now applied to the prewarped s-plane transfer function to yield the following z-plane result:

$$G_N(z) = \frac{u^*}{e}(z) = \tag{65}$$

THE NUMERATOR ROOTS ARE:

NO.	REAL	IMAG.	OMEGA	ZETA
1	0.58328360	-0.71795952	0.92503278	-0.63055452
2	0.58328360	0.71795952	0.92503278	-0.63055452

THE DENOMINATOR ROOTS ARE:

NO.	REAL	IMAG.	OMEGA	ZETA
1	0.42863631	-0.42421031	0.60306175	-0.71076687
2	0.42863631	0.42421031	0.60306175	-0.71076687

Z-PLANE DC GAIN (Z=1) = 0.99999993

which, in turn, yields the difference equation:

$$u[k] = (-0.3636835)u[k-2] + (0.8572726)u[k-1] + (0.6288157)e[k-2] + (-0.8572726)e[k-1] + (0.7348677)e[k] \tag{66}$$

If the prewarping technique is not applied, the center-frequency of the digital notch-filter is shifted downward by about 2 rad/sec. When designing by emulation, this prewarping technique should be applied to compensation elements which have modal frequencies of about $\omega_n \geq 0.1\ \omega_s$. Frequency prewarping can be applied in all cases: If the Tustin distortion is small, the prewarping correction will also be small.

With the required difference equations now in hand, the emulation design is complete. At this stage, the performance of the system is usually evaluated using real-time and nonreal-time simulation models. Such models are generally very sophisticated and often include higher-order and nonlinear dynamics. Also included are the effects of quantization in the sampler and zero-order hold, and finite word length. These simulations allow the determination of the actual digital gain and phase margins for comparison with the simplified analog analysis results. Highly sophisticated digital simulations often include "hardware in-the-loop" setups to evaluate the performance of the actuators and failure management systems. When the emulation technique is used for design, such simulations are essential to "tune-up" the digital control laws.

In the next section, the direct digital analysis techniques introduced in Section II are used to analyze the digital response of the 4 rad/sec emulation design.

III.I Digital Analysis of the $\omega_{c_\theta} = 4$ rad/sec, $\omega_s = 30.3$ Hz Emulation Design

In this section, the 4 rad/sec emulation system is analyzed in the digital domain using the z-plane and w-plane techniques of Section II. This analysis exposes the differences between the preceding s-plane results and the exact response of the digital system.

III.I.1 Response at the Even-Sample Instants- Bode plot comparisons between the s-plane and w-plane frequency responses directly show the effects of Tustin conversions and zero-order hold elements on the system response at the even-sample instants. Hybrid frequency responses show the level of sideband amplification in intersample response. Time-domain analyses are useful in exposing the exact responses of the actuator systems at the even-sample instants and during the intersample period. Finally, the effect of adding computational delay is examined.

The direct digital analysis uses the z-plane transfer functions for the equalization elements given in equations (57), (61), (62), (65), and (66) along with the discrete equivalents of the analog elements (actuators, rotor, rigid body dynamics). Thus, the key step is the discretization of the transfer functions between the input to the zero-order hold and the respective analog signals which immediately precede the sampler. Referring to the control system diagram of figure 31, the required transfer functions are from u^* to $\bar{q}^*$ and from u^* to $\bar{\theta}^*$.

The z-plane zero-order hold equivalent G(z) of an s-plane transfer function G(s) is calculated by:

$$G(z) = \frac{z - 1}{z} \mathcal{Z}\left[\frac{G(s)}{s}\right] \tag{67}$$

where the z-transform is computed using partial fraction expansions of the s-plane transfer function within the parentheses (ref. 20).

As an example, the z-plane transfer function of a low-pass continuous element preceded by a zero-order hold is:

$$G(s) = \frac{1}{s + 1} \tag{68}$$

$$G(z) = \frac{z - 1}{z} \mathcal{Z}\left[\frac{1}{s(s + 1)}\right] \tag{69}$$

$$G(z) = \frac{z - 1}{z} \mathcal{Z}\left[\frac{1}{s} - \frac{1}{s + 1}\right] \tag{70}$$

Referring to the z-transform table in reference 20,

$$G(z) = \frac{z - 1}{z}\left(\frac{z}{z - 1} - \frac{z}{z - e^{-T}}\right) \tag{71}$$

For T = 0.1 sec, this becomes:

$$G(z) = \frac{0.09516}{z - 0.9048} \tag{72}$$

The application of this discretization process to figure 31 gives the z-plane transfer functions for the filtered pitch-rate and pitch-attitude responses to inputs at the zero-order hold, u*. Before manipulating the z-plane transfer functions, they are immediately converted to the w-plane (eq. (16)) for improved numerical accuracy in the rest of the analysis. The needed w-plane transfer functions for $(\bar{q}/u)(w)$ and $(\bar{\theta}/u)(w)$ are:

$$\frac{\bar{q}}{u}(w) = \tag{73}$$

THE NUMERATOR ROOTS ARE:

NO.	REAL	IMAG.	OMEGA	ZETA
1	60.884855	-1.2174791	60.897027	-0.99980013
2	60.884855	1.2174791	60.897027	-0.99980013
3	-0.15991543E-01	-0.13430034E-01	0.20882894E-01	0.76577236
4	-0.15991543E-01	0.13430034E-01	0.20882894E-01	0.76577236
5	-14.526635	0.00000000E+00		
6	78.971772	0.00000000E+00		
7	-69.569996	0.00000000E+00		
8	-63.715483	0.00000000E+00		
9	-60.266334	0.00000000E+00		
10	-94.092678	0.00000000E+00		
11	241.61721	0.00000000E+00		
12	-222.70145	0.00000000E+00		
13	0.00000000E+00	0.00000000E+00		

THE DENOMINATOR ROOTS ARE:

NO.	REAL	IMAG.	OMEGA	ZETA
1	-29.174910	-28.940714	41.094286	0.70995053
2	-29.174910	28.940714	41.094286	0.70995053
3	-14.541695	4.2698003	15.155596	0.95949345
4	-14.541695	-4.2698003	15.155596	0.95949345
5	-62.101592	11.723561	63.198494	0.98264355
6	-62.101592	-11.723561	63.198494	0.98264355
7	-0.31263946E-01	-0.21179526	0.21409032	0.14603157
8	-0.31263946E-01	0.21179526	0.21409032	0.14603157
9	-28.979299	-57.336299	64.243684	0.45108402
10	-28.979299	57.336299	64.243684	0.45108402
11	0.90608512E-01	0.00000000E+00		
12	-0.57989066	0.00000000E+00		
13	-51.732669	0.00000000E+00		

LOW-FREQUENCY GAIN = -0.61944474E-01

$\frac{\theta}{u}(w)$ =

THE NUMERATOR ROOTS ARE:

NO.	REAL	IMAG.	OMEGA	ZETA
1	57.888266	26.768010	63.777564	-0.90765878
2	57.888266	-26.768010	63.777564	-0.90765878
3	-53.739649	15.515736	55.934676	0.96075732
4	-53.739649	-15.515736	55.934676	0.96075732
5	-0.15991542E-01	0.13430030E-01	0.20882891E-01	0.76577244
6	-0.15991542E-01	-0.13430030E-01	0.20882891E-01	0.76577244
7	-92.048744	63.127705	111.61576	0.82469305
8	-92.048744	-63.127705	111.61576	0.82469305
9	45.802112	0.00000000E+00		
10	-14.524550	0.00000000E+00		
11	-53.659084	0.00000000E+00		
12	253.11050	0.00000000E+00		
13	721.22230	0.00000000E+00		

THE DENOMINATOR ROOTS ARE:

NO.	REAL	IMAG.	OMEGA	ZETA
1	-29.174910	-28.940714	41.094286	0.70995053
2	-29.174910	28.940714	41.094286	0.70995053
3	-14.541695	4.2698003	15.155596	0.95949345
4	-14.541695	-4.2698003	15.155596	0.95949345
5	-62.101592	11.723561	63.198494	0.98264355
6	-62.101592	-11.723561	63.198494	0.98264355
7	-0.31263946E-01	-0.21179526	0.21409032	0.14603157
8	-0.31263946E-01	0.21179526	0.21409032	0.14603157
9	-28.979299	-57.336299	64.243684	0.45108402
10	-28.979299	57.336299	64.243684	0.45108402
11	0.90608512E-01	0.00000000E+00		
12	-0.57989066	0.00000000E+00		
13	-51.732669	0.00000000E+00		

LOW-FREQUENCY GAIN = -0.61944455E-01

(74)

Similarly, the z-plane control law transfer functions (eqs. (58), (61), (62), and (65)) are also converted to the w-plane:

$\frac{\delta_{c_\theta}}{\theta_m}(w)$ =

THE NUMERATOR ROOTS ARE:

NO.	REAL	IMAG.	OMEGA	ZETA
1	-1.5422562	-0.99267616	1.8341102	0.84087435
2	-1.5422562	0.99267616	1.8341102	0.84087435
3	-6.9987147	0.00000000E+00		

THE DENOMINATOR ROOTS ARE:

NO.	REAL	IMAG.	OMEGA	ZETA
1	-4.9296797	0.00000000E+00		

LOW-FREQUENCY GAIN = 14.520462

(75)

$$\frac{\theta_m}{\theta_c}(w) =$$ (76)

THE NUMERATOR ROOTS ARE:
THERE ARE NO ROOTS

THE DENOMINATOR ROOTS ARE:

NO.	REAL	IMAG.	OMEGA	ZETA
1	-1.4996561	-1.3230697	1.9998704	0.74987664
2	-1.4996561	1.3230697	1.9998704	0.74987664

LOW-FREQUENCY GAIN = 1.0000001

$$G_N(w) =$$ (77)

THE NUMERATOR ROOTS ARE:

NO.	REAL	IMAG.	OMEGA	ZETA
1	-2.8939760	-28.794874	28.939936	0.99999392E-01
2	-2.8939760	28.794874	28.939936	0.99999392E-01

THE DENOMINATOR ROOTS ARE:

NO.	REAL	IMAG.	OMEGA	ZETA
1	-17.363979	-23.151936	28.939936	0.60000061
2	-17.363979	23.151936	28.939936	0.60000061

LOW-FREQUENCY GAIN = 0.99999993

Comparing equations (73)-(77) with equations (24)-(28) (combined), (37), (39), and (48) shows that the numerical values of the w-plane and s-plane transfer function poles and zeroes are very close for the lower frequency modes, with larger differences at mid- and high-frequency. The numerical similarity of the w- and s-plane modes is very helpful in reducing the risk of computational error in the digital analysis. Since each s-plane pole and zero has a numerically similar w-plane counterpart, gross errors are quickly exposed. The additional w-plane (nonminimum phase) zeroes in the rigid body responses (eqs. (73) and (74)) are associated with the zero-order hold element. In contrast, the z-plane poles are tightly clustered around the unit circle and numerical equivalences between s- and z-plane roots cannot be easily anticipated.

The $j\omega$ digital frequency response (versus actual frequency) for each of the digital compensation elements (command model, feed forward, lead equalization, and notch filter) was calculated and compared with its s-plane counterpart (Section III.F). The digital and analog responses are indistinguishable for all the elements except for the notch filter. As is shown in figure 42, the Tustin transformation with prewarping closely preserves the magnitude characteristics of the filter but not its phase characteristics above 40 rad/sec. In the present case, the digital system has a phase lag of nearly 20 deg greater than the analog system at a frequency of 100 rad/sec. Associated discrepancies in the stability margins and closed-loop damping ratios of the mid- and high-frequency modes can be expected. When slightly damped structural modes (such as pylon or wing bending modes) are present along with computational delays, the phase distortion as in figure 42 can lead to significant errors in the emulation-based estimate of digital system gain and phase margins as shown in Section III.I.4.

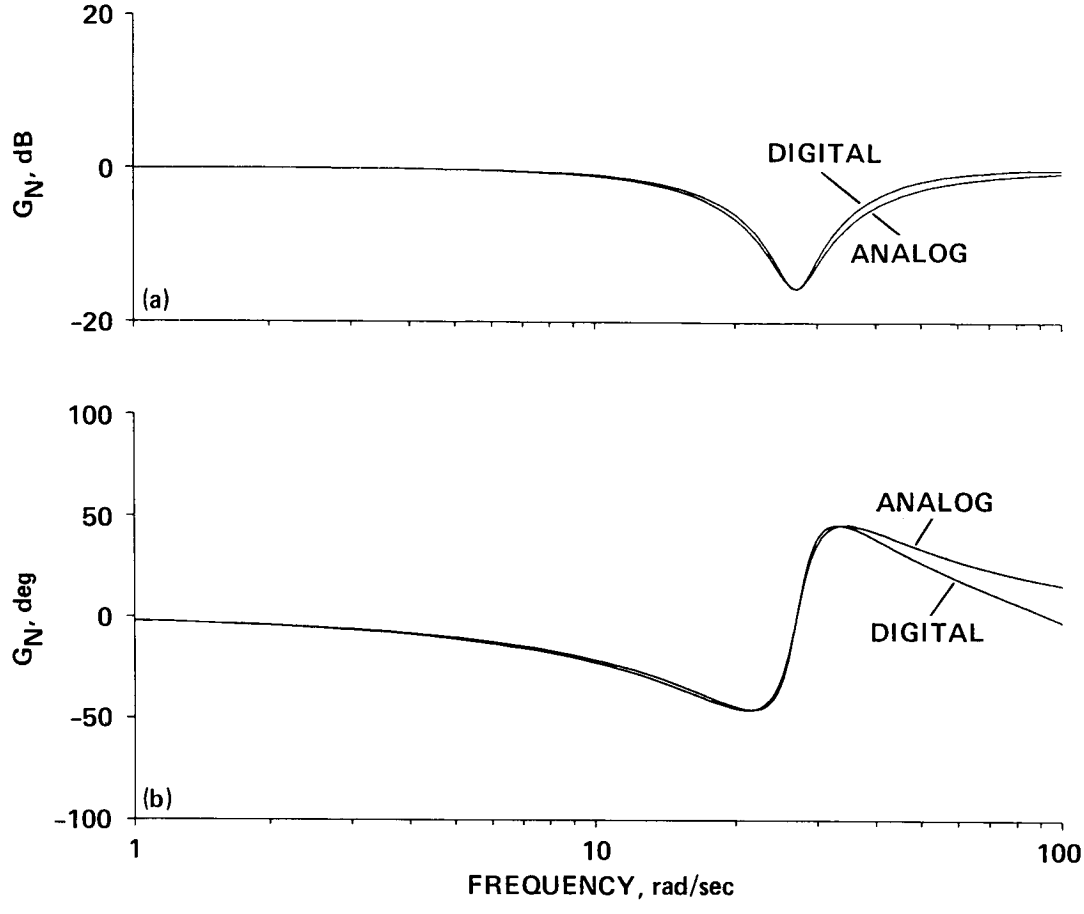

Figure 42.- Analog and digital notch filter responses. (a) Magnitude; (b) phase.

The equalized transfer function for the stabilization loop (δ_f^*/e, fig. 31) is obtained using transfer function arithmetic in the w-plane:

$$\frac{\delta_f^*}{e}(w) =$$ (78)

THE NUMERATOR ROOTS ARE:

NO.	REAL	IMAG.	OMEGA	ZETA
1	-67.677399	-10.872247	68.545139	0.98734060
2	-67.677399	10.872247	68.545139	0.98734060
3	-0.16011344E-01	0.13413453E-01	0.20887410E-01	0.76655481
4	-0.16011344E-01	-0.13413453E-01	0.20887410E-01	0.76655481
5	-2.8939760	-28.794874	28.939936	0.99999392E-01
6	-2.8939760	28.794874	28.939936	0.99999392E-01
7	-3.2397878	0.00000000E+00		
8	57.196293	0.00000000E+00		
9	69.726517	0.00000000E+00		
10	-1.5870633	0.00000000E+00		
11	-14.527479	0.00000000E+00		
12	72.732826	0.00000000E+00		
13	-54.760460	0.00000000E+00		
14	-98.288071	0.00000000E+00		
15	242.21391	0.00000000E+00		
16	-224.03806	0.00000000E+00		

THE DENOMINATOR ROOTS ARE:

NO.	REAL	IMAG.	OMEGA	ZETA
1	-29.174885	-28.940725	41.094276	0.70995009
2	-29.174885	28.940725	41.094276	0.70995009
3	-14.541688	4.2698035	15.155590	0.95949335
4	-14.541688	-4.2698035	15.155590	0.95949335
5	-62.101601	-11.723643	63.198518	0.98264331
6	-62.101601	11.723643	63.198518	0.98264331
7	-0.31264544E-01	-0.21185417	0.21414869	0.14599456
8	-0.31264544E-01	0.21185417	0.21414869	0.14599456
9	-28.979311	-57.336304	64.243694	0.45108413
10	-28.979311	57.336304	64.243694	0.45108413
11	-17.363979	-23.151936	28.939936	0.60000061
12	-17.363979	23.151936	28.939936	0.60000061
13	-4.9296803	0.00000000E+00		
14	0.90607889E-01	0.00000000E+00		
15	-0.57989144	0.00000000E+00		
16	-51.732666	0.00000000E+00		

LOW-FREQUENCY GAIN = -0.89847779

The δ_f^*/e response is plotted versus actual frequency in figure 43, for the frequency range of $0.1 \leq \omega \leq \omega_s$. In the frequency range $\omega_{Nyq} \leq \omega \leq \omega_s$, the input sinusoid is aliased to $\omega - \omega_s$. Thus the magnitude response is a mirror image with respect to the Nyquist frequency (ω_{Nyq}); the phase response is an antisymmetric image because the negative alias frequency changes the sign of the phase angle. Beyond the sampling frequency (ω_s) the magnitude and phase responses repeat (starting from $\omega = 0$) in a cyclic fashion. Also shown here is the s-plane response repeated from figure 30 (but with $K_\theta = 14.52$ included in the magnitude response this time). The digital and analog frequency characteristics (including the crossover frequency, stability margins, and phase delay) are seen to be identical up to a frequency of $\omega = 40$ rad/sec. Beyond this value, the distortion caused by the notch filter becomes apparent, although it appears very small because of the plotting scales which are used for this wideband figure. Clearly, the overall pitch response of the digital system is adequately modeled using s-plane analysis techniques.

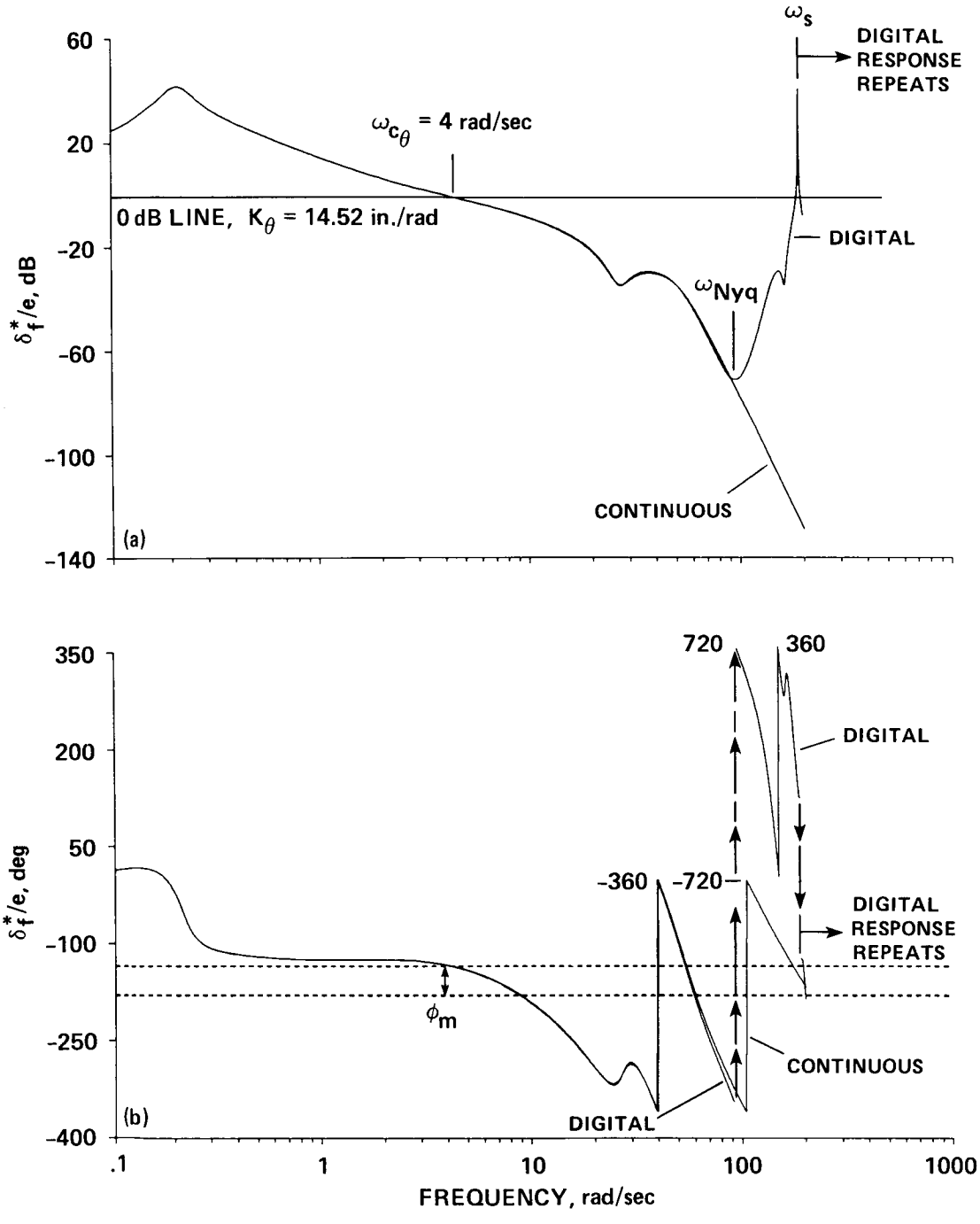

Figure 43.- Equalized open-loop frequency response of δ_f/e for the 30.3 Hz digital and continuous systems. (a) Magnitude; (b) phase.

The closed-loop pitch-attitude response of θ/δ_{c_θ} is:

$$\frac{\theta}{\delta_{c_\theta}}(w) = \qquad (79)$$

THE NUMERATOR ROOTS ARE:

NO.	REAL	IMAG.	OMEGA	ZETA
1	-2.8939760	-28.794874	28.939936	0.99999392E-01
2	-2.8939760	28.794874	28.939936	0.99999392E-01
3	-29.174885	-28.940725	41.094276	0.70995009
4	-29.174885	28.940725	41.094276	0.70995009
5	-0.16008502E-01	0.13416393E-01	0.20887119E-01	0.76642940
6	-0.16008502E-01	-0.13416393E-01	0.20887119E-01	0.76642940
7	74.666145	21.430130	77.680652	-0.96119359
8	74.666145	-21.430130	77.680652	-0.96119359
9	-116.22800	26.612307	119.23575	0.97477481
10	-116.22800	-26.612307	119.23575	0.97477481
11	-53.080788	11.840668	54.385397	0.97601177
12	-53.080788	-11.840668	54.385397	0.97601177
13	-4.9296803	0.00000000E+00		
14	51.248173	0.00000000E+00		
15	-14.530321	0.00000000E+00		
16	2762.7004	0.00000000E+00		

THE DENOMINATOR ROOTS ARE:

NO.	REAL	IMAG.	OMEGA	ZETA
1	-1.9212861	-1.0091232	2.1701774	0.88531293
2	-1.9212861	1.0091232	2.1701774	0.88531293
3	-3.0554237	-6.4664707	7.1519828	0.42721352
4	-3.0554237	6.4664707	7.1519828	0.42721352
5	-39.488152	30.114729	49.660961	0.79515481
6	-39.488152	-30.114729	49.660961	0.79515481
7	-13.659637	-27.413446	30.628136	0.44598330
8	-13.659637	27.413446	30.628136	0.44598330
9	-62.320236	11.473867	63.367669	0.98347055
10	-62.320236	-11.473867	63.367669	0.98347055
11	-27.112633	58.405384	64.391643	0.42105825
12	-27.112633	-58.405384	64.391643	0.42105825
13	0.13155873E-02	0.00000000E+00		
14	-0.37520643E-01	0.00000000E+00		
15	-52.396923	0.00000000E+00		
16	-13.916929	0.00000000E+00		

LOW-FREQUENCY GAIN = -0.61015987

Once again the low-frequency closed-loop roots in the w-plane are numerically close to the associated s-plane values (compare eqs. (79) and (35)); so gross numerical errors have been avoided.

An exact comparison of the closed-loop digital modes with the closed-loop analog modes is obtained by converting the digital roots back to the s-plane, through the inverses of transformation equations (17) and (15). This process yields the "image s-plane" pole locations, which indicate the response of the digital system in terms of s-plane parameters. The image s-plane poles corresponding to equation (79) yields the results presented in table 3. These are compared with the closed-loop s-plane results of equation (51). This comparison is an indication of the level of accuracy of the emulation approximation. The results of table 3 show that the dominant low-frequency modes are very accurately predicted, with only a slight underestimation of the closed-loop pitch/rotor mode frequency (ω'_{sp}). The rotor, actuator, and high-frequency filter closed-loop modes are also accurately

TABLE 3.- COMPARISON OF IMAGE S-PLANE DIGITAL POLES WITH EMULATION ANALYSIS POLES OF θ/δ_{c_θ}, ω_s = 30.3 Hz

Root no.	Digital analysis equivalent s-plane denominator roots		Emulation analysis roots		
	Omega	Zeta	Omega	Zeta	
1	2.1707037	0.88514914	2.1776541	0.88669961	
2	2.1707037	.88514914	2.1776541	.88669961	
3	7.1308960	.42399324	7.0312719	.41772429	
4	7.1308960	.42399324	7.0312719	.41772429	
5	29.056019	.39194133	28.902218	.42816064	
6	29.056019	.39194133	28.902218	.42816064	
7	49.395633	.64074464	48.474715	.66963436	
8	49.395633	.64074464	48.474715	.66963436	
9	51.446185	.26390626	51.652155	.26496461	
10	51.446185	.26390626	51.652155	.26496461	
11	90.282137	.79374504	89.780894	.79777119	
12	90.282137	.79374504	89.780894	.79777119	
13			207.43495	.86604091	Padé roots for
14			207.43495	.86604091	zero-order hold
	Real		Real		
15	0.13155873E-02		0.13033364E-02		
16	-.37520648E-01		-.37460167E-01		
17	-14.169584		-14.190777		
18	-79.459586		-79.548866		

predicted. However, the closed-loop mode associated with the notch filter dynamics has a damping ratio which is overestimated by 10% in the s-plane analysis. This

error is associated with the phase response discrepancy seen in figure 42. Again, the need to accurately analyze the digital system response is emphasized.

While there is some discrepancy in the closed-loop notch filter mode, the closed-loop pitch response (θ/δ_{c_θ}) is very accurately predicted from the emulation analysis. The frequency response of θ/δ_{c_θ} is shown for both the digital and emulation analyses in figure 44. Once again, the responses are nearly identical up

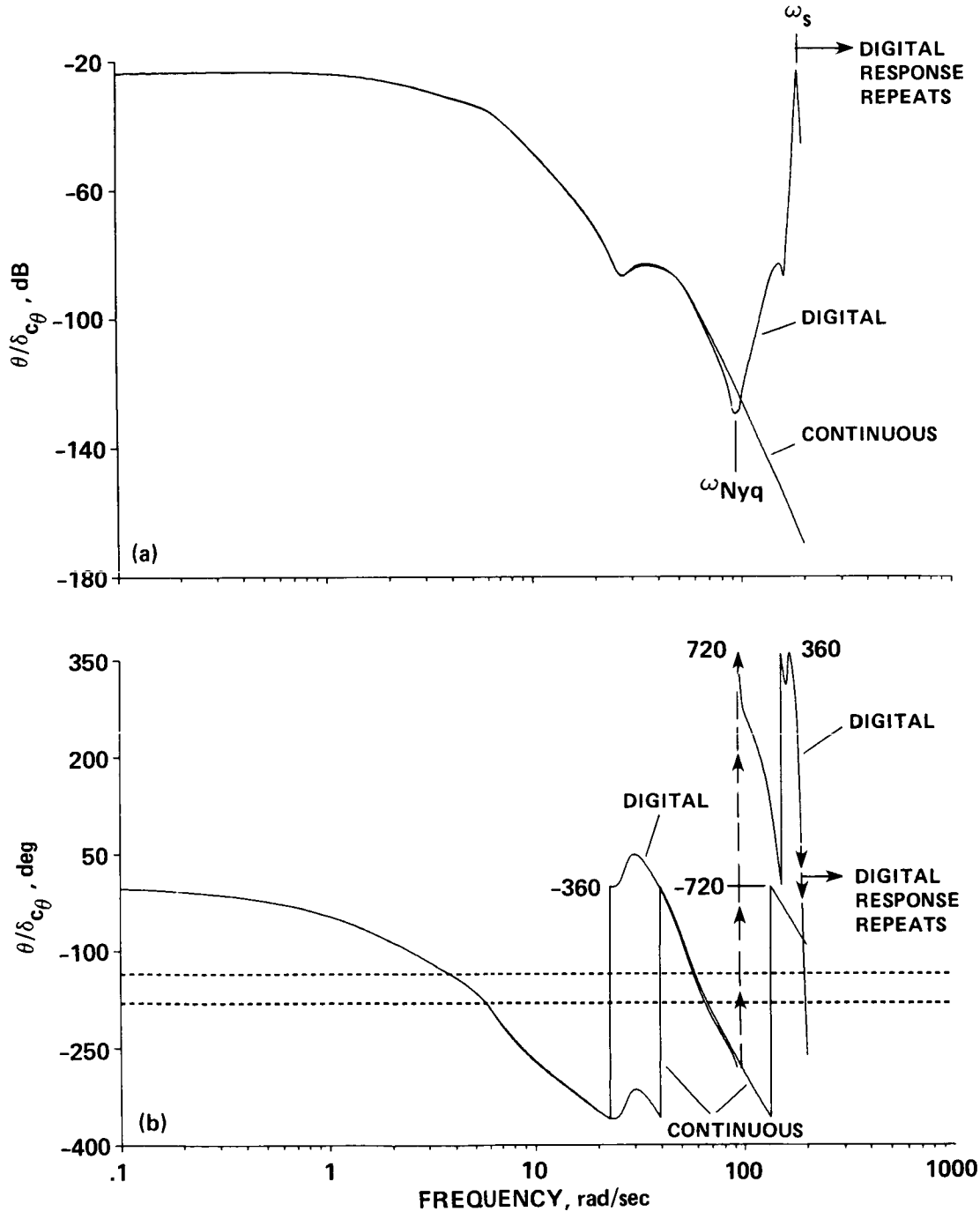

Figure 44.- Closed-loop pitch attitude response (θ/δ_s) for the 30.3 Hz digital and continuous systems. (a) Magnitude; (b) phase.

to ω = 40 rad/sec, and do not differ greatly until the Nyquist frequency (ω_{Nyq} = 95.2 rad/sec) is approached. The overall output response of the closed-loop stabilization system is accurately modeled by the emulation technique.

Since the frequency responses of the command model and feedforward functions are identical in the s- and z-planes, the overall pitch response to stick inputs (θ/δ_s) is essentially identical to that shown in figure 39. Comparisons with figures 40 and 41 show that emulation and exact overall step responses of pitch attitude for the 30.3 Hz are also identical. Therefore, the overall frequency and time-domain handling qualities parameters for the emulation and digital analyses are the same (i.e., ω_{BW_θ}, τ_p, $t_{R_{10}}$, $t_{R_{50}}$, $t_{R_{90}}$). The important conclusion can be drawn that for calculating the overall response of the digital system for performance and handling qualities considerations, the emulation technique is certainly satisfactory for this example. The phase discrepancy associated with the Tustin transformation of the notch filter suggests that the digital response of the higher frequency elements must be analyzed more accurately.

III.I.2 Intersample Response- The digital analysis presented thus far reflects the response of the system at the even sample instants only. No information has been obtained concerning the intersample response of the actuators and other analog elements. To assess this intersample behavior in the frequency domain, the hybrid frequency technique is used. Referring to figure 31, each succeeding analog element (actuator, rotor, rigid body system, filter) acts as a low-pass filter, progressively suppressing the sidebands of the preceding signal. Thus, the most extreme effects of the sidebands will be felt by the analog elements which are closest to the zero-order hold--that is, the ADOCS and upper-boost actuators. The signal which is most sensitive to the sidebands is the ADOCS actuator rate ($\dot{\delta}_{A_\theta}$).

The hybrid frequency response for the ADOCS actuator rate ($\dot{\delta}_{A_\theta}/\delta_{c_\theta}$) shown in figure 45 is determined from the evaluation of (ref. 17):

$$\frac{\dot{\delta}_{A_\theta}}{\delta_{c_\theta}}(s,w) = \left[\left(\frac{G_{zoh}(s)}{T}\,\frac{\dot{\delta}_{A_\theta}}{u}(s)\right)\Bigg|_{s=j\omega}\right]\left[\frac{u}{\delta_{c_\theta}}(w)\Bigg|_{w=\frac{2}{T}\frac{(e^{j\omega T}-1)}{(e^{j\omega T}+1)}}\right] \tag{80}$$

where

$G_{zoh}(s)$ is given in equation (13)

$\frac{\dot{\delta}_{A_\theta}}{u}(s) = s\,\frac{89^2}{[0.8,\ 89]}$, from equation (28)

$\frac{u}{\delta_{c_\theta}}(w)$ is obtained from figure 31 using block diagram algebra

The <u>total</u> continuous (analog) $\dot{\delta}_{A_\theta}$ time response due to a digital sinusoidal input at δ_{c_θ} with a frequency $\omega_{in} < \omega_{Nyq}$ is obtained by <u>summing</u> sine waves of

frequencies $\omega = \omega_{in}$, and of all succeeding positive and negative aliases, $\omega_{in} + \omega_s$, $\omega_{in} - \omega_s$, $\omega_{in} + 2\omega_s$, ..., each with the appropriate magnitude ratio and phase angle as obtained from figure 45. The hybrid response in the "primary strip" $\omega_{in} < \omega_{Nyq}$ will approach the digital frequency response $(\dot{\delta}_{A_\theta}/\delta_{c_\theta})(w)$ when the sideband contribution to the total analog response is small (e.g., for large relative sample rates); then, the corresponding intersample ripple will also be small, and the digital response at the even sample instants is a good indicator of the continuous system behavior.

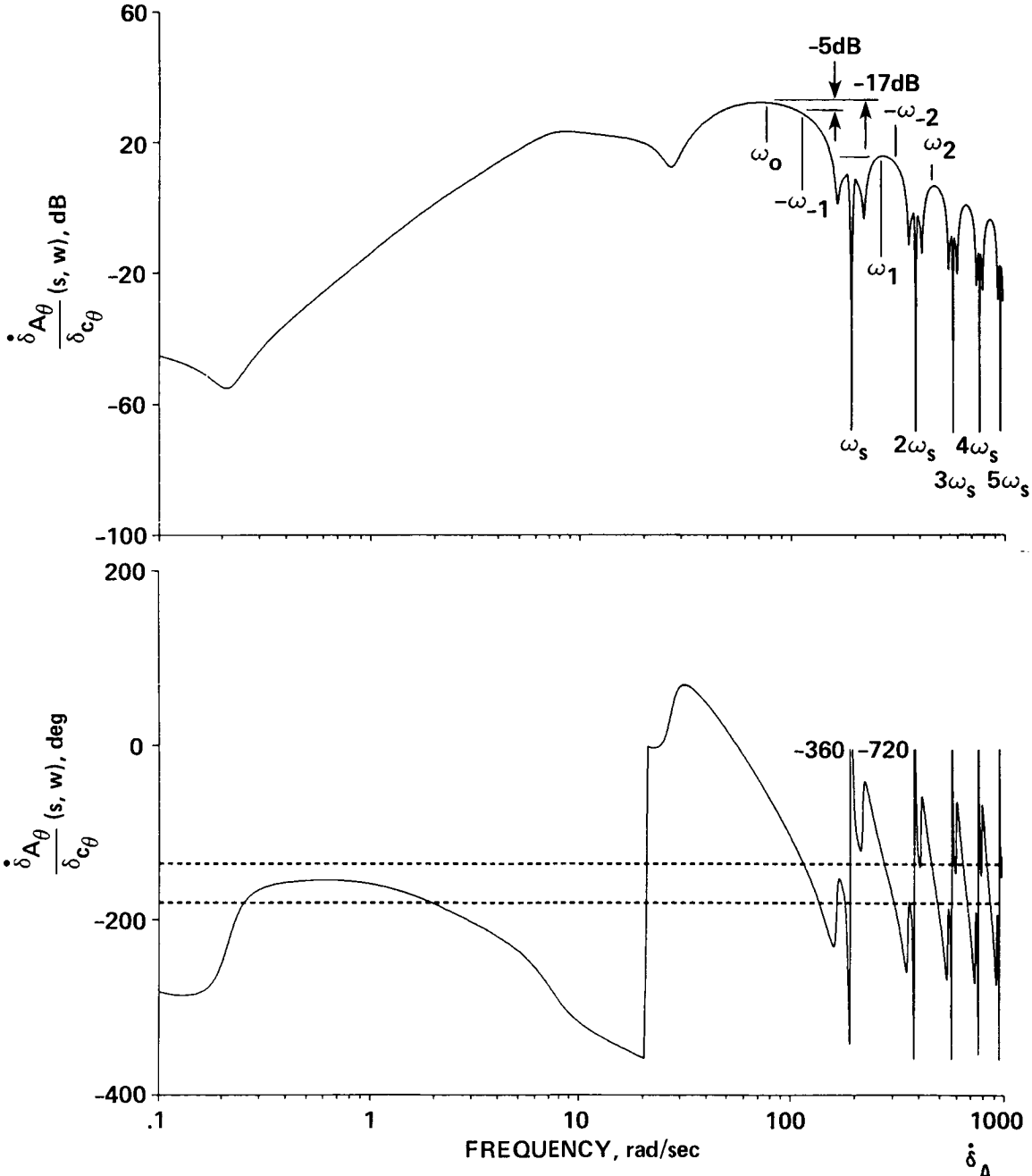

Figure 45.- Hybrid frequency response of the ADOCS actuator rate, $\frac{\dot{\delta}_{A_\theta}}{\delta_{c_\theta}}(s,w)$ (a) Magnitude; (b) phase.

Figure 45 shows that (in the primary strip), the maximum $\dot{\delta}_{A_\theta}$ response occurs at input frequencies of ω_o = 73 rad/sec, which is near the ADOCS actuator open-loop natural frequency of ω_a = 89 rad/sec. The contribution of the sidebands to the total response of the actuator rate at this frequency is obtained from the hybrid response at the positive aliases, ω_1 = 263 rad/sec, ω_2 = 453 rad/sec, etc., and the negative aliases, ω_{-1} = -117 rad/sec, ω_{-2} = -308 rad/sec, etc. From the figure, it is clear that the dominant sideband contribution occurs at the first aliases, ω_1 and ω_{-1}. Each succeedding sideband adds a smaller contribution. A rough measure of the total contribution of all of the sidebands to the overall response at the basic frequency is obtained from the magnitude ratio of the largest sideband response to that at the dominant response frequency. In this case, the maximum sideband response is at ω_{-1}, with an associated magnitude ratio (read from fig. 45 at $-\omega_{-1}$ = 117 rad/sec) of -5 dB. An appreciation for this relatively high level of sideband power will be more apparent when the associated time-domain responses are obtained. For now, it is sufficient to monitor the sideband ratio for each succeeding analog signal. For example, the hybrid magnitude response of the position signal of the ADOCS actuator δ_{A_θ} is shown in figure 46. For this signal the dominant frequency corresponds to the closed-loop coupled rotor/pitch mode at $\omega_o = \omega'_{sp}$ = 7 rad/sec. The first aliases of this frequency are at ω_1 = 197 rad/sec and ω_{-1} = -183 rad/sec, with an associated maximum sideband magnitude ratio at ω_{-1} of -41 dB. Thus, it can be expected that the intersample response of the actuator deflection will be much smaller than that associated with the actuator rate. By the time the analog signal reaches the pitch attitude response, the digital sidebands are almost entirely suppressed, as shown in figure 47. The dominant pitch response (the 3 dB down point, in this case) occurs as expected at roughly the open-loop frequency of $\omega_o = \omega_{c_\theta}$ = 4 rad/sec; the first aliases occur at ω_1 = 194 rad/sec and ω_{-1} = -186 rad/sec with an associated magnitude drop at ω_{-1} of nearly -165 dB. Therefore, the intersample ripple of the attitude response should be negligible. The consistent frequency domain result is that the hybrid response $(\theta/\delta_{c_\theta})(s,w)$ and the digital response $(\theta/\delta_{c_\theta})(w)$ are essentially identical in the primary strip, $\omega < \omega_{Nyq}$.

Further appreciation for the physical interpretation of the hybrid frequency responses can be gained from the associated time response behavior in between the even sample instants. These time responses can be generated using the advanced z-transform technique as described in Section II.C.4. The direct inversion expansion of the z-plane closed-loop transfer function coefficients as is used in LCAP2 to obtain digital system time responses is very sensitive to numerical accuracy. Accurate step responses of the high frequency elements can often only be obtained for the first 0.3-0.5 sec of the time history. Beyond this point, the numerical precision breaks down, and the time response cannot be determined by the direct method. The time responses should be simulated with more exact and numerically stable methods.

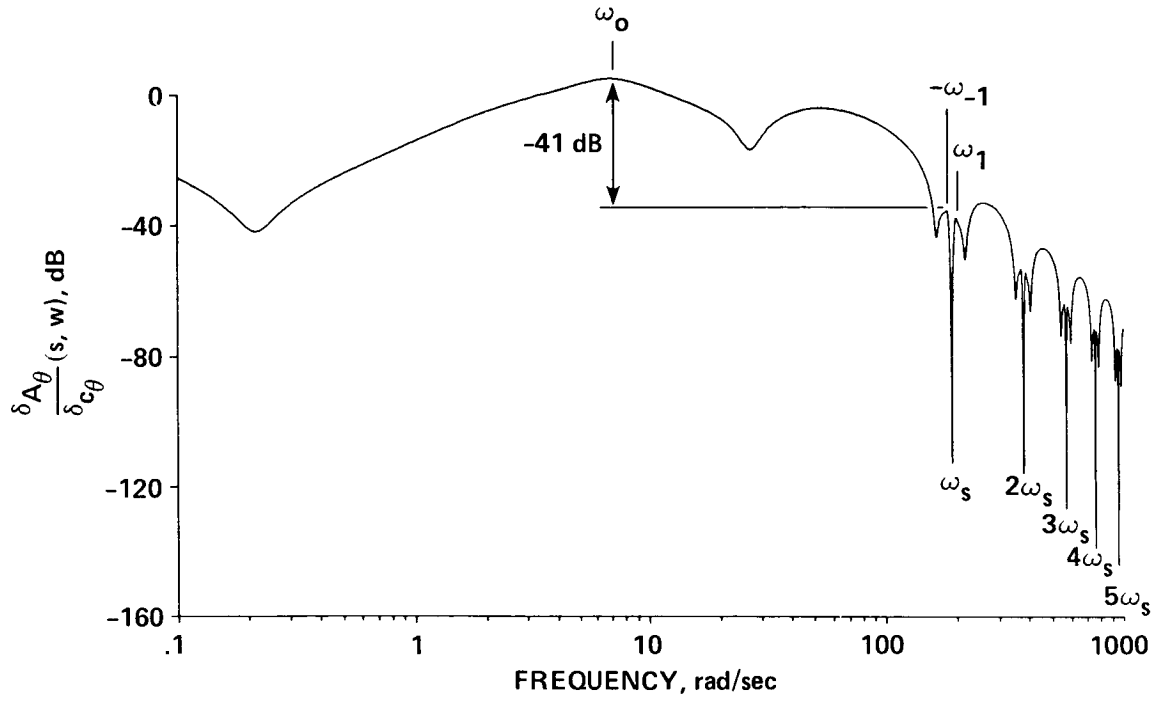

Figure 46.- Hybrid frequency response (magnitude) of the ADOCS actuator deflection, $\frac{\delta A_\theta}{\delta c_\theta}(s,w)$.

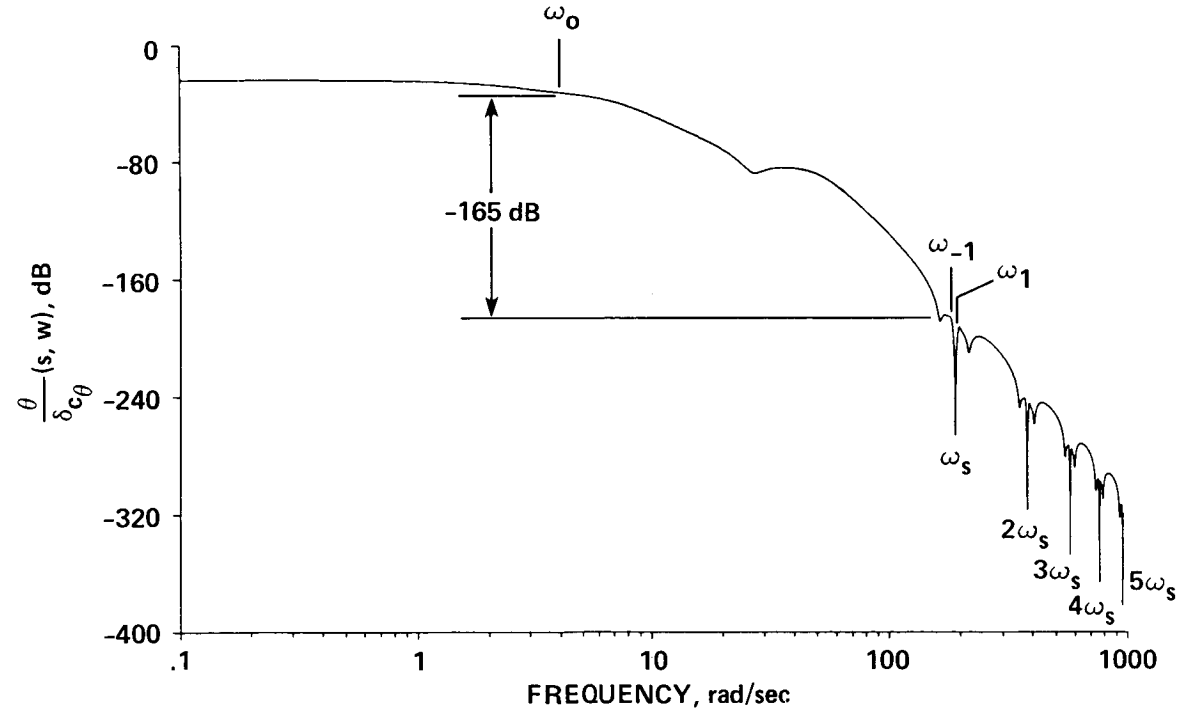

Figure 47.- Hybrid frequency response (magnitude) of pitch attitude, $\frac{\theta}{\delta c_\theta}(s,w)$.

The digital step response of the ADOCS actuator rate signal ($\dot{\delta}_{A_\theta}$) to a step input of $\delta_{c_\theta} = 1$ is shown for a 1/2 sec time duration in figure 48(a). The intersample response at 3 points within the even frame is shown in the figure. Also shown is the analog result obtained from the s-plane emulation analysis.[5] The s-plane response roughly follows the exact digital response including the intersample behavior. No large discrepancies between the s-plane and digital responses are apparent. It is clear from the figure that the responses at the even sample instants (the closed dots of fig. 48) are a very poor reflection of the response during the first few cycles. The reason is the large contribution of the sidebands previously shown in the hybrid frequency response of figure 45. If the z-plane transfer function for ADOCS actuator rate is used to estimate requirements for actuator rate authority using RMS calculations, a considerable error would result. Figure 48 shows that the error may be on the order of 200% if only the even sample response is used. In fact, the results of this analysis suggest the s-plane result is a far better descriptor of the intersample response than is the z-plane result--a rather unexpected finding. Nonetheless, it is clear that a workable design requires an accurate description of the intersample response of the high frequency actuator signals.

Based on the hybrid frequency responses, it is expected that the intersample ripple associated with the actuator deflection signal will be much less than the ripple associated with the actuator rate. This is borne out in the ADOCS actuator deflection response of figure 48(b). Again, the emulation response is shown in the figure. Now, the responses at the even sample instants (closed-dots) are much more representative of the character of the actuator deflection response. For this signal, the emulation analysis underestimates the maximum value by about 10%.

Finally, the pitch attitude response, shown in figure 49, is seen to be very smooth between the sample instants, as was expected from the hybrid frequency response of figure 47. Once again, the digital response closely matches the emulation result.

This analysis of intersample behavior shows that neither z-plane nor emulation s-plane analyses is sufficient to predict the transient (high-frequency) behavior of the analog elements which are closest to the zero-order hold. Hybrid frequency responses are very useful because they show the relative contribution of

---

[5]When a <u>step</u> input is inserted at $\delta^*_{c_\theta}$ in the digital system, the zero-order hold output (u, in fig. 31) responds instantly without the (average) T/2 delay. For this special case, the emulation <u>time response</u> must be advanced by T/2 sec for comparison with the discrete result. For other nonsharp input forms (e.g., ramps, sinusoids) at $\delta^*_{c_\theta}$, and for inputs <u>including steps</u> at any point where smoothing occurs before $\delta^*_{c_\theta}$ is reached (e.g., θ^*_m, θ^*_c, δ_s, in fig. 31) the T/2 (average) delay is <u>retained</u> in the emulation time response.

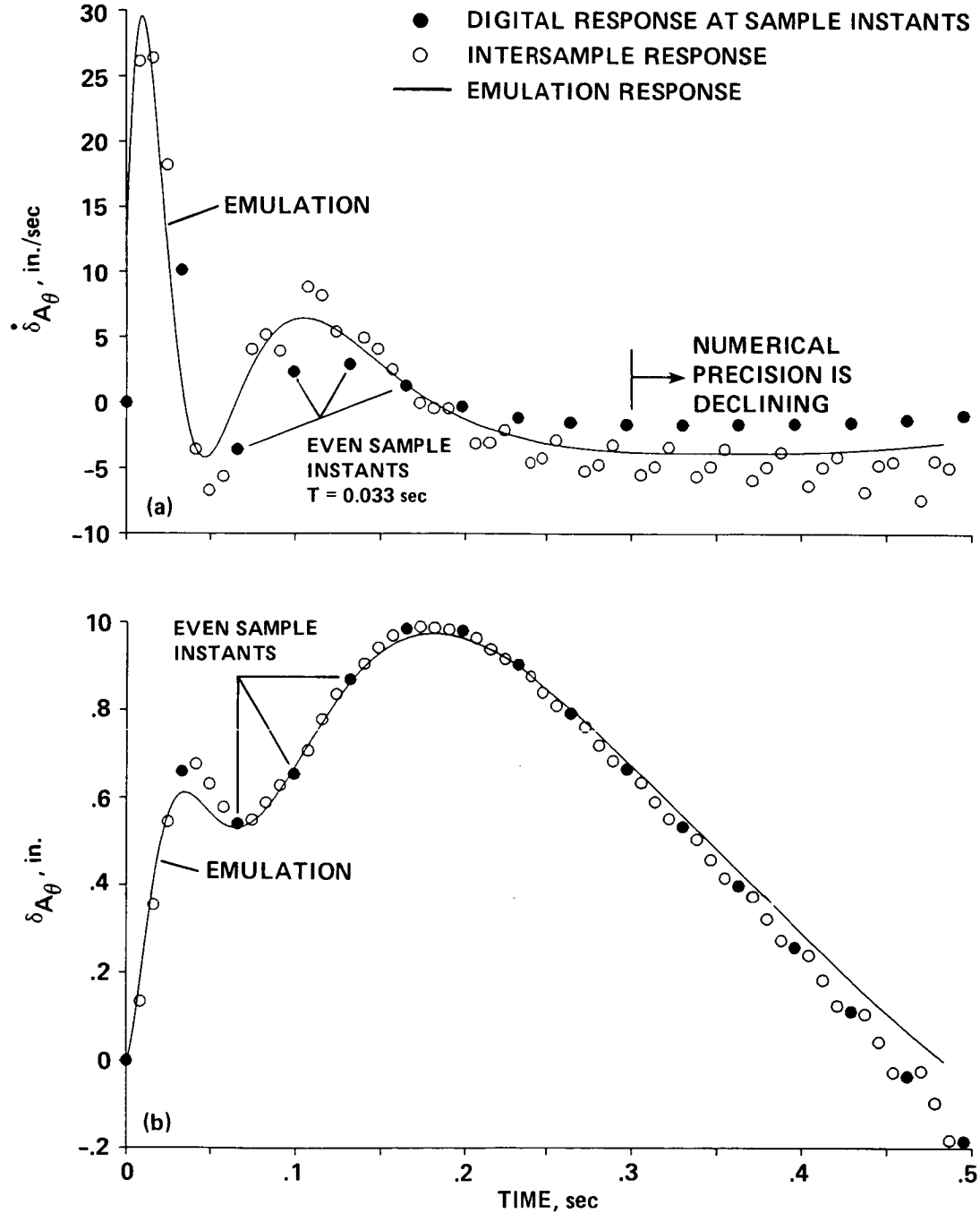

Figure 48.- Response to a step input, $\delta_{c_\theta} = 1$, digital and emulation analyses (30.3 Hz system). (a) ADOCS actuator rate ($\dot{\delta}_{A_\theta}$); (b) ADOCS actuator deflection (δ_{A_θ}).

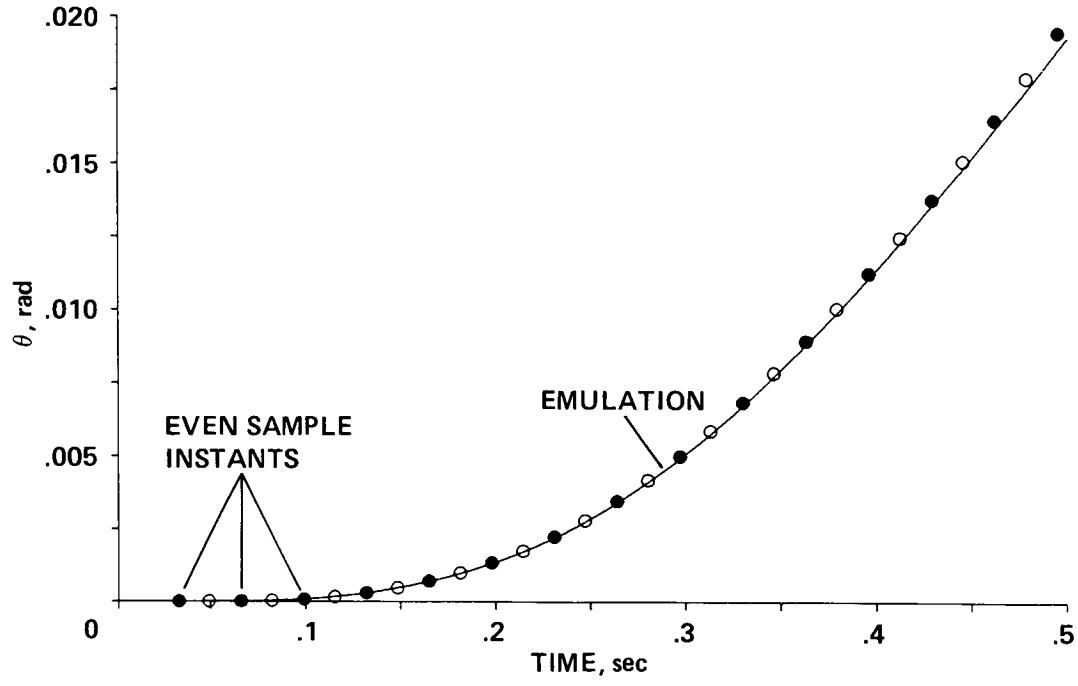

Figure 49.- Pitch attitude response (θ) to a step input, $\delta_{c_\theta} = 1$; digital and emulation analyses (30.3 Hz system).

each sideband as compared to the basic response at the even sample instants. When the intersample actuator response is excessive, a smoothing filter is often inserted between the zero-order hold and the first actuator.

The comparison of hybrid frequency responses and time-domain responses suggests that the magnitude at the first sideband should be reduced from the level at the dominant frequency ω_o by 40 dB if intersample behavior is to be safely ignored. Then, the selection of actuator rate and surface deflection limits can be based on the z-plane response, which is exact at the even sample instants.

The preceding analyses show that the intersample response of the high-frequency actuators must be monitored at a sample rate which is higher than the basic sample rate of the control system. Redundancy management systems which compare the actuator outputs from parallel channels will sense unexpectedly large differences if the system is running in an asynchronous configuration. In the present case, a monitoring rate of at least 4 to 5 times the basic sample rate is needed to accurately monitor the activity of the actuators.

III.I.3 Maximum Achievable Pitch Attitude Response $(\theta_1)_{max}$- The maximum achievable pitch attitude for the digital system depends, as before, on the swashplate actuator and pitch attitude responses to a unit ramp-step input ($\Delta t = 0.5$ sec) at the stick. The existence of the analog prefilter in between the stick and the stick-sampler (fig. 31) complicates this time response computation, as will be discussed in detail later in Section III.J.5. Using the method of Section III.J.5,

the required actuator time responses (δ_{s_θ}, $\dot{\delta}_{s_\theta}$) of figure 50(a) and (b) are generated. (The actual ramp time is $\Delta t = 0.495$ sec, which is the nearest integer multiple of the cycle time.) Numerical precision is maintained for 2 sec in this case. The swashplate deflection shown in figure 50(a) for the even sample instants matches the previous emulation result (replotted from fig. 41(a)) almost identically. This is because the swashplate deflection signal is "downstream" of the ADOCS and swashplate actuators, so the sideband lobes are substantially suppressed. The swashplate rate response (fig. 50(b)) does exhibit some intersample ripple (open circles are response at mid-cycle), although not nearly as severe as in the rate response of the ADOCS actuator. The emulation result (replotted from fig. 41(b)) predicts the average digital response. The maximum actuator rate is $\dot{\delta}_{s_\theta} = -42.8$ in./sec, which is 14% above the emulation result. The associated digital response of pitch attitude (not shown) is identical to the emulation result of fig. 41(c) ($\theta_1 = 0.5$ rad) as expected. Thus the maximum achievable pitch attitude (based on actuator rate) is reduced to $(\theta_1)_{max} = 6.7$ deg. While the digital system performance is lower than the emulation estimate, the current (exact) value of $(\theta_1)_{max} = 6.7$ deg is still within the 5 deg requirement.

III.I.4 Effects of Computational Time Delay (τ_c) and Structural Dynamics- Up until now, the assumption has been made that there is no delay between the time that the updated sample is taken and the time that the updated control is issued to the zero-order hold. As has been discussed in Section II, poor software architecture may introduce up to a one-full-cycle delay ($\tau_c = T$) between the sensor update and the control update. Since the Tustin transformation yields difference equations in which the updated control value depends on the sensor value at the same instant, this computational delay τ_c introduces unmodeled errors in the closed-loop response. The effects of computational time delay are most significant when lightly damped structural modes are present. In this section, the effects of unmodeled computational delays on the stabilization loop stability margins are examined for the 30.3 Hz digital system with one added structural mode.

When a flexible beam is attached to a rigid central body, the angular response transfer function contains additional lightly damped quadratic factors. If the angular rate sensors and control moment effectors are both located in the central body, the added zeroes and poles will alternate in a stable interacting manner (ref. 63). In the helicopter, tail-boom flexibility will generate such alternating quadratic pairs in the pitch response transfer function. For illustration purposes, the first tail boom bending mode is assumed to be:

$$G_{flex}(s) = \frac{[0.002,40]}{[0.002,50]} \tag{81}$$

When this flexible mode is appended to the q/δ_θ transfer function shown in figure 31 (with no additional computational delay), the open-loop digital response characteristics (δ_f^*/e^*) are essentially unchanged from those shown in figure 43 at the first (rigid body) crossover frequency, $\omega_{c_\theta} = 4.0$ rad/sec. The frequency response in the range of the second crossover, $10.0 \leq \omega \leq 100$ rad/sec, is shown on

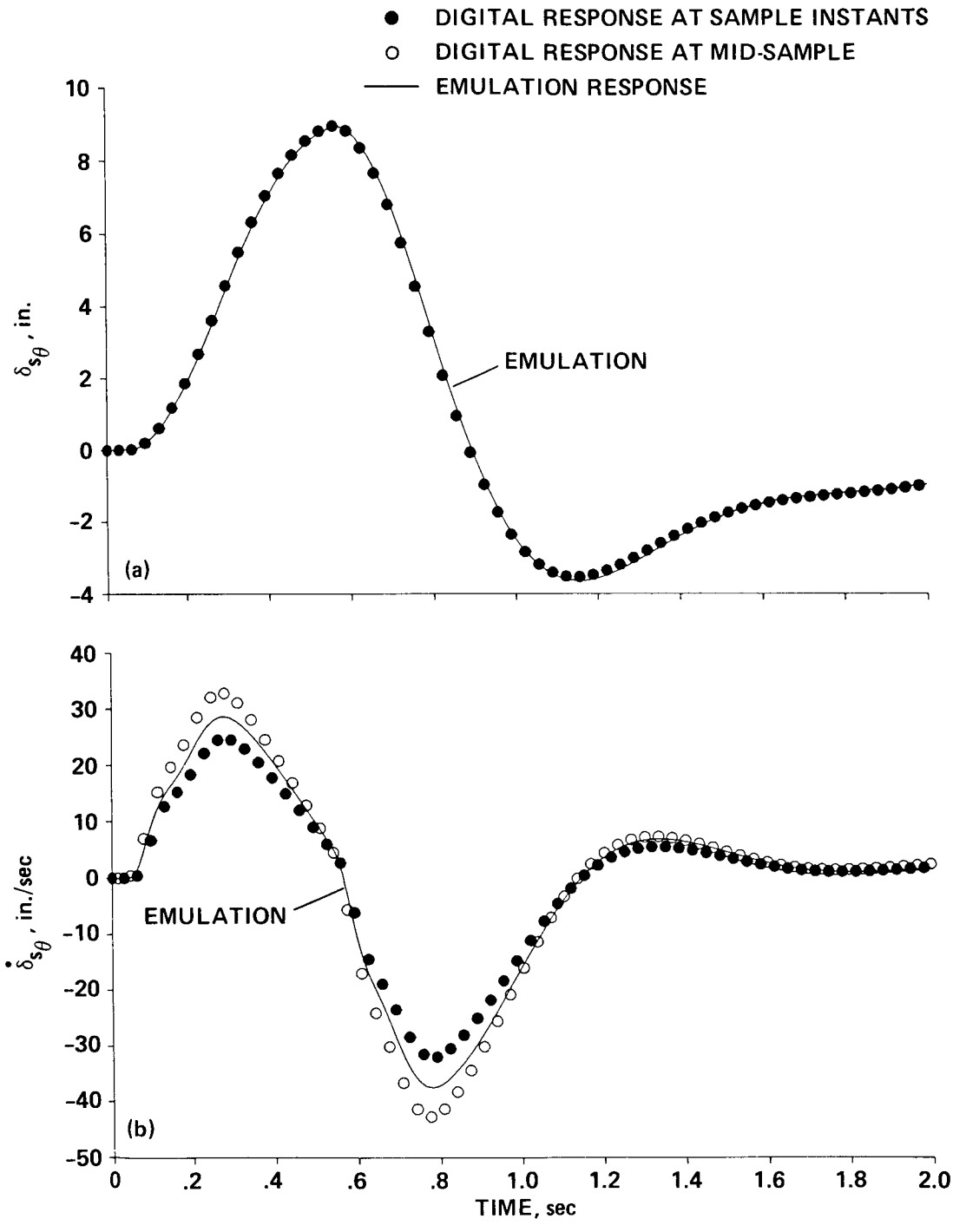

Figure 50.- Responses to a ramp-step stick input δ_s, (Δt = 0.495 sec), digital and emulation analyses (30.3 Hz system). (a) Swashplate angle (δ_{s_θ}); (b) swashplate rate ($\dot{\delta}_{s_\theta}$).

the magnitude ratio versus phase margin (Nichols) plot (fig. 51). The structural mode digital phase and gain margins are quite acceptable:

$$\Phi_m = 97 \text{ deg}$$
$$GM = 33 \text{ dB} \qquad (82)$$

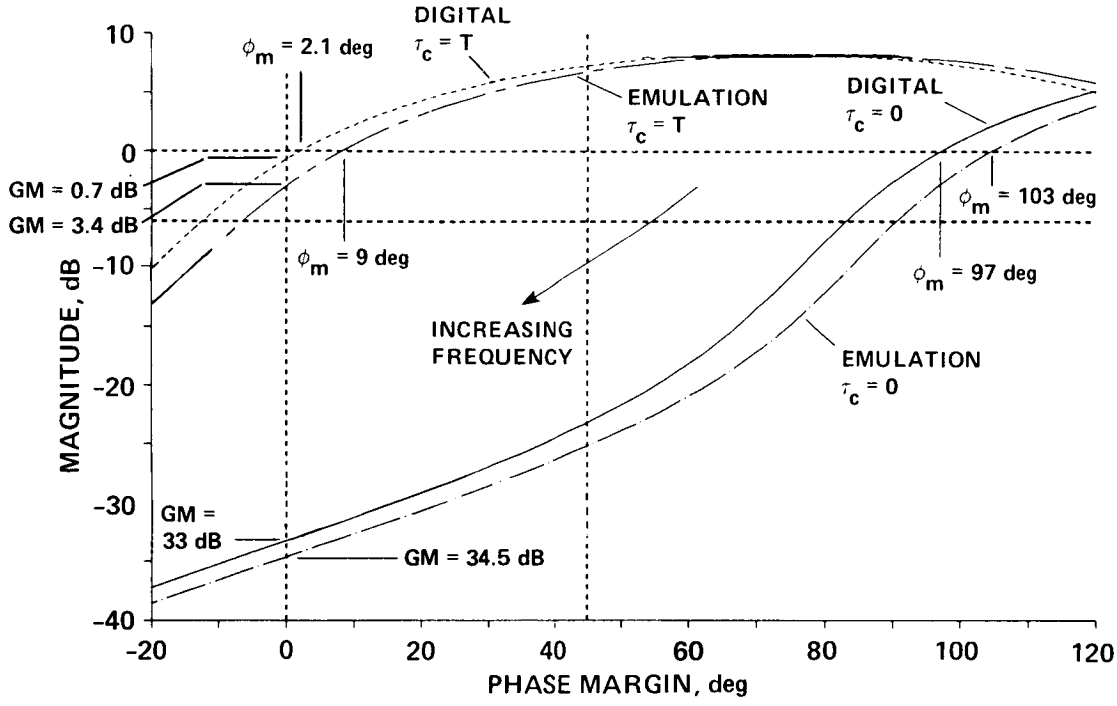

Figure 51.- Digital and emulation analyses of the effect of computational time delay (τ_c) on stability margins.

Using emulation analysis, the corresponding margins are slightly overestimated as shown in figure 51:

$$\Phi_m = 103 \text{ deg}$$
$$GM = 34.5 \text{ dB} \qquad (83)$$

This overestimation results largely from the discrepancy between the analog and digital notch-filter frequency responses (fig. 42). If a full frame of computational time delay (τ_c = T) is included, the rigid-body phase margin (at ω_{c_θ} = 4 rad/sec) is reduced as indicated from the linear phase law by 7.6 deg using both the digital and emulation analysis methods. The stability margin reduction at the structural mode crossover is more severe. As shown in figure 51, both methods predict a sharp reduction in margins caused by the added computational delay; however, the (exact) digital analysis shows that the remaining margins are unacceptable and the computation delay must be reduced:

Direct digital analysis	Emulation analysis
Φ_m = 2.1 deg	Φ_m = 9 deg
GM = 0.7 dB	GM = 3.4 dB

(84)

The overestimation of the remaining stability margins in the emulation result makes the use of the direct digital approach essential for assessing allowable computational time delay levels when structural modes are present. A direct digital analysis of a fixed-wing fighter aircraft which includes the first few structural modes shows that some levels of time delays will cause stabilization of particular modes and destabilization of others (ref. 21). A rule-of-thumb given in reference 21 suggests a limit on computational time delay of:

$$\tau_c \leq T/4 \tag{85}$$

This requirement precludes the use of the synchronized input/output software architecture of figure 12(b).

III.I.5 General Concluding Comments on Emulation-Based Design- The emulation design technique involves a complete s-plane analysis, and then reconversion via the Tustin transformation to the z-plane. The design will be workable if all of the appended system elements required for practical implementation are considered and if discrepancies in intersample response, notch filter performance, and structural mode stability margins are not severe. Thus, the emulation approach is quite sufficient for initial design trade-off studies and handling qualities evaluations. However, when a more exact appreciation for the response of the individual system elements is needed, direct digital analysis techniques are required. Specifically, the response of the actuators and other high-frequency dynamic elements may not be accurately modeled with the emulation methods. This is a critical concern if high-frequency lightly damped modes such as those associated with rotor-pylon or structural dynamics are in the frequency range near the Nyquist frequency. In the desire to allow sufficient margins of safety for these poorly modeled effects, the designer using the emulation technique may be overly conservative in the setting of system performance. Alternatively, the increased accuracy of the direct digital methods allows greater design leeway. In the following section, a control system using a 15 Hz sample rate is designed using direct digital methods.

III.J Direct Digital Design of a 15 Hz Sample Rate System

Modern interactive computational tools such as LCAP2 (ref. 37) and other widely available commercial software packages (refs. 38,43,44) make design by direct digital methods an attractive alternative to historically popular emulation methods. Further, the w-plane transformation allows the designer to achieve the same degree of physical insight as can be achieved using s-plane techniques, but without employing the approximations associated with the emulation method. By conducting the design entirely in the digital domain, a separate digital analysis to check the

analog design is no longer necessary. In this section, direct digital methods are used to design a 15 Hz sample rate system with a stabilization loop crossover frequency of $\omega_{c_\theta} = 4$ rad/sec. The 15 Hz sample rate was selected for illustration purposes, but may also be useful for a low sample rate backup digital system.

III.J.1 Effect of Reduced Sample Rate on Vehicle Dynamics and Filter Selection- A key effect of reducing the sample rate from 30.3 Hz to 15 Hz is to reduce the location of the folded-down 4/rev vibration component from $\omega = 82.4$ rad/sec to $\omega = 13.75$ rad/sec. This reflected 4/rev vibration is now roughly 1/2 of the 1/rev frequency, and if not properly attenuated, will contribute significantly to actuator and rotor jitter. Also, the reduced Nyquist frequency ($\omega_{Nyq} = 47.1$ rad/sec) requires a corresponding reduction in the anti-alias filter corner frequency. The feedback signal filter:

$$G_F(s) = \frac{400}{[0.6,\ 20]} \tag{86}$$

maintains an attenuation of -15 dB (82%) at the Nyquist frequency, with an increased attenuation to -29 dB (97%) at the 4/rev frequency.

The analog stick filter frequency is maintained at 40 rad/sec (eq. (47)), which retains the 4/rev biodynamic attenuation at -17 dB (86%). A lower frequency (stronger attenuation) stick filter (e.g., eq. (86)) may be required since any remaining 4/rev feedthrough will be aliased to low frequency ($\omega = 13.75$ rad/sec).

Besides the additional phase lag associated with the lower filter frequencies, the increased sample period causes its own added phase lag of $\phi = -3.8$ deg resulting from the zero-order hold delay. Stick sampling skew is similarly affected.

III.J.2 Direct Digital Design Procedure- As in the digital analysis of the 30.3 Hz system (Section III.I), the first step of the direct digital design procedure is to obtain the required open-loop w-plane transfer functions from u^* to $\bar{q}^*$ and from u^* to $\bar{\theta}^*$ of figure 31. Based on the current 15 Hz sample rate (T = 0.067 sec), these w-plane transfer functions are:

$\frac{\bar{q}}{u}(w)$ =

(87)

THE NUMERATOR ROOTS ARE:

NO.	REAL	IMAG.	OMEGA	ZETA
1	-0.15995381E-01	-0.13426822E-01	0.20883768E-01	0.76592409
2	-0.15995381E-01	0.13426822E-01	0.20883768E-01	0.76592409
3	-30.357182	-5.5266681	30.856159	0.98382893
4	-30.357182	5.5266681	30.856159	0.98382893
5	30.306238	-0.23522519	30.307151	-0.99996988
6	30.306238	0.23522519	30.307151	-0.99996988
7	-71.074280	-17.484913	73.193411	0.97104751
8	-71.074280	17.484913	73.193411	0.97104751
9	-1.5858353	0.00000000E+00		
10	-13.710724	0.00000000E+00		
11	-26.012909	0.00000000E+00		
12	-41.928234	0.00000000E+00		
13	59.706169	0.00000000E+00		

THE DENOMINATOR ROOTS ARE:

NO.	REAL	IMAG.	OMEGA	ZETA
1	-14.659279	-14.408139	20.554536	0.71318950
2	-14.659279	14.408139	20.554536	0.71318950
3	-13.906674	3.5846815	14.361251	0.96834699
4	-13.906674	-3.5846815	14.361251	0.96834699
5	-30.302084	0.22198629	30.302897	0.99997317
6	-30.302084	-0.22198629	30.302897	0.99997317
7	-0.31264652E-01	0.21180928	0.21410430	0.14602534
8	-0.31264652E-01	-0.21180928	0.21410430	0.14602534
9	-63.485500	9.8703337	64.248208	0.98812873
10	-63.485500	-9.8703337	64.248208	0.98812873
11	-0.57983506	0.00000000E+00		
12	0.90607882E-01	0.00000000E+00		
13	-29.507824	0.00000000E+00		

LOW-FREQUENCY GAIN = -0.61944547E-01

$\frac{\bar{\theta}}{u}(w)$ =

THE NUMERATOR ROOTS ARE:

NO.	REAL	IMAG.	OMEGA	ZETA
1	29.690960	-2.3508849	29.783884	-0.99688005
2	29.690960	2.3508849	29.783884	-0.99688005
3	-0.15994776E-01	0.13427403E-01	0.20883678E-01	0.76589842
4	-0.15994776E-01	-0.13427403E-01	0.20883678E-01	0.76589842
5	-32.106342	14.412673	35.192930	0.91229522
6	-32.106342	-14.412673	35.192930	0.91229522
7	-23.074619	4.7532392	23.559103	0.97943539
8	-23.074619	-4.7532392	23.559103	0.97943539
9	-62.453083	24.250065	66.995919	0.93219234
10	-62.453083	-24.250065	66.995919	0.93219234
11	-13.683243	0.00000000E+00		
12	41.311447	0.00000000E+00		
13	730.79321	0.00000000E+00		

THE DENOMINATOR ROOTS ARE:

NO.	REAL	IMAG.	OMEGA	ZETA
1	-14.659279	-14.408139	20.554536	0.71318950
2	-14.659279	14.408139	20.554536	0.71318950
3	-13.906674	3.5846815	14.361251	0.96834699
4	-13.906674	-3.5846815	14.361251	0.96834699
5	-30.302084	0.22198629	30.302897	0.99997317
6	-30.302084	-0.22198629	30.302897	0.99997317
7	-0.31264652E-01	0.21180928	0.21410430	0.14602534
8	-0.31264652E-01	-0.21180928	0.21410430	0.14602534
9	-63.485500	9.8703337	64.248208	0.98812873
10	-63.485500	-9.8703337	64.248208	0.98812873
11	-0.57983506	0.00000000E+00		
12	0.90607882E-01	0.00000000E+00		
13	-29.507824	0.00000000E+00		

LOW-FREQUENCY GAIN = -0.61944547E-01

(88)

Comparing these results with those of equations (73) and (74) shows that the numerical values of the low-frequency w-plane poles (ν < 10 rad/sec) are unchanged, while the mid- and high-frequency poles are significantly altered by the warping effect of the lower sample rate.

Before the level of required stabilization loop equalization can be determined, the digital notch filter must first be designed. A good estimate of the required w-plane center frequency for the notch filter is obtained from the pre-warping transformation of equation (63). For the present sample period, T = 0.067 sec, the analog notch filter frequency of ω_1 = 27 rad/sec is shifted to the pre-warped center frequency of ω_a = 38 rad/sec. A "first guess" for the w-plane notch filter transfer function is obtained by using the same numerator and denominator damping ratios as in the s-plane filter (eq. (48)), which yields:

$$G_N(w) = \frac{[0.1,\ 38]}{[0.6,\ 38]} \tag{89}$$

The $j\omega$-frequency response (versus actual frequency) of this digital notch filter is compared with the analog notch filter frequency response of equation (48) in figure 52. The responses show that the pre-warping technique has maintained the proper center frequency location, but the digital notch is very narrow when compared with the analog notch. A trial-and-error approach was used to obtain the following

w-plane notch filter which, as shown in figure 52, more closely matches the analog characteristics at low and mid frequency:

$$G_N(w) = \frac{[0.15,\ 38]}{[0.9,\ 38]} \tag{90}$$

The differences in the high-frequency matching (fig. 52) are associated with the folding effects of the lower sample rate, so they cannot be eliminated by adjusting the filter characteristics.

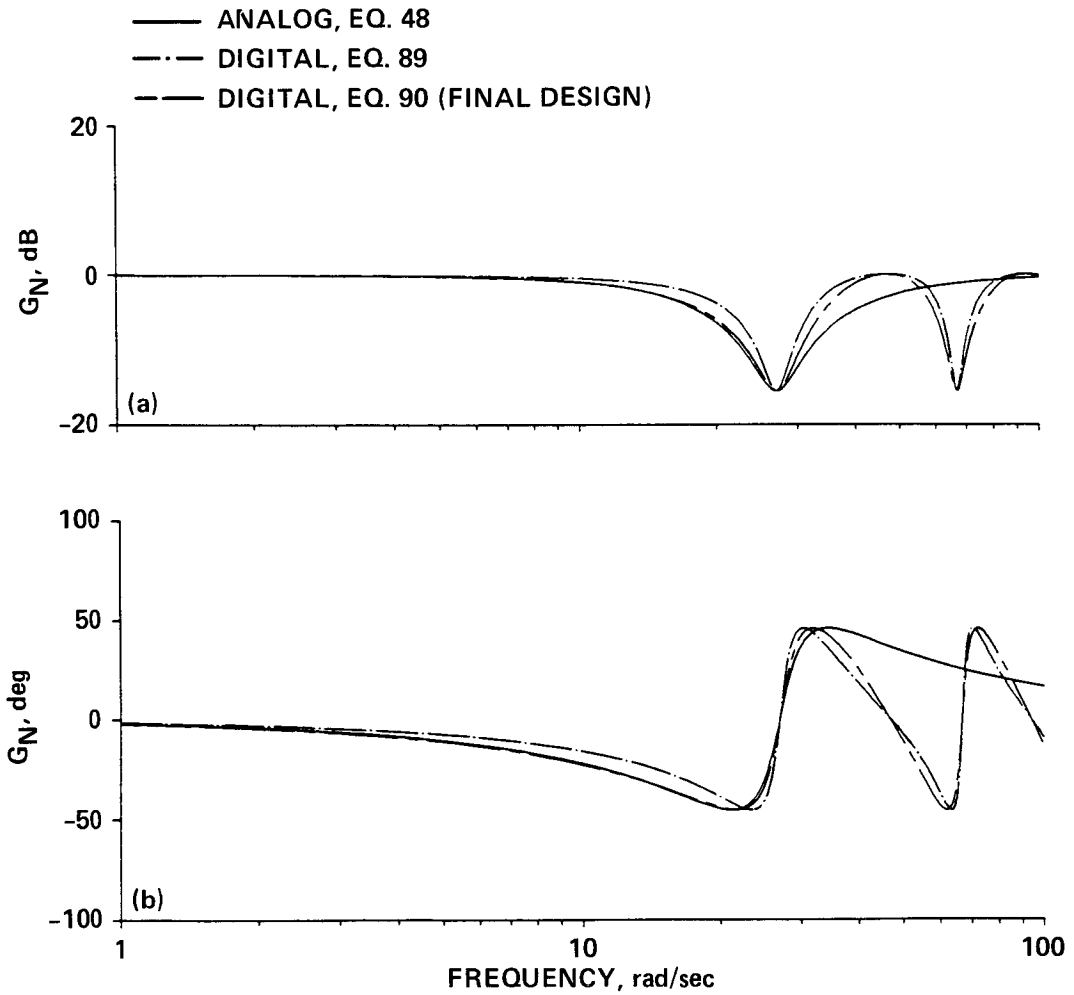

Figure 52.- Digital and analog notch filters for the 15 Hz system. (a) Magnitude; (b) phase.

Compared to the 30.3 Hz open-loop response depicted in figure 32, the total additional phase lag which is due to the lower sensor filter, new notch filter, and increased zero-order hold delay is $\phi = -14.5$ deg at the crossover frequency, $\omega_{c_\theta} = 4$ rad/sec. To compensate the open-loop system for this additional phase lag, the following design changes are made:

• The ratio of pitch rate gain to pitch attitude gain is increased from $T_q = 0.63$ rad/sec (for the 30.3 Hz system) to $T_q = 0.91$ rad/sec, thereby reducing the location of the compensation zero to $1/T_q = 1.1$ rad/sec. This yields 6.6 deg of additional phase lead at the crossover frequency.

• The following w-plane lead compensation element generates the remaining required 8 deg of phase lead (above the previous 12 deg generated by the 30.3 Hz system lead element) (see ref. 40 for lead compensation technique):

$$G_{1c}(w) = \frac{2(w + 2.83)}{(w + 5.66)} \tag{91}$$

The equalized open-loop transfer function δ_f^*/e (from fig. 31) is obtained using transfer function arithmetic in the w-plane. The associated jν-frequency response (ν being fictitious frequency) is plotted in figure 53. In this jν-format, which is preferable for design, the asymptote break points correspond to the w-plane transfer function pole and zero frequencies. The design (warped) crossover frequency $\nu_{c_\theta} = 4.024$ rad/sec obtained from equation (63) is essentially identical to the actual crossover $\omega_{c_\theta} = 4$ rad/sec. The frequency warping becomes more apparent at higher frequencies, with the plotted upper limit $\nu = 100$ rad/sec corresponding to $\omega = 38.23$ rad/sec. The Nyquist frequency $\omega = \omega_{Nyq}$ corresponds to $\nu = \infty$. It is important to recognize that this warping simply reflects a deformation of the frequency scale, but that the gain-phase interrelationship is <u>strictly preserved</u>. Thus, the stability margins obtained from jν-response are correct, even at high frequencies. The phase and gain margins obtained from figure 53 are:

$$\begin{aligned} \Phi_m &= 48 \text{ deg} \\ GM &= 4.72 \text{ dB} \end{aligned} \tag{92}$$

This 15 Hz design is seen to have a satisfactory phase margin, but a somewhat low gain margin. Once again the desired phase margin has been retained at the expense of a gain margin loss. The primary source of the gain margin reduction is the increase in effective phase delay caused by the lower frequency anti-alias filter, and the larger zero-order hold delay. The only way to improve the gain margin of the system is to further decrease the crossover frequency of the system below the $\omega_{c_\theta} = 4$ rad/sec value. For the present case study, the crossover frequency will be maintained and the somewhat low gain margin will be accepted. We can expect the resulting closed-loop damping of the dominant roots to be somewhat less than desirable.

Figure 54 shows the variations in w-plane closed-loop roots with attitude feedback gain (K_θ). The design crossover frequency of $\omega_{c_\theta} = 4$ rad/sec ($\nu_{c_\theta} = 4.024$ rad/sec, in fig. 53) corresponds to rate and attitude feedback gains of:

$$\begin{aligned} K_q &= 8.25 \text{ in./rad} \\ K_\theta &= 9.06 \text{ in./rad} \end{aligned} \tag{93}$$

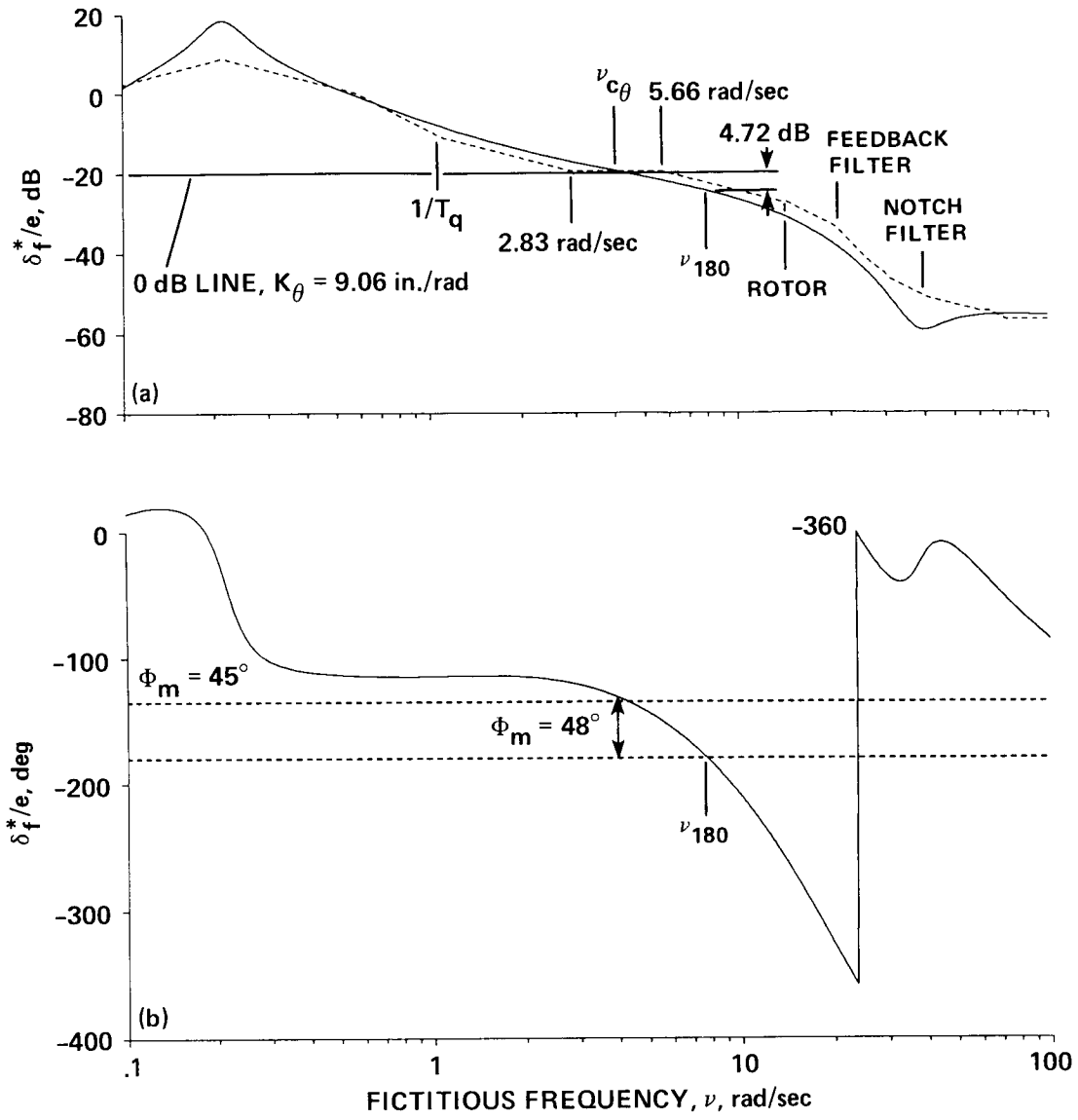

Figure 53.- Equalized open-loop (δ_f/e) digital frequency response versus fictitious frequency, ν (15 Hz system). (a) Magnitude; (b) phase.

The associated closed-loop roots marked by the rectangular symbols in figure 54 are the denominator factors of the closed stabilization loop response:

$$\frac{\theta}{\delta_{c_\theta}}(w) =$$ (94)

THE NUMERATOR ROOTS ARE:

NO.	REAL	IMAG.	OMEGA	ZETA
1	-5.6999998	-37.539711	37.969987	0.15011856
2	-5.6999998	37.539711	37.969987	0.15011856
3	-14.659279	-14.408139	20.554536	0.71318950
4	-14.659279	14.408139	20.554536	0.71318950
5	30.668222	-1.1513257	30.689826	-0.99929607
6	30.668222	1.1513257	30.689826	-0.99929607
7	-27.597452	-2.2099857	27.685798	0.99680899
8	-27.597452	2.2099857	27.685798	0.99680899
9	-0.15994823E-01	0.13427422E-01	0.20883726E-01	0.76589890
10	-0.15994823E-01	-0.13427422E-01	0.20883726E-01	0.76589890
11	-43.752934	5.4353952	44.089259	0.99237173
12	-43.752934	-5.4353952	44.089259	0.99237173
13	-5.6599998	0.00000000E+00		
14	-13.726160	0.00000000E+00		
15	-56.223125	0.00000000E+00		
16	116.91941	0.00000000E+00		

THE DENOMINATOR ROOTS ARE:

NO.	REAL	IMAG.	OMEGA	ZETA
1	-1.4805235	0.48449898	1.5577834	0.95040396
2	-1.4805235	-0.48449898	1.5577834	0.95040396
3	-1.8032087	-6.7447028	6.9815885	0.25828058
4	-1.8032087	6.7447028	6.9815885	0.25828058
5	-31.042093	4.5796666	31.378096	0.98929181
6	-31.042093	-4.5796666	31.378096	0.98929181
7	-45.693302	13.371584	47.609632	0.95974910
8	-45.693302	-13.371584	47.609632	0.95974910
9	-15.767879	21.957205	27.032293	0.58329787
10	-15.767879	-21.957205	27.032293	0.58329787
11	-59.660259	5.2086258	59.887196	0.99621059
12	-59.660259	-5.2086258	59.887196	0.99621059
13	0.73756748E-02	0.00000000E+00		
14	-0.46454545E-01	0.00000000E+00		
15	-26.615421	0.00000000E+00		
16	-13.498746	0.00000000E+00		

LOW-FREQUENCY GAIN = -0.14117429

The w-plane damping ratio of the dominant closed-loop pitch/rotor mode is $\zeta = 0.26$ compared to the previous value of $\zeta = 0.43$ in equation (79) for the 30.3 Hz digital system. The lower damping ratio results from the reduced stability margins (eq. (92)).

An emulation analysis of the 15 Hz system was completed to further expose the digital system artifacts. The s-plane open-loop frequency response δ_f/e is plotted together with the $j\omega$ digital response in figure 55. These results show that the emulation analysis is accurate up to a frequency of $\omega = 30$ rad/sec, beyond which significant digital distortions are apparent. Moreover, the rigid-body phase and gain margins are correctly obtained by the emulation analysis technique.

The closed-loop roots obtained from the emulation procedure are compared with the image s-plane results of the digital analysis in table 4. For the closed loop modes with natural frequencies of $\omega < 40$ rad/sec, the emulation analysis yields closed-loop damping ratios and natural frequencies to within 5% of the digital

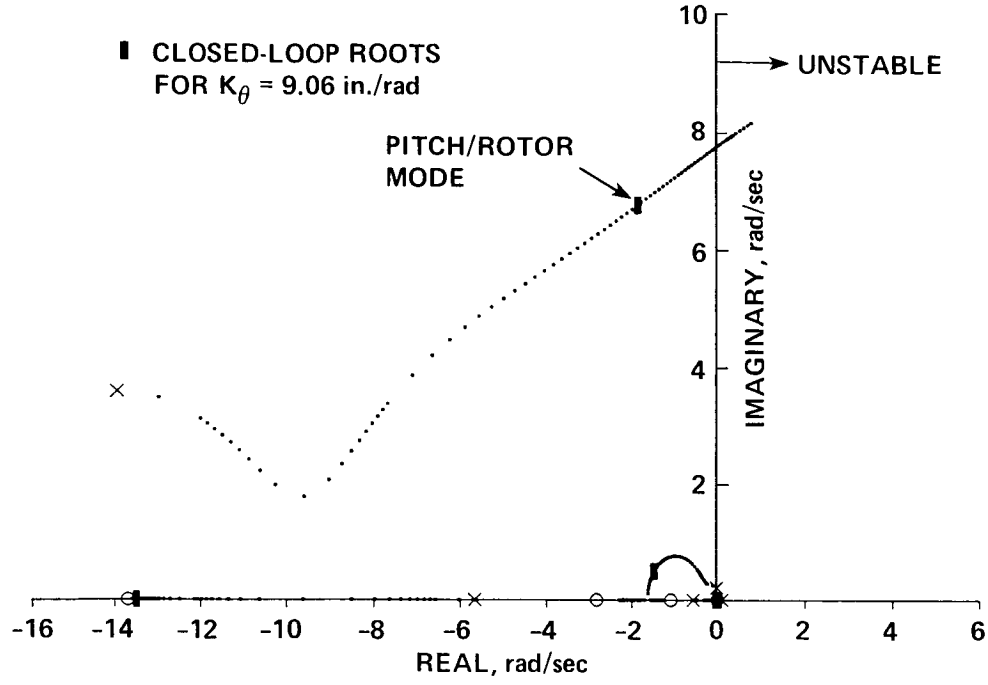

Figure 54.- w-plane root locus for the 15 Hz system.

analysis. However, for higher frequencies $\omega > 40$ rad/sec, the digital effects yield completely different closed-loop roots, as expected. The closed stabilization loop frequency response of $\theta/\delta_{c_\theta}(w)$ for the digital and emulation analyses compare very well up to the Nyquist frequency of $\omega_{Nyq} = 47.1$ rad/sec and diverge thereafter as shown in figure 56. Once again the low-frequency vehicle response characteristics are accurately determined by using emulation analysis. However, the large differences for higher frequencies $\omega > 40$ rad/sec suggest associated errors in the actuator response characteristics which is shown next.

III.J.3 ADOCS Actuator Intersample Response- The actuator rate $\dot{\delta}_{A_\theta}$ and deflection δ_{A_θ} responses to the step input $\delta_{c_\theta} = 1$ are shown in figures 57 and 58, along with the result using emulation analysis. Again, accurate digital responses are obtainable for about the first 0.35 sec. There is a considerable discrepancy as before (fig. 48) between the emulation results and the digital response for the actuator rate response $\dot{\delta}_{A_\theta}$. While the maximum actuator rates are well predicted by the emulation result, some of the large fluctuations during the initial transient are not well captured by the s-plane analysis. Also, it is interesting to note that at the even sample instants, the true (digital) response is exactly zero. Therefore, an estimate of actuator rate requirements based on the responses at the even sample instants would result in a grossly underestimated specification. Clearly, the redundancy management system must also take the intersample response into account, requiring a monitoring rate of at least 4 to 5 times the basic sample rate, as before.

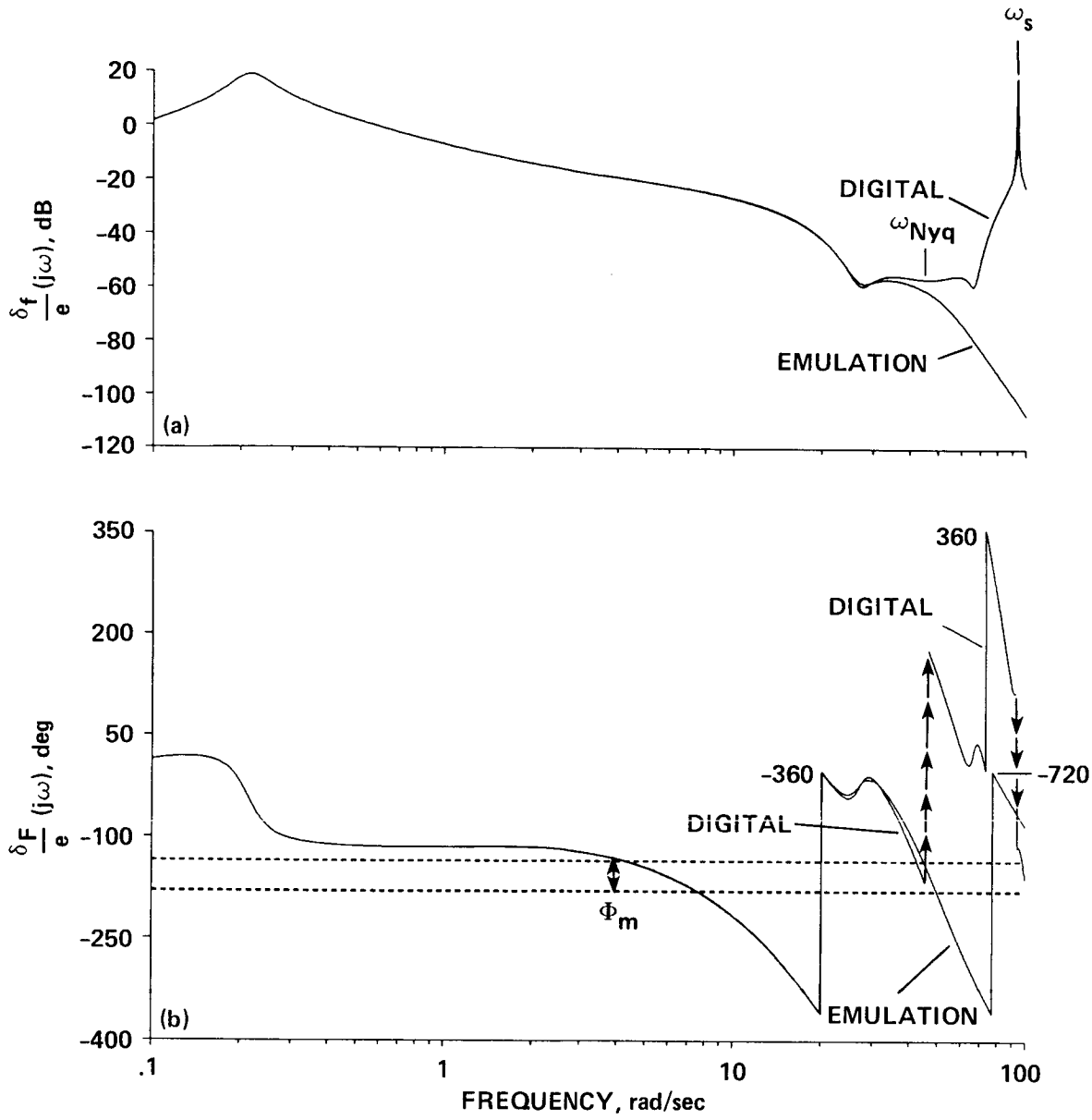

Figure 55.- Comparison of the equalized open-loop frequency response (δ_f/e) for the digital and emulation analyses versus actual frequency, ω (15 Hz system). (a) Magnitude; (b) phase.

TABLE 4.- COMPARISON OF IMAGE s-PLANE DIGITAL POLES WITH EMULATION ANALYSIS POLES OF θ/δ_{c_θ}, ω_s = 15 Hz

Root no.	Digital analysis equivalent s-plane denominator roots		Emulation analysis roots	
	Omega	Zeta	Omega	Zeta
1	1.5589249	0.95023659	1.5550470	0.94946734
2	1.5589249	.95023659	1.5550470	.94946734
3	6.8736277	.24982788	6.9611793	.25031764
4	6.8736277	.24982788	6.9611793	.25031764
5	23.785382	.41611367	23.326519	.39592373
6	23.785382	.41611367	23.326519	.39592373
7	43.653559	.44738182	35.703320	.69405991
8	43.653559	.44738182	35.703320	.69405991
9	47.556777	.80267585	51.378302	.28462759
10	47.556777	.80267585	51.378302	.28462759
11	47.995959	.33777322	90.045342	.79346326
12	47.995959	.33777322	90.045342	.79346326
13			105.05334	.86727413
14			105.05334	.86727413
	Real		Real	
15	0.73756750E-02		-0.46449121E-01	
16	-.46454583E-01		.73760743E-02	
17	-42.679286		-14.485390	
18	-14.551414		-78.996353	

Additional insight into the actuator response characteristics is gained from the hybrid frequency response of the actuator rate $(\dot{\delta}_{A_\theta}/\delta_{c_\theta})(s,w)$ which is shown in figure 59. First, note that the actuator response peaks at 29 dB with an input

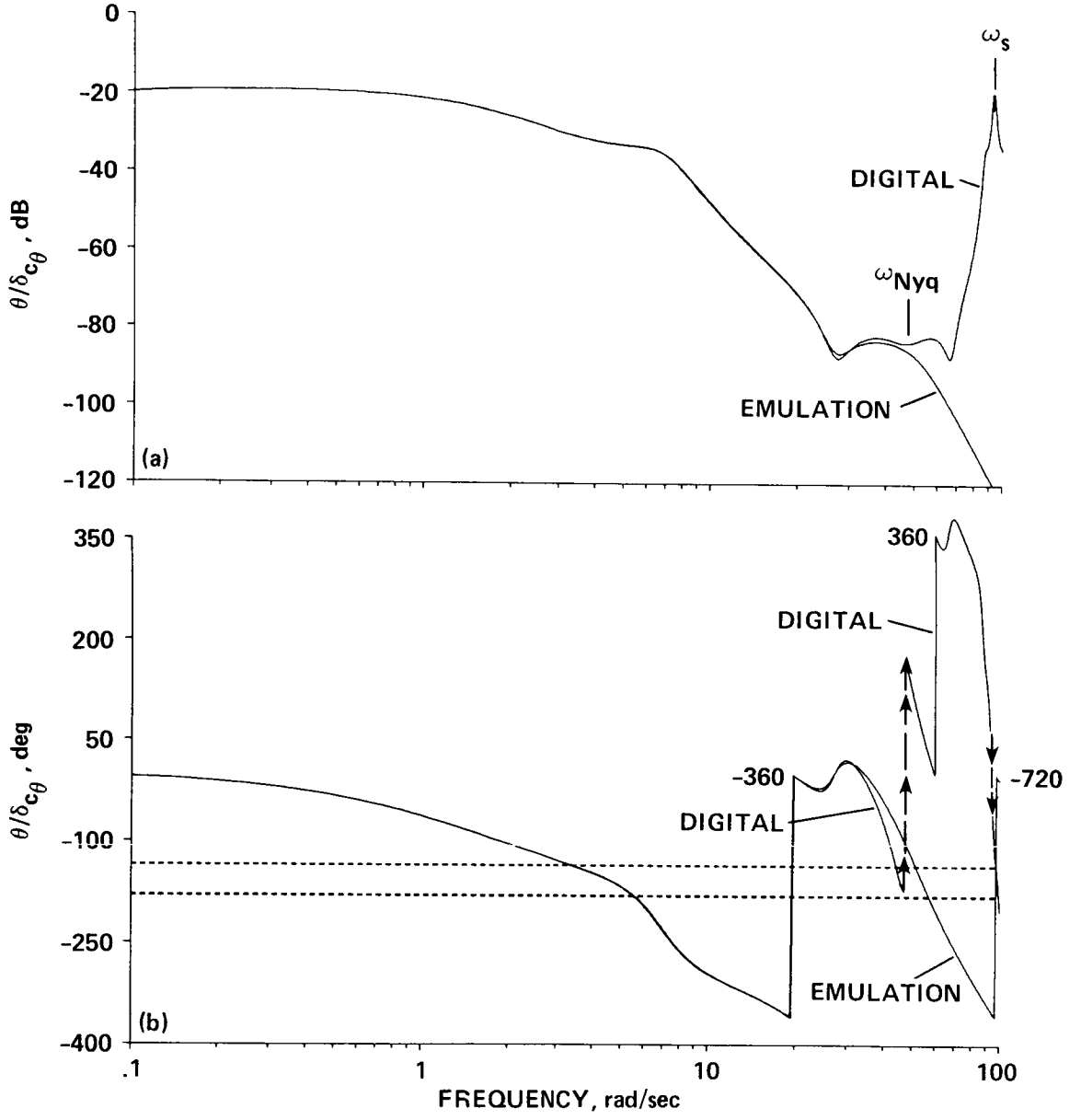

Figure 56.- Comparison of the closed stabilization loop frequency response (θ/δ_{c_θ}) for the digital and emulation analyses (15 Hz system). (a) Magnitude; (b) phase.

frequency of ω_o = 46 rad/sec ($\doteq \omega_{Nyq}$)compared to 32 dB for an input frequency of ω_o = 73 rad/sec in the 30.3 Hz system (fig. 45). So now the digital system resonance is far removed from the actuator natural frequency (ω_a = 89 rad/sec), and the dominant response (at ω_o) has been reduced by 30% (-3 dB). A comparison of figures 57 and 48 shows roughly the same attenuation in the maximum actuator rate time response. Next we note that there is essentially no magnitude attenuation at first negative alias ω_{-1} = -48 rad/sec, and only -8 dB at the first positive alias ω_1 = 140 rad/sec and at the second negative alias ω_{-2} = -142 rad/sec. Therefore, significant intersample actuator response is clearly indicated. Also, the possible excitation of higher frequency structural modes by the large sideband energy content

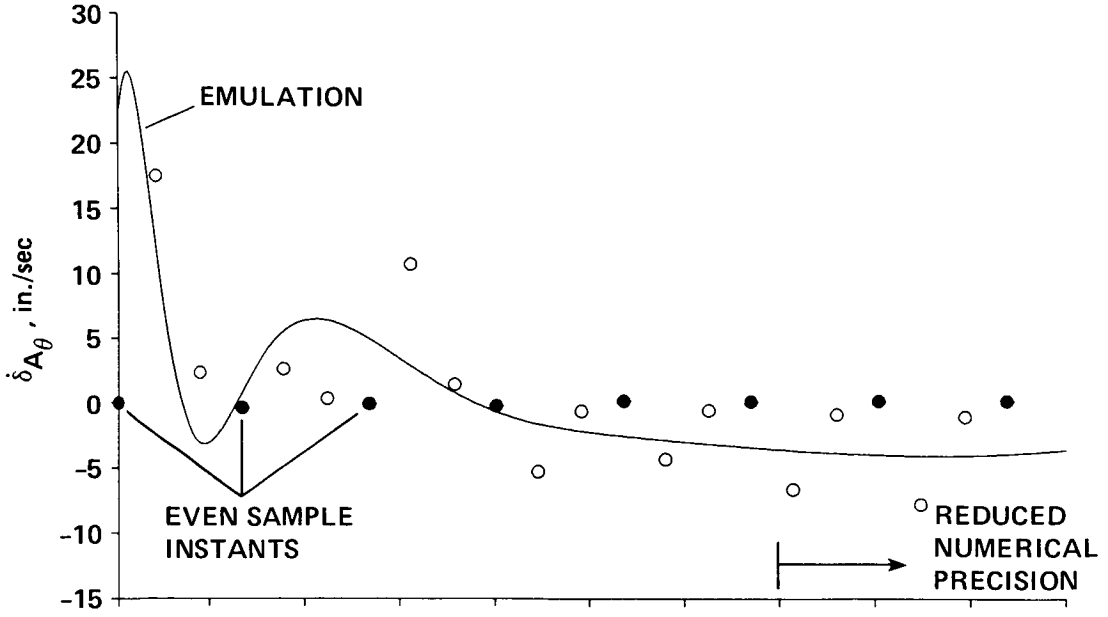

Figure 57.- ADOCS actuator rate ($\dot{\delta}_{A_\theta}$) response to a step input, δ_{c_θ} = 1; digital versus emulation results (15 Hz system).

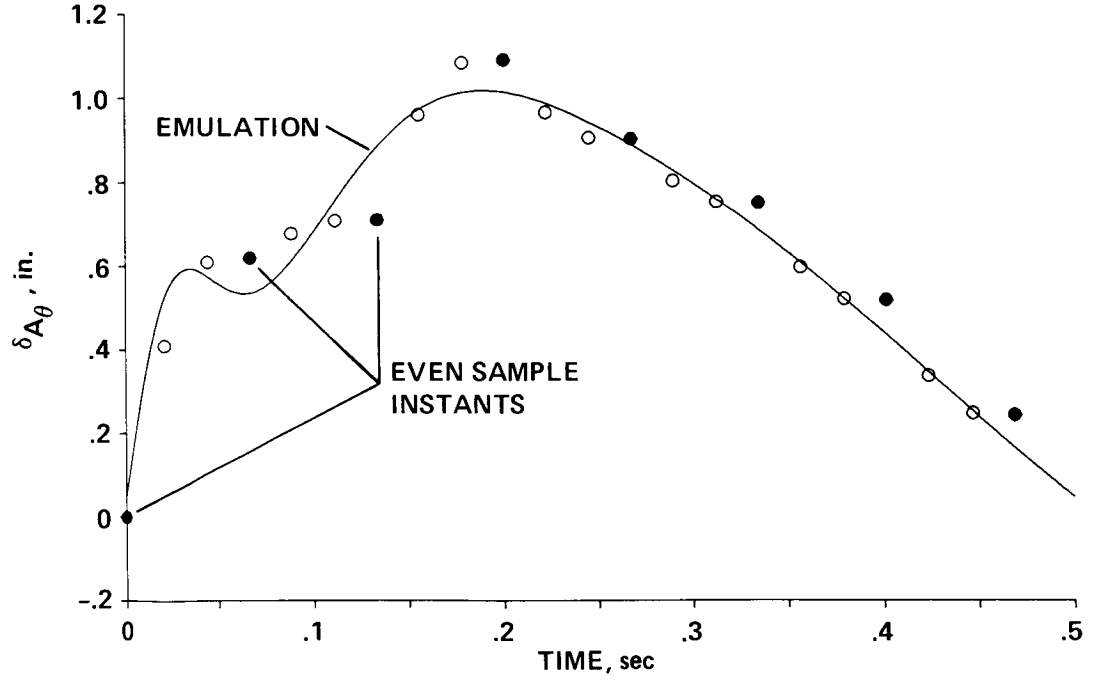

Figure 58.- ADOCS actuator deflection (δ_{A_θ}) response to a step input, δ_{c_θ} = 1; digital versus emulation analyses (15 Hz system).

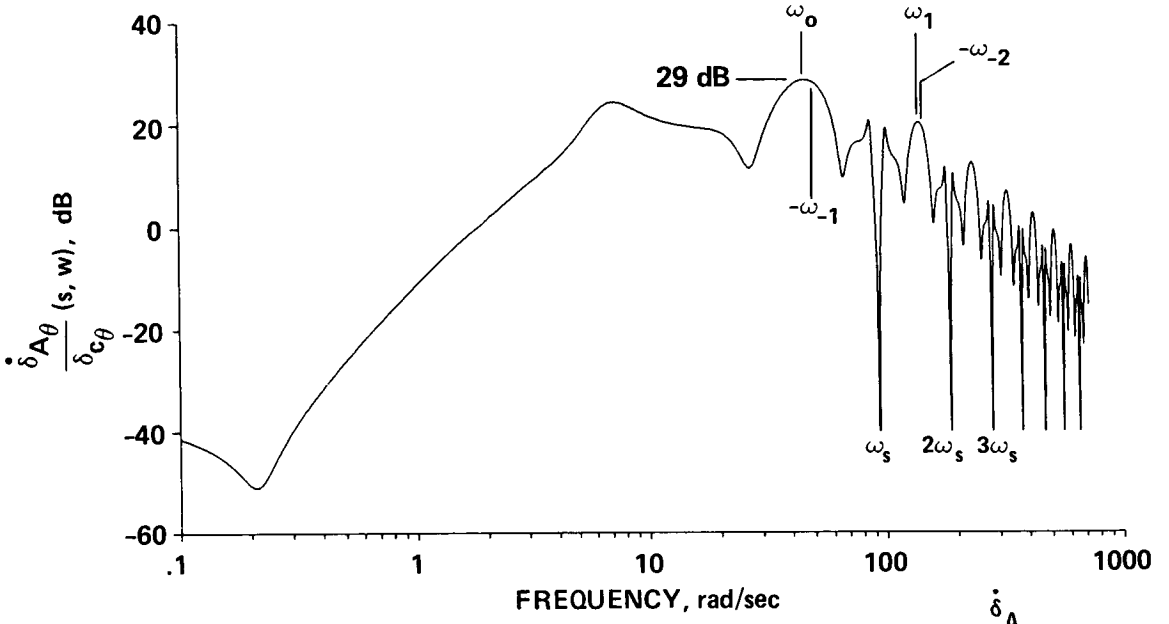

Figure 59.- Hybrid frequency response of the actuator rate $\frac{\dot{\delta}_{A_\theta}}{\delta_{c_\theta}}(s,w)$ (15 Hz system).

should be considered. Finally, there is a "crease" in the hybrid response for input frequencies $\omega = 94$ rad/sec ($= \omega_s$), which also roughly corresponds to double the frequency for peak response, $2\omega_o = 92$ rad/sec. Thus, the step response should "ring" at a period of twice the sample period ($2T = 0.134$ sec) and have no response at all at the even sample instnats! Reference to figure 57 shows that this is precisely the time-domain behavior.

III.J.4 Command Block Design- As discussed earlier in Sections III.C and E, the command block contains a feedforward element and a command model. In the digital design approach, the feedforward element is comprised of discrete inverse plant approximation and the effective discrete feedback equalization transfer function:

$$\frac{\delta_{c_\theta}}{\theta_m}(w) = P^{-1}(w) + H(w) \qquad (95)$$

One obvious approach for obtaining the inverse plant model is to use the zero-order hold equivalent of the attitude response, $(\theta/\delta_\theta)(w)$ which is obtained as in equation (74), but without the anti-alias filter. However, this transfer function contains nonminimum phase zeroes (caused by the zero-order hold) which yield unstable poles in the inverse model. Therefore, the zero-order hold equivalent model is not suitable for this purpose. Instead, it is necessary to use the w-plane Tustin transformed equivalent of the inverse s-plane model obtained from equation (25). For the 15 Hz sample rate, the w-plane inverse model is:

$P^{-1}(w)$ =

THE NUMERATOR ROOTS ARE:

NO.	REAL	IMAG.	OMEGA	ZETA
1	-0.60566300	0.00000000E+00		
2	0.24766069E-01	0.00000000E+00		

THE DENOMINATOR ROOTS ARE:
THERE ARE NO ROOTS

LOW-FREQUENCY GAIN = -0.45591764E-01 (96)

The second element of equation (95) is the effective discrete feedback equalization transfer function. While the combination of pitch rate and pitch attitude feedback with a lead compensation element gives the simple s-plane transfer function,

$$H(s) = \frac{\delta_f}{\theta} = (K_q s + K_\theta)[G_{1c}(s)] \tag{97}$$

the direct digital counterpart, H(w), is not so easily obtained. Unlike the Tustin transform, the w- and z-transforms do not have a cascade property,

$$H(w) = \frac{\delta_f^*}{\theta}(w) \neq \mathscr{W}[K_q s + K_\theta][G_{1c}(w)] \tag{98}$$

Instead, the required transfer function is (see fig. 31)

$$H(w) = \frac{\delta_f^*}{\theta}(w) = [K_\theta \frac{\bar{\theta}}{u}(w) + K_q \frac{\bar{q}}{u}(w)][\frac{u}{\theta}(w)][G_{1c}(w)] \tag{99}$$

where $(\bar{q}/u)(w)$ and $(\bar{\theta}/u)(w)$ are given in equations (87) and (88) and $G_{1c}(w)$ is given in equation (91).

In the analog system, the pitch attitude and rate response transfer functions have the same factors, except for the extra free s in the latter response. The resulting cancellations in the s-plane equivalent of equation (99) are the reason for the simple form of equation (97). Reference to equations (87) and (88) shows that the cancellation in equation (99) is far from complete, so the simple form of equation (97) is in general invalid. This illustrates numerically the fact stated in equation (98) that the w- and z-transforms do not have the cascade property of the s- and Tustin transforms.

While the exact expressions of equations (87) and (88) for the pitch responses could be used to determine H(w) in equation (99), this results in a very high order and unstable feedforward transfer function. Instead, the simplified pitch attitude and rate responses are obtained from the zero-order hold equivalents of the lower-order model of equation (26).

The resulting expression for H(w) is very simple and, in fact, is close to the form of equation (97):

$H(w) =$ (100)

THE NUMERATOR ROOTS ARE:

NO.	REAL	IMAG.	OMEGA	ZETA
1	-2.8299999	0.00000000E+00		
2	-1.0992508	0.00000000E+00		

THE DENOMINATOR ROOTS ARE:

NO.	REAL	IMAG.	OMEGA	ZETA
1	-5.6599998	0.00000000E+00		
2	-4534.3960	0.00000000E+00		

LOW-FREQUENCY GAIN = 9.0600000

Combining H(w) with the inverse plant model of equation (96) results in the final feedforward transfer function of:

$\frac{\delta_{c_\theta}}{\theta_m}(w) =$ (101)

THE NUMERATOR ROOTS ARE:

NO.	REAL	IMAG.	OMEGA	ZETA
1	-1.2385697	-0.54172087	1.3518567	0.91619899
2	-1.2385697	0.54172087	1.3518567	0.91619899
3	-9.1963329	0.00000000E+00		
4	-4528.9634	0.00000000E+00		

THE DENOMINATOR ROOTS ARE:

NO.	REAL	IMAG.	OMEGA	ZETA
1	-5.6599998	0.00000000E+00		
2	-4534.3960	0.00000000E+00		

LOW-FREQUENCY GAIN = 9.0144082

The θ/θ_m transfer function is obtained by combining the feedforward and closed-loop stabilization responses (eqs. (94) and (101)) giving the frequency response of figure 60. As in figure 38 for the 30.3 Hz system, good model following requires a magnitude ratio of unity (0 dB) with minimal phase lag. The digital frequency response seen in figure 60 indicates that good phase response following is preserved to about $\omega = 4$ rad/sec; this is achieved at the expense of significant magnitude distortions which peak at a frequency of about $\omega = 7$ rad/sec, corresponding to the closed-loop natural frequency of the coupled pitch/rotor mode. This is similar to the previous 30.3 Hz characteristic. The large peak in magnitude near the Nyquist frequency is due to the Tustin-transform implementation of the inverse plant model $P^{-1}(s)$. This peaking can be reduced by adjusting the w-plane parameters of the feedforward transfer function $(\delta_{c_\theta}/\theta_m)(w)$ as was done with the notch filter (Section III.J.2). This is not necessary in the present case because the command model $(\theta_m/\theta_c)(w)$ exhibits an attenuation peak in the same frequency range, which is also due to the Tustin transform. Thus, the combined command block $(\delta_{c_\theta}/\theta_c)(w)$ is well behaved near the Nyquist frequency.

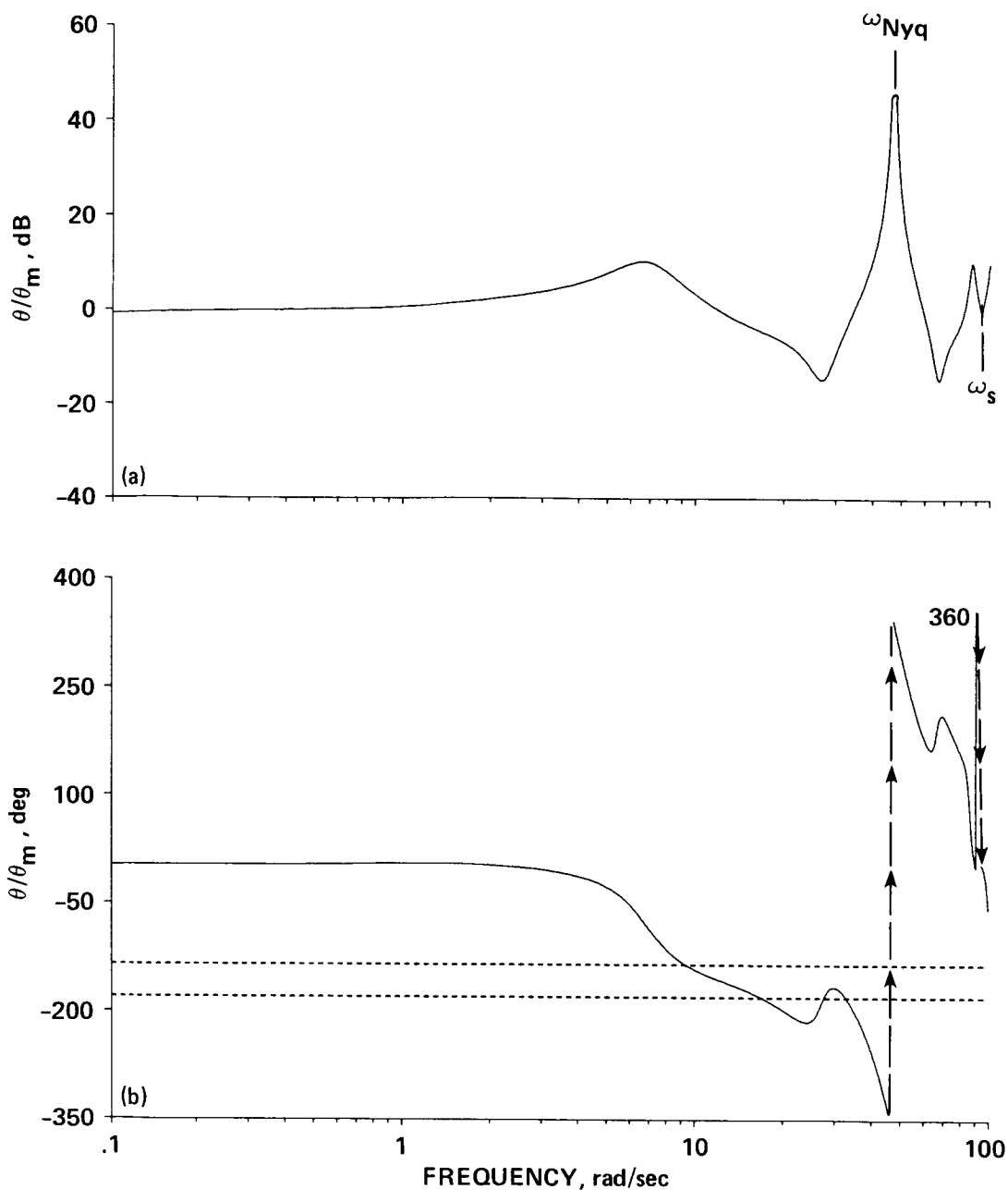

Figure 60.- Digital frequency response of θ/θ_m for the 15 Hz system. (a) Magnitude; (b) phase.

To implement the feedforward block of equation (101), a z-plane transfer function must be formed. This is completed using the w- to z-plane transformation of equation (17) which results in:

$$\frac{\delta_{c_\theta}}{\theta_m}(z) =$$ (102)

THE NUMERATOR ROOTS ARE:

NO.	REAL	IMAG.	OMEGA	ZETA
1	0.95979540	-0.17166601E-01	0.95994890	-0.99984009
2	0.95979540	0.17166601E-01	0.95994890	-0.99984009
3	0.73650379	0.00000000E+00		
4	-0.97358965	0.00000000E+00		

THE DENOMINATOR ROOTS ARE:

NO.	REAL	IMAG.	OMEGA	ZETA
1	0.82917349	0.00000000E+00		
2	-0.97362088	0.00000000E+00		
3	-1.0000000	0.00000000E+00		
4	-1.0000000	0.00000000E+00		

Z-PLANE DC GAIN (Z=1) = 9.0144082

As in the 30.3 Hz design, the second-order command model is generated using the Tustin transform procedure to convert from the s-plane transfer function of equation (39) to the following z-plane transfer function:

$$\frac{\theta_m}{\theta_c}(z) =$$ (103)

THE NUMERATOR ROOTS ARE:

NO.	REAL	IMAG.	OMEGA	ZETA
1	-1.0000000	0.00000000E+00		
2	-1.0000000	0.00000000E+00		

THE DENOMINATOR ROOTS ARE:

NO.	REAL	IMAG.	OMEGA	ZETA
1	0.90092629	-0.80155626E-01	0.90448499	-0.99606549
2	0.90092629	0.80155626E-01	0.90448499	-0.99606549

Z-PLANE DC GAIN (Z=1) = 1.0006295

The closed-loop w-plane transfer function from the command model input to pitch attitude output, $(\theta/\theta_c)(w)$ is obtained by combining the w-plane equivalent transfer functions of the model response (eq. (103)), the feedforward (eq. (102)) and the closed stabilization loop response (eq. (94)).

The overall digital response to stick inputs, θ/δ_s of figure 31 cannot in general be expressed in closed form. This is because, as in equation (98), the w-transform does not possess the cascade property, so:

$$\theta(w) = \mathcal{W}[\delta_s(s)G_f(s)e^{-Ts/2}]\ \frac{\theta}{\theta_c}(w) \tag{104}$$

$$\theta(w) \neq \delta_s(w)\mathcal{W}[G_f(s)e^{-Ts/2}]\ \frac{\theta}{\theta_c}(w) \tag{105}$$

so,

$$\frac{\theta}{\delta_s}(w) \neq \mathcal{W}[G_f(s)e^{-Ts/2}]\ \frac{\theta}{\theta_c}(w) \tag{106}$$

However, a good low-frequency solution ($\omega < 10$ rad/sec) can be obtained by approximating the stick filter of equation (47) by the pure time delay:

$$G_f(s) \doteq e^{-0.0335s} \tag{107}$$

which fits the actual response of equation (47) very well in the critical handling qualities range of $0.1 \leq \omega \leq 10$ rad/sec. Combining equation (107) with the stick sampling skew, $e^{-0.0335s}$, gives:

$$\theta(w) = \mathcal{W}[\delta_s(s)e^{-0.067s}]\ \frac{\theta}{\theta_c}(w) \tag{108}$$

The time delay is one full period (T = 0.067 sec), and so it is unaffected by the sampling process (refs. 17 and 30). Since $\mathcal{Z}[e^{-Ts}] = z^{-1}$, equation (108) becomes:

$$\frac{\theta}{\delta_s}(w) = \frac{[1 - (T/2)w]}{[1 + (T/2)w]}\ \frac{\theta}{\theta_c}(w) \tag{109}$$

which is the desired final closed-form result needed for frequency-response calculations.

The overall $j\omega$-frequency response of θ/δ_s is shown in the valid frequency range ($0.1 < \omega < 10$ rad/sec) in figure 61. The attitude bandwidth is gain margin limited as before:

$$\begin{aligned} \omega_{BW_\theta} &= 2.5 \text{ rad/sec} \\ \tau_p &= 0.280 \text{ sec} \end{aligned} \tag{110}$$

For comparison with previous results, figure 61 also shows the response of the 30.3 Hz system (repeated from fig. 39) and the response of the command model (eq. (103)). The 15 Hz and 30.3 Hz system responses are nearly identical for frequencies $\omega < 5$ rad/sec, which is why the bandwidths of the two systems are the same (compare eqs. (110) and (54)). At higher frequencies, the difference between the systems is mostly in the phase response; this is reflected in the phase delay of the 15 Hz system being 63 msec higher than for the 30.3 Hz system. Also shown in figure 61 is the response of the analog command model (eq. (39)). The poor model-following performance of the 15 Hz system suggests the elimination of the command block (model and feedforward) entirely, using simple response feedback for a low sample rate backup digital system.

The exact discrete time response to a unit step, $\delta_s = 1/s$, is obtained (following eq. (104)) from:

$$\theta(t) = \mathcal{Z}^{-1}\left[\mathcal{Z}\left(\frac{1}{s} G_f(s)e^{-Ts/2}\right)\frac{\theta}{\theta_c}(z)\right] \qquad (111)$$

and is plotted in the solid dots of figure 62. Numerical precision is maintained up to t = 4.0 sec. The resulting handling qualities criterion times are:

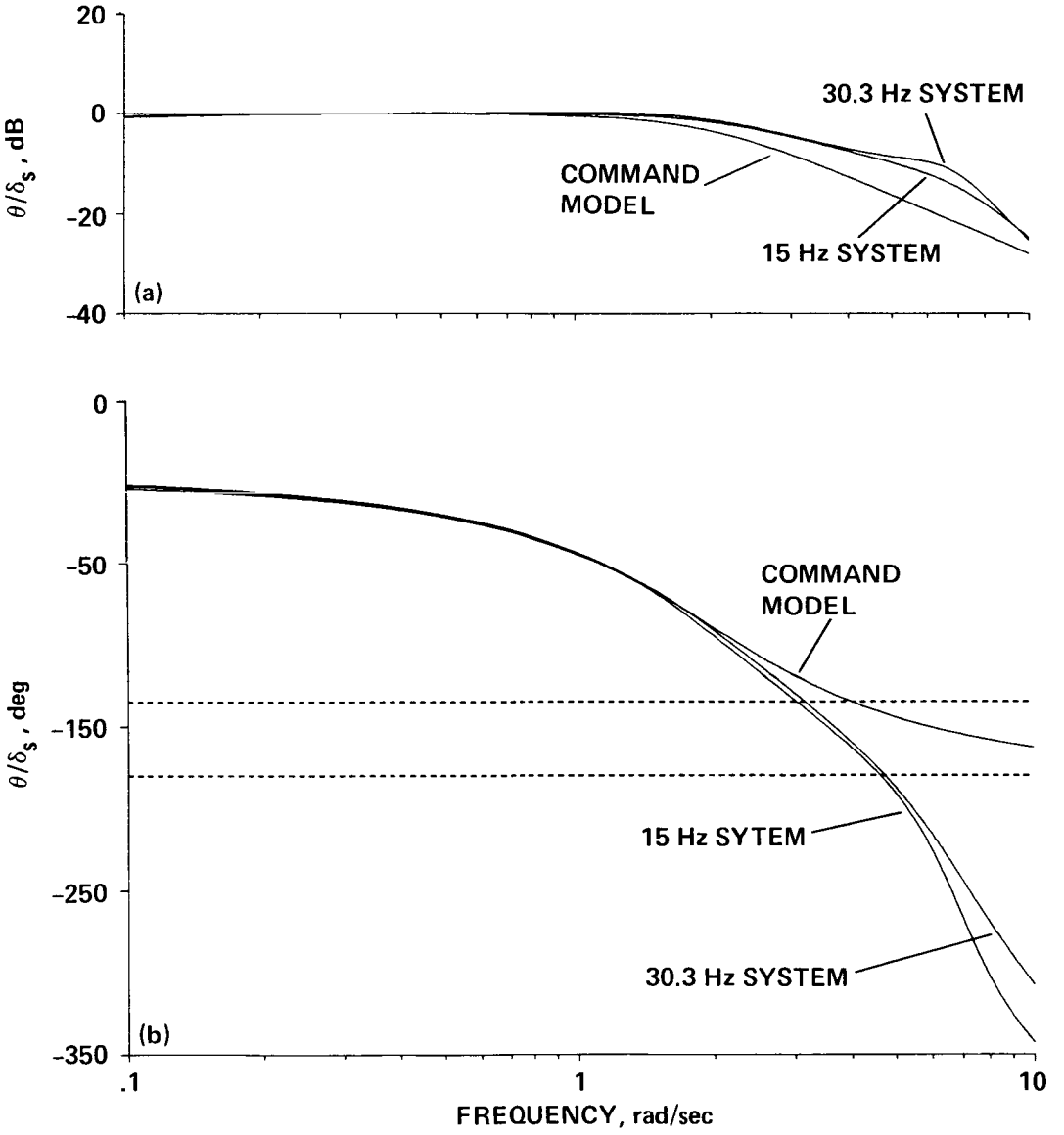

Figure 61.- Comparison of the overall frequency responses (θ/δ_s) for the 15 Hz and 30.3 Hz systems and command model. (a) Magnitude; (b) phase.

$$t_{R_{10}} = 0.44$$

$$t_{R_{50}} = 0.76 \qquad (112)$$

$$t_{R_{90}} = 1.39$$

$$\zeta_e = 0.78 \ (\doteq \text{command model damping ratio})$$

The discrete time response of the 30.3 Hz system (determined from eq. (112) using the appropriate 30.3 Hz transfer functions) is shown in the open dots of figure 62. As expected from the frequency response comparison of figure 61, the time responses of the two systems are nearly identical, except for the larger time delay for the 15 Hz system. This difference is also reflected in the higher delay time $t_{R_{10}}$ for the 15 Hz system.

III.J.5 Maximum Achievable Pitch Attitude Response, $(\theta_1)_{max}$- The digital response to a ramp-step stick input is determined as in eq. (111), but with an alteration to δ_s. The ramp time must be an integer multiple of the cycle time (T = 0.067 sec), so the closest value is taken, Δt = 0.469 sec. A ramp input which reaches unity at t = 0.469 sec is described by:

$$\delta_{s_1} = \frac{2.132}{s^2} \qquad (113)$$

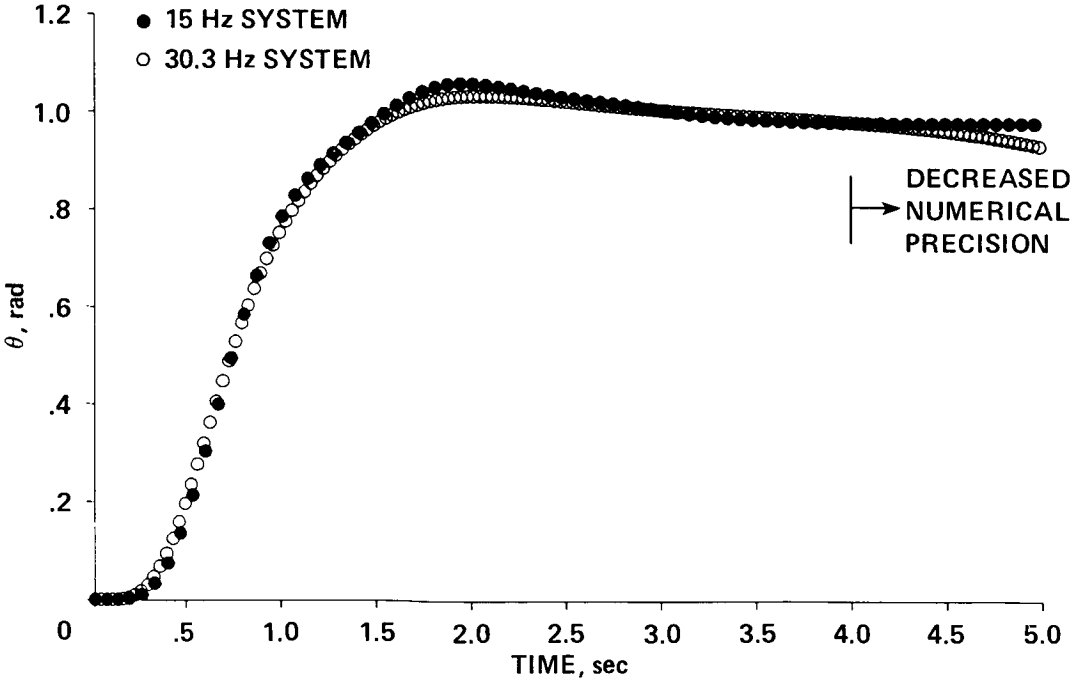

Figure 62.- Comparison of the pitch attitude step responses of the 15 Hz and 30.3 Hz digital systems.

Substituting equation (113) into equation (111) and evaluating the inverse z-transform yields the response to a pure-ramp. The calculation is now repeated for a negative ramp $-\delta_{s_1}$, but the time axis is shifted to make the input begin at t = 0.469 sec. If these two ramp responses are summed, the desired ramp-step is achieved.

The resulting pitch attitude (θ), swashplate angle (δ_{s_θ}) and swashplate rate ($\dot{\delta}_{s_\theta}$) responses are shown in figure 63(a), (b), and (c). Numerical precision is maintained for the full 5 sec duration. The expanded time scale plots of swashplate responses in figure 63(d) and (e), show that the level of intersample ripple in the rate response is only slightly reduced from that displayed in the ADOCS actuator rate response of figure 57. (Now the rate is nonzero at the even sample instants.) Comparing the swashplate responses with the analogous results for the 30.3 Hz digital system (fig. 50) shows that the intersample rate response has now been substantially increased. This is reflected in the maximum achievable attitude response:

$$\left(\frac{\dot{\delta}_{s_\theta}}{\theta_1}\right)_{max} = \frac{68.3}{(0.53)(57.3)} = 2.25 \text{ in./sec/deg in 1 sec} \qquad (114)$$

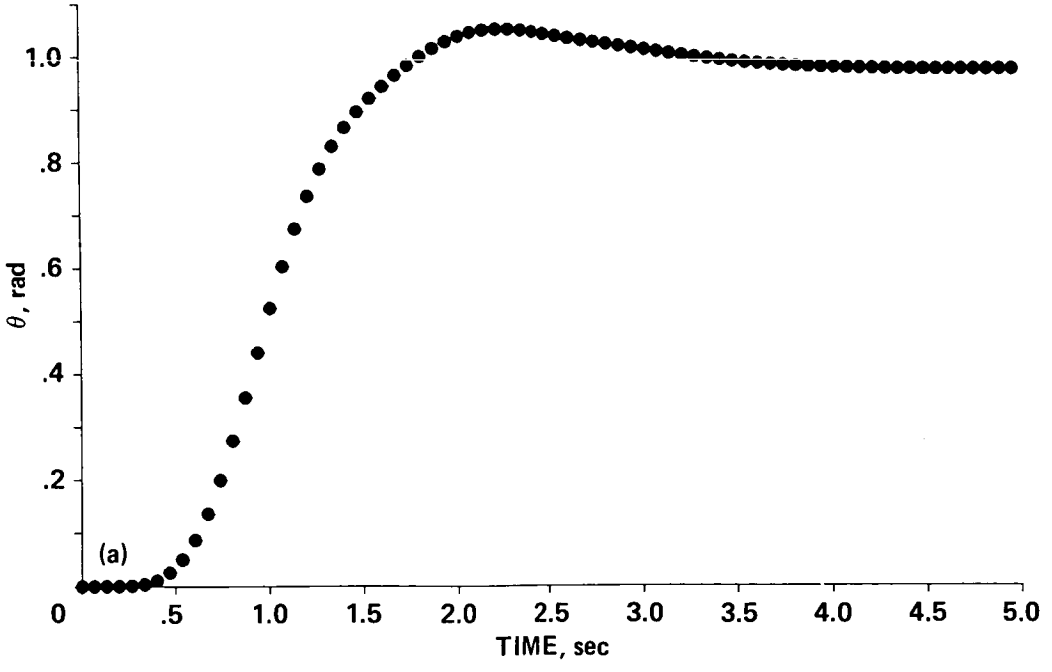

Figure 63.- Response to a ramp-step stick input (Δt = 0.469 sec) for the 15 Hz digital system. (a) Pitch attitude (θ); (b) swashplate angle (δ_{s_θ}); (c) swashplate rate ($\dot{\delta}_{s_\theta}$); (d) expanded time scale replot of δ_{s_θ}; (e) expanded time scale replot of $\dot{\delta}_{s_\theta}$.

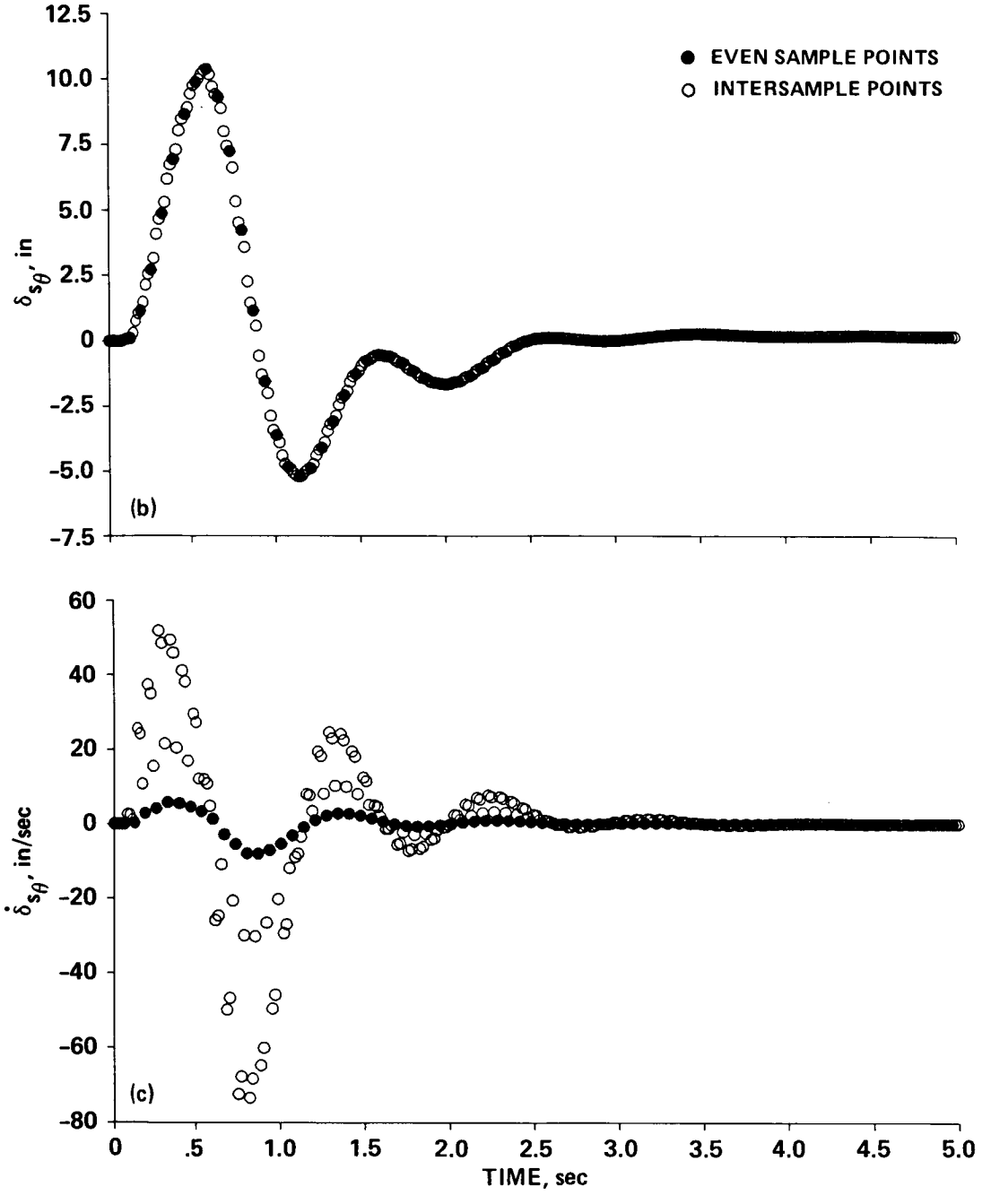

Figure 63.- Continued.

which for a maximum rate of 10 in./sec yields:

$$(\theta_1)_{max} = 4.5 \text{ deg}$$

This capability is just below the suggested value of $\theta_1 = 5$ deg, and is 33% below the level for the 30.3 Hz digital system. (The $(\theta_1)_{max} = 4.5$ deg value is slightly conservative because of the 5% reduction in ramp time.) This analysis shows that

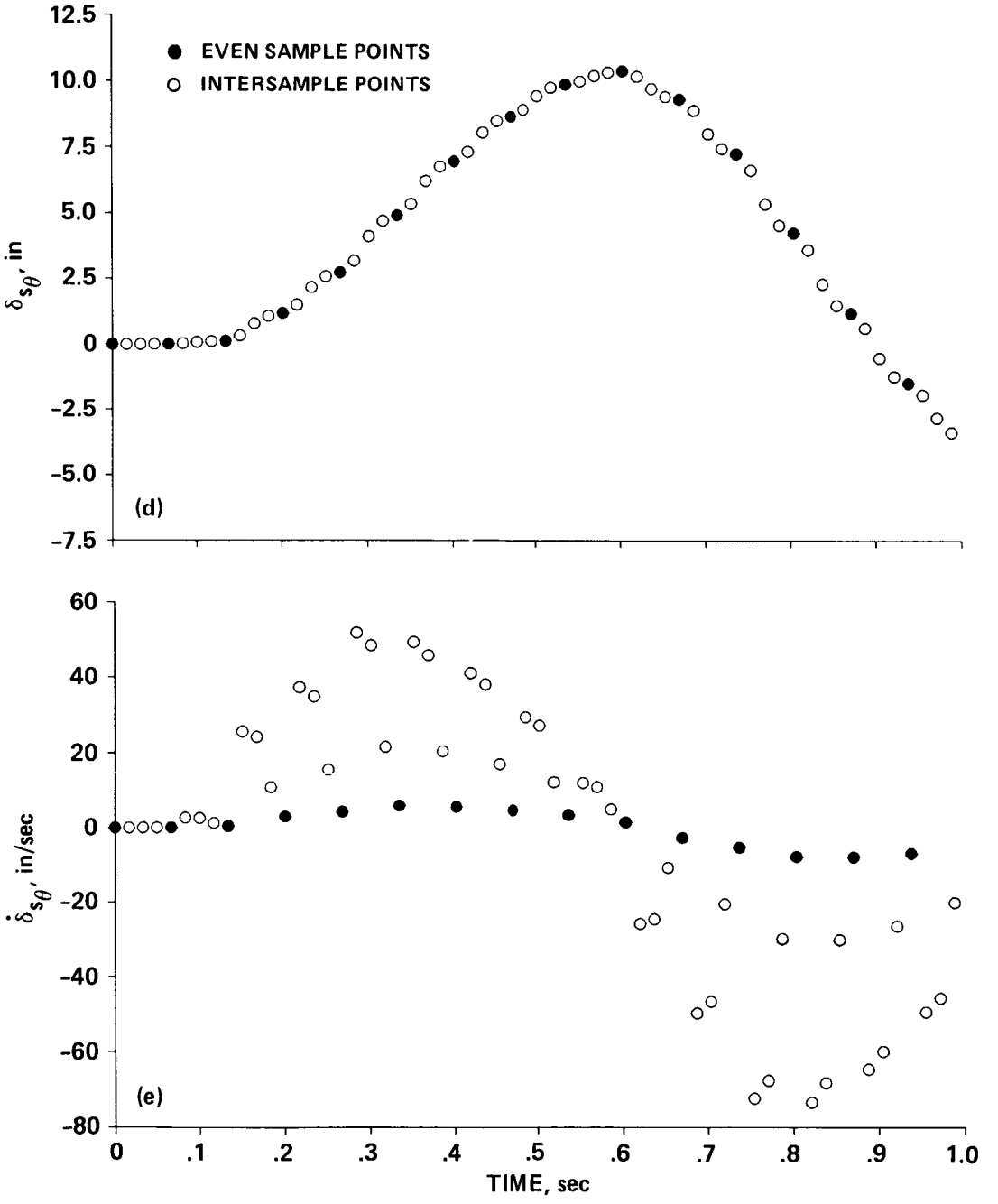

Figure 63.- Concluded.

for a desired level of overall performance (ω_{BW}, $(\theta_1)_{max}$), the minimum sample rate is limited by the actuator rate-authority.

III.J.6 Assessment of Direct Digital Design and Analysis Techniques- The preceding discussion illustrates the key aspects of direct digital design and analysis. The 15 Hz system displays the same overall bandwidth (and roughly the same 50%

rise time) as the 30.3 Hz digital system, but the phase delay is about 30% greater and the maximum attitude response is about 33% lower. Also, the gain margin of the 15 Hz system is reduced by 2.5 dB. While probably not desirable as a nominal operational configuration, this lower performance system is suitable as a low sample rate, digital backup system.

The overall attitude response dynamics of the 15 Hz (relatively low sample rate) configuration are still adequately modeled by emulation techniques. However, significant digital effects which have been exposed in the higher frequency elements, such as the actuator and notch filter, and on the flexible structure mode stability margins clearly demonstrate the need for direct digital methods. The wide availability of modern interactive analysis programs should reduce the engineer's apprehension in applying direct digital methods.

III.K Case Study Assessments and Conclusions

This case study has discussed the design and analysis of four control systems for the UH-60 based on the ADOCS model-following concept:

System A: Nominal s-plane system, ω_{c_θ} = 6 rad/sec, ω_s = 40 Hz.

System B: Practical s-plane control system implementation, ω_{c_θ} = 4 rad/sec, ω_s = 30.3 Hz.

System C: Practical digital system implementation, ω_{c_θ} = 4 rad/sec, ω_s = 30.3 Hz.

System D: Low sample rate digital system, ω_{c_θ} = 4 rad/sec, ω_s = 15 Hz.

Table 5 compares the overall frequency and time domain performance metrics for these systems relative to the command model and the more restrictive LHX specifications of reference 50.

A number of important conclusions can be drawn from the comparison shown in table 5:

1. All four systems fail the Level I, 100 msec requirement on phase delay, τ_p, while system A passes the comparable delay time test, $t_{R_{10}}$. The practical 4 rad/sec, 30.3 Hz system exhibits over 200 msec of phase delay, nearly double that of the nominal system.

2. All four systems pass the Level I requirements on rise time given in terms of $t_{R_{50}}$ and $t_{R_{90}}$, while systems B, C, and D fail the comparable bandwidth specification, ω_{BW_θ}.

3. Conclusions 1 and 2 above indicate that the frequency-domain specifications are more restrictive than the time-domain specifications.

TABLE 5.- SUMMARY OF PERFORMANCE RESULTS

System	ω_{BW_θ}, rad/sec	τ_p, msec	$t_{R_{10}}$, sec	$t_{R_{50}}$, sec	$t_{R_{90}}$, sec	θ_1, deg
Reference 50 Spec requirements (ζ = 0.75)	>3.0	<100	<0.34	<1.0	<1.92	>5
Command model	3.8	0	0.26	0.75	1.48	---
System A s-plane 6 rad/sec, 40 Hz	3.6	117	0.32	0.71	1.43	9.0
System B s-plane 4 rad/sec, 30.3 Hz	2.5	217	0.41	0.75	1.33	7.6
System C digital 4 rad/sec, 30.3 Hz	2.5	217	0.41	0.75	1.33	6.7
System D digital 4 rad/sec, 15 Hz	2.5	280	0.44	0.76	1.39	4.5

4. Systems A, B, and C meet the requirement of achieving 5 deg of pitch attitude within 1 sec, while system D marginally exceeds this limit.

Some key ideas which were introduced in Sections I and II and illustrated in this case study are:

5. The ADOCS model-following concept will provide task-tailored handling qualities, with independent control of disturbance and command responses provided that reasonable separation is maintained between the stabilization loop crossover frequency and the command model natural frequency.

6. The high bandwidth specifications for combat rotorcraft result in closed-loop dynamics which are dominated by the control system parameters and the high-frequency response of the basic aircraft elements.

7. The ADOCS UH-60 rotor/actuator system alone absorbs the traditionally recommended time-delay limit for high precision tasks of τ_p = 100 msec, while the practical 30.3 Hz digital system exhibits over twice this value. Combat rotorcraft that are expected to perform the highly agile and precise maneuvering tasks of the LHX must have faster actuator/rotor systems and reduced lags in the control system elements.

8. Reasonable predictions of the closed-loop digital performance of advanced combat rotorcraft require careful consideration of many system elements and requirements often neglected in the preliminary control system design studies. These considerations are:

Anti-alias filtering
Biodynamic interference
Lead-lag rotor mode dynamics
Throughput requirements and sample rate reduction
Stick sampling skew
Actuator authority limits

These considerations result in significantly higher phase lags and lower achievable crossover frequencies than are predicted in simplified preliminary design studies.

9. Besides the stability and performance analyses which are common in the state-of-the-art design of analog and digital rotorcraft systems, successful rotorcraft digital control system design requires careful direct digital analysis in the following important areas:

Aliasing of high-frequency noise, especially rotor and structural vibrations

Digital frequency responses of the higher frequency dynamic elements

Intersample response of the control system elements closest to the zero-order hold. Coordinated analyses of the interrelation of actuator authority, desired maximum attitude response, sample rate selection, and monitoring requirements

Combined effect of computational time-delay and lightly damped structural modes on closed-loop stability margins

Control law design for low sample-rate digital backup systems

10. The availability of comprehensive computer-aided interactive tools is essential for analyzing modern rotorcraft systems. Computer tools must allow easy transition between analog (s-plane) and discrete (z- and w-plane) representations.

IV. SUMMARY

This report has presented a review of state-of-the-art digital control technology for application to advanced combat rotorcraft and a case study illustration of the key concepts in system design and analysis. Among the most heavily stressed general concepts in this report are:

1. The attainable bandwidth of high gain flight control systems has consistently been overestimated in design studies; this overestimation is generally not exposed until after hardware implementation and flight test.

2. Command response delays have historically been a key cause of handling qualities deficiencies in high bandwidth systems; time delay-related handling qualities deficiencies are generally not exposed in piloted simulations conducted during the preliminary design phase. Equivalent time delays can be rapidly accumulated in the actuator/rotor system, filters, and software architecture used in modern combat rotorcraft. Therefore, careful design and analysis are needed to anticipate and minimize unnecessarily large delays.

3. Biodynamic interference effects are present in all small displacement sidestick systems. Rotorcraft are especially susceptible to these effects because of high levels of rotor and structural vibration. Methods for eliminating biodynamic interference must be further studied and flight tested.

4. Frequency domain modeling and analysis are essential for developing the physical understanding needed to implement practical high bandwidth control systems in modern combat rotorcraft--regardless of the method of control system design (modern or classical control).

5. Block diagram development in the preliminary design phase must anticipate the numerous special elements of a practical digital system in order to reduce the heavy and costly reliance on redesign and design optimization during the flight testing phase.

7. Emulation analysis is useful for preliminary design and performance tradeoff studies, but direct digital analysis is necessary to accurately evaluate the many important high-frequency dynamic characteristics of a modern digital system.

8. The analysis methods presented in this report require the availability of flexible, interactive computational tools.

REFERENCES

1. Andreson, Ronald K. (B.G. USAF): Light Helicopter Family (LHX) Program Overview. Vertiflite, Nov./Dec. 1986, pp. 22-24.

2. Van Vliet, Brian W.: Flight Testing a Digital Flight Control System: Issues and Results. Paper 7, AGARD Flight Test Techniques, Lisbon, Portugal, April 1984, pp. 24-01 to 24-10.

3. Moran, W. A.: Operational and Developmental Experience With the F/A-18A Digital Flight Control System. AGARD CP-384: Active Control Systems: Review, Evaluation and Projections. 1984, pp. 12A-1 to 12A-13.

4. Korte, U.: Some Flight Test Results With Redundant Digital Flight Control Systems. AGARD CP-384: Active Control Systems: Review, Evaluation and Projections, 1984, pp. 9-1 to 9-14.

5. Powers, B. G.: Active Control Technology Experience With the Space Shuttle in the Landing Regime. NASA TM-85910, 1984.

6. McClellan, R. D.; and Spruer, W. E.: Test Report for the Flying Qualities Demonstration, YAH-64 Advanced Attack Helicopter. (Rep. No. 77-FT-8012-2, Hughes Helicopters, Inc.; Contract No. DAAJ01-77-C-0064.), 1981.

7. Landis, Kenneth H.; and Glusman, Steven I.: Development of ADOCS Controllers and Control Laws. Vol. 1, Executive Summary; Vol. 2, Literature Review and Preliminary Analysis; Vol. 3, Simulation Results and Recommendations. (D210-12323-1, -2, -3, Boeing Vertol Company; NASA Contract NAS2-10880.) USAAVSCOM TR84-A-7, also NASA CR-177339, 1985.

8. Glusman, Steven I.; Landis, Kenneth H.; and Dabundo, Charles: Handling Qualities Evaluation of the ADOCS Primary Flight Control System. 42nd Annual Forum of the American Helicopter Society, Washington, DC, June 1986.

9. Hendrick, Russell; Ramohalli, Gautham; Yanke, David; Fortenbaugh, Robert; and Freeman, Thomas: Advanced Flight Control Development for Single-Pilot Attack Helicopters. 42nd Annual Forum of the American Helicopter Society, Washington, DC, June 1986.

10. Velger, M.; Merhav, S.; and Grunwald, A.: Effects of Adaptive Filtering in Manual Control on Board Moving Platforms. TAE 583, Technion Israel Institute of Technology, 1985.

11. McRuer, D. T.; Johnston, D.; and Myers, T.: A Perspective on Superaugmented Flight Control Advantages and Problems. AGARD Conference on Active Control Systems, Ontario, Canada, October 1984.

12. Ly, Uy-Loi; Bryson, Arthur E.; and Cannon, Robert H.: Design of Low-Order Compensators Using Parameter Optimization. Automatica, vol. 21, no. 3, 1985, pp. 315-318.

13. Doyle, J. D.; and Stein, G.: Multivariable Feedback Design: Concepts for a Classical/Modern Synthesis. IEEE Trans. on Automatic Control, vol. AC-26, no. 1, February 1981, pp. 4-16.

14. Hoh, Roger H.; Mitchell, David G.; Ashkenas, Irving L.; Klein, Richard H.; Heffley, Robert K.; and Hodgkinson, John: Proposed Mil Standard and Handbook--Flying Qualities of Air Vehicles. Vol. II, Proposed MIL Handbook. (AFWAL-TR-82-3081, Vol. 2, Systems Technology Incorporated; F33615-80-C-3604.) AFWAL-TR-82-3081, 1982.

15. Hoh, Roger H.; Mitchell, David G.; Ashkenas, Irving L.; Aponso, Bimal L.; Ferguson, Samuel W.; Rosenthal, Theodore J.; Key, David L.; and Blanken, Chris L.: Background Information and User's Guide for Proposed Handling Qualities Requirements for Military Rotorcraft. STI TR-1194-3, December 20, 1985.

16. Atzhorn, David; and Stengel, Robert F.: Design and Flight Test of a Lateral-Directional Command Augmentation System. J. of Guidance, Control and Dynamics, vol. 7, no. 3, 1984, pp. 361-368.

17. Whitbeck, R. F.; and Hofmann, L. G.: Analysis of Digital Flight Control Systems With Flying Qualities Applications. Volume II. Technical Report. (TR-1101-1, Systems Technology, Inc.; Contract No. F33615-77-C-3026.) AFFDL-TR-78-115, 1978.

18. Chen, Robert T. N.; and Hindson, William S.: Influence of High-Order Dynamics on Helicopter Flight-Control System Bandwidth. J. of Guidance, Control, and Dynamics, vol. 9, no. 2, 1986, pp. 190-197.

19. Katz, Paul: Digital Control Using Microprocessors. Prentice/Hall International, 1981.

20. Franklin, Gene F.; and Powell, J. David: Digital Control of Dynamic Systems. Addison-Wesley Publishing Company, 1980.

21. Konar, A. Ferit; Mahesh, J. K.; and Kizilos, B.: Digital Flight Control System for Tactical Fighter, Volume I. (F-0131-IR1, 08001, Honeywell Inc.; Contract F33615-72-C-1058.) AFFDL-TR-73-119, 1974.

22. Whitbeck, R. F.; and Hofmann, L. G.: Digital Control Law Synthesis in the W' Domain. J. of Guidance and Control, vol. 1, no. 5, 1978, pp. 319-326.

23. McLees, R. E.: Design Aids for Digital Control Systems--A Survey. Doc. no. D6-48896TN, The Boeing Company, 1984. (Available from DTIC and Boeing Commercial Airplane Company, Attn: Technical Library, Seattle, WA.)

24. Katz, Paul: Selection of Sampling Rate for Digital Control of Aircraft. Ph.D. dissertation, Stanford University, Dept. of Aeronautics and Astronautics, Stanford, CA, September 1974.

25. Berry, D. T.; Powers, B. G.; Szalai, K. J.; and Wilson, R. J.: A Summary of an In-Flight Evaluation of Control System Pure Time Delays During Landing Using the F-8 DFBW Airplane. AIAA Paper 80-1626, AIAA Atmospheric Flight Mechanics Conference, Danvers, MA, August 1980.

26. Hodgkinson, J.; and Johnston, K. A.: Initial Results of an In-Flight Simulation of Augmented Dynamics in Fighter Approach and Landing. AIAA Paper 79-1783, Guidance and Control Conference, Boulder, CO, 1979.

27. Hess, Ronald A.: The Effects of Time Delays on Systems Subject to Manual Control. AIAA Paper 82-1523, Guidance and Control Conference, San Diego, CA, August 1982, pp. 165-172.

28. Ferguson, Samuel W.; Clement, Warren F.; Cleveland, W. B.; and Key, David L.: Assessment of Simulation Fidelity Using Measurements of Piloting Technique in Flight. 40th Annual Meeting of the American Helicopter Society, Arlington, VA, 1984, pp. 67-92.

29. Walker, Laurence A.; and LaManna, William J.: Development of the F/A-18 Handling Qualities Using Digital Flight Control Technology. SETP Technical Review, 1982 Report to the Aerospace Profession; 26th Symposium Proceedings, 1982, pp. 41-67.

30. Jury, E. I.: Sampled-Data Control Systems. John Wiley and Sons, Inc., 1958.

31. Ragazzini, John R.; and Franklin, Gene F.: Sampled-Data Control Systems. McGraw-Hill Book Company, Inc., 1985.

32. Truxal, John G.: Automatic Feedback Control System Synthesis. McGraw-Hill Book Company, Inc., 1955.

33. Kuo, Benjamin C.: Digital Control Systems. Holt, Rinehart and Winston, Inc., 1980, 2nd ed.

34. Lee, E. A.: Stability Analysis of Multi-Loop Digital Autopilots With Computational Delay and Sampling Skews. Rep. TOR-0073(3413-02)-8, The Aerospace Corporation, El Segundo, CA, 1972. (Available from SAMSO (LTV).)

35. Holzman, J.; Neumann, J. W.; Rockey, R. J.; Calcar, H. Van; and Wakamiya, Y.: Digital Control System Design for Saturn Class Vehicles. Vol. II., NASA CR-62968, 1965, and Digital Control System Design for Saturn Class Vehicles--Techniques for Missiles. Vol. III, Digital Control System Design For Saturn Launch Vehicles, NASA CR-62974, 1965.

36. Greensite, A. L.: Analysis and Design of Space Vehicle Flight Control Systems. Vols. I and II. Spartan Books, New York, 1970.

37. Lee, Eugene A.: LCAP2-Linear Controls Analysis Program. IEEE Control Systems Magazine, vol. 2, no. 4, December 1982, pp. 15-18.

38. Mahesh, J. K.; Konar, A. F.; and Ward, M. D.: Interactive Flight Control System Analysis Program, Vol. II, Digikon IV User Reference Manual, Honeywell Inc., Minneapolis, MN, F0789-TR, NASA Contract NAS1-16438, 1982.

39. Isermann, Rolf: Digital Control Systems. Rev. and enl. translation of Digital Regelsysteme. Springer-Verlag (Berlin, New York, Heidelberg), 1977.

40. Phillips, Charles L.; and Nagle, H. Troy, Jr.: Digital Control System Analysis and Design. Prentice-Hall, Inc., 1984.

41. Saucedo, Roberto; and Schiring, Earl E.: Introduction to Continuous and Digital Control Systems. The Macmillan Company, 1968.

42. Beh, H.; Korte, U.; and Loebert, G.: Stability and Control Aspects of the CCV-F104G. Paper 33, AGARD Flight Mechanics Panel Meetings on Stability and Control, Ottawa, Canada, September 1978.

43. Matrix User's Guide, Version 5.0. Integrated Systems Inc., 1985.

44. CTRL-C. A Language for the Computer-Aided Design of Multivariable Control Systems. Systems Control Technology, 1983.

45. Landis, K. H.; Dunford, P. J.; Aiken, Edwin W.; and Hilbert, Kathryn B.: Simulator Investigation of Side-Stick Controller/Stability and Control Augmentation Systems for Helicopter Visual Flight. J. Amer. Helicopter Soc., vol. 30, no. 2, 1985, pp. 3-13.

46. Tactical Aircraft Guidance System Advanced Development Program Flight Test Report, Vols. 1 and 2, Boeing Vertol Co., Philadelphia, PA, Doc. No. D214-40006-1, -2, June 1972.

47. Advanced Technology Component Program Flight Control System--Task 1--Summary Report. Boeing Vertol Co., Philadelphia, PA, Doc. No. D301-10095-1, December 1971.

48. Anonymous: Helicopter Flying and Ground Handling Qualities; General Requirements For, MIL-H-8501A, 1961.

49. Hoh, Roger H.; and Ashkenas, Irving L.: Development of VTOL Flying Qualities Criteria for Low Speed and Hover. (TR-1116-1, Systems Technology, Inc.; Contract N62269-77-C-0278.) NADC-77052-30, 1979.

50. Clement, Warren F.; Hoh, Roger H.; Ferguson, Samuel W.; Mitchell, David G.; Ashkenas, Irving L.; and McRuer, Duane T.: Specification and Background Information and User's Guide (BIUG) for Flying and Ground Handling Qualities of the LHX. STI TR 1194-2, May 29, 1985.

51. Mitchell, David G.; and Hoh, Roger H.: Preliminary Results of Flight Tests Conducted in Support of MIL-H-8501A Upgrade. (WP No. 1194-100-2, Systems Technology, Inc.; NASA Contract NAS2-11304.) 1985.

52. Ringland, Robert F.; and Clement, Warren F.: Systems Definition Phase NAVTOLAND Rotary Wing Program, SH-2F Control Laws Development. Vol. I, Analytical Development. Rep. STI-TR-1177-1, Vol. I, Systems Technology Inc., 1981. (Available from NASC as NADC-80251-60 or COMNAVAIRDEVCEN.)

53. Heffley, Robert K.: A Compilation and Analysis of Helicopter Handling Qualities Data. Vol. Two. Data Analysis. (STI TR No. 1087-2, Systems Technology, Inc.; NASA Contract NAS2-9344.) NASA CR-3145, 1979.

54. McRuer, Duane T.; Ashkenas, Irving; and Graham, Dunstan: Aircraft Dynamics and Automatic Control. Princeton University Press, 1974.

55. McRuer, D. T.; Ashkenas, I. L.; and Pass, H. R.: Analysis of Multiloop Vehicular Control Systems. TD-ASD-TDR-62-1014, Systems Technology, 1964. (Available from DDC as ASD-TDR-62-1014.)

56. Curtiss, H. C., Jr.: Stability and Control Modelling. Twelfth European Rotorcraft Forum, Garmisch-Partenkirchen, Federal Republic of Germany, Sept. 1986.

57. Johnson, Wayne: Helicopter Theory. Princeton University Press, 1980.

58. Foster, W. C.; Gieseking, D. L.; and Waymeyer, W. K.: A Nonlinear Filter for Independent Gain and Phase (With Applications). J. of Basic Engineering, no. 2, June 1966, pp. 457-462.

59. Tischler, Mark B.; Fletcher, Jay W.; Diekmann, Vernon L.; Williams, Robert A.; and Cason, Randall W.: Demonstration of Frequency-Sweep Testing Technique Using a Bell 214-ST Helicopter. NASA TM 89422 and USAAVSCOM Technical Memorandum 87-A-1.

60. Peled, U.: A Design Method With Application to Prefilters and Sampling-Rate Selection in Digital Flight Control Systems. Ph.D. Dissertation, Stanford University, Stanford, CA, 1978.

61. Borow, M. S.; Gaabo, R. O.; Hendrick, R. C.; Konar, A. F.; Lahn, T. G.; Markusen, D. L.; Smith, F. L.; Schmitz, H. G.; and Sowada, D. J.: Navy Digital Flight Control System Development. Honeywell, Inc., Minneapolis, MN, Document No. 21857-FR, Defense Logistic Agency. CNT: N62269-72-C-0141, 1972.

62. Allen, Merle G.: AFTI/F-16 Pilot Coupled Roll Oscillation. AIAA Paper 83-2282, AIAA Guidance and Control Conference, Gatlinburg, Tennessee, 1983.

63. Bryson, Arthur E., Jr.: Control of Spacecraft and Aircraft. Published by author. Stanford University, Stanford, CA, 1985.

NASA
National Aeronautics and Space Administration

Report Documentation Page

1. Report No.	2. Government Accession No.	3. Recipie
NASA TM-88346 USAAVSCOM TR 87-A-5		

4. Title and Subtitle

Digital Control of Highly Augmented Combat Rotorcraft

5. Report

May 1987

6. Performing Organization Code

7. Author(s)

Mark B. Tischler

8. Performing Organization Report No.

A-86369

10. Work Unit No.

992-21-01

9. Performing Organization Name and Address

Ames Research Center, Moffett Field, CA 94035
Aeroflightdynamics Directorate, U. S. Army Aviation Research and Technology Activity, Ames Research Center, Moffett Field, CA 94035-1099

11. Contract or Grant No.

13. Type of Report and Period Covered

Technical Memorandum

12. Sponsoring Agency Name and Address

National Aeronautics and Space Administration
Washington, DC 20546-0001 and U. S. Army Aviation Systems Command, St. Louis, MO 63120-1798

14. Sponsoring Agency Code

15. Supplementary Notes

Point of Contact: Mark B. Tischler, Ames Research Center, M/S 211-2
Moffett Field, CA 94035 (415) 694-5563 or FTS 464-5563

16. Abstract

Proposed concepts for the next generation of combat (scout/attack) helicopters are to be embodied in a complex, highly maneuverable, multiroled vehicle with avionics systems which are as important to mission success as the airframe itself. Single pilot and nap-of-the Earth operations require handling qualities which minimize the involvement of the pilot in basic stabilization tasks. To meet these requirements will demand a full authority, high-gain, multimode, multiply-redundant, digital flight-control system. The gap between these requirements and current low-authority, low-bandwidth operational rotorcraft flight-control technology is considerable. This research aims at smoothing the transition between current technology and advanced concept requirements. The report: (a) extensively reviews the state of the art of high-bandwidth digital flight-control systems; (b) exposes areas of the specific concern for flight-control systems of modern combat; and (c) illustrates the important concepts in design and analysis of high-gain, digital systems with a detailed case study involving a current rotorcraft system.

17. Key Words (Suggested by Author(s))	18. Distribution Statement
Rotorcraft Digital control Automatic flight-control systems Handling qualities	Unclassified-Unlimited Subject Category - 08

19. Security Classif. (of this report)	20. Security Classif. (of this page)	21. No. of pages	22. Price
Unclassified	Unclassified	160	A08

NASA FORM 1626 OCT 86

For sale by the National Technical Information Service, Springfield, Virginia 22161 GPO 787-805/79159